

Universität Stuttgart
Institut für Physikalische Chemie

Dissertation

The Electronic and Geometric Structure of Chemically Immobilised Catalysts in Mesopores

Mario Winkler
2023

The Electronic and Geometric Structure of Chemically Immobilised Catalysts in Mesopores

Von der Fakultät Chemie der Universität Stuttgart
zur Erlangung der Würde eines Doktors der Naturwissenschaften
(Dr. rer. nat.) genehmigte Abhandlung

Vorgelegt von
Mario Winkler
aus Ostfildern

Hauptberichter:	Prof. Dr. J. van Slageren
Mitberichter:	Prof. Dr. M.R. Buchmeiser
Prüfungsvorsitzender:	Prof. Dr. F. Gießelmann

Tag der mündlichen Prüfung: 16.05.2023

Institut für Physikalische Chemie der Universität Stuttgart
2023

Eidesstattliche Erklärung

Hiermit versichere ich, dass ich die hier vorliegende Arbeit mit dem Titel "The Electronic and Geometric Structure of Chemically Immobilised Catalysts in Mesopores" selbstständig verfasst und keine anderen als die angegebenen Quellen und Hilfsmittel verwendet habe. Aus fremden Quellen entnommene Passagen und Gedanken wurden als solche kenntlich gemacht.

Declaration of Authorship

I hereby certify that the dissertation entitled "The Electronic and Geometric Structure of Chemically Immobilised Catalysts in Mesopores" is entirely my own work except where otherwise indicated. Passages and ideas from other sources have been clearly indicated.

Stuttgart, 1. Juni 2023

Mario Winkler

Contents

Summary	x
Zusammenfassung	xvi
1 Introduction	1
2 Theoretical Background and Experimental Techniques	3
2.1 The Spin System	3
2.1.1 The Magnetic Moment of an Electron	4
2.1.2 Electron Zeeman Interaction - The g tensor	6
2.1.3 Nuclear Zeeman Interaction	10
2.1.4 Hyperfine Interaction - The A tensor	11
2.1.5 Nuclear Quadrupole Interaction	13
2.1.6 Zero-Field Interaction	15
2.1.7 Electron-Electron Interaction	16
2.1.8 Spin Dynamics	18
2.2 Spectroscopy and Magnetometry	19
2.2.1 Interactions of Spins with Microwaves	20
2.2.2 Continuous-Wave Electron Paramagnetic Resonance	23
2.2.3 Pulsed Electron Paramagnetic Resonance Spectroscopy	26
2.2.4 Magnetic Circular Dichroism	36
2.2.5 X-Ray Absorption and Emission	38
2.2.6 SQUID Magnetometry	41
2.2.7 Mössbauer Spectroscopy	44
2.3 Click Chemistry	59
3 Set-up of a Mössbauer Spectrometer	61
3.1 Parts of the Spectrometer	61
3.1.1 Velocity Drive Unit and Mössbauer Source	63
3.1.2 Detector Unit	65
3.1.3 Cryostat	66
3.1.4 Sample Holder	68
3.1.5 Measurement Computer and Software	70
3.2 Measurement and Evaluation of a Spectrum	73
3.2.1 Sample Positioning and Setting of Apertures	73
3.2.2 Sample Composition and Preparation	76

3.2.3	Sample Amount	78
3.2.4	Measurement Time	80
3.3	Data Analysis	81
3.3.1	Calibration of the Velocity Axis	81
3.3.2	Fitting of the Spectrum	83
3.4	Spectrometer Performance over Time and Source Lifetime	83
3.5	Example Measurements	86
3.5.1	Structure Determination of a Potential Photoswitch	86
3.5.2	Oxidation States in Synthetic Tochilinite	90
3.5.3	Temperature-Induced Spin Crossover	94
4	The Electronic and Geometric Structure of a Probe Molecule	99
4.1	Catalytic Behaviour of the Iron Compound	101
4.2	Magnetic Circular Dichroism Spectroscopy	102
4.3	X-Ray Absorption and Emission Spectroscopy	107
4.3.1	Core-to-Core and Valence-to-Core X-Ray Emission Spectroscopy	107
4.3.2	High Energy Resolution Fluorescence-Detected X-Ray Absorption Near Edge Structure	109
4.4	Mössbauer Spectroscopy	110
4.5	Electron Paramagnetic Resonance Spectroscopy	116
4.5.1	The Static Electronic Structure of the Molecule	116
4.5.2	Spin Dynamics of the Molecule from Pulsed EPR	121
4.5.3	Advanced Pulsed Electron Paramagnetic Resonance Methods	125
4.5.4	Immobilisation of the Probe Molecule into the Silica Material SBA-15131	
5	Chemically Immobilised Radicals in Mesopores	134
5.1	Why TEMPO? The Advantages of the Organic Radical as a Probe Molecule	135
5.2	The Electronic Structure of TEMPO and its Click-Ready Derivatives	138
5.2.1	The Static Electronic Structure - The g and Hyperfine Tensors	138
5.2.2	The Mobility of the Radical in different Matrices as a Model for Chemically Immobilised Species	144
5.2.3	The Spin Dynamics of TEMPO and its Derivatives	150
5.3	TEMPO in Covalent Organic Frameworks	155
5.3.1	The Synthetic Procedure to Immobilise the Organic Radical	157
5.3.2	Spin-Spin Interactions in the Model Compound	157
5.3.3	The Electronic Structure of immobilised TEMPO probed by Con- tinuous Wave Electron Paramagnetic Resonance	159

5.3.4	Spin Relaxation of TEMPO in COFs	165
5.3.5	Radical Distances in the COF from Double Electron-Electron Resonance Spectroscopy	170
5.4	TEMPO in the Porous Silica Material SBA-15	172
5.4.1	Synthetic Procedure to Immobilise the Radical in Azide-Functionalised SBA-15	172
5.4.2	The Electronic Structure Probed with Continuous Wave Electron Paramagnetic Resonance	174
5.4.3	The Spin Dynamics of TEMPO in SBA-15 as determined with Pulsed Electron Paramagnetic Resonance	176
5.5	Clicking into Ordered Mesoporous Carbon	178
6	Experimental Section	180
6.1	Experimental Techniques and Sample Preparation	180
6.1.1	Continuous-Wave EPR spectroscopy	180
6.1.2	Pulsed EPR spectroscopy	181
6.1.3	Mössbauer spectroscopy	182
6.1.4	MCD spectroscopy	182
6.1.5	SQUID magnetometry	182
6.1.6	Cyclic Voltammetry	183
6.1.7	ATR-IR Spectroscopy	183
6.1.8	X-Ray Emission Spectroscopy	183
6.1.9	NMR Spectroscopy	183
6.1.10	Elemental Analysis	183
6.1.11	Mass Spectrometry	183
6.1.12	Visualisation	184
6.2	Syntheses	184
	References	I
	Appendix	XVIII
A.1	Set-up of a Mössbauer Spectrometer	XVIII
A.1.1	Fit Parameters for the Different Aperture Settings	XVIII
A.2	The Electronic and Geometric Structure of a Probe Molecule	XX
A.2.1	Fit Parameters for the Mössbauer Spectra	XX
A.2.2	EPR Spectra and Spin Relaxation Times	XXI
A.2.3	ESEEM, HYSCORE and ENDOR Measurements and Simulations	XXV
A.2.4	Immobilisation of the Probe Molecule	XXXIII

A.3	Chemically Immobilised Radicals in Mesopores	XXXIII
A.3.1	Immobilisation with a Ruthenium catalyst	XXXIII
A.3.2	EPR spectroscopy and SQUID magnetometry	XXXV
A.3.3	Spin Dynamics of the Derivatives of TEMPO	XXXVI
A.3.4	Click Reaction	XLI
A.3.5	EPR Measurements of TEMPO-Terephthalate	XLI
A.3.6	Spin Dynamics of TEMPO immobilised in the COF	XLIV
A.4	Experimental Section	XLVIII
A.4.1	IR and Mass Spectra of the Synthesised Compounds	XLVIII

List of Abbreviations

a	Amplitude
A	Hyperfine interaction constant, absorption
A_{iso}	Isotropic component of the hyperfine interaction constant
ATR-IR	Attenuated total reflection infrared
B	Magnetic field
B_{hf}	Magnetic hyperfine field
c	concentration, speed of light, coefficient
C	Count rate, conversion factor
CtC	Core-to-core
COF	Covalent organic framework
D	Second rank axial zero-field splitting parameter
DEER	Double electron-electron resonance
δ_{IS}	Isomer shift
δ_{SOD}	Second-order Doppler shift
Δ	Energy barrier
e	Elementary charge
E	Second rank rhombic zero-field splitting parameter
ΔE_{Q}	Quadrupole splitting
$\Delta B_{\text{pp,G}}$	Gaussian peak-to-peak linewidth
$\Delta B_{\text{pp,L}}$	Lorentzian peak-to-peak linewidth
EEI	Electron-electron interaction
ENDOR	Electron-nuclear double resonance
EFG	Electric field gradient
EPR	Electron paramagnetic resonance
ESEEM	Electron spin echo envelope modulation
EZI	Electron Zeeman interaction
ε	Dielectric constant
g	g value
g_{e}	Free electron g value
g_{iso}	Isotropic g value
g_{N}	Nuclear g value
γ	Gyromagnetic ratio
Γ	Linewidth
Γ_{SD}	Interaction parameter in the Slichter-Drickamer model

h	Planck's constant
HERFD	High energy-resolution fluorescence detected
HFI	Hyperfine interaction
HYSCORE	Hyperfine sublevel correlation
i	Current
I	Nuclear spin, intensity
ICP-OES	Inductively coupled plasma optical emission spectrometry
J	Exchange interaction parameter
k	Rate constant, exponent
\mathbf{k}	Wave vector
m	Mass
m_I	Magnetic nuclear spin quantum number
m_S	Magnetic electron spin quantum number
μ	Magnetic moment
μ_0	Vacuum permeability
μ_B	Bohr magneton
μ_e	Mass absorption coefficient
μ_N	Nuclear magneton
MCD	Magnetic circular dichroism
MW	Microwave
NQI	Nuclear quadrupole interaction
NZI	Nuclear Zeeman interaction
ν	Frequency
η	Symmetry parameter of electric field gradient
OMC	Ordered mesoporous carbon
P	Microwave power
PMT	Photomultiplier tube
ϕ	Azimuthal angle
Ψ	Wave function
q	Charge
Q	Quadrupole moment
R	Distance
RF	Radio frequency
ρ	Rhombic component of the HFI, (charge) density
S	Electron spin
SNR	Signal-to-noise ratio
SQUID	Superconducting quantum interference device

σ	Standard deviation
t	Time, constant time between pulses
t'	Absorber thickness
T	Temperature, axial component of the hyperfine interaction
T_1	Spin-lattice relaxation time
T_2	Spin-spin relaxation time
T_M	Phase-memory time
τ	Incremented time between pulses
τ_{corr}	Rotational correlation time
θ	Polar angle
θ_D	Debye temperature
v	Velocity
V	Volume, potential energy
V_{zz}	Electric field gradient
VtC	Valence-to-core
$\tilde{\nu}$	Wavenumber
ω	Angular frequency
ω_I	Nuclear Larmor frequency
x	Molar/mass/volume ratio, position
XANES	X-ray absorption near-edge structure
χ	Susceptibility
ZFI	Zero-field interaction

Summary

Catalysis plays an important role in all aspects of life. Nature, for example, uses the confinement effect in enzymes to catalyse essential processes for the survival of all living species. [1–3] Humans have been taking advantage of catalytic processes to produce everyday chemicals, pharmaceuticals and all sorts of materials. [4–6] In the last century, it has become clear that the modern lifestyle is not sustainable, since humans will run out of raw materials and the negative aspects of environmental pollution have made life more and more difficult. Here, catalysis might play an important role, both for the energy-efficient production of materials and the reduction of environmental pollution. Two of the most prominent examples are the formation of H_2 as an alternative fuel and the reduction of CO_2 in the atmosphere. [7–9] Both can be achieved through processes with higher yields and lower energy consumption with new types of catalysts and catalytic reactions. Here, new catalytic systems that mimic the confinement effects in enzymes might help in realising these goals. [10, 11] Consequently, catalysis research has been shifting its focus to this field by developing porous materials where catalysts can be immobilised, thereby essentially copying enzymes. In order to understand and subsequently improve on these systems, the influence of the confinement on the catalytic system needs to be understood and correlated with the changes in catalytic activity. This is where this Thesis is linked to the research topic. Here, the influence of the functionalisation and immobilisation into porous materials on the electronic structure of a probe molecule are investigated. The chosen probe molecule, $(dppf)Fe(CO)_3$, was chosen for its many spectroscopic handles. This previously reported bimetallic iron compound [12] can be investigated with many spectroscopic methods, such as Mössbauer, X-ray emission and absorption, nuclear magnetic resonance (NMR) and infrared (IR) spectroscopies. Since a catalyst most often undergoes a change in the oxidation state, e.g. in redox reactions, the stable paramagnetic form of the compound was to be investigated as well. Here, in addition to the mentioned techniques, methods such as electron paramagnetic resonance (EPR) and magnetic circular dichroism (MCD) spectroscopies as well as magnetometry are great tools to study the paramagnetic compound. Preliminary results given in [12] indicated the oxidation to take place on the carbonyl iron. This is evident from IR spectroscopy where an increase of the vibration frequency of the carbonyl groups that are attached to one of the iron atoms in the molecule most likely results from the removal of an electron from an anti-bonding orbital. In order to support and expand on these results, the aforementioned experimental techniques were used to study both the neutral and oxidised compounds in great detail, in order to investigate the changes that result from the oxidation to learn about the catalytic activity and mechanism, as well as those changes that result from

the functionalisation and immobilisation to allow for the understanding of the catalytic activity under confinement.

In order to perform Mössbauer spectroscopy, a new spectrometer was set up as part of this work. The set-up is presented in the first results Chapter and the investigation of the probe molecule outside of the pores is presented in the second results Chapter. Since the immobilisation of the molecule proved to be very challenging, instead the organic radical TEMPO was immobilised in three different porous materials. The measurements and their analyses are presented in the third results Chapter. The results of all three research areas are summarised in the following.

For the set-up of the Mössbauer spectrometer, an available Janis SVT400 cryostat was coupled with an RCTM 3rd Generation MS-96 Mössbauer spectrometer. A ^{57}Co source in a rhodium matrix by RitVerc was used. After the installation of the spectrometer, the design and construction of a sample holder and first measurements to confirm the functionality of the spectrometer were done. Subsequently, the influences of the individual parts of the set-up were tested carefully. It was shown that the correct adjustment of height and angle of the sample holder relative to the centre of the gamma ray beam path are crucial to maximise the signal-to-noise ratio. Here, discrepancies of more than a millimetre in height and 5° in angle lead to a substantial drop of the signal intensity. The setting of the apertures on either side of the sample was shown to also impact the number of counts at the detector, i.e. larger openings increased the area the gamma rays can pass through, which in turn increases the signal intensity. In the literature, a Gaussian broadening of the absorption line could be observed for large aperture settings. [13, 14] This could not be seen here, possibly due to the design of the aluminium sample holder that acts as a third aperture itself with a relatively small opening compared to aperture settings for which a Gaussian broadening would be expected. It was shown that an optimal sample amount in terms of the absolute number of iron ions exists, which was determined to be ca. 0.3 mg of ^{57}Fe . In our set-up this is more than the sample amounts that were used in the measurements presented in this Thesis due to a low availability of typical research samples. Sample holders for the measurement of loose powders, pressed pellets and frozen solutions were designed, manufactured and tested, where it was observed that loose powders are preferred as these samples are the easiest to handle and give the best signal-to-noise ratio after comparable measurement times, as it is easiest to place the sample into the centre of the gamma ray beam without the requirement set by the availability of pellet press diameters. It was shown that spectra at temperatures

between 3 and 300 K could be recorded and the influence of the temperature on the spectra was investigated. For samples that do not show temperature-dependent phenomena, such as spin crossover, slow relaxation of the magnetic moment or temperature-dependent isomerisation and charge distribution, lowering the temperatures increases the signal intensity due to an increase of the recoil-free fraction. Unless a temperature dependence below 80 K was expected, e.g. from magnetometry measurements, the Mössbauer spectra were recorded at 80 K by cooling with liquid nitrogen and compared to room temperature measurements. Whenever significant differences between the two spectra could be observed spectra at intermediate temperatures were recorded. It was chosen to cool with liquid nitrogen as it is much cheaper and easier to handle than liquid helium and the signal intensity does not increase drastically from 80 to 4 K. The Chapter concludes with the presentation of the measurements of three different samples showing the capabilities of Mössbauer spectroscopy. The investigation of an azo compound, a potential photo-switch, confirmed the presence of two isomers, the ratio of which could be determined with Mössbauer spectroscopy. Furthermore, the relative amounts of Fe^{II} and Fe^{III} species in different environments in synthetic iron sulfide minerals could be determined, helping in the characterisation of the newly synthesised compounds. Lastly, the temperature dependent ratio of low-spin and high-spin Fe^{II} during spin crossover was investigated, helping in understanding the behaviour of these potential magnetic switches for data storage or quantum sensors.

In the second Chapter, the spectroscopic investigation of the probe molecule is presented. Firstly, the catalytic activity in the hydrogen evolution reaction was investigated with cyclic voltammetry. Although the molecule (dppf)Fe(CO)₃ does catalyse the hydrogen production in acidic solutions, a very low reaction rate was observed. In order to understand this behaviour, the electronic structure was investigated in detail. Preliminary results indicated the oxidation to take place on the carbonyl iron. This was concluded from the shift of the energy of the CO vibrations which is only expected for a change of the number of electrons in (anti-)bonding CO orbitals, and the presence of an EPR signal. The EPR signal was attributed to an Fe^I species with two isomers existing at room temperature with a temperature dependent isomer ratio. These results were expanded on in the scope of this Thesis. The MCD spectrum of the oxidised compound differs strongly from both the neutral compound and ferrocenium, a low-spin Fe^{III} compound for comparison. These differences suggest that the oxidation does not take place on the ferrocene iron in the probe molecule. X-ray absorption and emission spectra confirmed the oxidation states in the neutral compound to be 0 and +2 and show a similarity of the

spectra of the oxidised form to those of a Fe^{I} species. Core-to-core X-ray emission spectra confirmed an increase of the electron spin during oxidation. Mössbauer spectroscopy unambiguously confirmed the oxidation states of 0 and +2 in the neutral compound and +1 and +2 in the oxidised species by comparison to compounds with known oxidation states. Also, the existence of two isomers at room temperature was confirmed. At lower temperatures only one of the isomers is present. Below 7 K, the Mössbauer spectrum shows an increase of the absorption linewidth that was attributed to a spin-lattice relaxation time on the order of the Mössbauer timescale. Similar, but more pronounced behaviour was observed for ferrocenium that gives a magnetically split sextet below 10 K. The magnetic relaxation was further investigated with SQUID magnetometry, where it was shown that the paramagnet acts as a field-induced single-molecule magnet with slow relaxation of the magnetic moment in applied fields. It was shown that the relaxation is weakly influenced by external fields. Lastly, EPR spectroscopy was used to investigate the open-shell oxidised species. X-Band EPR spectra confirmed the presence of only one isomer at low temperatures with a hyperfine coupling to the surrounding ^{31}P nuclei. High-field EPR spectra confirmed the spin to be $S = 1/2$ as all observed signals arose from transitions within the $m_S = \pm 1/2$ states for microwave frequencies up to 400 GHz. Pulsed EPR showed that the spin-lattice relaxation can be modelled as a combination of direct and Raman processes with relaxation times that are longer in frozen solution than in the powder, possibly due to different spin-spin distances and different phonon spectra of the two samples. The long phase-memory times allowed for the use of advanced pulsed EPR methods such as electron-nuclear double resonance (ENDOR) and hyperfine sub-level correlation (HYSCORE) spectroscopies. Both methods are used to better determine the hyperfine tensor components. HYSCORE spectra allowed for the resolution of the coupling to hydrogen and carbon nuclei that is usually unresolved in EPR spectra due to coupling strengths below the natural linewidth. ENDOR spectra confirmed the coupling to the phosphorus nuclei and additionally showed a coupling to fluorine atoms that are only present in the counter ion, suggesting a close association between the complex and the counter ion. This may explain the low catalytic activity of the compound. Although it was planned to immobilise the molecule in mesopores, the oxidised species of the functionalised probe molecule proved to be very unstable, preventing its immobilisation into porous materials. Therefore, the organic radical TEMPO was chosen instead.

In order to quantify the influence of the confinement on the electronic structure of a catalyst, the behaviour of the catalyst outside of the pores must be understood first. The electronic and geometric structure of the organic radical TEMPO has been the focus of

many research projects. [15, 16] It has been used to catalyse the oxidation of alcohols, i.e. its catalytic activity is established. [17, 18] It has also been used as a spin label for the elucidation of the structure of proteins, meaning it can also function as such a label inside the pores. [19, 20] The EPR signal of TEMPO is unique due to the hyperfine coupling of the electron spin to the nitrogen nucleus and it is strongly affected by intermolecular distances and the mobility of the radical due to the behaviour of anisotropic interactions in mobile species. All of these aspects make TEMPO the perfect probe molecule to study the confinement effects. In this Thesis, the changes in the electronic structure of the radical and its orientation within the pore were investigated. The g and A tensors of TEMPO and its click-ready derivatives 4-azido-TEMPO and 4-propargyl ether TEMPO were determined with EPR spectroscopy at ca. 10, 35 and 320 GHz. It was shown that the principal values of the tensors depend on temperature, magnetic field and the surroundings of the molecule. The hyperfine tensor becomes more axial when going from TEMPO to the functionalised derivatives which may be attributed to a different localisation of the unpaired electron due to a change in the molecular orbitals. With X-Band EPR the influence of different surroundings on the mobility was studied to compare the results to those of the immobilised radical. For very low mobilities, i.e. in frozen solutions and a sugar matrix, powder-like EPR spectra were obtained. In liquid solutions the anisotropic interactions are averaged out and only the isotropic hyperfine interaction could be observed. It was shown that the linewidth of the EPR signal increases with the concentration due to exchange interactions, albeit at slower rates in frozen solutions compared to liquids. In polymer matrices, mobility values between those in liquids and solids could be observed at room temperature. This mobility could be frozen at low temperatures. The investigation of the spin relaxation times showed that the spin-lattice relaxation time is different for excitations in the three orientations g_{xx} , g_{yy} and g_{zz} , possibly due to an anisotropy of the vibrations that induce relaxation. The temperature dependence of the spin-lattice relaxation (T_1) and phase-memory (T_M) times behave as is observed in literature for TEMPO and its derivatives. T_1 decreases exponentially with increasing temperatures and T_M first increases from 7 to ca. 20 K and then decreases slowly for higher temperatures.

Different catalysts for the clicking reaction were tested before the final system was chosen because of high yields and fast reaction times. TEMPO was clicked into covalent organic frameworks (COFs) with different amounts of alkyne groups, mesoporous silica SBA-15 and ordered mesoporous carbon (OMC). In order to study the influence of the short distances in the COF due to the attachment of two radicals to one building block of the COF, this building block was investigated in parallel. It was shown that the spin-lattice relaxation time decreases by an order of magnitude compared to the free radical

because of the intramolecular exchange interactions. Furthermore, this interaction also slightly increases the EPR linewidth. For SBA-15, different molar ratios of TEMPO to the number of azide groups in the material were investigated. For both types of materials it was shown that chemically immobilised species can be distinguished from mobile, physisorbed molecules with EPR spectroscopy. For both COFs and SBA-15, the EPR absorption line broadened for higher concentrations of TEMPO due to the decreased mobility, that was similar to that of TEMPO in polystyrene, and increased exchange interactions due to decreasing intermolecular distances. This also explained the shorter spin-relaxation times, rendering pulsed EPR measurements impossible. The relaxation was further accelerated because of leftover paramagnetic copper species from the click reaction. Nonetheless, it proved to be possible to carry out a double electron-electron resonance (DEER) measurement for one of the COF concentrations. From these DEER measurements it could be shown that radical-radical distances in the range of 2 nm exist in the COF. These can only be explained when radicals point towards the centre of the pore. Another indication for that is that A_{zz} is unchanged in the COF compared to the free radical. A_{zz} originates predominantly from the dipolar interaction with the nitrogen nucleus and is therefore a marker for the surrounding as it would significantly increase with the polarity of the surrounding. [21] This increase in A_{zz} could be observed in SBA-15, indicating a collapse of the radical to the pore wall. Alternatively this increase could be explained with residual water that remained in the polar pores even after subsequent washing with unpolar solvents. For OMC a range of different radical distances could be observed from the EPR spectrum but no mobile species could be seen from the spectrum, confirming the successful immobilisation of TEMPO in the porous material.

Zusammenfassung

Katalyse spielt in allen Aspekten des Lebens eine wichtige Rolle. So nutzt zum Beispiel die Natur die räumliche Einschränkung in Enzymen für lebensnotwendige Prozesse. [1–3] Dabei können unter anderem durch den geringen zur Verfügung stehenden Platz und die damit dirigierende Geometrie selektiv chemische Reaktionen durchgeführt werden. Auch die Industrie nutzt katalytische Prozesse um Alltagsprodukte wie Nahrungsmittel, Medikamente, Baustoffe, Verpackungsmaterialien und Brennstoffe herzustellen. [4–6] Dabei hat sich im letzten Jahrhundert herausgestellt, dass diese Prozesse rohstoff- und energieeffizienter stattfinden müssen um der Ressourcenknappheit und Verschmutzung der Atmosphäre entgegenzuwirken. Hier kann insbesondere die Entwicklung neuer Katalysatoren zur Problemlösung beitragen, weshalb sich die Forschung in Richtung der Untersuchung von katalytischen Prozessen entwickelt hat. Dabei geht es insbesondere um die katalytische Reduktion von atmosphärischem CO₂, der Herstellung alternativer Brennstoffe wie Wasserstoff und der Zersetzung von Polymeren zur Verhinderung weiterer Verschmutzung durch Plastik. [7–9] Einer der Lösungsansätze ist das Ausnutzen der räumlichen Beschränkung der katalysierten Reaktion, so wie es in Enzymen der Fall ist, und die Verwendung von in der Natur häufig vorkommendem Eisen. [10, 11] Dabei ist es von Vorteil, wenn der Katalysator in der Pore fest mit der Porenwand verbunden ist um die Reaktion in diesem Bereich zu erzwingen. Das erlaubt auch das selektive Anbringen von Cokatalysatoren in der Nähe der immobilisierten Katalysatoren. Dazu wurden verschiedene Immobilisierungsverfahren entwickelt. Eines der prominentesten Beispiele zur Erzeugung einer chemischen Bindung in Poren ist die sogenannte Klick-Chemie bei der eine terminale Azid-Gruppe und ein Alkin in Anwesenheit einer Kupfer(I)-Spezies zu einem Triazol-Ring reagieren. Diese Strategie wurde auch in dieser Arbeit verwendet. Um die Einflüsse der Immobilisierung zu verstehen und daraus neue Katalysatorsysteme abzuleiten, muss untersucht werden, wie sich die elektronische und geometrische Struktur des Katalysators durch die Immobilisierung verändern. Um das zu erreichen wurde in dieser Arbeit das Sondenmolekül (dppf)Fe(CO)₃ [12] gewählt, da es viele verschiedene spektroskopische Untersuchungen zulässt. Dazu gehören neben Mössbauer-, Röntgenabsorption-, Röntgenemission-, Infrarot-, Kernspinresonanz- und optischer Spektroskopie für den neutralen Zustand zusätzlich Elektronenspinresonanz- (ESR-), magnetische Zirkulardichroismus- (MCD-)-Spektroskopie und Magnetometrie für den oxidierten Zustand. Für die Immobilisierung bieten sich an dem Ferrocen-Ring des Moleküls einige Funktionalisierungsmöglichkeiten an. Für die Untersuchung mittels Mössbauer-Spektroskopie musste ein neues Spektrometer aufgebaut werden. Dieser Aufbau wird im ersten Ergebnis-Kapitel thematisiert und im zweiten Ergebnis-Kapitel werden die Untersuchun-

gen des Sondenmoleküls außerhalb der Pore beschrieben. Da sich herausgestellt hat, dass das funktionalisierte Molekül im oxidierten Zustand nicht stabil ist wurde stattdessen das organische Radikal TEMPO untersucht und in verschiedenen porösen Materialien, nämlich einen COF (engl. covalent organic frameworks), SBA-15 und OMC (engl. ordered mesoporous carbon) immobilisiert. Die Ergebnisse dazu werden im dritten Ergebnis-Kapitel gezeigt. Im Folgenden werden die wichtigsten Ergebnisse kurz zusammengefasst.

In dem in dieser Arbeit verwendeten Aufbau wurde ein RCTM 3rd Generation Mössbauer-Spektrometer mit einem Janis SVT400 Kryostaten gekoppelt. Als Quelle wurde ⁵⁷Co in einer Rhodium-Matrix der Firma RitVerc verwendet. Nach der Installation des Spektrometers, der Konstruktion und Fertigung des Probenhalters, sowie ersten Testmessungen zur Bestätigung der Funktion des Aufbaus wurden die Einflüsse der einzelnen Messparameter untersucht. Dabei stellte sich heraus, dass die genaue Position der Probe im Strahlengang relevant ist um die Messzeit zu minimieren. Hier sollten Abweichungen von weniger als ein Millimeter in der Höhe und 5° im Winkel eingehalten werden um das Verhältnis aus Signal-zu-Rauschen bei gleichbleibender Messzeit zu maximieren. Auch die Größe der Blenden auf beiden Seiten der Probe hat einen Einfluss auf die Intensität der auf den Detektor fallenden Strahlung. Obwohl bekannt ist, dass zu große Blendeneinstellungen zu einer Gauß-Verbreiterung der Absorptionslinien führen können [13, 14], wurde dieses Verhalten hier nicht beobachtet, vermutlich weil der Aluminiumprobenhalter selbst als Blende fungierte. Es wurde gezeigt, dass es einen Bereich optimaler Probenmengen gibt, da darüber Streuung die Strahlungsintensität am Detektor unverhältnismäßig stark reduziert. Es wurden Probenhalter für drei verschiedene Probentypen konstruiert und gefertigt um die Messung von losen Pulvern, Presslingen und gefrorenen Lösungen zu erlauben. Dabei stellte sich heraus, dass, für die hier entwickelte Konstruktion, die Messung von losen Pulvern die intensivsten Signale und einfachste Probenvorbereitung bei vergleichbarer Messzeit lieferte. Mit Hilfe des Kryostaten konnten Temperaturen zwischen 3 und 300 K erreicht werden und der Einfluss der Temperatur auf die Messungen wurde untersucht. Hier wurden Phänomene wie Spin Crossover, Valenz-Tautomerie, Isomerisierung und langsame Relaxation des magnetischen Moments beobachtet. Für Proben bei denen keiner dieser Effekte auftrat, führte eine Temperaturniedrigung nur zu intensiveren Signalen aufgrund des höheren Anteils an rückstofffreien Absorptionsprozessen. Diese Proben wurden dementsprechend nur bei Zimmertemperatur oder 80 K gemessen, wobei die Kühlung mit flüssigem Stickstoff realisiert wurde. Am Ende des Kapitels werden drei Proben vorgestellt bei denen Mössbauer-Spektroskopie wichtige Ergebnisse liefern konnte. Dabei wurde für zwei Azoverbindungen gezeigt, dass jeweils zwei Isomere vorliegen, deren

Verhältnis per Bestrahlung mit Licht gesteuert werden können soll. Des Weiteren konnte für synthetisches Mackinawit, ein Eisensulfid, der Anteil an Eisen in den Oxidationsstufen +2 und +3 in Oktaeder- und Tetraederlücken per Mößbauer-Spektroskopie bestimmt werden, was bei dem Verständnis der Chemie der Verbindung hilft. Zuletzt wurde für eine Eisenverbindung der temperaturabhängige Spin Crossover untersucht. Diese Verbindung stellt damit ein potentiellen magnetischen Schalter oder Quanten-Temperatursensor dar.

Im zweiten Kapitel werden die spektroskopischen Messungen des gewählten Sondenmoleküls $(\text{dppf})\text{Fe}(\text{CO})_3$ präsentiert. Es konnte gezeigt werden, dass das Molekül die Wasserstoffherstellung aus sauren Lösungen katalysiert, jedoch bei sehr geringen Reaktionsraten. Um dieses Verhalten zu verstehen wurde die elektronische Struktur der Verbindung untersucht. Vorläufige Ergebnisse ließen vermuten, dass die Oxidation am Carbonyl-Eisen stattfindet, da ein typisches Fe^{I} ESR-Signal zu beobachten war und die Schwingungsfrequenz der Carbonyl-Schwingung zu höheren Energien verschoben wurde. In dem ESR-Spektrum waren zwei Signale zu beobachten, woraus geschlossen wurde, dass zwei Isomere vorlagen. An diese Messungen wurde in dieser Arbeit angeknüpft. Mittels MCD-Spektroskopie konnte gezeigt werden, dass sich die oxidierte und neutrale Verbindung maßgeblich unterscheiden und die oxidierte Verbindung auch keine Ähnlichkeiten zu der Fe^{III} -Verbindung Ferrocenium aufweist. Auch Messungen mittels Röntgenabsorption und -emission stützen die Hypothese einer Oxidation am Carbonyl-Eisen wodurch Eisenionen in den Oxidationsstufen +1 und +2 vorlägen. Auch konnte gezeigt werden, dass sich der Gesamtspin der Verbindung durch die Oxidation erhöhte. Die Messung von Mössbauer-Spektren der neutralen und oxidierten Verbindung im Vergleich mit ähnlichen Proben mit bekannten Oxidationsstufen bestätigte dann den Ort der Oxidation endgültig. Außerdem konnte die Temperaturabhängigkeit des Isomerverhältnisses bestimmt werden. Unterhalb von 50 K lag dabei nur noch eines der beiden Isomere vor, was auch die spätere Untersuchung mittels ESR-Spektroskopie vereinfachte. Unterhalb von 7 K konnte außerdem in den Mössbauer-Spektren eine Erhöhung der Linienbreite erkannt werden, was auf langsame Relaxation des paramagnetischen Moments zurückgeführt wurde. Ein ähnliches, aber deutlich ausgeprägteres Verhalten konnte in Ferrocenium beobachtet werden, das unterhalb von 10 K das typische Sextett für magnetische Proben zeigt. Die Spin-Gitter-Relaxation in angelegtem Magnetfeld wurde daraufhin mittels SQUID-Magnetometrie untersucht. Es konnte gezeigt werden, dass der Paramagnet als feldinduzierter Einzelmolekülmagnet agiert und dass die magnetische Relaxation kaum durch externe Magnetfelder beeinflusst wurde. Die Untersuchung mittels ESR-Spektroskopie bei Mikrowellenfrequenzen zwischen ca. 10 und 400 GHz bestätigte den

angenommenen Elektronenspin $S = 1/2$ und eine Hyperfeinwechselwirkung des Elektronenspins mit den umliegenden Phosphoratomen. Diese wurde auch mittels fortgeschrittenen Methoden der gepulsten ESR untersucht, wobei festgestellt werden konnte dass zusätzlich zur Kopplung zu den Phosphor-, Wasserstoff- und Kohlenstoffatomen auch eine Wechselwirkung mit Fluoratomen beobachtet werden konnte. Diese ist auf eine räumliche Nähe des Gegenions zurückzuführen, was möglicherweise auch die geringe katalytische Aktivität erklärt. Zuletzt wurde gezeigt, dass die Spin-Gitter-Relaxation mittels direkten und Raman-Relaxationsprozessen erklärt werden kann. Obwohl geplant war, die Verbindung in Poren zu immobilisieren, war die Funktionalisierung des Ferrocen-Rings sehr herausfordernd, und alle Immobilisierungsversuche führten zu Zersetzung des Komplexes und es musste eine andere Verbindung für die Immobilisierung gewählt werden.

Als Alternative zu $(\text{dppf})\text{Fe}(\text{CO})_3$ wurde das organische Radikal TEMPO gewählt. Dessen elektronische Struktur wurde weitreichend untersucht und es wird schon länger als Spinsonde eingesetzt, zum Beispiel für die Bestimmung der Struktur von Proteinen, indem die Abstände der an das Protein in bekannten Positionen fixierten Radikale bestimmt wurden. [15, 16, 19, 20] Zusätzlich ist das Radikal TEMPO im Gegensatz zu $(\text{dppf})\text{Fe}(\text{CO})_3$ tatsächlich ein guter Katalysator. [17, 18] Einer der Hauptgründe für die zahlreichen Einsatzgebiete von TEMPO sind dessen lange Spin-Relaxationszeiten, die fortgeschrittene Pulssequenzen, z. B. DEER (engl. double electron-electron resonance), zulassen. Außerdem macht das einzigartige ESR-Spektrum von TEMPO eine eindeutige Unterscheidung von eventuellen Hintergrundsignalen möglich. Dies ist besonders bei geringen Probenmengen, wie sie in Poren zu finden sind, von großem Vorteil. Zusätzlich dazu ist das ESR-Signal von TEMPO stark von intermolekularen Abständen und der Beweglichkeit des Moleküls abhängig, was die Untersuchung der Mobilität des Katalysators in der Pore ermöglicht. In dieser Arbeit wurden die g - und A -Tensoren von TEMPO und seinen klickbaren Derivaten 4-Azido-TEMPO und 4-Propargylether-TEMPO untersucht. Dazu wurden ESR-Spektren zwischen 6 K und Zimmertemperatur und bei ca. 10, 35 und 320 GHz aufgenommen. Dabei wurde aus der Veränderung des A -Tensors festgestellt, dass sich die Position des ungepaarten Elektrons bei der Funktionalisierung leicht verändert. Auch konnte eine Abhängigkeit der Tensorelemente von der Temperatur, dem Magnetfeld und der Umgebung des Radikals erkannt werden. Hier ist besonders A_{zz} von der Polarität der Umgebung abhängig. Um den Einfluss der Beweglichkeit des Moleküls zu untersuchen wurden Proben in verschiedenen Matrizen gemessen. In Flüssigkeiten fand bereits bei relativ geringen Radikalkonzentrationen eine Austausch-Wechselwirkung zwischen den Molekülen statt. In gefrorener Lösung fand diese auch

statt, jedoch erst bei deutlich höheren Konzentrationen. In Polystyrol konnte eine mittlere Beweglichkeit bei Zimmertemperatur beobachtet werden. Bei tiefen Temperaturen konnte diese Beweglichkeit eingefroren werden und das Spektrum ähnelte sehr stark dem von gefrorenen Lösungen. Mittels gepulster ESR-Spektroskopie konnte gezeigt werden, dass die Relaxation des angeregten Spins in die drei Richtungen g_{xx} , g_{yy} und g_{zz} unterschiedlich ist. Das liegt vermutlich an der Anisotropie der Schwingung der NO-Bindung über dessen Kopplung zum Spin die Relaxation stattfindet. Die beiden Relaxationszeiten T_1 (Spin-Gitter-Relaxationszeit) und T_M (Phasengedächtniszeit) verhalten sich wie aus der Literatur bekannt. T_1 sinkt exponentiell mit steigender Temperatur aufgrund der beiden relevanten Relaxationsprozesse, dem direkten und Raman-Prozess, und T_M steigt zunächst bei Temperaturerhöhungen von 7 auf ca. 20 K, erreicht da ein Plateau und sinkt dann bei weiter steigender Temperatur, vergleiche [22–25].

Für die Klickreaktion wurden verschiedene Katalysatorsysteme getestet bevor die Wahl nach Reaktionszeit und Ausbeute getroffen wurde. TEMPO wurde anschließend in einen COF, SBA-15 und OMC geklickt, wobei bei dem COF Materialien mit unterschiedlichen Alkin-Konzentrationen und bei SBA-15 unterschiedliche Verhältnisse TEMPO zu Azid-Gruppen im Material untersucht wurden. Da im COF aufgrund der Bindung von zwei TEMPO-Radikalen an einen Baustein kurze Radikalabstände erwartet wurden, wurde zusätzlich dieser Baustein untersucht. Dabei stellte sich heraus, dass eine intramolekulare Austauschwechselwirkung zu beobachten war, wodurch auch die Spin-Gitter-Relaxationszeit um eine Größenordnung sank. Sowohl in COFs als auch in SBA-15 konnte gezeigt werden, dass chemisch gebundene TEMPO-Radikale ein anderes ESR-Spektrum aufweisen als TEMPO das sich frei in der Pore bewegen kann. Damit konnte gezeigt werden, dass bei ausreichend langen Klickreaktionszeiten ein vollständiger Umsatz stattfindet. Bei beiden Materialien konnte auch gezeigt werden, dass bei steigender TEMPO-Konzentration die Beweglichkeit der Moleküle in der Pore sank und die Austausch-Wechselwirkung zunahm. Diese Effekte spiegelten sich auch in den verkürzten Relaxationszeiten wider. In den COFs blieben zusätzlich paramagnetische Kupferionen aus der Klickreaktion in den Poren. Die magnetische Wechselwirkung zu diesen wirkte sich ebenfalls negativ auf die Lebenszeiten des angeregten Spinzustandes in den TEMPO-Radikalen aus. Dennoch konnten in einer der TEMPO-COF-Proben DEER-Messungen durchgeführt werden. Diese zeigten Abstände im Bereich von 2 nm und im Bereich der Porengröße von ca. 3 nm. Ersteres ist ein Indiz darauf, dass die TEMPO-Radikale, die zu einem Spin-Echo im DEER-Experiment führen, in die Porenmitte zeigen, da sonst geringere Abstände beobachtet hätten werden müssen. Letzteres beweist die regelmäßige Struktur des porösen Materials. Für TEMPO in SBA-15 hingegen konnte gezeigt werden, dass tatsächlich eine Annäherung an die polare

Porenwand stattfand. Dies wurde durch die Erhöhung von A_{zz} in polaren Umgebungen erklärt. [21] Alternativ könnte diese Erhöhung auch mit zurückgebliebenem Wasser, mit dem die Poren nach der Immobilisierung von TEMPO gereinigt wurden, zusammenhängen, obwohl im letzten Schritt noch mit organischen Lösemitteln gewaschen wurde. Im COF ist A_{zz} gleich wie für TEMPO in organischen Lösemitteln, jedoch ist hier die Porenwand auch deutlich unpolarer als in SBA-15. Das spricht wie auch die DEER-Messungen dafür, dass TEMPO in die Porenmitte zeigt. Für OMC konnte gezeigt werden, dass eine Reihe an unterschiedlichen TEMPO-TEMPO-Abständen nach dem Klicken vorliegt, was für eine bevorzugte Immobilisierung in nächster Nähe zueinander spricht, zum Beispiel am Poreneingang. Eine gleichmäßige Verteilung der TEMPO-Radikale über die gesamte Pore hätte zu deutlich geringeren Linienbreiten geführt. Es konnten keine mobilen Spezies beobachtet werden, was für eine erfolgreiche Immobilisierung spricht.

1 Introduction

In the early days of earth, life was impossible. Only by the formation of first catalytically active systems, assumed to be iron sulfides made from two of the most abundant elements at the time, chemical reactions towards small molecules and later life-enabling proteins were feasible. [26–32] Now, billions of years later, nature still uses iron complexes in enzymes, most prominently in [FeFe] hydrogenase. [1–3, 33–35] Similarly, industry takes advantage of catalysis to produce everyday materials such as plastics, pharmaceuticals and food. [4–6, 36–38] Resource depletion, especially in the last decades, has driven research towards finding more efficient chemical processes, alternative fuels and cleaning of the greenhouse gas polluted atmosphere. [7–9, 39] To achieve these goals, while ensuring sustainability, it was recently proposed to mimic nature by using predominantly abundant iron as the catalytically active centre and by copying the confinement effect of enzymes that allow improving the selectivity of chemical reactions. [10, 11, 40]

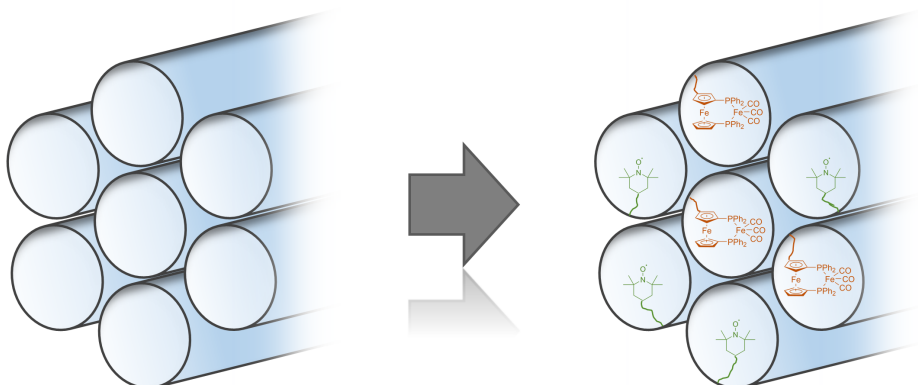


Figure 1.1: Schematic representation of the immobilisation of the probe molecules (dppf)Fe(CO)₃ (orange) or TEMPO (green) in porous materials via click chemistry.

The aim of this Thesis is to understand the changes in the electronic and geometric structure of the catalysts as a result of immobilisation in porous materials, i.e. under confinement. In order to force the catalysed reaction to take place within the confined space in the pores, as only then confinement-enhanced catalysis can be achieved, the catalyst is to be chemically linked inside the pore, thereby effectively using one of the main advantages of enzymes. Since the general influence of the immobilisation is of interest, it is not necessary to study a high-performance catalytic system but rather a model compound that is straightforward to measure with a multitude of spectroscopic methods while being easy to functionalise to allow the chemical immobilisation. To this end, the widely used

azide-alkyne Huisgen cycloaddition, the so-called click reaction, was chosen as it proved to be quick while giving high yields. [41–44] The probe molecule $[(\text{dppf})\text{Fe}(\text{CO})_3]$ ($\text{dppf} = 1,1'$ -bis(diphenylphosphino)ferrocene, see Figure 1.1) was chosen as the probe molecule, as it provides the required spectroscopic handles, primarily in the form of electron paramagnetic resonance (EPR). EPR is widely used to study the structure of open-shell transition metal compounds, i.e. the stable oxidation product of $(\text{dppf})\text{Fe}(\text{CO})_3$ [12]. Other methods that allow for the investigation of the electronic and geometric structure of the probe molecule and the confirmation of the successful functionalisation of the ferrocene ring for the click reaction are nuclear magnetic resonance (NMR) spectroscopy to study the chemical composition and geometric structure of diamagnetic compounds, infrared (IR) spectroscopy to investigate the changes at the carbonyl iron as the carbonyl vibration frequencies are highly dependent on the atom they are bound to, UV/Vis spectroscopy to study the absorption spectra giving an idea of the electronic structure, X-ray absorption and emission as well as Mössbauer spectroscopies to investigate the element-specific electronic structures and immediate surroundings. For the latter a Mössbauer spectrometer had to be set up.

The process of installation and characterisation of the Mössbauer spectrometer that was used to investigate the probe molecule, as well as exemplary measurements that are related, amongst others, to the study of iron sulfide catalysts that are assumed to be involved in the formation of life on earth, are presented in the first results Chapter of this Thesis. The investigation of the chosen probe molecule is presented in the second results Chapter. Unfortunately, the functionalisation of the ferrocene moiety turned out to be prohibitively challenging and the easily functionalisable [45, 46] and well-known [47–50] radical TEMPO (TEMPO = (2,2,6,6-tetramethylpiperidin-1-yl)oxyl, see Figure 1.1) was immobilised in the porous materials instead. As examples of such materials, covalent organic frameworks (COFs), mesoporous silica SBA-15 and ordered mesoporous carbon (OMC) were selected. COFs give well-defined, tailorable structures where azide or alkyne groups can be precisely positioned, making them one of the most promising candidates for catalysis in confined spaces. [51–54] SBA-15 is a material for which simple post-synthetic functionalisation methods are known, including the option for ion pairing by exchanging silicium with charged species in the porous framework. [55–58] OMC is another relatively new type of materials that is promising due to a wide range of possible pore sizes and similar functionalisation strategies as for SBA-15. [59–61] The investigation of the electronic structure of TEMPO and its click-ready derivatives as well as the effect of the immobilisation in the three materials is presented in the third results Chapter.

2 Theoretical Background and Experimental Techniques

In this Chapter, the theoretical background for understanding the properties of compounds with unpaired electrons in magnetic fields and their experimental investigation with spectroscopy and magnetometry is presented. Furthermore, an overview over click chemistry is given.

2.1 The Spin System

The behaviour of unpaired electrons is the basis of many phenomena in nature. Most importantly, they are the reason for magnetism and magnetic order. Furthermore, paramagnetic molecules play an important role in catalysis. Understanding paramagnetism of molecules is therefore important in the research of applications where magnetism is to be employed, e.g. magnetic data storage in single-molecule magnets, and in the study of catalytic systems. Although the magnetic moment resulting from the spin of an electron is a quantum mechanical phenomenon that can not be explained with classical physics, its properties can be understood to a certain level with classical concepts. On the other hand, phenomena such as the superposition of energy levels requires the quantum mechanical explanation of the same. In the following a brief introduction to both concepts is given.

The most important Hamiltonians to model the behaviour of both electron and nuclear spins as well as their interactions are given in Equation (2.1). The individual interactions are the electron Zeeman interaction (EZI), nuclear Zeeman interaction (NZI), hyperfine interaction (HFI), nuclear quadrupole interaction (NQI), zero-field interaction (ZFI) and electron-electron interaction (EEI). The first three are of importance whenever both nuclear and electron spins exist in close proximity. NQI is relevant only for nuclear spins $I \geq 1$, ZFI is relevant for electron spins $S \geq 1$ and EEI is important when two electron spins are in close proximity.

$$\hat{\mathcal{H}} = \underbrace{\mu_B \mathbf{B}^T \mathbf{g} \hat{S}}_{\hat{\mathcal{H}}_{EZI}} - \underbrace{g_N \mu_N \mathbf{B}^T \hat{I}}_{\hat{\mathcal{H}}_{NZI}} + \underbrace{\hat{S}^T \mathbf{A} \hat{I}}_{\hat{\mathcal{H}}_{HFI}} + \underbrace{\hat{I}^T \mathbf{Q} \hat{I}}_{\hat{\mathcal{H}}_{NQI}} + \underbrace{\hat{S}^T \mathbf{D} \hat{S}}_{\hat{\mathcal{H}}_{ZFI}} + \underbrace{\hat{S}_1^T \mathbf{J} \hat{S}_2}_{\hat{\mathcal{H}}_{EEI}} \quad (2.1)$$

The spin operators \hat{S} and \hat{I} as well as the magnetic field \mathbf{B} are vectors composed of the individual components in the three directions x , y and z . The tensors \mathbf{g} , \mathbf{A} , \mathbf{Q} , \mathbf{D} and \mathbf{J} contain also off-diagonal elements, as is shown for the g tensor.

$$\hat{S} = \begin{pmatrix} \hat{S}_x \\ \hat{S}_y \\ \hat{S}_z \end{pmatrix}, \quad \mathbf{B}^T = \begin{pmatrix} B_x & B_y & B_z \end{pmatrix}, \quad \mathbf{g} = \begin{pmatrix} g_{xx} & g_{xy} & g_{xz} \\ g_{yx} & g_{yy} & g_{yz} \\ g_{zx} & g_{zy} & g_{zz} \end{pmatrix}$$

These directions are arbitrary. Typically, one distinguishes between the lab frame (z is typically in the direction of the most important experimental parameter, e.g. the magnetic field), the molecular frame (z is the axis of highest symmetry in the molecule) and the tensor frames, where each tensor has their own frame (z is chosen so that the tensor is diagonal and the element for z has the highest magnitude). For a high-symmetry molecule, the molecular and tensor z axes coincide. As an example, the orientation of the g tensor in the organic radical TEMPO is shown in Figure 2.1.

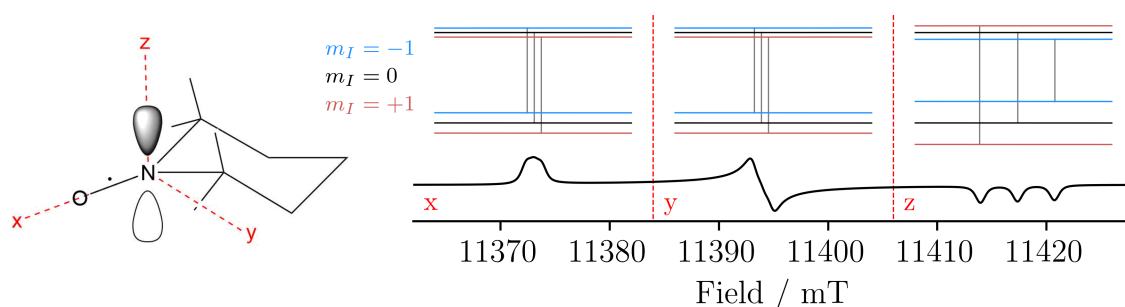


Figure 2.1: Orientation of the g tensor in the organic radical TEMPO and the resulting high-field EPR spectrum with the energy schemes in the three principal axes under the assumption of only EZI, NZI and HFI. For better visibility, NZI and HFI were overestimated by factors of 750 and 2000, respectively. Otherwise the three lines for $m_S = +1/2$ (top) and $m_S = -1/2$ (bottom) would overlap.

Detailed explanations of the magnetic moment of the electron and nuclear spins, their interaction and the resulting EPR spectrum are given in the following.

2.1.1 The Magnetic Moment of an Electron

In classical physics, a magnetic moment results from an accelerated charge, e.g. a charged particle rotating about an axis with an angular momentum \mathbf{L} . Electrons possess two different angular momenta, i.e. the spin angular momentum \mathbf{S} that was shown to give a magnetic moment even for the free electron, and the orbital angular momentum \mathbf{L} that results from the circular motion of the electron around the nucleus in an atom. The magnetic moment $\boldsymbol{\mu}$ resulting from orbital motion can be calculated with

$$\boldsymbol{\mu} = g \frac{q}{2m} \mathbf{L} = \gamma \mathbf{L} \quad (2.2)$$

where the g value results from the quantum mechanical calculation of the energy of an electron in a weak magnetic field in first-order perturbation theory. q and m are the charge and mass of the particle, respectively, and γ is the gyromagnetic ratio. This makes two things obvious: the magnetic moment of an electron is higher than that of

a proton due to the difference in g ($g = 1$ for orbital angular momentum and $g_e = 2.00231930436256(35)$ including the spin angular momentum, $g_N(^1H) = 5.58569468$, $g_N(^{13}C) = 1.404824$, $g_N(^{14}N) = 0.40376100$) and the relevant Bohr and nuclear magnetons ($\mu_B = 9.2740100783(28) \cdot 10^{-24} \text{ J T}^{-1}$, $\mu_N = 5.050783699(31) \cdot 10^{-27} \text{ J T}^{-1}$) and the orientation of the magnetic moment is opposite to the direction of angular momentum in electrons. Nuclei can have both positive and negative values of their gyromagnetic ratio, i.e. the magnetic moment can be oriented parallel and opposite to the direction of angular momentum, respectively. In addition to the orbital momentum that results from the motion of the electron around the nucleus, electrons also possess an intrinsic angular momentum, the spin. Stern and Gerlach discovered that free electrons are also influenced by a magnetic field and therefore must possess a magnetic moment. The angular momentum given in Equation (2.2) can then be expanded by the spin \mathbf{S} giving $\boldsymbol{\mu} = \gamma(\mathbf{L} + \mathbf{S})$. Under the assumption that the orbital angular momentum is much smaller than the spin angular momentum (it is typically quenched) one obtains $\boldsymbol{\mu} = \gamma\mathbf{S}$. In quantum mechanical calculations spins are most often represented as operators \hat{S} for the electron spin angular momentum and \hat{I} for the nuclear angular momentum or quantum numbers S and I . By defining z to be the quantization axis (and later to be the direction of an applied magnetic field with which the magnetic moment aligns (anti)parallelly), the spin angular momentum \mathbf{S} of an electron can be described with the reduced Planck constant \hbar and the spin quantum number m_S . By defining the Bohr magneton μ_B ($\mu_B = 9.2740100783(28) \cdot 10^{-24} \text{ J T}^{-1}$) to be

$$\mu_B = \frac{e\hbar}{2m_e} \quad (2.3)$$

with the elemental charge e and the mass of the electron m_e , Equation (2.2) can be simplified to

$$\mu_{S,z} = -g\mu_B m_S \quad (2.4)$$

for the electron magnetic moment. The negative sign shows that the magnetic moment of an electron is antiparallel to the spin angular momentum. For significant spin-orbit coupling, the spin operator must be exchanged for the total angular momentum operator, e.g. $\mathbf{J} = \mathbf{L} + \mathbf{S}$ in Russell-Saunders coupling. For organic radicals and first-row transition metals, deviations of the magnetic moments from the spin-only value as a result of weak spin-orbit coupling result in a deviation of the g tensor to that of the free electron. The spin-orbit coupling is only relevant in second-order of perturbation theory. The direction dependent interaction of the magnetic moment with a magnetic field is explained by the

electron Zeeman interaction, where the g tensor becomes relevant.

2.1.2 Electron Zeeman Interaction - The g tensor

The potential energy of the magnetic moment of the electron $\boldsymbol{\mu}_S$ in a magnetic field \mathbf{B} can be calculated with

$$\mathbf{E} = -\boldsymbol{\mu}_S \cdot \mathbf{B} = \mu_B \mathbf{S} \cdot \mathbf{g} \cdot \mathbf{B}. \quad (2.5)$$

By exchanging the angular momentum \mathbf{S} with the spin operator $\hat{\mathbf{S}}$, the Hamiltonian for the electron Zeeman interaction is obtained, see Equation (2.1). When the applied magnetic field is oriented parallel to z and the electron Zeeman interaction is larger than all other interactions, the potential energy becomes

$$E = g_{\text{eff}} \mu_B B m_S \quad (2.6)$$

The corresponding Hamiltonian is given by

$$\mathcal{H} = g_{\text{eff}} \mu_B B \hat{S}_z \quad (2.7)$$

The value g_{eff} given here is not necessarily the highest value in \mathbf{g} for which the g tensor is also diagonal, but that in direction of the applied magnetic field. Only when the molecule is oriented in the way that the z axis of the g tensor coincides with the z axis of the magnetic field, g_{eff} given in Equation 2.6 is the same as g_{zz} in the diagonalised g tensor.

Figure 2.2 shows the dependence of the potential energy on the applied magnetic field, given in Equation (2.6). The shown resonance fields B_{res} can be calculated from the resonance condition $\Delta m_S = \pm 1$ (because of conservation of angular momentum of photons in linearly polarised light) with

$$B_{\text{res}} = \frac{\Delta E}{g_z \mu_B} = \frac{h\nu}{g_z \mu_B} \quad (2.8)$$

where h is the Planck constant and ν is the microwave frequency. For one specific magnetic field in one direction two levels for $m_S = -1/2$ and $m_S = +1/2$ result. This case is depicted in Figure 2.3.

As was briefly mentioned, g is anisotropic because of the matrix elements of the components of the orbital angular momentum operator. The g values in all directions are proportional to the spin-orbit coupling parameter ζ and the energy difference to electron-

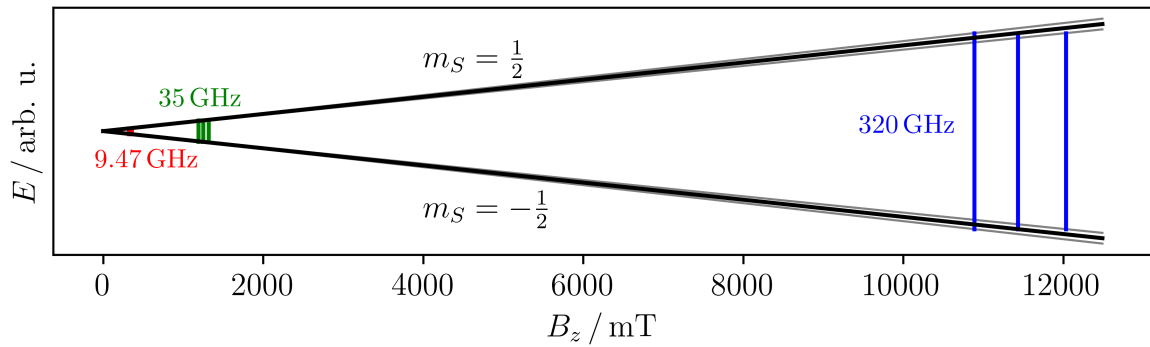


Figure 2.2: Electron Zeeman interaction given in Equation (2.6) versus the magnetic field for three g values $g_1 = 2.1$ (grey, highest slope), $g_2 = 2.0$ (black) and $g_3 = 1.9$ (grey, lowest slope). With the resonance condition, see Equation (2.8), the resonance fields for given microwave frequencies can be calculated. Here, transitions for the typical X-Band (9.47 GHz), Q-Band (35 GHz) and HFEPR (320 GHz) microwave frequencies are plotted, showing the advantage of high magnetic fields and microwave frequencies for the precise determination of the g tensor.

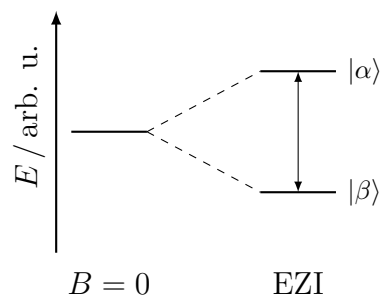


Figure 2.3: Electron Zeeman interaction (EZI) for $B \neq 0$ with the allowed transition from $|\beta\rangle$ ($m_S = -1/2$) to $|\alpha\rangle$ ($m_S = 1/2$).

ically excited states, e.g. the ligand-field splitting ΔE_{LFT} .

$$g \propto \frac{\zeta}{\Delta E} \quad (2.9)$$

Imagine an electron in a d_{xy} orbital moving around the nucleus in an octahedral ligand field. In order to realise the motion, the electron has to pass the $d_{x^2-y^2}$ orbital, i.e. the motion becomes easier for a small energy difference between the two orbitals. Spin-orbit coupling increases the influence of the orbital motion to the total magnetic moment. Since both ζ and ΔE are direction dependent, the principal values of the g tensor are not identical. For spin-orbit couplings, the orbital angular momentum must be considered explicitly, e.g. as is the case in Russell-Saunders coupling where $\mathbf{J} = \mathbf{L} + \mathbf{S}$. For most low-symmetry complexes \mathbf{L} is quenched.

Whichever orientation of the g tensor is aligned with the applied magnetic field can be investigated as the spin is always oriented along the direction of the applied magnetic field. The x direction of the g tensor can therefore be excited by a microwave only when the x axis of the g tensor coincides with the applied magnetic field. It is therefore possible to investigate the orientation of the g tensor from a single crystal of a radical. The simulations of EPR spectra for different orientations of a single crystal of TEMPO is given in Figure 2.4. For a powder, all orientations of the molecule exist and the sum over all orientations is obtained. One such spectrum is shown in Figure 2.1, where the three principal values of the g tensor can be clearly distinguished.

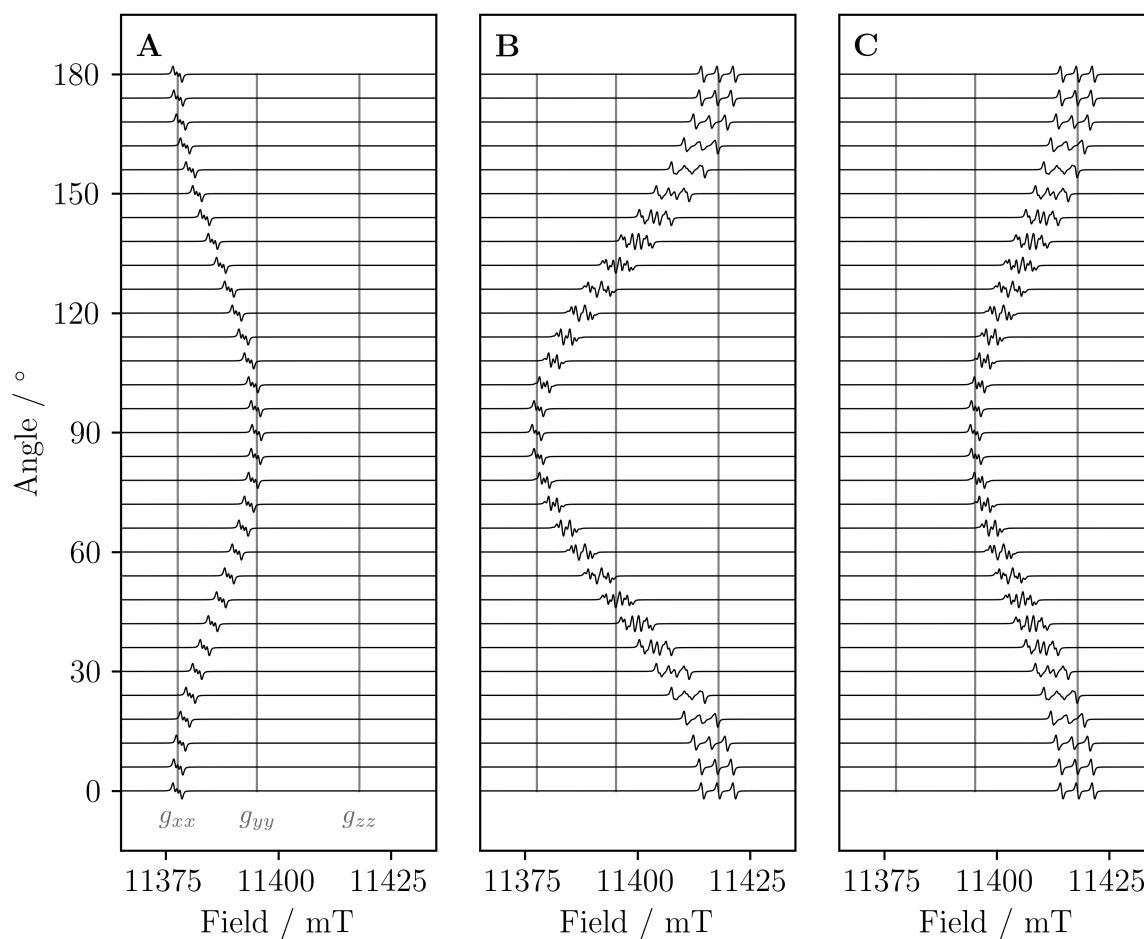


Figure 2.4: A) Single crystal EPR simulations of the organic radical TEMPO with hyperfine coupling to a ^{14}N nucleus ($g_{xx} = 2.009$, $g_{yy} = 2.006$, $g_{zz} = 2.002$, $A_{xx} = A_{yy} = 20$ MHz, $A_{zz} = 98$ MHz). The crystal is oriented so that the x axis of the g tensor is parallel for an initial angle of 0° to the applied magnetic field and the crystal is rotated around the z axis. B) Same as A but with the z axis of the g tensor being parallel to the applied field for an angle of 0° and a rotation around the y axis of the g tensor. C) Same as B but with a rotation around the x axis of the g tensor.

2.1.3 Nuclear Zeeman Interaction

The Hamiltonian for the nuclear Zeeman interaction is given by

$$\mathcal{H}_{\text{NZI}} = g_{\text{N}}\mu_{\text{N}}\mathbf{B}^T\hat{I} = g_{\text{N}}\mu_{\text{N}}\sum_{i=xyz}B_i\hat{I}_i \quad (2.10)$$

Not just electrons experience a torque and potential energy in a magnetic field. Nuclear spins also give rise to a magnetic moment that interacts with magnetic fields. Analogously to the derivation for the electron spin angular momentum, the nuclear Zeeman energy can be calculated with the nuclear g value g_{N} ($g_{\text{N}}(^1\text{H}) = 5.58569468$, $g_{\text{N}}(^{14}\text{N}) = 0.40376100$), the nuclear magneton μ_{N} ($\mu_{\text{N}} = 5.050783699 \cdot 10^{-27} \text{ J T}^{-1}$) and the nuclear spin angular momentum m_I .

$$E_z = g_{\text{N}}\mu_{\text{N}}B_z m_I \quad (2.11)$$

The nuclear Zeeman interaction leads to an additional splitting of the energy levels resulting from the electron Zeeman interaction. This much smaller interaction (due to the nuclear magneton compared to the Bohr magneton) leads to a change of the energy of the individual levels resulting from the Zeeman interactions. The energy scheme for electron and nuclear Zeeman interaction is shown in Figure 2.5. EPR transition energies are not influenced by the nuclear Zeeman interaction, because $\Delta m_I = 0$.

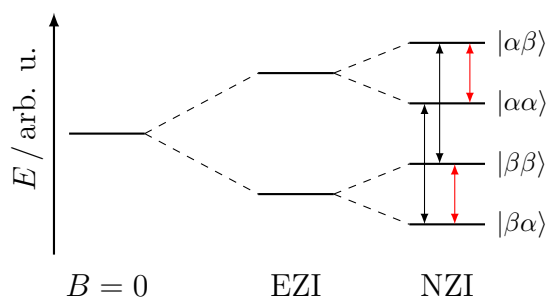


Figure 2.5: Electron and nuclear Zeeman interactions EZI and NCI, respectively, for $B \neq 0$ with the allowed EPR transitions (black, $\Delta m_S = \pm 1, \Delta m_I = 0$) with equal energies and NMR transitions (red, $\Delta m_I = \pm 1, \Delta m_S = 0$).

2.1.4 Hyperfine Interaction - The A tensor

The Hamiltonian of the hyperfine interaction is given by

$$\hat{\mathcal{H}}_{\text{HFI}} = \hat{S}^T \mathbf{A} \hat{I} = \begin{pmatrix} \hat{S}_x & \hat{S}_y & \hat{S}_z \end{pmatrix} \begin{pmatrix} A_{xx} & A_{xy} & A_{xz} \\ A_{yx} & A_{yy} & A_{yz} \\ A_{zx} & A_{zy} & A_{zz} \end{pmatrix} \begin{pmatrix} \hat{I}_x \\ \hat{I}_y \\ \hat{I}_z \end{pmatrix} = \sum_{i=xyz} \sum_{j=xyz} A_{ij} \hat{S}_i \hat{I}_j \quad (2.12)$$

As was mentioned in the previous section, nearby magnetic moments interact with each other. As the magnetic moments at the position of the spin preferably orient antiparallely to the applied field, their axial dipolar field is parallel to the applied magnetic field, see Figure 2.6. This dipolar field increases or decreases the local magnetic field of nearby magnetic moments, effectively changing the magnetic field in the equation for the Zeeman energy. Another possible mechanism for the hyperfine interaction is due to finite electron density at the position of the nucleus, i.e. when the unpaired electron resides in an orbital with s-character. This Fermi-contact interaction can be calculated to

$$\hat{\mathcal{H}}_{\text{FC}} = \frac{2\mu_0}{3\hbar} g\mu_B g_N \mu_N |\Psi(0)|^2 = A_{\text{iso}} \hat{S}^T \hat{I} \quad (2.13)$$

The interaction is isotropic, i.e. the same in all directions while the dipolar hyperfine interaction is axial. For quickly rotating molecules dipolar interactions are averaged out and only the isotropic hyperfine interaction can be observed in the spectrum.

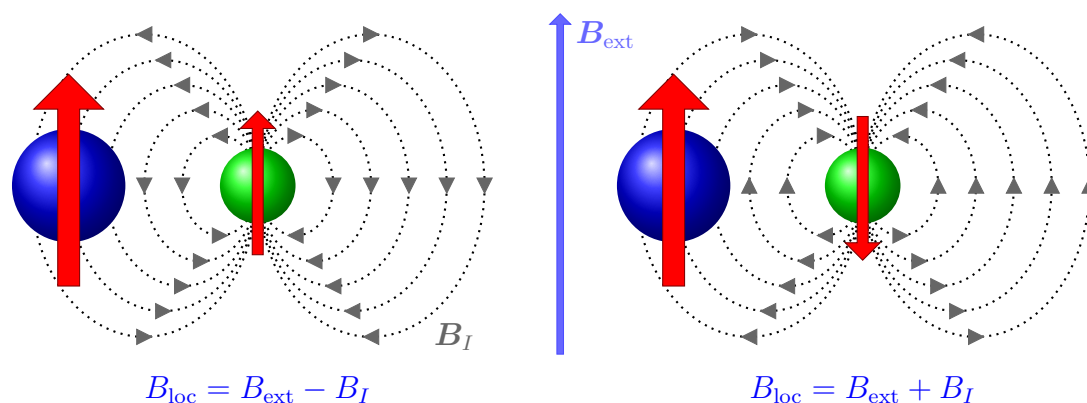


Figure 2.6: Dipolar field (grey) of a nuclear spin (green) with an electron spin (blue) in its immediate surrounding. The spins are coloured red. The magnetic moment at the position of the spin is parallel to the orientation of the spin for nuclei. For the case shown on the right side, the local magnetic field at the electron spin is increased, which lowers the absolute Zeeman energy and stabilises the $m_S = -1/2$ level.

The energy scheme resulting from electron and nuclear Zeeman interaction as well as the hyperfine interaction is depicted in Figure 2.7. It is shown that the energy of the

levels is decreased when the spins are antiparallel (see right side of Figure 2.6).

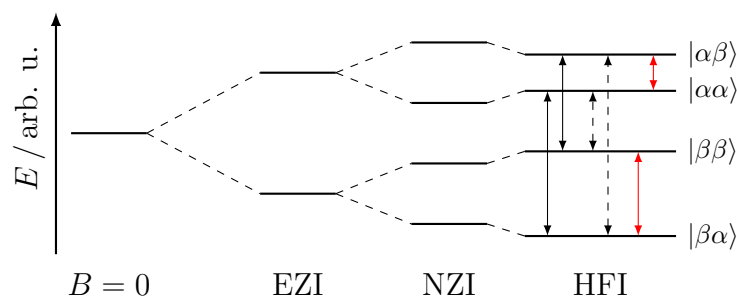


Figure 2.7: Electron and nuclear Zeeman interactions EZI and NCI, respectively, and hyperfine interaction (HFI) for $B \neq 0$ with the allowed EPR (black) and NMR (red) transitions and the forbidden transitions (dashed, $\Delta m_S = \pm 1$, $\Delta m_I = \pm 1$).

The quantitative change of the local magnetic field under the assumption that $\text{EZI} \gg \text{HFI}$ is given in the hyperfine interaction parameter A and the simplified Hamiltonian $\mathcal{H}_{\text{HFI}} = A\hat{S}_z\hat{I}_z$ can be solved in z direction to

$$E = Am_S m_I \quad (2.14)$$

giving a decrease of the $|\beta\alpha\rangle$ state by $1/4A$ for $S = I = 1/2$. Due to the arbitrary position of the spins relative to each other, A is given in the tensor \mathbf{A} with contributions A_{iso} from the isotropic interaction, T from the axial dipolar coupling and ρ from additional rhombic interactions.

$$\mathbf{A} = A_{\text{iso}}\mathbf{1} + \mathbf{T} = \begin{pmatrix} A_{\text{iso}} & 0 & 0 \\ 0 & A_{\text{iso}} & 0 \\ 0 & 0 & A_{\text{iso}} \end{pmatrix} + T \begin{pmatrix} -(1-\rho) & 0 & 0 \\ 0 & -(1+\rho) & 0 \\ 0 & 0 & 2 \end{pmatrix} \quad (2.15)$$

The axial component of the hyperfine interaction T can be calculated from Equation (2.16) for an $S = I = 1/2$ system. [62]

$$T = \frac{\mu_0}{4\pi h} \frac{g\mu_B g_N \mu_N}{R^3} \quad (2.16)$$

It is dependent on the g value of the electron that can be determined experimentally and the distance R between the electron and nuclear spin. All other values are known in literature. Typically, A_{xx} , A_{yy} and A_{zz} (in the g frame) can be determined from the EPR spectrum and A_{iso} , T and ρ can be calculated with

$$A_{\text{iso}} = \frac{1}{3}(A_3 + A_2 + A_1) \quad (2.17)$$

$$T = \frac{1}{6}(2A_3 - A_1 - A_2) \quad (2.18)$$

$$\rho = \frac{1}{2T}(-A_1 + A_2) \quad (2.19)$$

with $A_1 \leq A_2 \leq A_3$. In the A frame they correspond to the principal values in the way that $A_1 = A_{xx}$, $A_2 = A_{yy}$ and $A_3 = A_{zz}$. For example when $A_{xx} = 10$ MHz, $A_{yy} = 5$ MHz and $A_{zz} = 30$ MHz, then $A_{\text{iso}} = 15$ MHz, $T = 7.5$ MHz and $\rho = 0.33$. The A and g tensor frames are not necessarily collinear but related through a rotation about the Euler angles α , β and γ .

2.1.5 Nuclear Quadrupole Interaction

The Hamiltonian of the nuclear quadrupole interaction is given by

$$\hat{\mathcal{H}}_{\text{NQI}} = \hat{I}^T \mathbf{Q} \hat{I} = \begin{pmatrix} \hat{I}_x & \hat{I}_y & \hat{I}_z \end{pmatrix} \begin{pmatrix} Q_{xx} & Q_{xy} & Q_{xz} \\ Q_{yx} & Q_{yy} & Q_{yz} \\ Q_{zx} & Q_{zy} & Q_{zz} \end{pmatrix} \begin{pmatrix} \hat{I}_x \\ \hat{I}_y \\ \hat{I}_z \end{pmatrix} = \sum_{i=xyz} \sum_{j=xyz} Q_{ij} \hat{I}_i \hat{I}_j \quad (2.20)$$

with the Q tensor

$$\mathbf{Q} = \frac{e^2 Q q / h}{4I(2I-1)} \begin{pmatrix} -(1-\eta) & 0 & 0 \\ 0 & -(1+\eta) & 0 \\ 0 & 0 & 2 \end{pmatrix} \quad (2.21)$$

where $e^2 Q q / h = 2I(2I-1)Q_3$ and $\eta = (Q_1 - Q_2) / Q_3$ with $Q_3 \geq Q_2 \geq Q_1$. eq is the largest component of the electric field gradient at the nucleus, Q is the literature known electric quadrupole moment of the nucleus and η is the asymmetry parameter that can assume values between 0 and 1. The quadrupole interaction shifts the energies of all energy levels that belong to a nuclear spin of $I \geq 1$, as nuclei with $I = 1/2$ have a spherical charge distribution, i.e. $Q = 0$. The resulting energy scheme for an $S = 1/2$, $I = 1$ system is depicted in Figure 2.8.

For quickly rotating molecules the field gradient is averaged out (\mathbf{Q} is traceless) and the energy shift of the transitions is only observed for slow motion of the molecule, e.g. in powders. Because the nuclear quadrupole interaction acts on both electron spin substates in the same way, it can not be observed in EPR spectra and only plays a role for techniques where NMR transitions are measured (in)directly, e.g. in ENDOR and HYSCORE

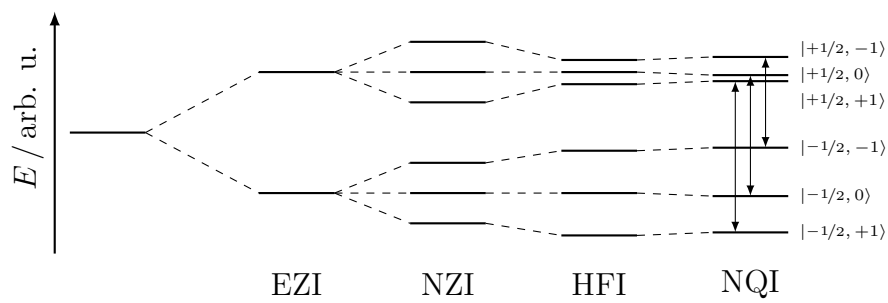


Figure 2.8: Electron and nuclear Zeeman interactions EZI and NZI, respectively, hyperfine interaction (HFI) and nuclear quadrupole interaction (NQI) for $B \neq 0$ with the allowed EPR transitions for the energy states $|m_S, m_I\rangle$.

spectroscopy, see the next Sections.

2.1.6 Zero-Field Interaction

The Hamiltonian of the zero-field interaction is given by

$$\hat{\mathcal{H}}_{\text{ZFI}} = \hat{S}^T \mathbf{D} \hat{S} = \begin{pmatrix} \hat{S}_x & \hat{S}_y & \hat{S}_z \end{pmatrix} \begin{pmatrix} D_{xx} & D_{xy} & D_{xz} \\ D_{yx} & D_{yy} & D_{yz} \\ D_{zx} & D_{zy} & D_{zz} \end{pmatrix} \begin{pmatrix} \hat{S}_x \\ \hat{S}_y \\ \hat{S}_z \end{pmatrix} = \sum_{i=xyz} \sum_{j=xyz} D_{ij} \hat{S}_i \hat{S}_j \quad (2.22)$$

The zero-field interaction exists in systems with $S \geq 1$ due to the individual electrons experiencing the magnetic field of the surrounding electrons even without an applied magnetic field. This internal magnetic field lifts the degeneracy of the m_S substates, see Figure 2.9.

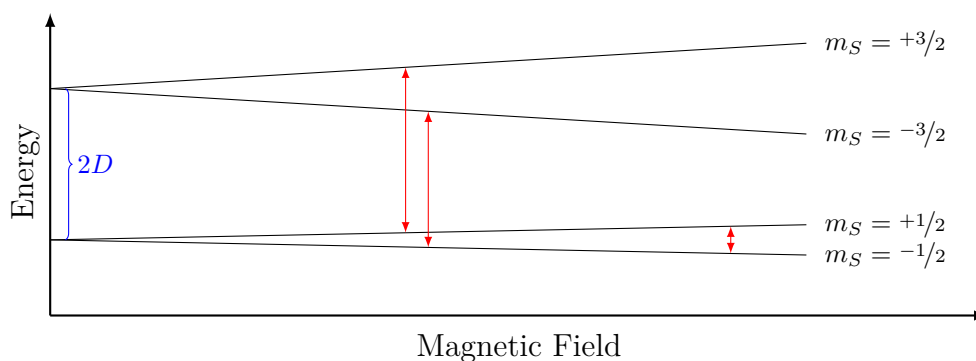


Figure 2.9: Zero-field splitting for $D > 0$ of an $S = 3/2$ system with the EPR transitions shown as red arrows.

For half-integer spin systems, transitions between the $\pm 1/2$ and $\pm 3/2$ Kramers doublets are only observed for microwave frequencies of the order of $2D$, see Equation (2.23). Transitions from $m_S = +1/2$ increase in intensity for increasing temperatures due to the thermal population of these states. The Hamiltonian can be expressed in its eigenframe as

$$\hat{\mathcal{H}}_{\text{ZFI}} = D_{xx} \hat{S}_x^2 + D_{yy} \hat{S}_y^2 + D_{zz} \hat{S}_z^2 = D \left(\hat{S}_z^2 - \frac{1}{3} S(S+1) \right) + E (\hat{S}_x^2 - \hat{S}_y^2) \quad (2.23)$$

with $D = 3/2 D_{zz}$ and $E = 1/2 (D_{xx} - D_{yy})$. For $D < 0$, the $m_S = \pm 3/2$ substates are lower in energy than the $m_S = \pm 1/2$ substates. Due to low population of the levels at higher energies typically no EPR lines are observed for $D < 0$ at low temperatures and microwave frequencies due to the selection rule $\Delta m_S = \pm 1$. E mixes the x and y states, i.e. transitions with $\Delta m_S = \pm 2$ become allowed.

2.1.7 Electron-Electron Interaction

Electron spins can interact with each other. A strongly coupled spin system can be treated as a particle with total spin S_{tot} . In the ferromagnetic coupling case, the total spin corresponds to $S_{\text{tot}} = \sum S_i$. Relatively weak couplings can be treated with the Hamiltonians of the individual spins to which the coupling is added, see Equation (2.24). In EPR, dipolar (for electron-electron distances $d \gtrsim 1.5$ nm) and exchange ($d \lesssim 1.5$ nm) interactions are the main contributions of electron-electron interactions. [63–65] They are explained in the following Sections.

$$\hat{\mathcal{H}}(S_1, S_2) = \hat{\mathcal{H}}(S_1) + \hat{\mathcal{H}}(S_2) + \hat{\mathcal{H}}_{\text{ex}} + \hat{\mathcal{H}}_{\text{dip}} \quad (2.24)$$

2.1.7.1 Exchange Interaction

The exchange interaction derives ultimately from the Pauli principle, that states that the total wave function must be antisymmetric under exchange of fermions. The general Hamiltonian can be expressed as

$$\hat{\mathcal{H}}_{\text{ex}} = \hat{S}_1^{\text{T}} \mathbf{J} \hat{S}_2 \quad (2.25)$$

with the exchange coupling tensor \mathbf{J} . The most important type of exchange interactions for paramagnetic molecules in solution is the quantum mechanical exchange of spin states of individual radicals during collision and overlap of the radical bearing orbitals, i.e. the SOMOs. At very short distances, e.g. in solids, the exchange interaction energy is larger than the thermal energy. This strong interaction leads to (anti-)ferromagnetic properties in the solid. Whether the interaction is ferro- or antiferromagnetic depends on the types and relative orientations of the overlapping orbitals. The exchange interaction is composed of the isotropic Heisenberg exchange interaction and super-exchange interaction (mediated via bridging orbitals between the two interacting orbitals) and anisotropic contributions that are negligible in solution. For purely isotropic exchange interactions, the J tensor becomes a scalar and the Hamiltonian can be simplified to

$$\hat{\mathcal{H}}_{\text{ex}} = J \hat{S}_1^{\text{T}} \hat{S}_2 \quad (2.26)$$

with the exchange coupling constant J for direct exchange given by the exchange integral

$$J = \left\langle \Psi_1 \Psi_2 \left| \frac{e^2}{4\pi\epsilon_0 r} \right| \Psi_1 \Psi_2 \right\rangle \quad (2.27)$$

accounting for the Coulomb interaction between the coupling electrons. Spin exchange in solution due to collisions is a special case of exchange interaction. The frequency of spin exchange for radicals colliding in solution can be expressed as

$$\omega_{\text{Exchange}} = \tau^{-1} p \frac{J^2 t^2}{1 + J^2 t^2} \quad (2.28)$$

with the frequency of orbital overlaps τ^{-1} , the time t that orbitals are overlapping and the efficiency of the collision p , i.e. how often each collision leads to spin exchange on average. p depends on the shape and charge of the molecule. For strong exchange interaction ($J^2 t^2 \gg 1$), the equation simplifies to

$$\omega_{\text{Exchange}} = \tau^{-1} p. \quad (2.29)$$

For this case, the exchange interaction is diffusion controlled and the exchange frequency can be expressed with

$$\omega_{\text{Exchange}} = c K_{\text{exchange}} \quad (2.30)$$

with the concentration c and the spin exchange rate K_{exchange} that is a function of the rate constant of diffusion. Experimentally, the spin exchange interaction leads to a broadening of the resonance lines in the EPR spectrum. Additionally, very high exchange frequencies lead to the collapse of the hyperfine split lines into one central line. This can be explained with the averaging of the nuclear magnetic moments as observed by the quickly flipping electron spin.

2.1.7.2 Dipolar Interaction

The mechanism of dipolar interaction of electron spins is the same as for the dipolar hyperfine interaction depicted in Figure 2.6. The Hamiltonian for two spins separated by the distance vector \mathbf{R} and the distance R can be expressed with

$$\hat{\mathcal{H}}_{\text{dip}} = \hat{S}_1^T \mathbf{D} \hat{S}_2 = -\frac{\mu_0}{4\pi\hbar} \frac{g_1 g_2 \mu_B^2}{R^3} \left(\hat{S}_1 \hat{S}_2 - \frac{3(\hat{S}_1 \mathbf{R})(\hat{S}_2 \mathbf{R})}{R^2} \right). \quad (2.31)$$

By expressing the Hamiltonian in spherical coordinates under the assumption of parallel dipoles one obtains the dipolar interaction ω_{dip} of the two spins.

$$\omega_{\text{dip}} = \frac{\mu_0}{4\pi\hbar} \frac{g_1 g_2 \mu_B^2}{R^3} (1 - 3 \cos^2 \theta) \quad (2.32)$$

Integration over the angle θ gives a typical shape called a Pake pattern in which the peaks are separated by the dipolar splitting. The Pake pattern can be obtained from DEER measurements giving the distance between the electron spins, see next Sections.

2.1.8 Spin Dynamics

As has become clear in the last Sections, the spin system can be excited to higher lying states governed by the selection rule of $\Delta m_S = \pm 1$. For the relaxation of the electron back to the Zeeman ground state, the surrounding must take up the released energy. The typical energy differences are in the range of Gigahertz, i.e. in the typical energy range of lattice vibrations (phonons). The relaxation therefore occurs via spin-phonon coupling. The most important mechanisms for the so-called spin-lattice relaxation are the direct, Raman and Orbach processes. At low magnetic fields and temperatures, quantum tunneling is also possible if a transverse interaction connecting the two states exists. Quantum tunneling is typically only relevant at very low temperatures and magnetic fields and will not be discussed here. The temperature dependence and mechanism of relaxation for the three mentioned processes are depicted in Figure 2.10 and given in Equation (2.33).

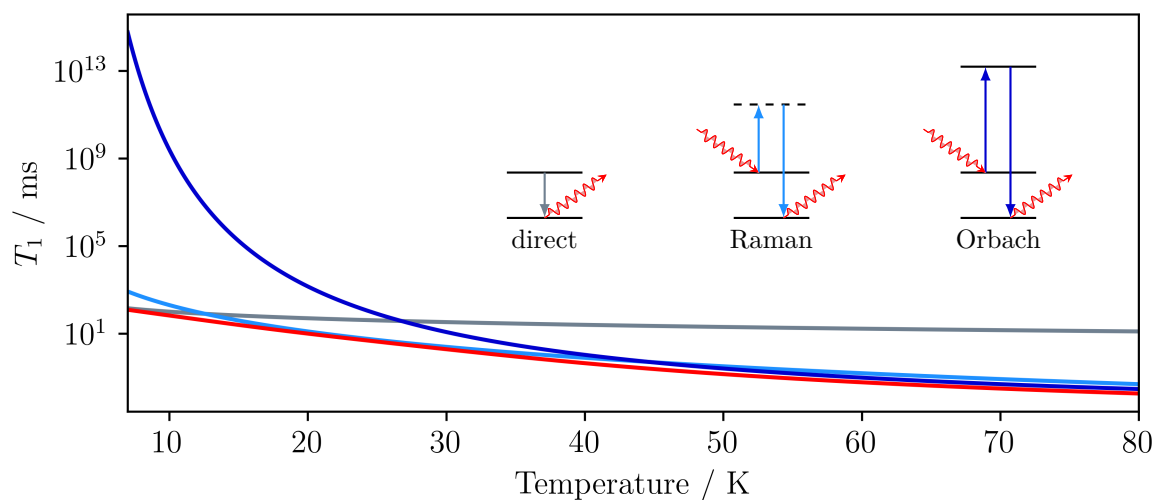


Figure 2.10: Temperature dependence of the relaxation times T_1 of the direct (grey, $c_{\text{direct}} = 10^{-3} \text{ s}^{-1} \text{ K}^{-1}$), Raman (light blue, $c_{\text{Raman}} = 5 \cdot 10^{-7} \text{ s}^{-1} \text{ K}^{-4}$, $n_{\text{Raman}} = 4$) and Orbach (dark blue, $\tau_{\text{O}}^{-1} = 8 \cdot 10^{-4} \text{ s}$, $U_{\text{eff}} = 200 \text{ cm}^{-1}$) processes. The resulting inverse relaxation time is the sum of the relaxation times of the individual processes, see Equation (2.33).

The direct process occurs via the relaxation of the electron spin under the emission of

a phonon, i.e. a lattice vibration. This is the case because lattice vibrations lead to an oscillation of the electric field around the electron spin which leads to a modulation of the crystal field. Spin-orbit coupling translates this modulation into an oscillating magnetic field that can interact with the electron spin. Because more phonons become energetically accessible at higher temperatures, it is more likely that a phonon with precisely the energy of the Zeeman transition exists in the lattice. Therefore, the frequency with which direct processes happen, i.e. the inverse relaxation time, increases linearly with the temperature. The Raman process is a two-phonon process, i.e. requires two phonons to simultaneously interact with the spin. One phonon is absorbed, exciting the spin to a virtual level. Because this state does not exist the electron can not reside in this virtual energy level and a phonon must be generated immediately. Although two phonons are required for this process, the only two requirements are that their energy difference must be equal to the energy difference of the two states and they must be thermally accessible. For low temperatures this is not the case and direct processes predominate the relaxation. At higher temperatures the Raman process occurs more frequently and the spin system relaxes via this pathway. Quantitatively, Raman relaxation is explained with the Debye model. For temperatures lower than the Debye temperature θ_D and higher than ca. $0.05\theta_D$ the relaxation rate is proportional to T^n . Both Raman and direct processes can happen in $S = 1/2$ systems. If an accessible energy state exists in the system, e.g. for $S > 1/2$, Orbach processes can take place. Analogous to the Raman process, the Orbach process is a two-phonon process. Because the electron spin can reside in the excited energy level a subsequent interaction with the two phonons is allowed, making the process more likely at higher temperatures. These higher temperatures are necessary because the energy difference to the excited state is higher than that to an arbitrary virtual state. The Orbach process is proportional to the Orbach relaxation time τ_O and the effective energy barrier U_{eff} , i.e. the energy difference to the excited state that enables relaxation.

$$\tau^{-1} = \underbrace{c_{\text{direct}} T}_{\text{direct}} + \underbrace{c_{\text{Raman}} T^n}_{\text{Raman}} + \underbrace{\tau_O^{-1} \cdot e^{-\frac{U_{\text{eff}}}{k_B T}}}_{\text{Orbach}} \quad (2.33)$$

For all aspects mentioned in this Section, literature with more detailed explanation of the phenomena exists, e.g. [62, 65–67].

2.2 Spectroscopy and Magnetometry

As was mentioned in the previous Sections, electron spins can be excited to higher energy levels by interaction with electromagnetic radiation. The energies of the possible

transitions are studied with spectroscopy. The extracted knowledge can be used to study the electronic structure of chemical compounds or to use the molecule-specific spectrum for the identification of known molecules in the research sample. This can help for the proof of presence of certain molecules or the quantification of chemicals in mixtures. The energy separation of the Zeeman levels is in the range of microwaves. In the next Sections, the interactions of microwaves with the spin angular momentum is briefly explained and the experimental methods electron paramagnetic resonance (EPR) and magnetic circular dichroism (MCD) are also explained. X-Ray absorption and emission are used to study complexes in general and is also explained briefly. SQUID magnetometry can be used to measure the magnetic moment of samples and is mentioned as well. Lastly, Mössbauer spectroscopy is explained in more detail.

2.2.1 Interactions of Spins with Microwaves

In an external magnetic field, the spin states, i.e. the $\pm m_S$ levels, split due to the Zeeman interaction and in case of electrons, the resulting magnetic moment from the spin angular momentum is opposite to the applied magnetic field. In the previous Section it was mentioned that a magnetic moment experiences a torque in a magnetic field. This leads to a precession of the spin magnetic moment around the magnetic field axis. The direction of the magnetic field is defined as \mathbf{z} . The lab frame is then completed with the other two directions \mathbf{x} and \mathbf{y} that are orthogonal to each other and the direction of the applied magnetic field B_0 . The precession direction is given by the sign of the gyromagnetic ratio γ and is counter-clockwise for electron spins. The precession frequency, i.e. the so-called Larmor frequency ω_L , is given by

$$\omega_L = -\gamma B_0. \quad (2.34)$$

By irradiation with a microwave with the magnetic field component in \mathbf{x} direction, the spins experience an oscillating microwave magnetic field \mathbf{B}_1 that can be quantified with

$$\mathbf{B}_1 = B_1 \cos(\omega t - k\mathbf{x}) \quad (2.35)$$

with the magnitude B_1 of the microwave magnetic field, the microwave frequency ω , the time t , the wave vector k and the position \mathbf{x} . This linearly polarised microwave is not an ideal model to explain the interaction with the precessing spins. Instead, linearly polarised light can be expressed as the superposition of left (\mathbf{B}_{left}) and right ($\mathbf{B}_{\text{right}}$) circularly polarised light.

$$\mathbf{B}_{\text{right}} = \frac{B_1}{2} (\cos(\omega t - k\mathbf{x}) + \sin(\omega t - k\mathbf{y})) \quad (2.36)$$

$$\mathbf{B}_{\text{left}} = \frac{B_1}{2} (\cos(\omega t - k\mathbf{x}) - \sin(\omega t - k\mathbf{y})) \quad (2.37)$$

The interaction with the microwave is best explained in a rotating coordinate frame where the vector $\boldsymbol{\omega}$ is in direction of the applied magnetic field \mathbf{B} , i.e. the frame rotates around \mathbf{z} . Its magnitude is the angular frequency ω , i.e. the microwave frequency. Alternatively, the frame could be rotating with the Larmor frequency of the spins. On resonance, i.e. when the microwave is resonantly interacting with the spins, the Larmor frequency and microwave frequency are identical, as will be seen later, and the two models become identical. In the rotating frame, that rotates with the microwave frequency, the new coordinates are given by \mathbf{x}' , \mathbf{y}' and \mathbf{z}' .

$$\mathbf{x}' = \cos(\omega t - k\mathbf{x}) - \sin(\omega t - k\mathbf{y}) \quad (2.38)$$

$$\mathbf{y}' = \sin(\omega t - k\mathbf{x}) - \cos(\omega t - k\mathbf{y}) \quad (2.39)$$

$$\mathbf{z}' = \mathbf{z} \quad (2.40)$$

The circularly polarised microwaves are then given by

$$\mathbf{B}_{\text{right}} = \frac{B_1}{2} (\cos(2\omega t - k\mathbf{x}') + \sin(2\omega t - k\mathbf{y}')) \quad (2.41)$$

$$\mathbf{B}_{\text{left}} = \frac{B_1}{2} \mathbf{x}' \quad (2.42)$$

with one component (the one rotating in the same direction as the spins) being static in the rotating frame and the other one rotating with twice the frequency in the other direction. The angular momentum of the circularly polarised waves is $\pm\hbar$, i.e. one of the two polarisation directions can excite transitions with $\Delta m_S = +1$ and the other with $\Delta m_S = -1$. The microwave that is oscillating in the same direction as the spins therefore excites the transition with $\Delta m_S = +1$. The rotating frame adds an effective field in z that does not exist as a constant value in the lab frame [68] and the effective Larmor precession frequency in the rotating frame becomes

$$\boldsymbol{\Omega} = -\gamma \mathbf{B}_{\text{eff}} = -\gamma \left(\mathbf{B} + \frac{\boldsymbol{\omega}}{\gamma} \right) = -\gamma \mathbf{B} - \boldsymbol{\omega} \quad (2.43)$$

with the rotation frequency of the rotating frame ω and its angular momentum in direction $\boldsymbol{\omega}$. The magnetic field \mathbf{B} is the sum of the applied and the microwave fields ($\mathbf{B} =$

$\mathbf{B}_0 + \mathbf{B}_1 = \mathbf{B}_0 + \mathbf{B}_{\text{right}} + \mathbf{B}_{\text{left}}$) and the vector of the angular frequency of the rotating frame is given by $\omega_{x'} = \omega_{y'} = 0$ and $\omega_{z'} = \omega$. The individual components of $\boldsymbol{\Omega}$ are then given by

$$\boldsymbol{\Omega}_{x'} = \frac{-\gamma B_1}{2} - \frac{\gamma B_1}{2} \cos(2\omega t) \quad (2.44)$$

$$\boldsymbol{\Omega}_{y'} = -\frac{\gamma B_1}{2} \sin(2\omega t) \quad (2.45)$$

$$\boldsymbol{\Omega}_{z'} = -\gamma B_0 - \omega \quad (2.46)$$

The spins therefore precess around the z' axis with a frequency given by the speed of the rotating frame ω and the applied magnetic field B_0 . In x' and y' the precession frequency is given by the strength of the microwave magnetic field and the rotation speed of the frame. For the case that the magnitude of the Larmor frequency $|\gamma B_0|$ is equal to the frequency of the rotating frame (that is given by the microwave frequency), $\boldsymbol{\Omega}_{z'}$ becomes zero and the magnetic moments precess only about x' with weak oscillations in x' and y' due to the remaining sine and cosine functions. This state is called resonance. For the whole duration of microwave irradiation, the magnetic moments and therefore the spins precess around x' . This so-called Rabi-precession can be visualised experimentally with the so-called nutation experiment for which the nutation angle, i.e. how far the magnetic moments were rotated around x' , can be measured as a function of a microwave pulse length. The theoretical result of the experiment is depicted in Figure 2.11 where the magnetisation decreases for longer pulse lengths due to spin-lattice relaxation T_1 (that drives the spins back to the initial energy level) and spin-spin relaxation T_2 (that reduces the magnetisation in x' and y'). The magnetisation in z' can be read with the Hahn echo sequence, see next Sections.

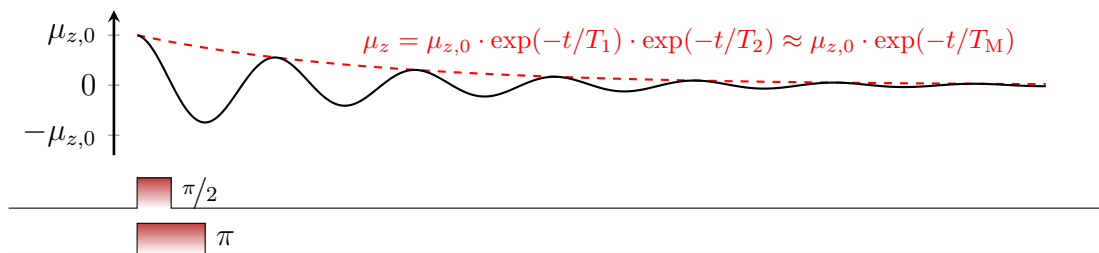


Figure 2.11: Depiction of the Rabi oscillations for different lengths of the nutation pulse. The pulse length that inverts the magnetisation in z is a 180° (π) pulse.

The measurement of the EPR spectrum from the interaction with continuously applied microwaves and the experimental determination of spin relaxation times and spin-spin interaction with microwave pulses is given in the next Sections.

2.2.2 Continuous-Wave Electron Paramagnetic Resonance

In continuous wave (cw) EPR spectroscopy, the resonant absorption of microwaves is measured. From that, the separation of the relevant energy levels can be determined, giving an idea of the electronic structure of the investigated radical. In the following, the experimental set-up of a typical EPR spectrometer is given.

Due to the low energy separation of the two Zeeman levels in a $S = 1/2$ system, high microwave powers are required to achieve high sensitivities and be able to observe the spectrum. In modern EPR spectrometers, the waveguide is critically coupled to the resonator with the sample inside in order to achieve the highest possible power transfer of the electromagnetic radiation from the waveguide into the resonator, i.e. to the sample. Critical coupling results from impedance matching of the waveguide with the resonator. This is achieved by changing the length of one dimension of the waveguide with an iris screw. The impedance can be calculated from the ratio of the electric field to the magnetic field at the centre of the waveguide. By changing one of the widths of the waveguide perpendicular to the direction of propagation of the microwave, one of the field components of the waves is attenuated, effectively changing the impedance of the waveguide. Furthermore, by using a resonator, the microwave magnetic field B_1 can be increased through the generation of standing waves in the cavity. These standing waves can be observed experimentally through the reflected power. When standing waves occur, less power coming from the microwave bridge is reflected from the cavity leading to a dip in the measured reflected power. This behaviour can be seen in Figure 2.12B.

The requirement that the microwave wavelength fits the resonator dimensions to form standing waves makes them usable in only a limited frequency range. Typical EPR frequencies are ca. 9.5 GHz (X-Band) and 35 GHz (Q-Band) with free-space wavelengths of ca. 3.17 and 0.86 cm, respectively. Low microwave frequencies (ca. 10 GHz) are used very often due to the availability of microwave sources, detectors and waveguides at that frequency. Furthermore, these frequencies require small magnetic fields that can be achieved with electromagnets. Higher frequencies (above ca. 100 GHz) require superconducting magnets and different means of wave propagation due to the small wavelengths. Nonetheless, EPR spectrometers with microwave frequencies well above 100 GHz are available.

As was mentioned, the EPR spectrum is recorded as a function of magnetic field. By sweeping the magnetic field, the Larmor frequency of the spins in the sample is changed and when it is equal to the microwave frequency, they interact and microwave is absorbed. The absorption of microwaves changes the impedance of the resonator and as a result it is not critically coupled to the waveguide any longer and an increased microwave power is reflected to the microwave bridge. This behaviour is shown in Figure 2.12B in red.

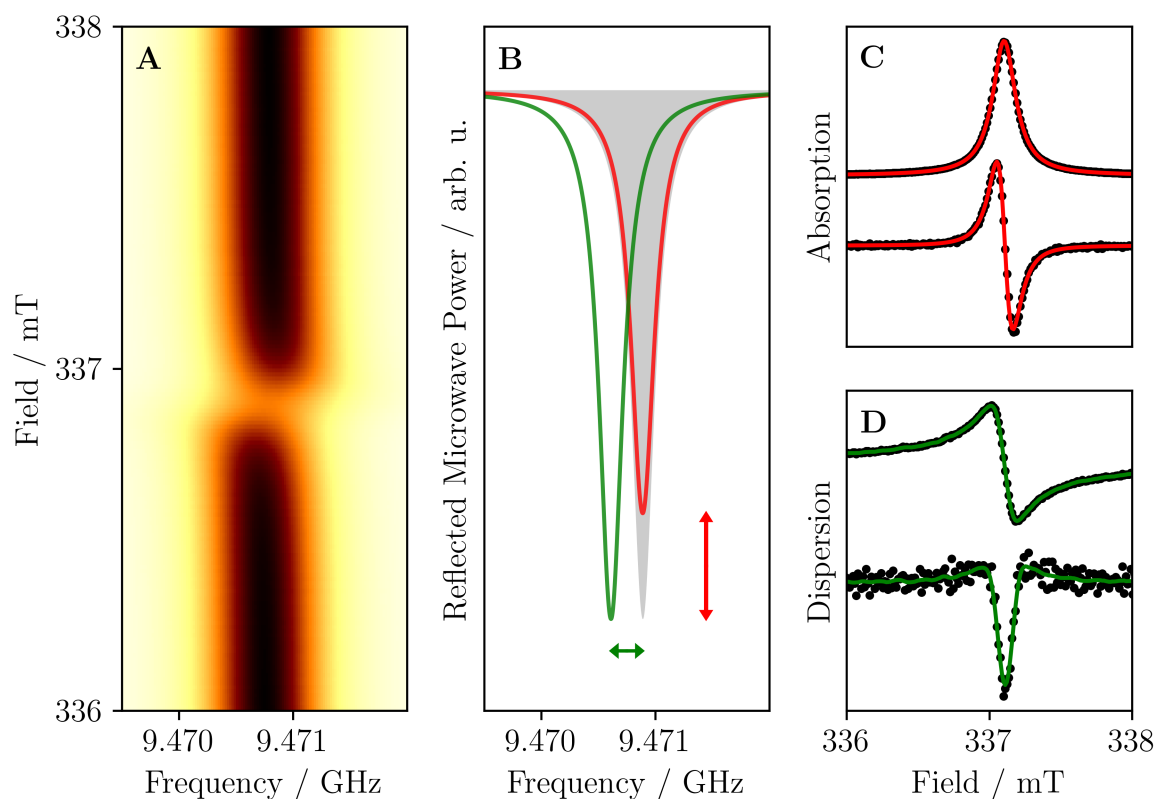


Figure 2.12: A) Field-frequency plot of the reflected power from the EPR resonator for dpph measured at room temperature. The power was measured with a vector network analyser. B) Resonator dip off-resonance (grey), during absorption (red) and dispersion (green). C) Absorption spectrum of dpph (black) as measured (top) and first derivative (bottom) that is usually observed in EPR spectra due to field modulation with fits (red) with a Lorentzian. D) Dispersion spectrum of dpph (black) as measured (top) and first derivative (bottom). The green line is just a guide to the eye.

Dispersion of the microwave can be observed by a shift in the resonance frequency of the resonator as is shown in Figure 2.12B in green. By measuring the reflected power at the centre of the resonator dip (realised by the automatic frequency control in the spectrometer that corrects for dispersion) as a function of the magnetic field, the microwave absorption, i.e. the EPR spectrum, is obtained. A typical EPR spectrum for a single transition is shown in Figure 2.12C. Here, the transition from $m_S = -1/2$ to $m_S = +1/2$ in the organic radical dpph (dpph = 2,2-diphenyl-1-picrylhydrazyl) was measured. The dispersion signal, that was extracted from the position of the resonator dip is shown in Figure 2.12D. Figure 2.12A shows the two-dimensional field-frequency plot that shows the absorption and dispersion simultaneously.

Although the signal-to-noise ratio is sufficient in the absorption spectrum shown in

Figure 2.12C, it was obtained using a sample amount that is typically not obtainable for research samples. In order to improve the signal-to-noise ratio, the applied magnetic field B_0 is modulated by two coils attached to the resonator that generate an oscillating magnetic field from an alternating current. The absorption is then also modulated at the modulation frequency and by demodulating the reflected power in a lock-in detector the intensity is obtained. This demodulated signal has reduced noise at lower and higher frequencies than the modulation frequency, i.e. white and $1/f$ -noise can be drastically reduced in the experiment. The modulation leads to the recording of the derivative signal, see Figure 2.13.

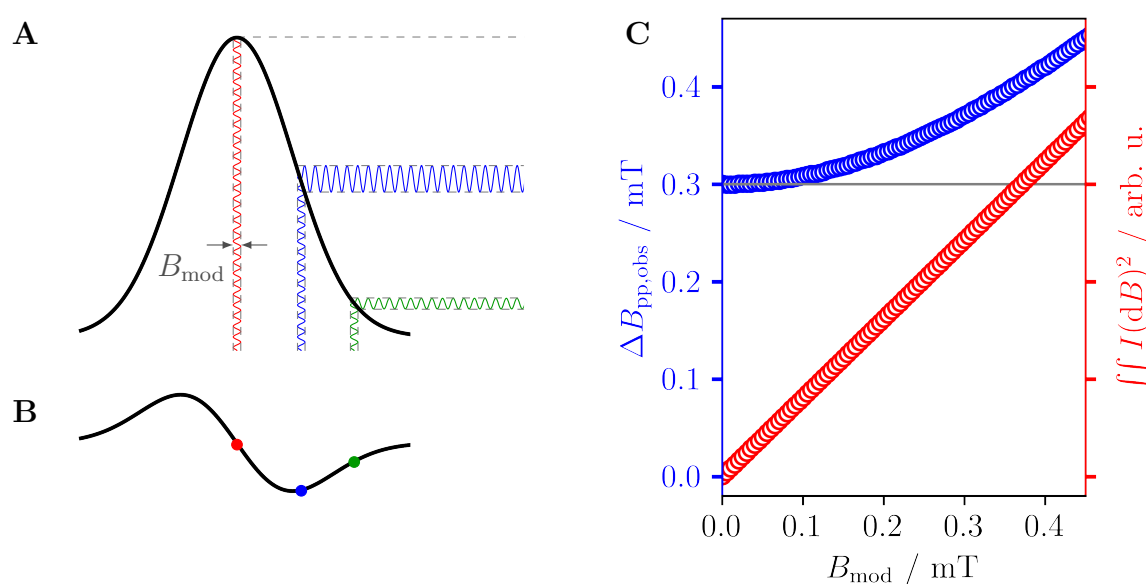


Figure 2.13: A) Absorption spectrum with the influence of field modulation B_{mod} . By changing the effective magnetic field at the sample the absorbed power is also modulated. Because the absorption changes the least for weakly changing fields at the maximum of the absorption spectrum, the measured intensity becomes zero (red). B) The EPR spectrum as a result of field modulation is the derivative of the absorption spectrum. C) Influence of the modulation amplitude on the linewidth and the intensity (second integral).

As becomes clear from Figure 2.13A, modulation amplitudes of the order of and larger than the natural linewidth lead to an increase of the observed linewidth. At field positions where no absorption takes place the field modulation might give effective magnetic fields where absorption does occur, leading to microwave absorption. The increase in modulation amplitude therefore has the same effect as an increase in bandwidth for optical spectroscopies.

A much more detailed introduction into the practical aspects of cw EPR spectroscopy can be found in [62, 69].

2.2.3 Pulsed Electron Paramagnetic Resonance Spectroscopy

Pulsed EPR gives access to the direct measurement of the spin relaxation times and dipolar interaction, i.e. the hyperfine interaction between electrons and surrounding nuclei and electron-electron interactions. These measurements are realised by rotating the magnetic moments of the spins away from the stable initial state set by the applied magnetic field and following the time dependent evolution of the magnetisation. In the simplest type of experiment, the magnetic moments are rotated by 90° into the xy plane and the evolution of the magnetic field generated by the spins is measured with a pickup coil in that plane, so it does not measure the microwave magnetic field which is much stronger than the field generated by the spins. This technique is used in pulsed NMR spectroscopy, where the total magnetic moment is much higher than in EPR spectroscopy. The measured response of the spins, the so-called free induction decay, is an oscillating field that is dampened by the relaxation of the spins back to their initial magnetisation. First pulsed EPR measurements were based on this technique but due to the much faster precession of the spins and faster relaxation and dephasing of electron spins compared to nuclear spins, precise measurements were much harder to achieve. Instead, the magnetisation is measured as a spin echo that is generated after two arbitrary microwave pulses that move the magnetisation (spin) away from the initial direction. Typically, the Hahn echo sequence (a 90° pulse followed by a 180° pulse) is employed as it gives the highest echo intensity. The pulse sequence and the response of the spins is depicted in Figure 2.14.

During the experiment two important relaxation phenomena of the magnetisation take place. The spin-lattice relaxation T_1 drives the spins back into the ground state, giving the favoured magnetisation antiparallel to the applied magnetic field. The spin-spin relaxation T_2 drives the magnetisation in \mathbf{x}' and \mathbf{y}' back to zero. The latter is responsible for the natural linewidth of absorption spectra as it is effectively the lifetime of the excited states. As spin coherence in the $\mathbf{x}'\mathbf{y}'$ plane can only exist if there is magnetisation in that plane, the spin-lattice relaxation time is the upper limit of T_2 . The most important contribution to the spin-spin relaxation is the loss of coherence of the spins. This coherence time is called phase-memory time T_M . Suppose the Larmor frequency changes during the experiment and the spins distribute themselves in the $\mathbf{x}'\mathbf{y}'$ plane randomly. Then, the sum magnetisation in that plane is zero and no spin echo can be observed. The main contributions to the loss of coherence are oscillating magnetic fields (that change B_{loc} of individual spins during the precession) from surrounding nuclear spins (e.g. from rotating

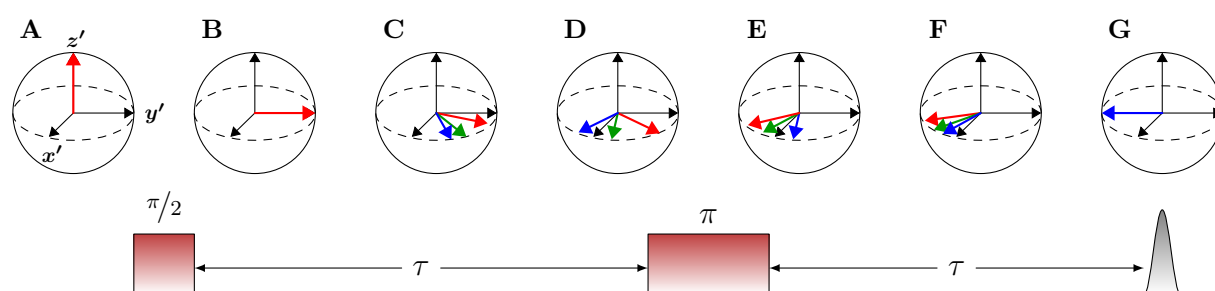


Figure 2.14: A) Initial orientation of the spins (coloured) in the rotating frame. B) A microwave pulse of the length and field strength to rotate the magnetic moments (spins) by exactly 90° ($\pi/2$) around the x' axis is applied. C) The magnetic moments start to precess about the z' axis when the microwave pulse is over. Due to the sign of the gyromagnetic ratio, the spins (and magnetic moments) rotate counterclockwise. D) Due to the different local magnetic fields as a result of slightly different magnetic surroundings of the individual spins their Larmor frequency is different and the spins rotate at different speeds. E) After a certain waiting time τ a 180° (π) pulse is applied, again rotating the magnetic moments around the x' axis. The faster spins (with higher local magnetic fields) now lie behind the slower spins. F) Assuming that the Larmor frequencies of the individual spins do not change during the experiment, the faster spins start to catch up. G) After the same time τ the spins now refocus at $-x'$. This can be seen as a 180° phase shift and the echo is often depicted as inverted. In a single-echo experiment, the direction of the echo is arbitrary and can be corrected for in the microwave bridge.

methyl groups) or flip-flop exchanges between spins (e.g. due to exchange interaction). The experimental procedures to determine T_1 and T_M are explained in the next Section.

2.2.3.1 Experimental Determination of the Spin Relaxation Times

As was explained in the previous Section, spin-lattice and spin-spin relaxation decrease the spin echo intensity that is effectively a measure of the magnetisation in the $x'y'$ plane at the time of the echo which is also influenced by the initial magnetisation in z' . The Hahn echo sequence can be used with varying times τ to follow the echo intensity for different evolution times of the precession of the spins. Figure 2.15 shows the Hahn echo sequence.

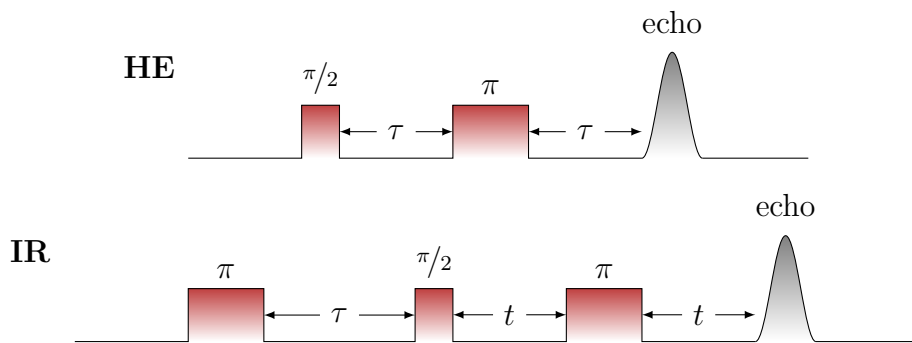


Figure 2.15: Hahn echo (HE) and inversion recovery (IR) pulse sequences with fixed times t and varied times τ . The experiment is performed at constant field to determine the relaxation times. The HE sequence can be repeated with the same τ at varying fields to measure the EPR spectrum.

For longer waiting times τ the Larmor frequency of more spins changes due to the varying local magnetic fields and the echo intensity decreases with an exponential decay. Because the loss of coherence starts as soon as the spins are rotated into the $x'y'$ plane, the echo intensity I_{echo} is a function of 2τ .

$$I_{\text{echo}} = a \cdot e^{-\frac{2\tau}{T_M}} \quad (2.47)$$

The factor a accounts for the initial echo intensity which depends on many experimental parameters (number of spins, spin polarisation, electronics in the microwave bridge, etc.). In some cases the echo decay follows a stretched exponential function.

$$I_{\text{echo}} = a \cdot e^{-\left(\frac{2\tau}{T_M}\right)^k} \quad (2.48)$$

The stretch parameter k indicates which dephasing process dominates. For example,

physical motion of nuclei leads to $1 \lesssim k \lesssim 1.5$ and nuclear spin diffusion gives $2 \lesssim k \lesssim 2.5$.

The initial $\mathbf{x}'\mathbf{y}'$ magnetisation is directly proportional to the initial number of spins in \mathbf{z}' , i.e. it is a quantitative measure of the absorption of microwaves and by repeating the pulse sequence (with the same times τ) at different field positions, the absorption spectrum can be obtained. It is important that the magnetisation is in equilibrium at the beginning of each pulse sequence, i.e. a sufficient repetition time between the first pulses of each sequence is necessary. It must be longer than ca. $5T_1$ to make sure that all spins relaxed into the initial state. Because the echo intensity is also a function of T_1 and spin-lattice relaxation is anisotropic, the spectrum might be distorted, i.e. a lower intensity is measured than in the cw spectrum at field positions where T_1 is much shorter than at other field positions. Additionally, the anisotropy of the phase-memory time can distort the electron spin echo EPR spectrum compared to the cw spectrum.

The spin-lattice relaxation time is a measure for the \mathbf{z}' magnetisation. As was shown, the Hahn echo sequence can be used to determine this value. By applying a 180° pulse and then performing the Hahn echo pulse sequence immediately afterwards, the $-\mathbf{z}'$ magnetisation can be measured and is seen as an inversion of the echo. The initial inversion due to the 180° pulse gives the pulse sequence its name and it is called inversion recovery experiment, see Figure 2.15. By varying the waiting time between the first pulse and the Hahn echo sequence (where the time between the two Hahn echo pulses is kept constant), the evolution of the \mathbf{z}' magnetisation can be followed. Every relaxation process (e.g. if two molecules absorb the microwave at that field, a second effective relaxation time is observed) gives an exponential decay with its own relaxation time T_1 . In this thesis, typically a biexponential function is fitted to the saturation echo intensity $I_{\text{echo,inf}}$. The most common second process is related to spectral diffusion. [70]

$$I_{\text{echo}} = -a_{\text{slow}} \cdot e^{-\frac{\tau}{T_{1,\text{slow}}}} - a_{\text{fast}} \cdot e^{-\frac{\tau}{T_{1,\text{fast}}}} + I_{\text{echo,inf}} \quad (2.49)$$

As was mentioned in the previous Sections, the magnetic moments of electron spins interact with the magnetic moments of surrounding electron and nuclear spins via dipolar coupling. This interaction can be observed as a modulation of the echo intensity or by selectively exciting nuclear transitions. These methods are briefly explained in the next Sections.

2.2.3.2 Electron Spin Echo Envelope Modulation Spectroscopy

The Electron Spin Echo Envelope Modulation (ESEEM) experiment can deliver hyperfine coupling parameters by analysing the modulation of the echo intensity as a function of the time between pulses. The simplest pulse sequence that can give this modulation is the Hahn echo sequence depicted in the previous Section. Often, the three-pulse ESEEM experiment, see Figure 2.16 is used because it offers a higher spectral resolution since the echo decay is dominated by the spin-lattice relaxation, rather than by the faster spin-spin relaxation, giving higher echo intensities.

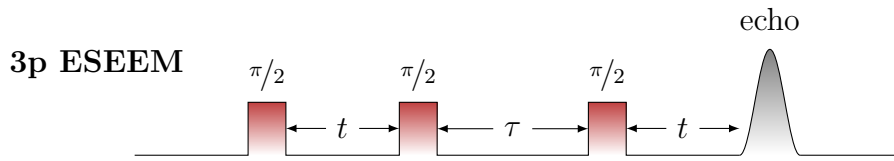


Figure 2.16: Pulse sequence of the three-pulse ESEEM experiment. During the measurement τ is varied and t is fixed. Because the experiment leads to blind spots at certain values of t , the measurement is usually repeated for different values of t .

In both cases the echo intensity is modulated with the frequency ω_{mod} that depends on the nuclear Larmor frequency ω_I and the hyperfine coupling.

$$\omega_{\text{mod}} = |\omega_I - m_S A| \quad (2.50)$$

The origin of this modulation can be explained with the energy diagram for weak (Figure 2.17A) and strong (Figure 2.17B) hyperfine interaction between electron and nuclear spins. It can be easily shown that the transition energies of the NMR transitions (that are $\Delta E = \omega_I$ without hyperfine coupling) are increased (decreased) by two times the influence of the hyperfine interaction on the energy level ($A m_S m_I$).

$$\omega_{1,2} = \omega_I - 2m_S A m_I \quad (2.51)$$

$$\omega_{3,4} = \omega_I + 2m_S A m_I \quad (2.52)$$

This straightforward weak coupling case ($A < 2\omega_I$) is depicted in Figure 2.18A. In contrast, for strongly interacting spins the frequency $\omega_{1,2}$ becomes negative, making the absolute value observable in the experiment. This case is depicted in Figure 2.18B. Knowing that the difference is negative, mathematically it is possible to instead calculate $-(\omega_I - 2m_S A m_I) = 2m_S A m_I - \omega_I$, giving two frequencies centred around $2m_S A m_I$ or $A/2$ for a $S = I = 1/2$ system.

Experimentally, the modulation $\omega_{1,2}$ is only observable when both the $|1\rangle \leftarrow |3\rangle$ and

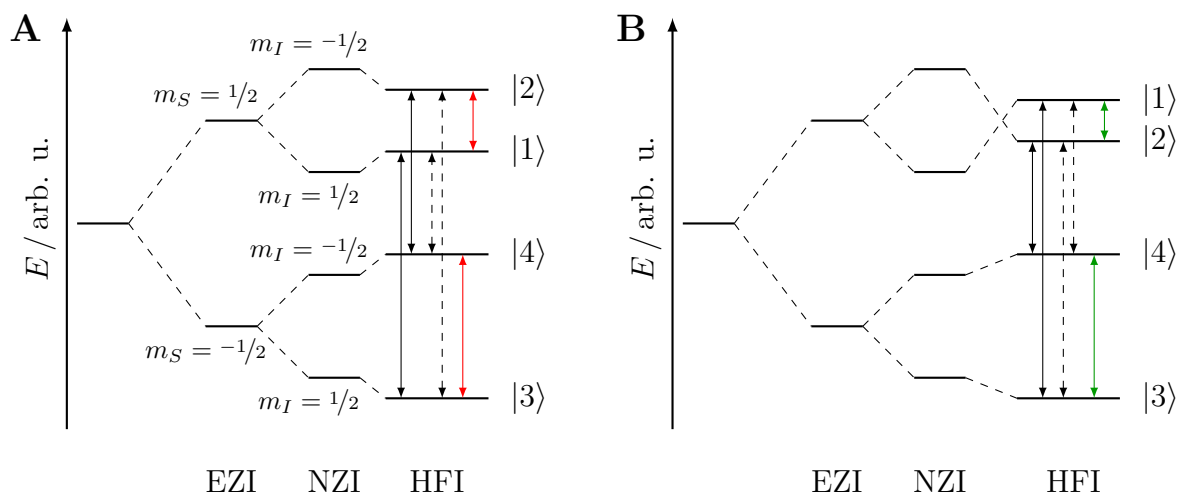


Figure 2.17: Energy diagrams for weak (A, $A < 2\omega_I$) and strong (B, $A > 2\omega_I$) hyperfine interaction between electron and nuclear spins. The allowed (forbidden) EPR transitions are given as solid (dashed) black arrows and the NMR transitions are depicted as coloured arrows.

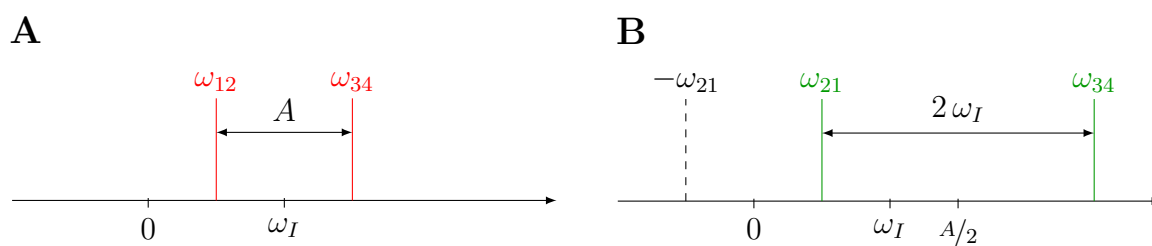


Figure 2.18: NMR spectra resulting from weak (A) and strong (B) hyperfine interaction for an $S = I = 1/2$ system.

$|2\rangle \leftarrow |3\rangle$ transitions are excited. Because the latter is formally forbidden ($\Delta m_S = 1$ and $\Delta m_I = -1$) it can only be excited in the presence of additional interactions. This is the case for significant nuclear quadrupole interaction and highly anisotropic hyperfine interaction. An ESEEM is therefore seldom seen for the weak coupling to ^1H nuclei. The full expression of the echo intensity is given in [64].

Because the resulting decay curve can be difficult to interpret, especially when many modulation frequencies occur, the experiment was expanded into the second dimension. This is called hyperfine sublevel correlation (HYSCORE) spectroscopy.

2.2.3.3 Hyperfine Sublevel Correlation Spectroscopy

The expansion of the ESEEM experiment into the second dimension is achieved by adding a 180° pulse between the second and third pulse of the three-pulse ESEEM sequence. The HYSCORE pulse sequence is given in Figure 2.19.

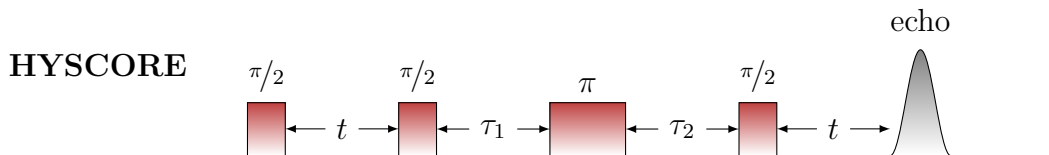


Figure 2.19: Pulse sequence of the HYSCORE experiment. The times τ are varied and t is fixed during the experiment.

The precession of the nuclear spins that can also be observed in the three-pulse 1D-ESEEM experiment after the second pulse creates nuclear coherence. This nuclear coherence is transferred from one spin-manifold to the other where the frequency changes, corresponding to the energy differences of the $\pm m_I, m_S$ states in the respective spin manifold. With the last pulse, the nuclear coherence is transferred back to electron coherence and an echo can be detected. The decay curve therefore includes both the $\omega_{1,2}$ and $\omega_{3,4}$ transitions in the modulation. By plotting the double Fourier transform of the echo intensities versus both incremented times between the pulses makes both NMR transitions visible. The resulting spectrum is shown in Figure 2.20.

The HYSCORE spectrum is separated into four quadrants, where the upper left (right) and lower right (left) contain the same information. The upper right quadrant has positive values for both frequencies ν_1 and ν_2 and is therefore denoted the $(+, +)$ quadrant while the upper left quadrant corresponds to negative values for ν_2 , making it the $(+, -)$ quadrant. As was discussed in the previous Section and shown in Figure 2.18, strongly hyperfine-coupled nuclei lead to the appearance of one nominally negative frequency. Signals from strongly coupled nuclei must therefore exist in the $(+, -)$ quadrant. The

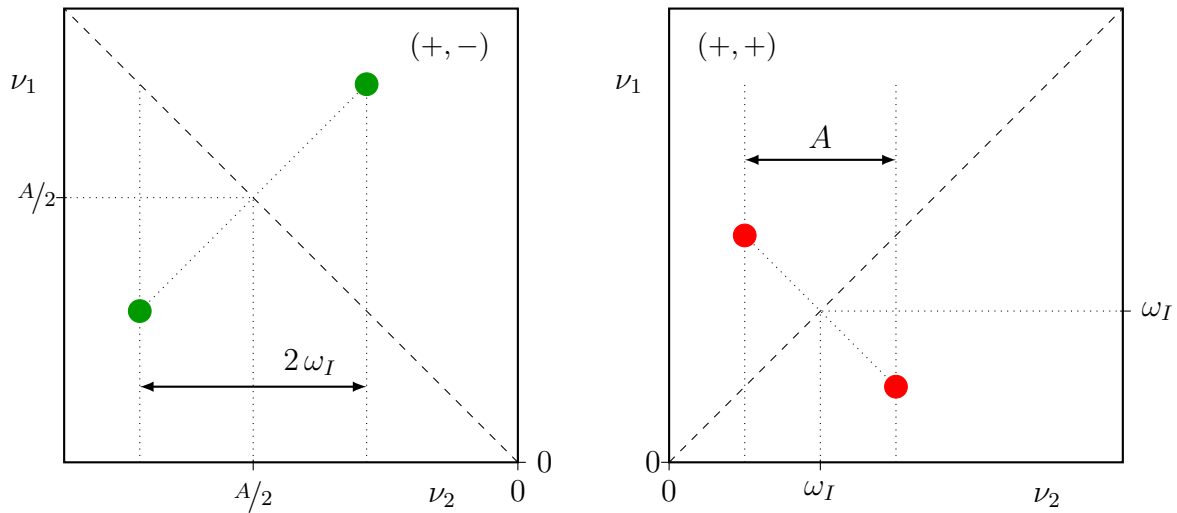


Figure 2.20: Theoretical HYSCORE spectrum for weakly (red) and strongly (green) coupled electron and nuclear spins. The shape of the signal is influenced by the anisotropy of the hyperfine interaction and the nuclear quadrupole splitting.

position and shape of the signals give information on the nuclear Larmor frequency, hyperfine interaction strength and the orientation of the A tensor relative to the g tensor. Due to the typically low signal intensity and therefore low resolution of the individual signals, the information of the tensor orientation from the signal shape is often experimentally limited. Nonetheless, the hyperfine interaction strength can be easily read from the distance of the signals to the diagonal. Due to the dependence on the nuclear Larmor frequency, the signal position is element specific and the information content is therefore much higher than in 1D-ESEEM experiments. A much more detailed explanation of the HYSCORE experiment is given in [64].

2.2.3.4 Electron-Nuclear Double Resonance Spectroscopy

Another experiment that can give the hyperfine interaction strength directly is the electron-nuclear double resonance (ENDOR) experiment. It is based on observing NMR transitions while the spin is in the ground or excited Zeeman states, i.e. during the EPR experiment. The two different pulse sequences for Davies and Mims ENDOR are given in Figure 2.21.

The Davies ENDOR experiment relies on the population difference of the ground and excited states which directly influences the echo intensity. The energy scheme of a four-level system (i.e. $S = I = 1/2$) and the level populations after irradiation with resonant microwave and radio frequencies is shown in Figure 2.22. Before resonant irradiation with microwaves, the lower levels ($m_S = -1/2$) are populated much more than the upper levels ($m_S = +1/2$) because of the Boltzmann distribution resulting from the Zeeman splitting.

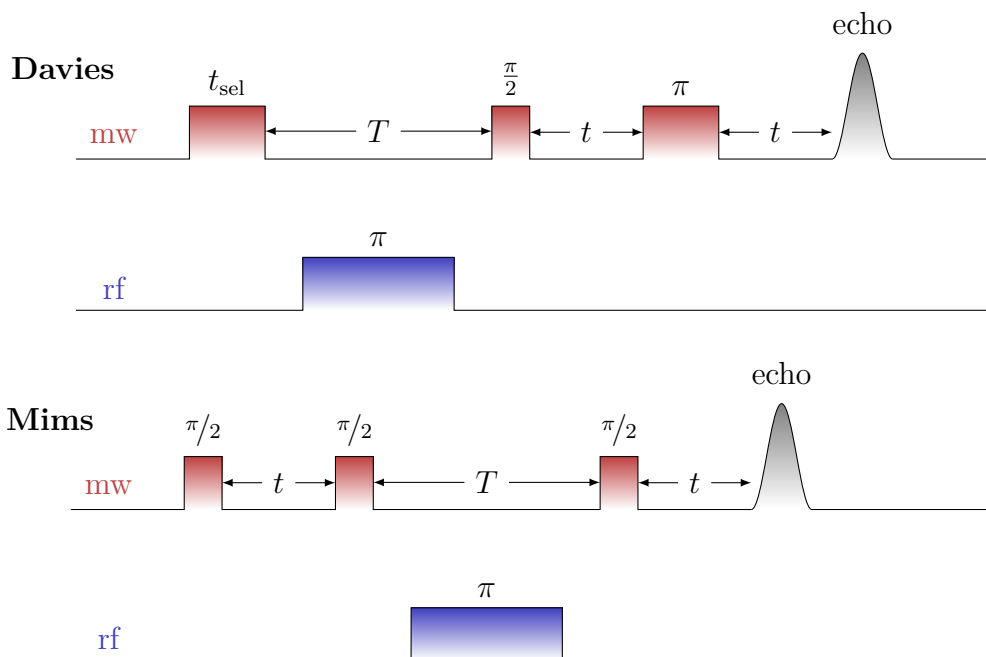


Figure 2.21: Pulse sequences for the two most common ENDOR experiments introduced by Davies (top) and Mims (bottom). All times are fixed during the experiment and only the radio frequency is varied.

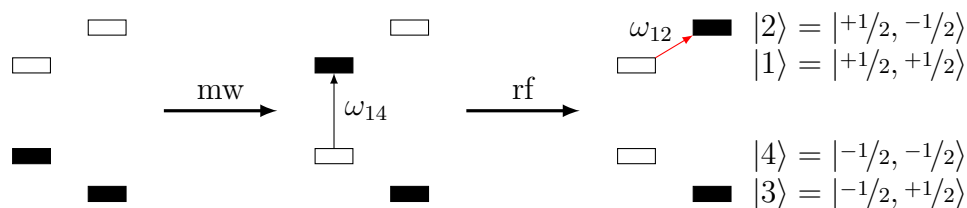


Figure 2.22: Energy level diagram of the $|m_S, m_I\rangle$ states in an $S = I = 1/2$ system with the more highly populated states marked in black.

After resonant microwave irradiation, the $|1\rangle \leftarrow |4\rangle$ or $|2\rangle \leftarrow |3\rangle$ transition is excited depending on the applied magnetic field that is kept constant during the experiment. This leads to a change of the population in the two levels that participate in the transition. As a result, both NMR transitions $|4\rangle \leftarrow |3\rangle$ and $|2\rangle \leftarrow |1\rangle$ now give much higher intensities due to higher population differences. Excitation of the NMR transitions decreases the 1,4 and 2,3 population differences compared to the Boltzmann equilibrium, leading to a decrease in EPR intensity. Effectively, the z' magnetisation is strongly decreased and therefore the subsequent Hahn echo is much weaker.

In the Mims ENDOR experiment, the signal intensity is modulated by $\cos At$, giving blind spots for $t = 2\pi n/A$. Although these blind spots make the analysis of the spectrum more difficult, the usage of nonselective pulses leads to more electron spins involved in

the experiment and the echo intensity is larger than in the Davies ENDOR experiment. As a rule of thumb, Davies ENDOR is better suited for large hyperfine coupling strengths and Mims ENDOR is better for weakly coupled spins.

2.2.3.5 Double Electron-Electron Resonance Spectroscopy

The methods described in the previous Sections allow for the determination of the hyperfine interaction parameters based on hyperfine coupling of electron and nuclear spins. As was shown in Section 2.1.7, dipolar interactions also exist between electron spins in near proximity. The interaction strength depends on the relative position and distance of the coupling spins and can therefore be used to extract intermolecular distances. This has been used, for example, to study the structure of proteins by attaching spin labels in precisely known positions in the protein and determining their distance. The corresponding experiment is called double electron–electron resonance (DEER). It is often also referred to as pulsed electron–electron double resonance (PELDOR). The pulse sequence is shown in Figure 2.23.

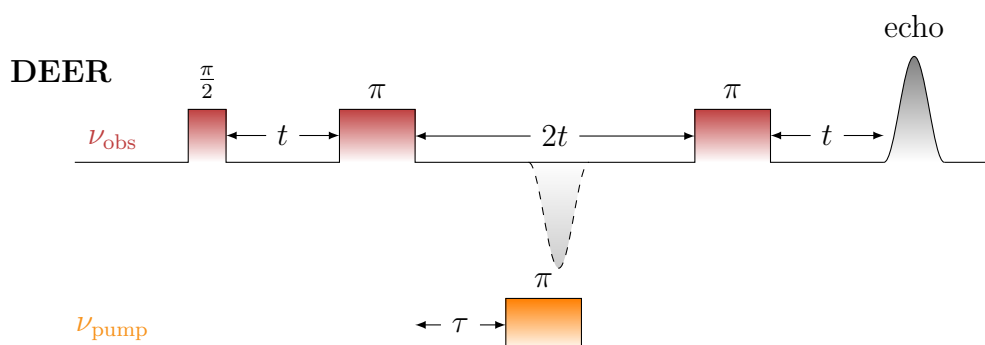


Figure 2.23: Pulse sequence of the DEER experiment. The pump frequency ν_{pump} is chosen so that the maximum spectral intensity is excited. The observer frequency ν_{obs} is chosen so that the excitation bandwidths do not overlap. The time τ , i.e. the timing of the pump pulse, is varied.

Because the time t , i.e. the observer pulse sequence, is kept constant, the echo intensity is not influenced by spin-lattice and spin-spin relaxation during the experiment. The first two pulses generate an echo (A spins) that is refocused with a third 180° pulse giving the detected echo at the observer frequency. The pulse at the pump frequency flips the electron spins at a different part of the spectrum (B spins). These B spins modulate the echo intensity depending on the relative phase of their precession and the precession of the A spins that lead to the echo. This of course happens only for those A and B spins that are coupled (dipolar or exchange) and resonant with the two microwave frequencies, respectively. From the point-dipole approximation it can be shown that the modulation

of the echo intensity I_{DEER} is given by the electron-electron coupling frequency ω_{ee} that is the sum of the dipolar and exchange interactions, ω_{dip} and J , respectively.

$$I_{\text{DEER}} = \cos(\omega_{\text{ee}}\tau) = \cos((\omega_{\text{dip}} + J)\tau) \quad (2.53)$$

Assuming that exchange interactions can be neglected, as is the case for A-B distances larger than 1.5 nm for non-conjugated systems, the oscillation frequency becomes $2\pi\omega_{\text{dip}}$, see Equation (2.32). For randomly distributed A and B spins, the Fourier transform of the echo intensity after background correction therefore gives a Pake pattern from which the distance distribution can be extracted. The background correction is necessary to subtract intramolecular interactions that depend on the number of excited spins giving an exponential decay. One drawback of the experiment is that mathematically many distance distributions can reproduce the DEER trace (the echo intensity as a function of τ). It is therefore assumed that the distance distribution follows a Gaussian and the smallest number of parameters is used to fit the DEER signal. The analysis is typically performed in the DeerAnalysis software that contain different distribution models. [71] An in-depth explanation of DEER is given in [72].

2.2.4 Magnetic Circular Dichroism

Optical spectroscopy refers to spectroscopic methods where the excitation wavelength is in the near-infrared, visible or ultraviolet regions of the electromagnetic spectrum. The observed signals typically arise from electric dipole transitions between electronic states but magnetic dipole and electric quadrupole transitions can be observed as well. Magnetic circular dichroism (MCD) spectroscopy is based on the difference in the absorption of left and right circularly polarised light, i.e. lcp and rcp, respectively.

The MCD signal is defined as the ratio of the difference in absorption of lcp and rcp ΔA divided by the total absorption E at each wavelength.

$$\text{MCD} = \frac{\Delta A}{E} = \frac{A_{\text{lcp}} - A_{\text{rcp}}}{A_{\text{lcp}} + A_{\text{rcp}}} \quad (2.54)$$

Because ΔA can be positive or negative, the MCD intensity is a signed quantity. This gives it a higher resolution than electronic absorption spectroscopy since overlapping signals can be more easily distinguished.

Linearly polarised light can be seen as the sum of same amounts of left and right circular polarised light. Because of the circular motion, these photons have an angular momentum of $+\hbar$ and $-\hbar$ for lcp and rcp, respectively, i.e. lcp photons can excite transitions with

$\Delta m_S = +1$ and rcp photons can excite transitions with $\Delta m_S = -1$. Linearly polarised light can therefore excite both EPR transitions. The MCD intensity is both a function of the Zeeman matrix element and the electronic dipole transition matrix element. Experimentally, linearly polarised light is periodically converted into lcp and rcp light by a photoelastic modulator (PEM). The PEM, which is oriented at 45° to the polarisation direction, delays one of the components (lcp or rcp) of the linear polarised light by periodic compression and elongation of the modulator crystal, leading to periodic modulation of its birefringence. The polarisation of transmitted light is modulated between lcp and rcp at the known PEM frequency that can then be used to demodulate the absorption signal at the detector. Typically, photomultiplier tubes and InGaAs detectors are used for visible and infrared spectra ranges, respectively.

Traditionally, the MCD intensity is divided into three different contributions, called *A*, *B*- and *C*-terms and are depicted in Figure 2.24. The general expression of the MCD effect is given by

$$\frac{A_{\text{lcp}} - A_{\text{rcp}}}{A_{\text{lcp}} + A_{\text{rcp}}} = \gamma \mu_B B \left(-A_1 \frac{\partial f(E)}{\partial E} + B_0 f(E) + C_0 \frac{f(E)}{k_B T} \right) \quad (2.55)$$

where γ includes a number of spectroscopic constants, $f(E)$ denotes the line shape, e.g. a Gaussian, and A_1 , B_0 and C_0 denote the aforementioned MCD terms.

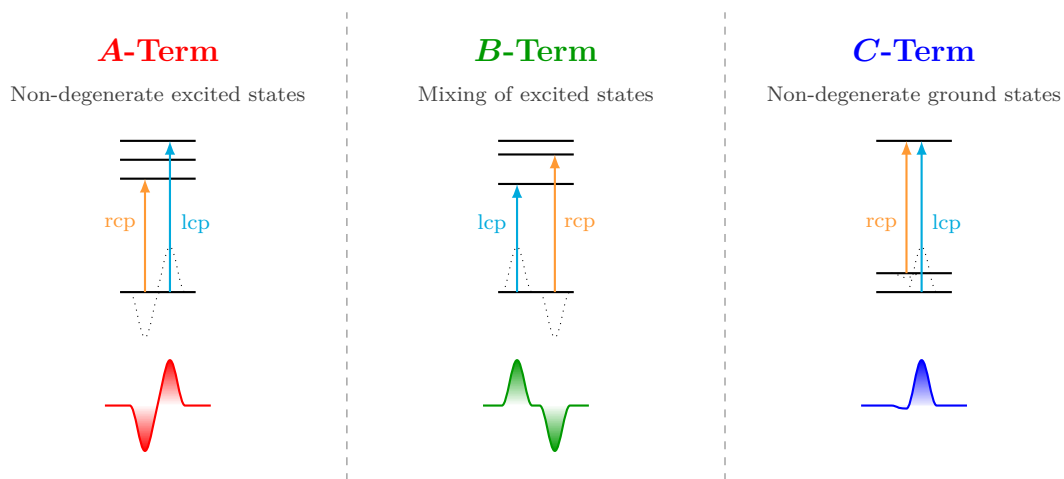


Figure 2.24: Origins of *A*, *B*- and *C*-terms in MCD spectroscopy.

A-terms result from the excitation of electrons from nondegenerate lower energy levels to a degenerate excited state split by the applied magnetic field. Since both the energies and angular momenta of the excited states are different, the two MCD transitions, excited by lcp and rcp photons, respectively, have different transition energies and different signs. The resulting spectral shape looks similar to the derivative signal of a Gaussian with

the rcp absorption at lower photon energies. As can be seen from Equation (2.55), A -terms are temperature independent. They are only observed in applied magnetic fields, as the excited states would be degenerate without the Zeeman interaction that lifts the degeneracy.

B -terms can be described by field-induced mixing of excited states. Because this is a second order effect, B -terms are often weak and absorption or emission-like. Like for A -terms, the signals arising from B -terms are temperature independent.

C -terms lead to the most important signals in paramagnetic compounds. They originate from degenerate ground states that are split by the external magnetic field. Because of a higher population of the lower of the two states, at low temperatures and high magnetic fields the intensity for the transition from the lower level is much higher in intensity. The overall spectral shape is typically that of a single asymmetric absorption line. Signals resulting from C -term behaviour can be easily assigned because of their pronounced field and temperature dependence. These signals are, at least for low temperatures, much more intense than signals resulting from A - and B -terms. The relative intensities can be calculated with

$$A : B : C \propto \frac{1}{\Gamma_{\text{BW}}} : \frac{1}{\Delta W} : \frac{1}{k_{\text{B}}T}. \quad (2.56)$$

A bandwidth $\Gamma_{\text{BW}} = 1000 \text{ cm}^{-1}$, an energy separation of the mixing states $\Delta W = 10000 \text{ cm}^{-1}$ and the thermal energy $k_{\text{B}}T = 1 \text{ cm}^{-1}$ for a temperature of 1.5 K lead to an intensity distribution of 1:0.1:1000, i.e. signals arising from C terms dominate the spectrum at low temperatures.

Typically, transitions are assigned by comparison to known absorption energies from UV/Vis measurements of related compounds or with the help of quantum mechanical calculations. A more complete theoretical and experimental background of MCD spectroscopy can be found in [73, 74].

2.2.5 X-Ray Absorption and Emission

X-ray spectroscopy is a powerful tool to investigate the electronic structure of chemical compounds. A typical X-ray emission spectrum is shown in Figure 2.25A and explained in the following. In X-ray emission spectroscopy, electrons are removed from a core orbital, such as 1s, by excitation with high-energy photons, see Figure 2.25B.

The relaxation of electrons from higher-lying orbitals to the hole orbital leads to the emission of photons. Here, the transition dipole moment $\mu_{fi} = \langle \psi_f | \mu | \psi_i \rangle$ must be non-zero for the transition to be allowed. This can be easily estimated from the symmetry of the

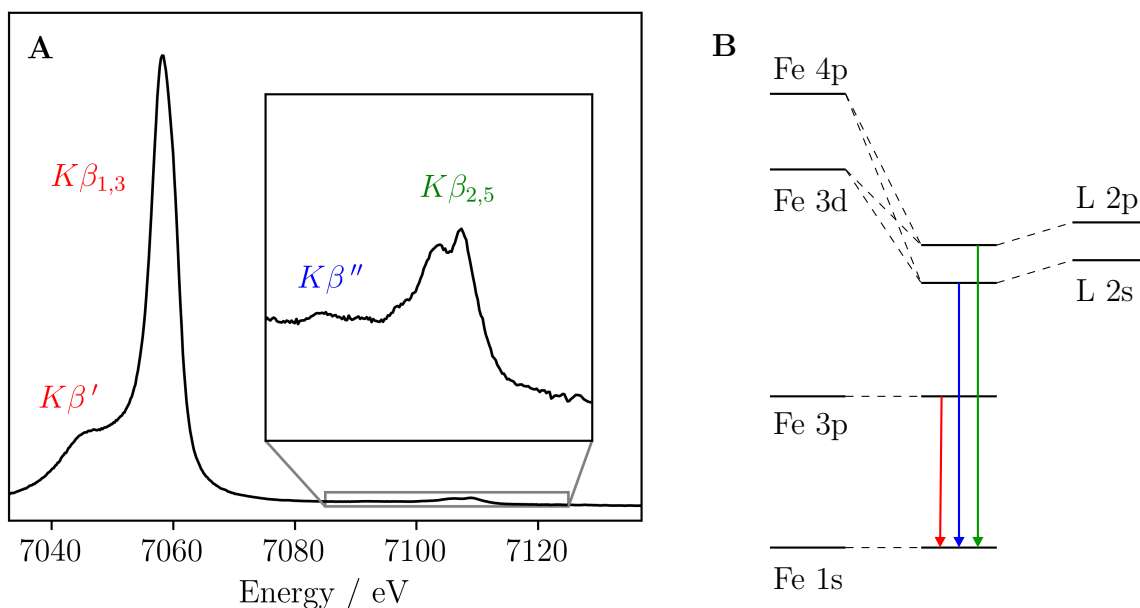


Figure 2.25: A) Typical shape of an X-ray emission spectrum with the CtC (red) and VtC (blue and green) regions. B) Origin of the lines in the spectrum.

wave functions of the orbitals with the knowledge that the dipole moment operator μ and p orbitals have u (ungerade) symmetry while s and d orbitals have g (gerade) symmetry, e.g. $\langle \psi_s | \mu_{sp} | \psi_p \rangle = g \times u \times u = g$ ($g \times g = g$, $g \times u = u$, $u \times u = g$). The most intense transitions that are experimentally observed are therefore those originating from a metal p orbital. Because these transitions are between core orbitals, they are called core-to-core (CtC) transitions. Here, the $K\alpha$ ($1s \leftarrow 2p$) and $K\beta$ ($1s \leftarrow 3p$) transitions are relevant for first-row transition metals, where the transitions from shells close to the nucleus are weakly influenced by the surroundings of the metal and therefore of minor interest in the study of the electronic structure. On the other hand, the $K\alpha$ and $K\beta$ energies are element dependent and CtC XES can therefore be used for determining the elemental composition of unknown samples. The $K\beta$ line is split into the $K\beta_{1,3}$ mainline and the $K\beta'$ shoulder for paramagnetic compounds. The origin of the latter lies in the exchange interaction between the multiple states resulting from the relaxation of an electron into the 1s orbital: Figure 2.26 depicts the situations that result after a spin-up or a spin-down electron is removed from the 1s core orbital. Because of the Pauli exclusion principle an electron with the same spin as the removed electron must relax, leaving a spin polarised 3p orbital. The spin-polarised 3d orbitals interact differently with the two possible configurations (see Figure 2.26) in the 3p orbitals via exchange interaction. The energies of the two states (labelled 5P and 7P in Figure 2.26) is therefore not the same and the $K\beta'$ shoulder results

in the spectrum. The energy separation of the two lines is dependent on the total spin of the sample. The energy of the $K\beta_{1,3}$ mainline depends mostly on the oxidation state of the metal and the ligand species, making the study of the mainline a great tool to determine the electronic structure and immediate surrounding of the metal centre.

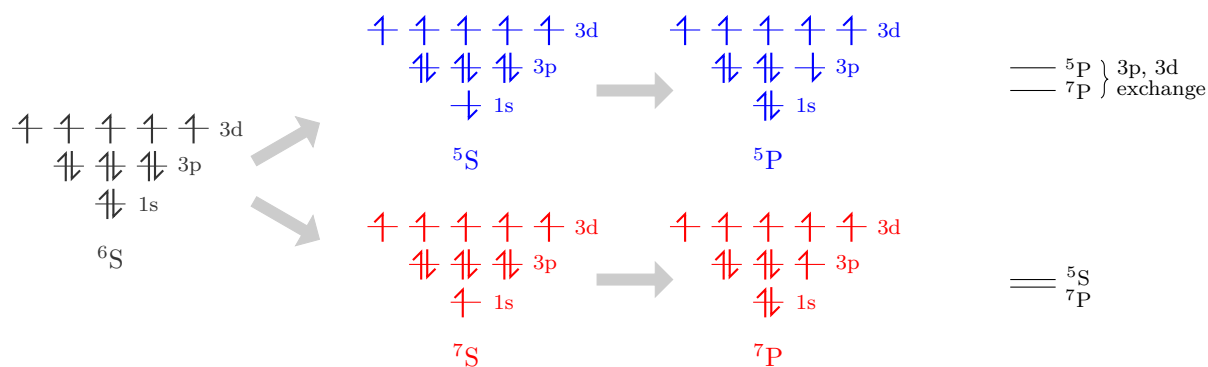


Figure 2.26: Origin of the splitting of the CtC region into the $K\beta_{1,3}$ mainline and the $K\beta'$ shoulder for paramagnetic samples.

At higher energies the valence-to-core (VtC) energies can be observed. It results from transitions from ligand centred orbitals mixed with metal p and d orbitals. Here, more information on the ligand can be obtained from the positions and relative intensities of the the two lines.

Although the X-ray emission spectrum gives a lot of information of the studied compound, the technique is often combined with absorption measurements. The X-ray absorption spectrum (XAS) is divided into pre-edge, edge, near-edge structure (XANES or NEXAFS) and extended X-ray absorption fine structure (EXAFS). In XANES, the energy of the incident X-rays is varied and the transmission is detected. As soon as the energy of the X-rays is sufficient to excite (or remove) a core electron, the X-rays are absorbed and a sudden jump (absorption edge) in the absorption spectrum can be observed. The region in the spectrum at the smallest energies above the absorption edge is the XANES region, whereas in the pre-edge region the compound is not actually ionised, but electrons are excited to bound states. Because of the short core-hole lifetime, the features in the spectrum are rather broad, limiting the information content. By detecting the fluorescence intensity at one specific energy (typically at the $K\beta_{1,3}$ mainline) rather than the transmission, as a function of excitation energy, the lifetime broadening is reduced because now the lifetime broadening depends on the hole lifetime in the higher-lying orbital and the linewidth of the spectral features is narrowed. This technique is called high-energy-resolution fluorescence detected XANES (HERFD-XANES). From these spectra the LUMO structure of the cen-

tral atom can be probed. This gives a precise measure of molecular orbitals that mix with ligand states, i.e. the influence of the immediate surrounding of the metal can be investigated. HERFD-XANES is typically used for the qualitative comparison of spectra of a known sample with the sample under investigation. A more complete theoretical and experimental background of X-ray absorption and emission spectroscopies can be found in [75, 76]

2.2.6 SQUID Magnetometry

It is known from the previous Sections that electron and nuclear spins have a magnetic dipole moment. In order to measure this quantity, one possibility is to measure the magnetic field at position \mathbf{r} generated by the magnetic dipole moment $\boldsymbol{\mu}$ of the spins, see Equation (2.4). It can be calculated with

$$\mathbf{B} = n \frac{\mu_0}{4\pi r^2} \frac{3\mathbf{r}(\boldsymbol{\mu} \cdot \mathbf{r}) - \boldsymbol{\mu}r^2}{r^3} \quad (2.57)$$

with the number of spins n , vacuum permeability μ_0 and distance r . For typical amounts of scientific research samples of ca. 0.01 mmol, the magnetic field generated in direction of the magnetic dipole moment in a distance of 1 cm under the assumption that all spins are oriented in parallel would be ca. 0.1 mT. This is lower than the earth's magnetic field and would be very difficult to measure, especially since a very stable applied magnetic field that polarises the spins would be required. Instead, modern magnetometers measure the change in voltage in the SQUID sensor due to the induced current by moving the sample through a number of superconducting coils (the pick-up coils), see Figure 2.27A.

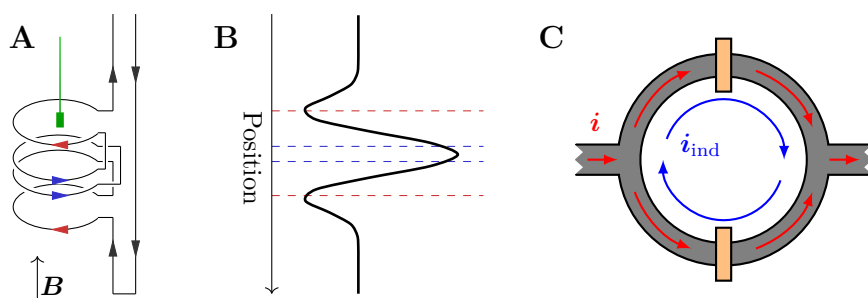


Figure 2.27: A) Arrangement of the four pick-up coils in the magnetometer with opposing directions of currents. The sample (green) is moved through the coils in direction of the applied magnetic field \mathbf{B} . B) Typical magnetometer response, i.e. measured voltages for the movement of the sample through the four coils. C) SQUID sensor with the two parallel Josephson junction (orange).

By arranging the coils in a way that the direction of the induced current is opposite for the two coils in the centre of the set-up to that in the outer coils, the typical magnetometer

response shown in Figure 2.27B can be obtained. These currents are still very low and the measurement is prone to electrical noise. In order to realise the precise measurement of the magnetic field of the sample, an additional superconducting coil is inductively coupled to the first set of coils. This new coil, the so-called SQUID (superconducting interference device) sensor (see Figure 2.27C), has one or two Josephson junctions, i.e. narrow regions that are not superconducting, in parallel. The change in current running through the first set of coils (that are far enough apart so that the current in the SQUID sensor can be related to only one of the loops) induces a screening current i_{ind} in the SQUID sensor in addition to a constantly applied current i , that is split equally to the two Josephson junctions in absence of the induced current. The newly induced current i_{ind} circulates in that direction so that the magnetic flux induced by the changing current is brought to an integer multiple of the magnetic flux quantum Φ_0 , which is required because of the Josephson junctions. For weak induced current, the closest value is the same as the initially applied current, i.e. the magnetic field is reduced by the new currents induced in the SQUID. Because the initial current through the SQUID sensor is not circular but the newly induced current is, the total current in one of the sides is reduced while the current in the other side is increased. If the difference in currents at the two junctions reaches a critical level, a voltage across the junctions appears. For further increasing current, i.e. when the value $\Phi_0/2$ on top of the initial current is exceeded, the nearest integer multiple of the magnetic flux quantum is an additional Φ_0 and the magnetic field is increased by the induced current, i.e. the direction of i_{ind} changes. A periodic oscillation of the direction of the current and therefore the voltage between the two Josephson junctions results. It reaches zero whenever the magnetic field induced in the SQUID coils by the changing current in the pick-up coils reaches an integer multiple of Φ_0 . Since frequencies can be measured much more precisely than absolute voltages and the frequency is dependent on the absolute voltage, the current and therefore the magnetic field induced by the sample can be measured. Suppose two samples with different magnetic moments are moved through the pick-up coils. For the sample with a higher magnetic moment integer values of Φ_0 are crossed more often in the same amount of time (assuming the same movement speed of samples), i.e. the frequency of the induced alternating current (and voltage) increases with the magnetic moment. This quantity can be used to learn about magnetic properties of the sample that influence the magnetic moment to be different from the value expected from equation 2.2. Most importantly, the population difference of the spin-up and spin-down spins influences the magnetic moment of the whole sample. The typical temperature and field dependence as a result of the Boltzmann distribution is shown in Figure 2.28A.

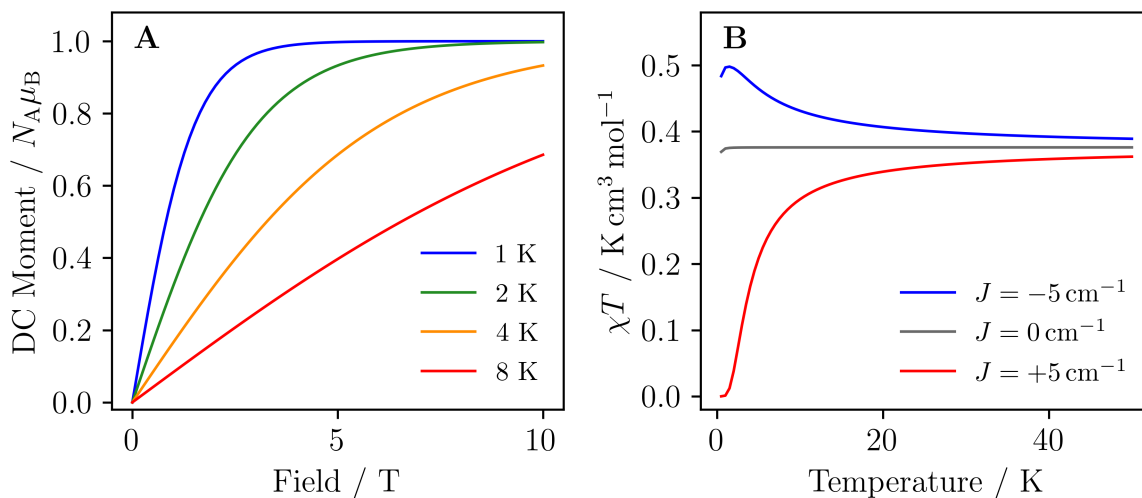


Figure 2.28: A) Typical field and temperature dependence of the magnetic moment of non-interacting spins with $S = 1/2$ and $g = 2$. B) Susceptibility-temperature product per spin for two spins ($S = 1/2$, $g = 2$) without intermolecular interaction ($J = 0$), anti-ferromagnetic ($J > 0$) and ferromagnetic ($J < 0$) spin-spin interactions.

For increasing fields the energy difference of the two Zeeman states (for $S = 1/2$) increases while decreasing temperatures lead to decreased population of the excited Zeeman states, i.e. both external stimuli increase the magnetisation of the sample. Above a certain magnetic field H and below a certain temperature T all spins are oriented in parallel and the saturation magnetic moment M of the sample (the product of the number of spins and the magnetic moment per spin μ_B) is reached. Spin interactions can increase or decrease the magnetic moment of the sample. These interactions are easiest to recognize in the susceptibility-temperature product χT ($\chi = dM/dH$), as depicted in Figure 2.28B. From the Curie-Weiss law it is known that χT is constant for non-interacting magnetic moments, which can be observed experimentally for thermal energies much higher than the interaction strength. The expected high-temperature value can be calculated to $\chi T \approx 1/8g^2S(S+1)$. At thermal energies of the order of and below the interaction strength ($5\ cm^{-1}$ correspond to 7.2 K in thermal energy, see Figure 2.28B) the magnetisation is affected by the interaction. Here, zero-field splitting and anti-ferromagnetic spin-spin interactions are the most prominent interactions that decrease the measured magnetic moment while ferromagnetic spin-spin interactions increase the magnetic moment. Temperature dependent phenomena such as spin crossover can be easily recognised by a rise in χT for increasing temperatures because an increasing number of molecules changes to the high-spin state. A more complete theoretical and experimental background of SQUID magnetometry can be found in [77, 78].

2.2.7 Mössbauer Spectroscopy

In this Section, the theory behind Mössbauer spectroscopy is explained. First, the generation, detection and absorption of the gamma rays are given and the general shape of the Mössbauer spectrum and the relevant interactions are explained briefly to give a short overview of the relevant experimental parameters. Then, these interaction are mentioned in more detail. A short overview over Mössbauer spectroscopy is given in [79] and a more complete theoretical background is given in [80].

2.2.7.1 Generation and Detection of Gamma Rays

The Mössbauer effect is the resonant emission and absorption of gamma radiation, due to transitions within the nucleus changing its spin state. The generation of gamma rays as a result of radioactive decay in ^{57}Co is depicted in Figure 2.29. Therein, a proton combines with the electron to a neutron, emitting an electron neutrino. The gamma rays then result from the relaxation of an electron of an outer shell into the resulting free orbital in the K shell.

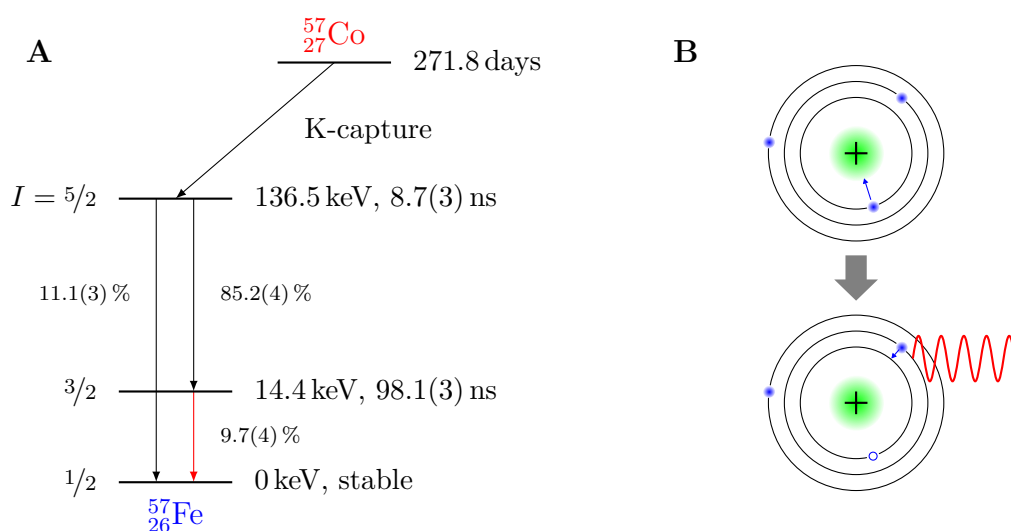


Figure 2.29: (A) Decay scheme of ^{57}Co to ^{57}Fe . The transition probabilities, calculated from the respective areas of the γ -ray photo peaks, and energies are taken from [81], the half-life of ^{57}Co is taken from [82] and the lifetimes of the excited states of ^{57}Fe are taken from [83]. (B) Schematic representation of the capture of an electron from the K shell, leading to the emission of an electron neutrino.

The gamma rays are detected with the help of a scintillator. Scintillators function by emitting light in or near the visible range, which is detected by highly sensitive photomultiplier tubes. In inorganic scintillators, the gamma photons excite an electron from

the valence band to either the conduction band or the exciton band, see Figure 2.30A. When the resulting exciton, i.e. the loosely bound electron-hole pair, is captured by an impurity centre, scintillation light is emitted by de-excitation. This is the fast component of the irradiation. When an electron from the valence band is excited, the generated hole is independent from the electron, i.e. no pair is formed. This creates a metastable state, from which the de-excitation happens via a recombination due to trapping. Therefore this process is slower than for the aforementioned pairs and it is denoted the slow component of scintillation. In comparison, noble gases in a combination with nitrogen, that can also be used as a scintillator, have much faster reaction times of the order of 1 ns compared to 16 ns for $\text{LaBr}_3(\text{Ce})$ and 230 ns for $\text{NaI}(\text{Tl})$ [84], but due to the low density of the gas, the photon yield is much lower than that for inorganic scintillators.

In order to detect the light emitted by the crystal, a photomultiplier tube is added directly behind the scintillator. Here, the photons hitting the conducting photocathode lead to a release of photoelectrons as a result of the photoelectric effect. By applying a voltage across the vacuum tube between the cathode and the anode and keeping the dynodes at an intermediate electrical potential, the electrons are accelerated towards the dynodes, where secondary emissions lead to an increase in the number of electrons hitting the anode, where a voltage that depends on the number of initial photons can be measured, see Figure 2.30.

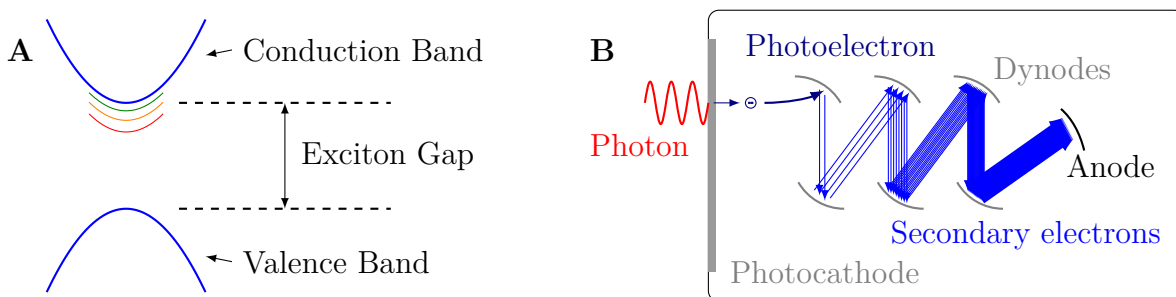


Figure 2.30: (A) Schematic band structure of an inorganic scintillator. (B) Diagrammatic representation of a photomultiplier tube.

2.2.7.2 Absorption of Gamma Rays

An emitter of light experiences recoil which shifts the energy of the emitted light by the recoil energy E_R . This recoil energy can be calculated from the kinetic energy resulting from the movement of the atom with the velocity v and the momentum p_n .

$$E_R = \frac{1}{2}mv^2 = \frac{p_n^2}{2m} = \frac{E_\gamma^2}{2mc^2} \approx \frac{E_0^2}{2mc^2} \quad (2.58)$$

The recoil energy is small compared to the energy of the emitted radiation, i.e. $E_0 \approx E_\gamma$. The recoil energy can be calculated to ca. 1.95 meV for $E_\gamma = 14.4$ keV and the speed of light c and the mass of the iron nucleus m . Due to the small natural linewidth of ca. 2 neV for ^{57}Fe Mössbauer transitions, no transition can be observed when the gamma source emits the same energy as is required for the absorption, e.g. when the relaxation of ^{57}Fe from the excited nuclear state is used for the excitation of ^{57}Fe in the absorber (see next Section). Fortunately, there is a non-zero probability of the emission and absorption to take place without recoil of the atom as no phonons are excited during the nuclear excitation. This so-called zero-phonon process does not lead to vibrations and instead the momentum is conserved by it being taken up by the whole lattice as a translation of the same in the same direction as the propagation of the gamma rays. Since the whole lattice takes up the energy, the recoil per atom is vanishingly small, because of the now much higher effective mass, drastically reducing E_R per atom. The recoil-free fraction f , i.e. the fraction of absorptions and emissions happening without the creation of a phonon can be expressed with the expectation value of squared vibrational amplitude $\langle x^2 \rangle$, i.e. the mean square displacement.

$$f = e^{-\frac{\langle x \rangle^2 E_\gamma^2}{(\hbar c)^2}} \quad (2.59)$$

For very high transition energies, the recoil-free fraction becomes very small. This explains why only certain isotopes are suitable for Mössbauer spectroscopy. Because of the temperature dependence of the mean square displacement, the recoil-free fraction increases for lower temperatures. Here, the Debye model with the Debye temperature θ_D gives reasonable results for the temperature dependence of the recoil-free fraction and therefore the signal intensity.

$$f(T) = \exp \left[\frac{-6E_R}{k_B \theta_D} \left\{ \frac{1}{4} + \left(\frac{T}{\theta_D} \right)^2 \int_0^{\theta_D/T} \frac{x}{e^x - 1} dx \right\} \right] \quad (2.60)$$

Here, E_R is the recoil energy of the free atom. The Debye temperature is typically high for metals and metal oxide compounds and low for metal-organic complexes, giving higher signal intensities for the former.

In order to measure the Mössbauer spectrum the gamma ray energy still needs to be modulated. The easiest way to achieve this is by moving the source (or sample) in a controlled back-and-forth motion, which modulates the gamma ray energy through the Doppler effect. In modern spectrometers, the source oscillates between two positions with a frequency of ca. 30 Hz allowing to measure typical isomer shifts, quadrupole

and magnetic splittings. The set-up of the spectrometer is explained in more detail in Chapter 3.

2.2.7.3 The Mössbauer Spectrum

Mössbauer spectroscopy is based on the resonant absorption of gamma radiation to excite the nuclear state via electric monopole, electric quadrupole and magnetic dipole interactions, as will be explained in the following. The energy of the gamma source is modulated by the Doppler energy resulting from the motion of the source. The transmitted gamma rays are detected with a scintillator that is coupled to a photomultiplier tube (PMT). Figure 2.31 depicts typical Mössbauer spectra highlighting the relevant interactions, namely the isomer shift δ_{IS} , quadrupole splitting ΔE_{Q} and magnetic hyperfine splitting resulting from the magnetic field B_{hf} at the nucleus.

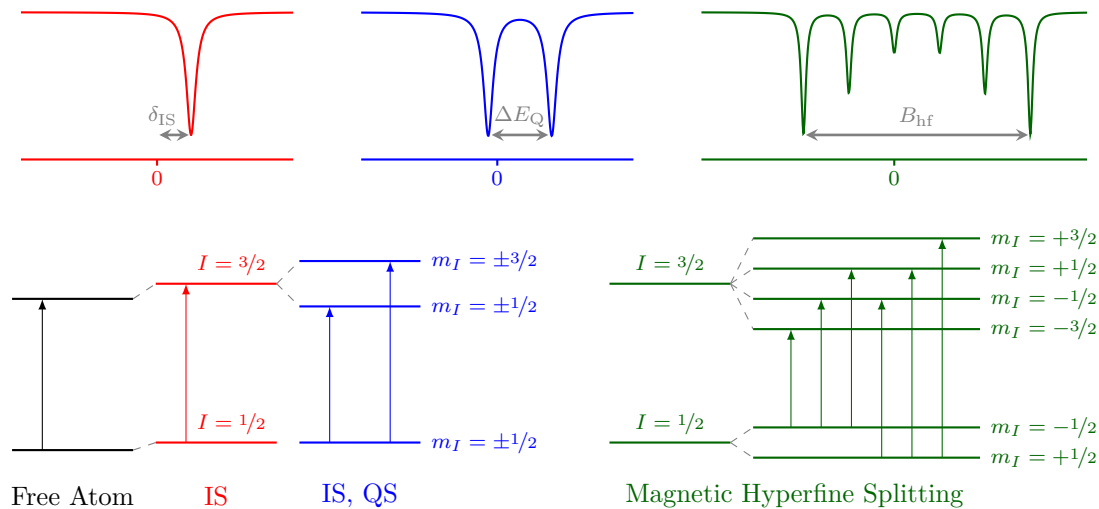


Figure 2.31: Schematic representation of typical ^{57}Fe Mössbauer spectra resulting from the relevant interactions of the nuclei with their surrounding. The electric monopole interaction results in the so-called isomer shift δ_{IS} , the electric quadrupole interaction splits the states by ΔE_{Q} , resulting in two absorption lines, and the magnetic dipole interaction leads to a hyperfine splitting by lifting the degeneracy of the m_I states in a magnetic field.

Iron is the most studied element with Mössbauer spectroscopy, while many elements do not show a Mössbauer effect at all. The reasons for that are usually too long lifetimes of the excited state, which in turn decrease the transition linewidth so much that they can not be resolved experimentally or too short lifetimes of the excited state which broadens the transition lines giving a low resolution of the spectrum. Another criterion is that the transition energies must not be too large as the recoil energy increases for increasing energies, thereby reducing also the recoilless fraction. A list of Mössbauer active nuclei is

given in [80].

The isomer shift results from the chemical surroundings of the investigated nuclei. Compared to a standard, the isomer shift shifts the resonance line to higher or lower energies by changing the energetic levels of ground and excited states. The isomer shift depends on oxidation state, spin state, number of ligands as well as their σ -donor and π -acceptor strength. The quadrupole splitting leads to a splitting of the resonance line into two lines with the size of the splitting depending on the oxidation state, spin state and site geometry. The hyperfine interaction splits the line according to the nuclear spin microstates which can be modelled as an effective magnetic field at the nucleus. It gives insight into magnetic ordering, e.g. (anti)ferromagnetism, as well as magnetization dynamics. The analysis of the Mössbauer spectrum can therefore give valuable insight into the electronic and geometric structure of the compound under investigation. Alternatively, it can be used to study the composition of samples by comparison of the spectrum to that of known compounds.

2.2.7.4 Isomer Shift

In general, the classical electrostatic interaction of the nucleus with surrounding charges can be expressed as an integral of the product of the nuclear charge density ρ_n and the Coulomb potential V of all surrounding charges at position \mathbf{R} with $d\tau = dx_1 dx_2 dx_3$.

$$E_{\text{el}} = \int \rho_n(\mathbf{R})V(\mathbf{R})d\tau \quad (2.61)$$

The integral can be expressed in a Taylor series, where the zeroth order term is of no interest as it only represents the arbitrary energy offset (in spectroscopy only relative energies are measured). The first order term vanishes because the expectation value of the dipole moment operator is zero for states of definite parity. Terms of third and higher order are very small and need not to be considered, leaving the second order term.

$$E_{\text{el}}^{(2)} = \frac{1}{2} \sum_{i,j=1}^3 V_{ij} \int \rho_n(\mathbf{R})x_i x_j d\tau \quad (2.62)$$

V_{ij} is the electric field gradient, i.e. the second derivative of the potential. Knowing that $r^2 = \sum x_i^2$ gives

$$\int \rho_n(\mathbf{R})x_i x_j d\tau = \underbrace{\frac{1}{3} \int \rho_n(\mathbf{R})r^2 d\tau}_{\text{monopole moment}} + \underbrace{\frac{1}{3} \int \rho_n(\mathbf{R})(3x_i x_j - \delta_{ij}R^2) d\tau}_{\text{quadrupole moment}}. \quad (2.63)$$

Under the assumption of a spherical charge distribution with the radius R_u of the positive charge of the nucleus with the same potential and gradient as a point charge, the first part of Equation (2.63) can be simplified.

$$\int \rho_n(\mathbf{R})r^2 d\tau = Ze \cdot \frac{3}{4\pi R_u^3} \int r^2 d\tau \quad (2.64)$$

This equation further simplifies by using spherical coordinates and with $R_u^2 = 5/3\langle R^2 \rangle \equiv 5/3R^2$.

$$Ze \cdot \frac{3}{4\pi R_u^3} \int r^2 d\tau = Ze \cdot \frac{3}{4\pi R_u^3} \frac{4\pi}{5} R_u^3 = Ze \frac{3}{5} R_u^5 = ZeR^2 \quad (2.65)$$

Because the electric field gradient tensor is symmetric, a coordinate frame that diagonalises the tensor exists. With Poisson's differential equations the following is obtained.

$$\left(\sum_{i=1}^3 V_{ii} \right)_0 = -4\pi e |\Psi(0)|^2 \quad (2.66)$$

Using Equations (2.66) and (2.62) gives the mathematical description of the electric monopole interaction.

$$E_1 = -\frac{2}{3}\pi Ze^2 R^2 |\Psi(0)|^2 \quad (2.67)$$

The energy of the Mössbauer transition is then the difference of the energies of the ground and excited states that are not equivalent because of different nuclear volumes of the excited and ground states R_e and R_g , respectively, that substitute for R in Equation (2.67) when calculating the energies of the relevant levels. The difference in transition energies of the gamma ray source and the sample under investigation is then the isomer shift. With typical isomer shifts of the order of $1 \text{ mm s}^{-1} \approx 48 \text{ neV}$, the isomer shift is very small compared to the transition energy of ca. 14.4 keV .

Similarly, the second term in Equation (2.63) can be used to express the quadrupole interaction.

$$\int \rho_n(\mathbf{R})(3x_i x_j - \delta_{ij} R^2) d\tau = Q_{ij} \quad (2.68)$$

This gives the expression for the quadrupole energy E_Q so that $E_{\text{el}}^{(2)} = E_I + E_Q$.

$$E_Q = \frac{1}{6} \sum_{i,j=1}^3 V_{ij} \cdot Q_{ij} \quad (2.69)$$

In the following, the calculation of the isomer shift and quadrupole splitting as well as their applications and extractions from the Mössbauer spectrum are explained in detail.

The isomer shift can be calculated from the difference of the energies of the excited and ground states with Equation (2.67).

$$\delta_{\text{IS}} = E_I(\text{e}) - E_I(\text{g}) = \frac{2}{3} \pi Z e^2 \cdot (\langle R_{\text{e}}^2 \rangle - \langle R_{\text{g}}^2 \rangle) \cdot (|\Psi(0)|_{\text{absorber}}^2 - |\Psi(0)|_{\text{source}}^2) \quad (2.70)$$

It is often represented as

$$\delta_{\text{IS}} = \alpha \left(|\Psi(0)|_{\text{absorber}}^2 - C \right) \quad \text{with} \quad \alpha = \left(\frac{3Ze^2cR^2}{5\varepsilon_0E_0} \frac{\Delta R}{R} \right) \quad (2.71)$$

The value α was determined to $-0.3666 \text{ mm s}^{-1} \text{ a.u.}$ and $-0.4032 \text{ mm s}^{-1} \text{ a.u.}$ for ^{57}Fe with DFT for B3LYP and BP86, respectively. [85] The difference of effective nuclear radii of excited and ground states in Equation (2.70) is negative for ^{57}Fe . From this it follows that for higher s-electron densities the isomer shift becomes smaller (more negative) for ^{57}Fe . Since the electron density that is relevant for the isomer shift is that at the nucleus, 1s and 2s orbitals have the highest influence on the isomer shift. 4s orbitals can become relevant if they participate in molecular orbitals. The influence of p,d and f orbitals is through screening effects that lead to a contraction of s orbitals. A higher number of d electrons gives an increased shielding of the s electrons, thereby decreasing the electron density at the nucleus, increasing the chemical shift.

In the Mössbauer spectrum, the centre of the signals corresponding to one iron site is shifted by the isomer shift δ_{IS} which consists of three distinct contributions, namely the chemical shift (used synonymously to isomer shift. It results from changes in the electron density at the nucleus, see Equation (2.70) [86]). The second and third contributions are second-order Doppler shift (resulting from the relative motion of source and absorber while including time dilation of special relativity [87]) and a temperature-dependent dynamical isomer shift (resulting from electron-phonon interactions [88]).

The contribution of the individual doubly filled s orbitals to the chemical shift in Fe^{3+} was calculated to 0.432 , 0.036 and 0.006 mm s^{-1} for the $2|\psi_{1s}(0)|^2$, $2|\psi_{2s}(0)|^2$ and $2|\psi_{3s}(0)|^2$ states, respectively. [89] When going from the free atom to the covalently bound Fe^{3+}F^- ,

the transfer of electron density of the fluorine ion to the 4s iron orbitals increases the chemical shift of the order of 0.1 mm s^{-1} . Additionally, the influence of the crystal field on the chemical shift is of the order of 0.025 mm s^{-1} . [89] These observations make it clear that the isomer shift can be used to determine the oxidation state of the nucleus under investigation. Since the 4s orbitals also influence the electron density at the nucleus, information on the binding situation around the nucleus can also be extracted from the isomer shift.

The temperature-dependent Doppler shift can be calculated with the mean squared velocity $\langle v^2 \rangle$ of the vibration of the absorbing or emitting atom to

$$\delta_{\text{SOD}} = -E_{\gamma} \frac{\langle v^2 \rangle}{2c^2}. \quad (2.72)$$

As it is related to the motion of the atoms, the second-order Doppler shift decreases with decreasing temperature. Thus, it becomes vanishingly small at temperatures of liquid helium and rarely exceeds -0.02 mm s^{-1} at liquid nitrogen temperature. At room temperature it can be as large as -0.1 mm s^{-1} . The other source of the temperature dependence is the mentioned temperature-dependent dynamical isomer shift, which results from the interactions of lattice electrons with lattice vibrations, so that the overlap of orbitals of the lattice atoms with the iron s orbitals changes dynamically. [88] As the phonon density is temperature dependent, this contribution to the isomer shift also changes with temperature. A quantification of the effect on the isomer shift is given in [89].

2.2.7.5 Quadrupole Splitting

Quantum mechanically, the Hamiltonian for the nuclear quadrupole interaction is represented with the shift operators $\hat{\mathcal{I}}_{\pm} = \hat{\mathcal{I}}_x \pm i\hat{\mathcal{I}}_y$.

$$\hat{\mathcal{H}}_{\text{NQI}} = \frac{eqV_{zz}}{4I(2I-1)} \left[3\hat{\mathcal{I}}_z^2 - I(I+1) + \frac{\eta}{2}(\hat{\mathcal{I}}_+^2 + \hat{\mathcal{I}}_-^2) \right] \quad (2.73)$$

For an axial electric field gradient, i.e. $\eta = 0$ the Hamiltonian can be solved to give

$$E_{\text{Q}}(m_I) = \frac{eqV_{zz}}{4I(2I-1)} \left[3m_I^2 - I(I+1) \right]. \quad (2.74)$$

This gives energies of the substates as $E_{\text{Q}}(\pm 3/2) = 1/4eQV_{zz}$ and $E_{\text{Q}}(\pm 1/2) = -1/4eQV_{zz}$ giving

$$\Delta E_{\text{Q}} = E_{\text{Q}}(\pm 3/2) - E_{\text{Q}}(\pm 1/2) = eQV_{zz}/2. \quad (2.75)$$

In case $\eta \neq 0$, the energy levels can be calculated with

$$E_Q(m_I) = \frac{eqV_{zz}}{4I(2I-1)} [3m_I^2 - I(I+1)] \sqrt{1 + \frac{\eta^2}{3}}. \quad (2.76)$$

Since the elemental charge e and quadrupole moment Q are constant ($Q(^{57}\text{Fe}) = 0 \text{ m}^2$ for the ground state and $Q(^{57}\text{Fe}) = 154.9(2) \cdot 10^{-31} \text{ m}^2$ for the excited state) the experimentally observed quadrupole splitting can be easily related to the electric field gradient. The electric field gradient and asymmetry parameter η can be calculated by the summation of all charges surrounding the nucleus with the angle θ between the charge and the z axis, where the z axis is either known from symmetry arguments or it is chosen so that V_{zz} is maximised.

$$V_{zz} = \sum_i qr^{-3}(3 \cos^2 \theta^2 - 1) \quad (2.77)$$

$$\eta = \frac{1}{V_{zz}} \sum_i q_i r_i^{-3} 3 \sin^2 \theta_i \cos 2\phi_i \quad (2.78)$$

If the principal axis is unknown, all elements V_{ij} have to be calculated individually and after diagonalisation the largest component V_{zz} can be obtained. The actual electric field gradient felt by the nucleus is different to that obtained from these equations as the electron shell of the atom under investigation might be distorted due to contributions of the iron 3d valence electrons involved in chemical bonds and the charge distribution of neighbouring atoms. When neglecting spin-orbit coupling, the effect of the valence electrons on the field gradient is a function of the energy difference of the d_{xy} ground orbital and the d_{xz} and d_{yz} orbitals. [90, 91] Spin-orbit coupling mixes the orbital characters and thereby complicates the situation. The lattice contribution for ionic compounds can be calculated by summation over the charge distribution and it was shown in [92] that this contribution is minor compared to that of the valence electrons. For covalent compounds, this approach is problematic as the approximation that the iron 3d orbitals in molecules behave as they do in the free atom is invalid and a computational approach must include a full molecular orbital treatment. [93, 94] As the energies separating the d_{xy} , d_{xz} and d_{yz} orbitals in only slightly distorted octahedral symmetry is of the order of the thermal energy, the valence contribution to the electric field gradient is temperature dependent while the lattice contribution of orbitals with $d_{x^2-y^2}$ and d_{z^2} character is temperature independent. Because low-spin compounds have stronger ligand-metal interactions and anisotropic bonding to the relevant valence orbitals, they show much less of a temperature dependence of the quadrupole splitting than high-spin compounds. [95]

The intensity ratio of the two Mössbauer lines split by the quadrupole splitting is given by [96] to be

$$\frac{I_{\pm 1/2 \rightarrow \pm 3/2}}{I_{\pm 1/2 \rightarrow \pm 1/2}} = \frac{3(1 + \cos^2 \theta)}{5 - 3 \cos^2 \theta}. \quad (2.79)$$

The resulting spectra are depicted in Figure 2.32. In the case that the orientations of the molecules are statistically distributed, as is true for amorphous and heavily ground crystalline samples, the sum of all orientations is measured and the two signals have the same intensity in the spectrum.

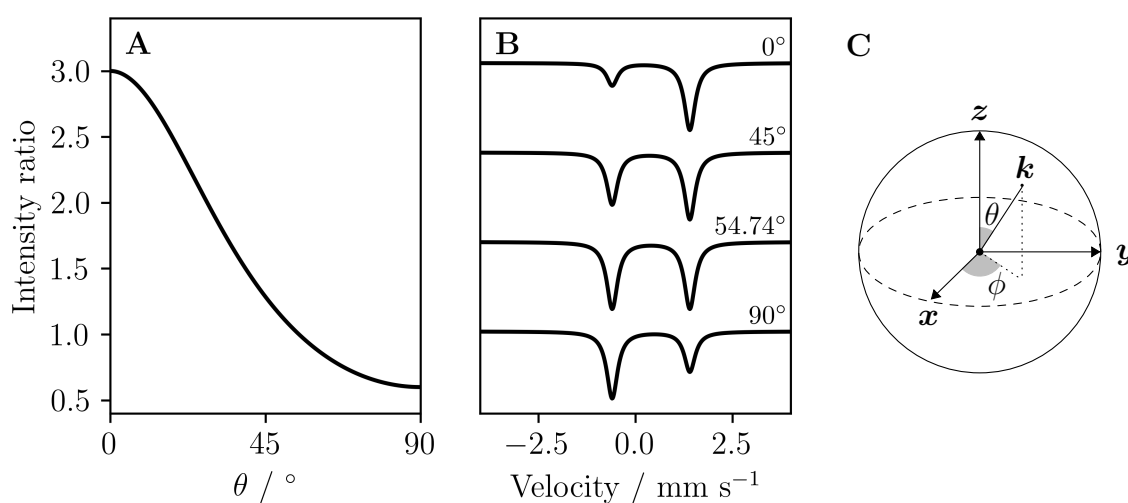


Figure 2.32: A) Intensity ratio of the two quadrupole split lines in the Mössbauer spectrum as given by equation 2.79. B) Exemplary Mössbauer spectra for different angles θ . For $\theta = 54.7356^\circ$, i.e. the magic angle, the intensity ratio is 1:1. C) Definition of the polar and azimuthal angles θ and ϕ , respectively. \mathbf{k} is the wave vector of the γ -rays. The electric field gradient V_{zz} is the second derivative of the potential in z direction.

The quadrupole splitting is strongly dependent on the spin of the investigated sample (that adds an electric field gradient) and can therefore be used in the determination of the spin and oxidation state. Since the lattice contribution to the quadrupole splitting is weaker than that from valence electrons, information on the surroundings, i.e. lattice, can only be obtained if molecular orbitals are formed with the ligands. Only then, the surroundings have a considerable contribution to the quadrupole splitting. Most often, the quadrupole splitting is used in the identification of the type and oxidation state of samples by comparison to similar compounds.

2.2.7.6 Magnetic Hyperfine Splitting

If the compound of interest has unpaired electrons, they generate an effective magnetic field at the iron nucleus which lifts the degeneracy of the $\pm m_I$ states, resulting in the energy level diagram depicted in figure 2.31. The energy change of the individual states compared to their zero-field energy, i.e. the nuclear Zeeman interaction, is given to be

$$E_{m_I} = -g_N \mu_N B m_I, \quad (2.80)$$

with the nuclear g value g_N , the nuclear magneton μ_N and the effective magnetic field B . Here, it is important to distinguish between the g value of the ground state $g_{N,\text{ground}} = 0.1812$ and that of the excited state $g_{N,\text{excited}} = -0.1035$ calculated from the magnetic moments $\mu_{\text{ground}} = 0.0906 \mu_N$ and $\mu_{\text{excited}} = -0.1553 \mu_N$ given in [97]. The effective magnetic field felt by the nuclei is the sum of all magnetic fields. These include the isotropic Fermi contact field B_C resulting from spin-polarization of the s-electrons at the nucleus, the anisotropic orbital motion of valence electrons B_L and the anisotropic spin-dipolar contribution B_d as well as the external applied magnetic fields B_{ext} .

$$B = B_C + B_L + B_d + B_{\text{ext}} \quad (2.81)$$

Due to the selection rule of $\Delta I = 1, \Delta m_I = 0, \pm 1$ this lifting of the degeneracy gives six lines in the resulting Mössbauer spectrum, as is shown in figure 2.31. The distance between the two outermost lines can be calculated with the hyperfine field B_{hf} , i.e. B in the direction of the gamma rays. The six lines show an orientation-dependent intensity ratio $3:n:1:1:n:3$ with

$$n = \frac{4 \sin^2 \theta}{1 + \cos^2 \theta} \quad (2.82)$$

for the angle θ between the gamma rays and the orientation of the magnetic field B .

The isomer shift is only additive to the energy and shifts all lines equally. Quadrupole and magnetic interactions both shift the levels and when they are of similar magnitude, it becomes necessary to evaluate the full Hamiltonian by numerical diagonalisation. Typically, high-field ($eQV_{zz}/2 \ll g_N \mu_N B$) and low-field ($eQV_{zz}/2 \gg g_N \mu_N B$) conditions are distinguished between. For the former, the quadrupole splitting can be calculated with first-order perturbation treatment from the positions of the lines L_i in mm s^{-1} when the

magnetic field is in direction of the electric field gradient.

$$2E_Q = \frac{1}{2} [(L_6 - L_5) - (L_2 - L_1)] \quad (2.83)$$

This also allows for the determination of the sign of E_Q , i.e. the direction of the electric field gradient. Measurements in large applied fields of ca. 1-10 T are therefore of great advantage. For arbitrary magnetic field directions, determined by the angles θ and ϕ to the electric field gradient, the energies of the individual lines have to be calculated explicitly.

$$E_{M,Q}(I = 3/2, m_I) = g_N B m_I + \mu_N E_Q(m_I, \theta, \phi) \quad (2.84)$$

with μ_N accounting for the strength of the electric field gradient along the magnetic field and

$$E_Q(m_I, \theta, \phi) = -1^{|m_I|+0.5} \cdot \frac{eQV_{zz}}{8} \cdot (3 \cos^2 \theta - 1 + \eta \sin^2 \theta \cos 2\phi) \quad (2.85)$$

In the low-field condition the quadrupole split lines are split by the magnetic splitting and the quadrupole interaction dominates the spectrum. The sign of the electric field gradient heavily determines the shape of the spectrum, as only the transitions $m_I = \pm 3/2 \leftarrow m_I = \pm 1/2$ are split into two lines by magnetic hyperfine splitting in small applied magnetic fields. This line is located at high velocities for $V_{zz} > 0$ and at low velocities for $V_{zz} < 0$. Therefore small applied fields can also help to better understand the electronic structure of a compound.

2.2.7.7 Magnetic Relaxation in Mössbauer Spectra

Mössbauer spectra are sensitive to the changing magnetic field induced by spin relaxation when the relaxation rate is of the order of the nuclear Larmor frequency. For typical hyperfine fields of ca. 50 T in Fe^{III} , the Larmor frequency is of the order of nanoseconds. The spectral shape depends strongly on the direction in which the hyperfine field fluctuates. For the simplest case of longitudinal relaxation (quantified with T_1), i.e. when the hyperfine field can only assume the two values $+B_{\text{hf}}$ and $-B_{\text{hf}}$, the spectral shape can be calculated with relatively simple models given by Blume and Tjon. [98]. Figure 2.33 shows calculated spectra with and without an electric field gradient, i.e. quadrupole splitting.

For relaxation times much longer than the Mössbauer time scale, i.e. the life time of the excited nuclear state (≈ 100 ns for ^{57}Fe), the typical sextet can be observed. For relaxation times on the order of the Mössbauer time scale, the lines broaden and collapse

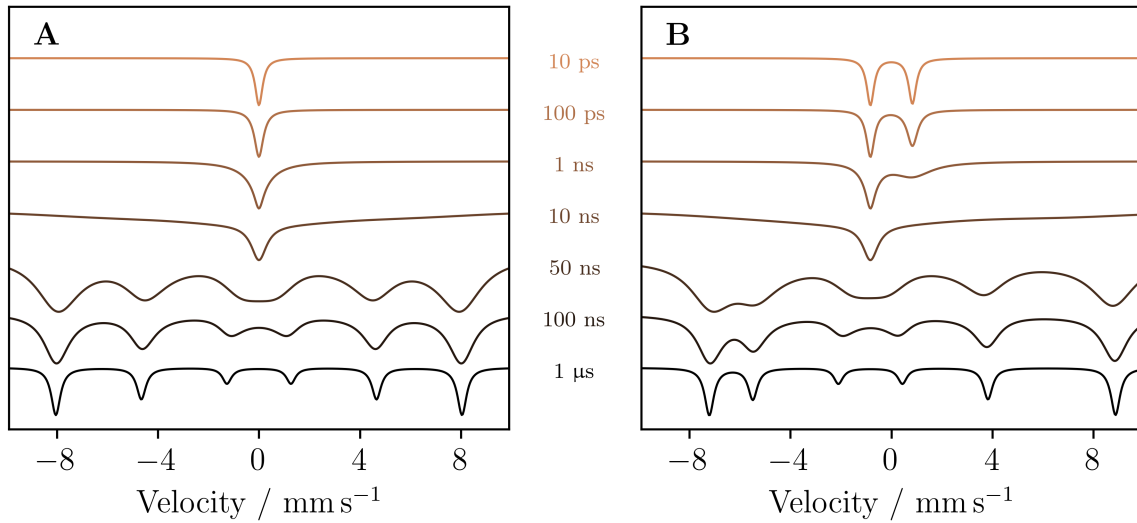


Figure 2.33: A) Normalised Mössbauer spectra resulting from slow relaxation of the magnetic moment with simulation parameters $B_{\text{hf}} = 50 \text{ T}$, $\Gamma = 0.35 \text{ mm s}^{-1}$, $\delta_{\text{IS}} = 0 \text{ mm s}^{-1}$, $V_{zz} = 0 \cdot 10^{21} \text{ V m}^{-2}$, $\eta = 0$. The relaxation times are given next to the plots. B) Same as (A) but with $V_{zz} = 10 \cdot 10^{21} \text{ V m}^{-2}$.

into one line only to then split due to quadrupole splitting for very short spin relaxation times. The lines start to collapse at a critical relaxation time τ_{cr} that depend on the nuclear Zeeman energies of ground and excited state.

$$\tau_{\text{cr}} = \frac{\hbar}{|g_{\text{N,e}}m_{I,\text{e}}\mu_{\text{N}}B_{\text{hf}} - g_{\text{N,g}}m_{I,\text{g}}\mu_{\text{N}}B_{\text{hf}}|} \quad (2.86)$$

This leads of a pairwise collapse of the two lines with identical m_I . The flipping between the two directions of the hyperfine field is a good approximation for two-level systems such as is the case for $S = 1/2$. For $S > 1/2$ the magnetic field fluctuates between different values $B_{\text{hf}} = aS_z$. For fields that do not fluctuate in direction of the electric field gradient, the calculation is also more complex, giving different line shapes depending on the direction of fluctuation. This effect can be used to determine the direction of the electric field gradient by measuring in a strong applied magnetic field where the direction of B_{hf} , which is the sum of all fields at the nucleus, is then known. Since the relaxation time is also field dependent, measurements in applied magnetic fields can help in distinguishing between line broadening as a result of relaxation effects or inhomogeneous broadening due to distribution of isomer shifts and quadrupole splittings. Here, small applied fields of a few hundred millitesla with permanent magnets close to the sample can be sufficient.

The Mössbauer spectra depicted in Figure 2.33 were calculated using MossWinn with

the model derived by Blume and Tjon. [98] It is based on a stochastic model, since a perturbation model of the Hamiltonian can only be solved to give exact line shapes for very fast and very slowly varying hyperfine fields. Blume and Tjon expanded the models known at that time to cases where the hyperfine field is not along the axis of the electric field gradient. In the following, only the case for $B_{\text{hf}} \parallel V_{zz}$ given in [99] is explained in detail. The collapse into a single line for fast spin relaxation is straightforward. The individual transitions for the two cases $\mathbf{B}_{\text{hf}} = (0, 0, \pm B_{\text{hf}})$ are depicted in Figure 2.34.

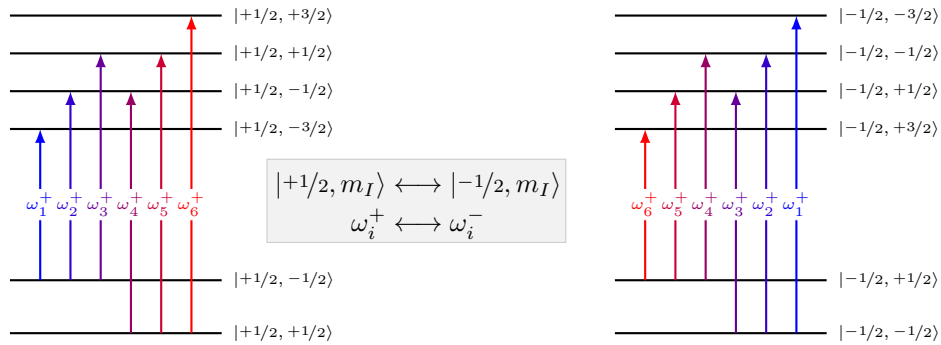


Figure 2.34: Effect of magnetic relaxation on the Mössbauer energy level scheme. As an example the line resulting from the $|m_S, -1/2\rangle \leftrightarrow |m_S, -3/2\rangle$ transition fluctuates between the highest and smallest possible energies. For quickly changing fields the energies are averaged out and a single line is observed in case of no additional quadrupole splitting.

For relaxation times between the two extreme cases the transition energy can be viewed as modulated by a random frequency. Since those transitions whose energies flip (see Figure 2.34) are related, they can be viewed as pairs for which the oscillating magnetic field has the same effect. The frequencies of these transitions are ω_A and ω_B . The energy of the transitions and the position on the velocity axis v are related by the Doppler energy

$$\Delta E = \frac{v}{c} E_\gamma \quad (2.87)$$

giving that 1mm s^{-1} is equivalent to 11.6 MHz. The natural line width is given by $\Gamma = \Gamma_A = \Gamma_B$. A system possessing two resonance frequencies can be solved with the modified Bloch equations in the rotating frame with $G \equiv G_A + G_B$, where G is the time dependent response of the system and the resonant absorption $I(\omega)$ is given by the real or imaginary part of G .

$$\frac{dG_A}{dt} + \alpha_A G_A = -iI_A + \tau_B^{-1} G_B - \tau_A^{-1} G_A \quad (2.88)$$

$$\frac{dG_B}{dt} + \alpha_B G_B = -iI_B + \tau_A^{-1} G_A - \tau_B^{-1} G_B \quad (2.89)$$

with

$$\alpha_A = \Gamma_A - i(\omega_A - \omega) \quad (2.90)$$

$$\alpha_B = \Gamma_B - i(\omega_B - \omega) \quad (2.91)$$

I are the intensities that can be calculated from the population difference of the states involved in the transition and the Clebsch-Gordan coefficients. τ_A^{-1} is the transition probability per unit time of a transition from ω_B to ω_A . These probabilities of the two transitions ω_A and ω_B depends on the population p of the two states under the assumption that only the nuclear ground states are populated. Therefore, it is often assumed that $p_A = p_B$. In the steady state where $dG_A/dt = dG_B/dt = 0$ and with knowing that $\tau = (\tau_A \tau_B)/(\tau_A + \tau_B)$, and $p_A = \tau_A/(\tau_A + \tau_B)$ one arrives at

$$I_{\text{sum}}(\omega, \tau) = \sum_{i=1}^3 I_i(\omega, \tau, \omega_i^+, \omega_i^-) \quad (2.92)$$

The line shapes of the pairs, i.e. ω_1/ω_6 , ω_2/ω_5 and ω_3/ω_4 , can then be calculated with

$$I(\omega) = \text{Im}(G) = \text{Im}(G_A + G_B) = -C \frac{(1 + \tau\Gamma)P + QR}{P^2 + R^2} \quad (2.93)$$

where the factor C includes the Clebsch-Gordan coefficient. For a polycrystalline sample the intensity ratio is 3:2:1:1:2:3, i.e. $C(\omega_{1,3}) = 3$.

$$P = \tau \left\{ \Gamma^2 - \left[\frac{1}{2}(\omega_A + \omega_B) - \omega \right]^2 + \frac{1}{4}(\omega_A - \omega_B)^2 \right\} + \Gamma \quad (2.94)$$

$$Q = \tau \left[\frac{1}{2}(\omega_A + \omega_B) - \omega - \frac{1}{2}(p_A - p_B)(\omega_A - \omega_B) \right] \quad (2.95)$$

$$R = \left[\frac{1}{2}(\omega_A + \omega_B) - \omega \right] (1 + 2\tau\Gamma) + \frac{1}{2}(p_A - p_B)(\omega_A - \omega_B) \quad (2.96)$$

The resulting relaxation-time dependent Mössbauer spectra for given resonance frequencies and linewidths are depicted in Figure 2.35. It can be seen that central lines collapse first with the spectrum showing a single line for very short relaxation times.

If an arbitrary direction of the hyperfine field relative to the electric field gradient needs to be considered, then Equation (2.97) can be used. It is not discussed here and the derivation is given in [98].

$$W(\mathbf{k}) = \frac{2}{\Gamma} \text{Re} \sum_i m_0, m_1 \frac{1}{4} | \langle I_0 m_0 \rangle | \hat{\mathcal{H}}^{(+)} | I_1 m_1 \rangle|^2 \sum_{ij} p_i(j) \left[\tilde{A}^{-1}(p) + 3Q^2 \eta^2 \tilde{B}(p) \right]^{-1} | i \rangle \quad (2.97)$$

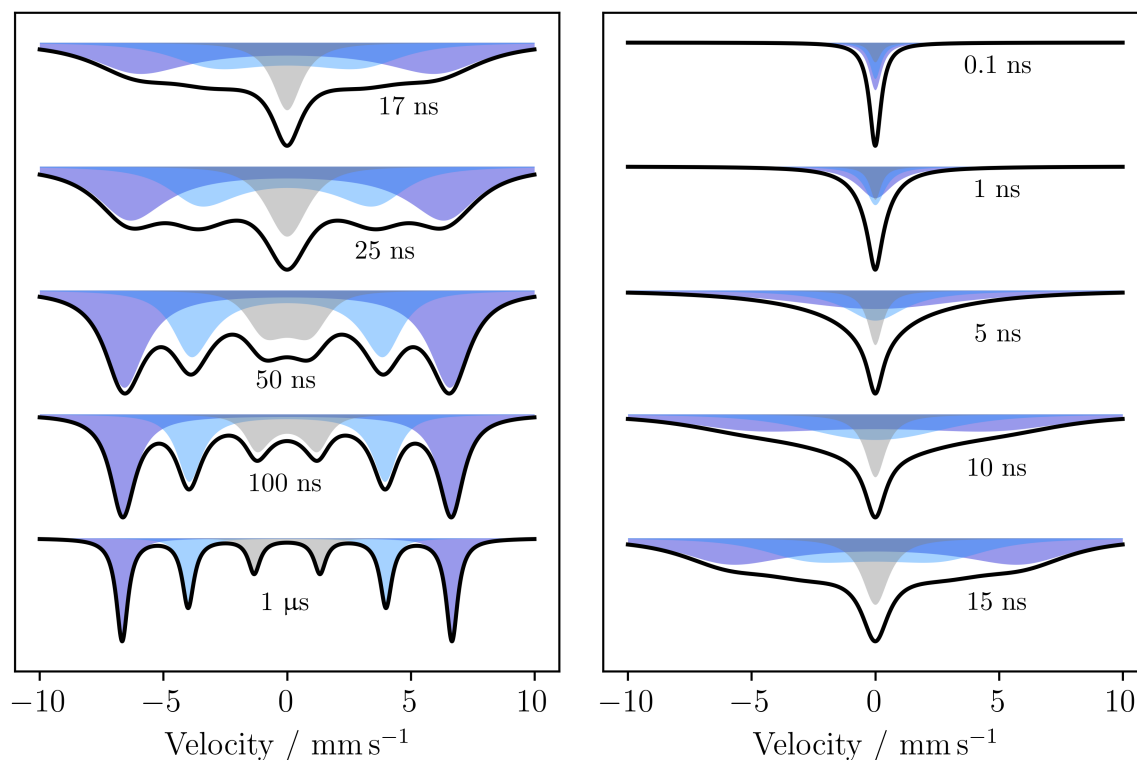
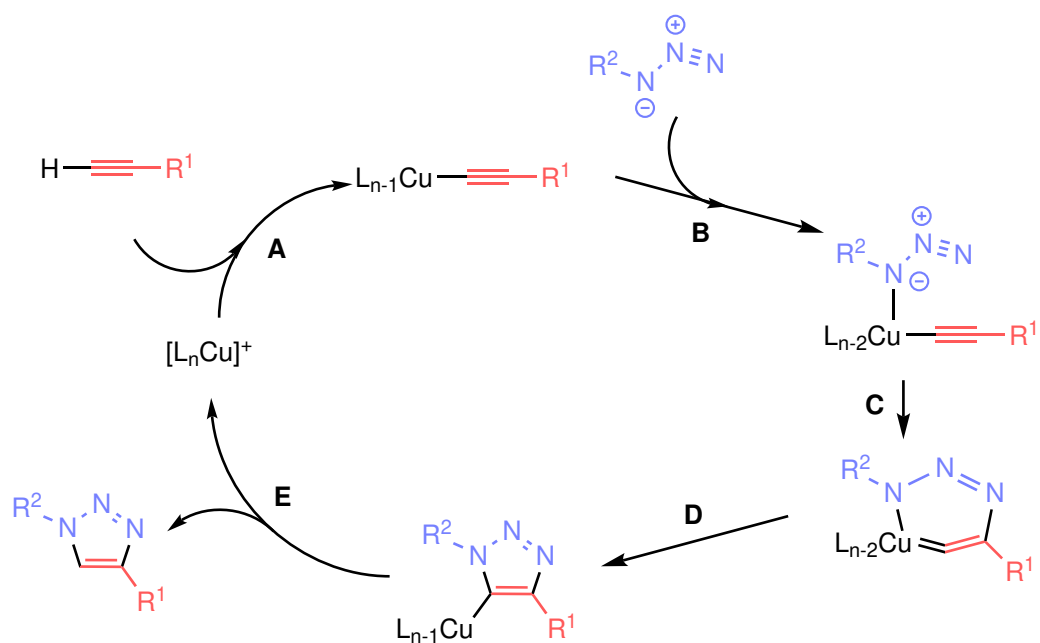


Figure 2.35: Mössbauer spectra for the related pairs calculated with Equation (2.93) with the typical intensity ratio 3:2:1:1:2:3 and their sum for the given magnetic relaxation times. Here, the hyperfine field is parallel to the electric field gradient without quadrupole splitting, giving the same result as in Figure 2.33A.

2.3 Click Chemistry

Click chemistry was introduced by Sharpless in 2001. [100] It combines a variety of different types of reactions that all share the same concept, namely the combination of two functional groups, effectively connecting two molecules with high yields, without side products, under mild conditions with an easy preparation of the reagents and a simple isolation of the product. The most famous examples are the Huisgen 1,3-dipolar cycloaddition, nucleophilic substitutions to strained rings and the thiol-ene reaction. In this work, the copper(I)-catalyzed azide-alkyne cycloaddition is of great interest as it can be used to immobilise molecules in pores. This is made possible by the straightforward modification of the molecules and pore walls with either azide or alkyne groups. Scheme 1 shows the reaction mechanism. [101]

The usage of the copper(I) species selectively yields the 1,4-product. Alternatively the reaction could be carried out by heating (giving both the 1,4 and 1,5-products) or with different catalysts, e.g. ruthenium based catalysts (giving either the 1,4 or 1,5-product).



Scheme 1: Reaction mechanism of the copper(I)-catalyzed azide-alkyne cycloaddition.

A complete review over click chemistry is given in [102].

3 Set-up of a Mössbauer Spectrometer

Mössbauer spectroscopy is a very powerful tool to investigate samples containing a Mössbauer active nucleus, where iron is by far the most investigated element with this method. The applications of Mössbauer spectroscopy range from the study of geological samples, e.g. the composition of the earth and the finding of water on Mars [103], as well as the study of the electronic and geometric structures of iron-containing compounds. Recently, iron has gained a lot of attention as a catalyst for the future, especially because of its low cost. Gamma sources are readily available in the form of ^{57}Co .

The fact that, in most cases, there are only two crucial parameters that influence the spectrum, namely the electron density at the nucleus which is quantified in the isomer shift and the electric field gradient of the surrounding charges which leads to quadrupole splitting of the absorption lines, makes Mössbauer a well-understood method. Still, a lot of information can be gained from the spectra, especially when expanding the measurements to multiple temperatures and applied magnetic fields.

One of the most famous applications of Mössbauer spectroscopy is the miniature Mössbauer spectrometer on the Mars rover that found the presence of the mineral hematite, which most preferably forms in aqueous environments, hinting at the presence of water on the planet. [104] Another very interesting experiment, that employs the Mössbauer effect, is the Pound-Rebka experiment where the gravitational redshift of light was determined by measuring the differences in the frequency of gamma rays moving towards and away from the gravitational centre of the earth. [105] There, the findings by Rudolf Mössbauer allowed finding a light source with a very precisely known frequency.

In this Chapter, the set-up and testing of a variable-temperature Mössbauer spectrometer is described. The instrument is based on a Mössbauer spectrometer bought from the Regional Centre of Advanced Technologies and Materials, the 3rd Generation MS-96 Mössbauer spectrometer, was coupled to a Janis SVT 400 cryostat and the complete set-up was tested and optimised. One of the goals was the investigation of the electronic structure of a probe molecule, $(\text{dppf})\text{Fe}(\text{CO})_3$, that serves as a model catalyst used to learn about the influences of the structure on the catalytic activity. Furthermore, multiple samples were investigated in cooperation in order to determine their geometric structures, oxidation states and temperature-dependent spin crossover behaviour.

3.1 Parts of the Spectrometer

The first spectrometer to measure the resonant absorption of gamma rays was built by Rudolf Mössbauer during his PhD thesis [106]. In his set-up, virtually the same compo-

nents as in today's Mössbauer spectrometers were used. A scintillator combined with a photomultiplier tube was used as a detector and the source was mounted on a rotating disk to allow for the modulation of the energy of the emitted gamma rays. As is mentioned in Section 2.2.7, the very narrow lines, i.e. the emission line of the gamma rays of the source and the absorption line in the absorber, do not overlap due to recoil. Contrary to his predecessors who tried to increase the temperature to decrease the lifetime of the excited state to broaden the transition lines to make them overlap [79], Mössbauer cooled down the source and absorber, hoping that strengthened bonds would decrease the recoil that separates the two lines. Indeed, the spectral intensity increased although the reason was slightly different: He concluded that the probability of zero-phonon processes that do not lead to vibrations of the lattice, i.e. recoil, decreases when lowering the temperature. This effect was named after him and is called the Lamb-Mössbauer factor or recoil-free fraction.

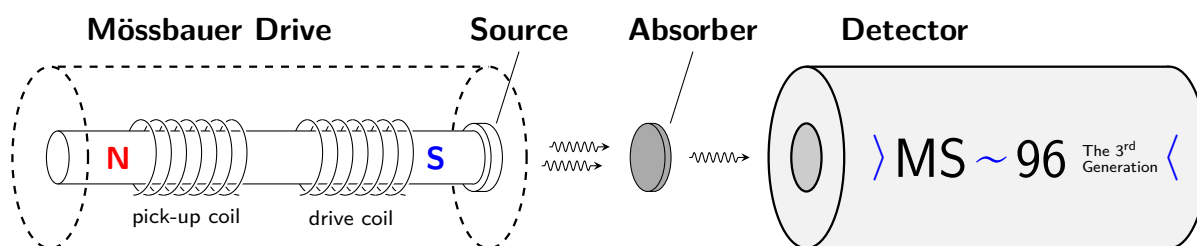


Figure 3.1: Diagrammatic representation of the Mössbauer drive and detector with the sample in between the two units. The source is moved by applying an alternating current to the drive coil which in turn moves the permanent magnet whose movement is measured by the pick-up coil. The generation of the waveform of the current as well as the analysis of the detector signal is performed by a computer that is connected to both devices.

The set-up of the used Mössbauer spectrometer is shown in Figure 3.1. The Mössbauer drive unit moves the source to modulate the gamma ray energy by the Doppler energy by applying an alternating current in a coil that then moves the source mounted on a permanent magnet and the detector, a scintillator in combination with a photomultiplier tube then detects the incoming radiation. Apertures on both units facing the sample act as a collimator.

In this work a Mössbauer spectrometer from the Regional Centre of Advanced Technologies and Materials, the 3rd Generation MS-96 Mössbauer spectrometer shown in Figure 3.2, was bought and combined with a Janis SVT400 cryostat to allow for measurement at temperatures down to 3 K. Finally, a new sample holder was designed and constructed. The individual parts of the spectrometer are explained in the following Sections.

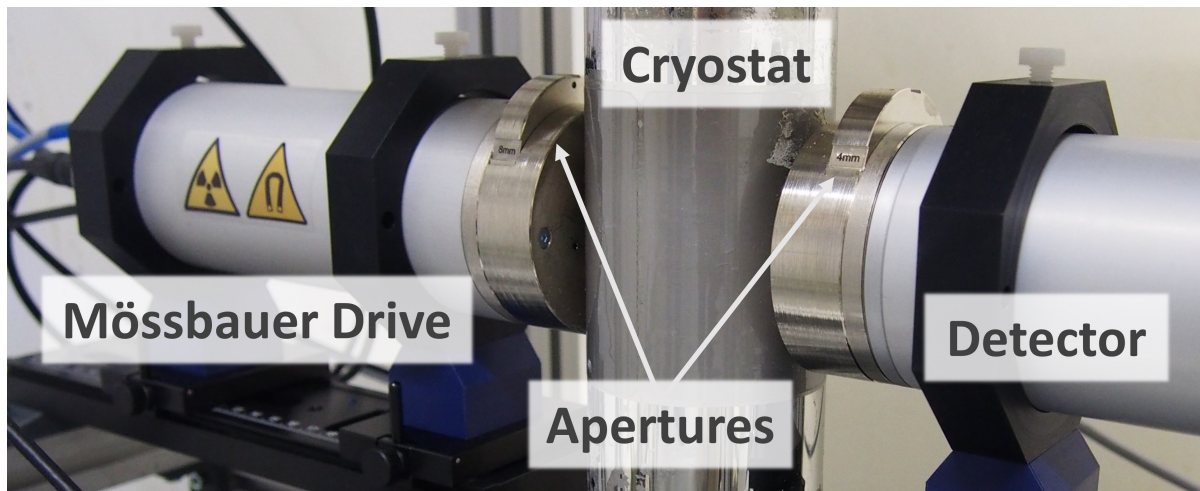
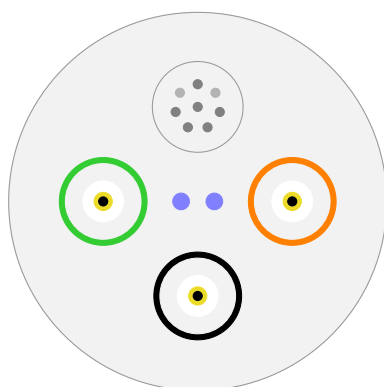


Figure 3.2: Picture of the Mössbauer spectrometer with the cryostat between the two units.

3.1.1 Velocity Drive Unit and Mössbauer Source

The velocity drive unit of the RCPTM MS-96 Mössbauer spectrometer houses the source as well as the set-up that allows the constant forwards and backwards motion of the same. This motion modulates the energy of the emitted gamma rays by the Doppler velocity, thereby enabling a scan of the count rate in dependence of the photon energy by synchronising the source movement with the channel advancement in the detector. Two coils can be found in the velocity drive unit, the drive coil and the pick-up coil, see Figure 3.1. The drive coil is supplied with an alternating reference voltage that induces a magnetic field, which moves a permanent magnet to which the source is mounted. In other Mössbauer spectrometers, the source could alternatively be mounted to the coils that are moving against the permanent magnet. The pick-up coil detects the motion of the construction.



Mössbauer Drive Unit

MIC326	Power supply
Green BNC	Actual velocity output
Orange BNC	Actual velocity error output
Black BNC	Reference velocity signal input

Detector Unit

MIC328	Power supply and detector control
Green BNC	All detected pulses output
Orange BNC	Single-channel analyser output
Black BNC	No connection

Figure 3.3: Connections on the Mössbauer drive and detector units as well as their output.

In our set-up, the reference voltage, e.g. 1.6 V for a maximum velocity of ca. 10 mm s^{-1} ,

is applied on the black BNC connector and supplied via the computer. The velocity is regulated via a PID control and measured with an oscilloscope on the green BNC connector (see Figure 3.3). The error voltages can be measured on the orange connectors. Both values measured over time are shown in Figure 3.4. As can be seen, every velocity is passed twice in one period, i.e. the spectrum is measured while the source is close to the sample (channels 513 to 1024 in Figure 3.4), both in the forwards and backwards motion, as well as when it is further away (channels 1 to 512 in Figure 3.4), also for both directions of motion.

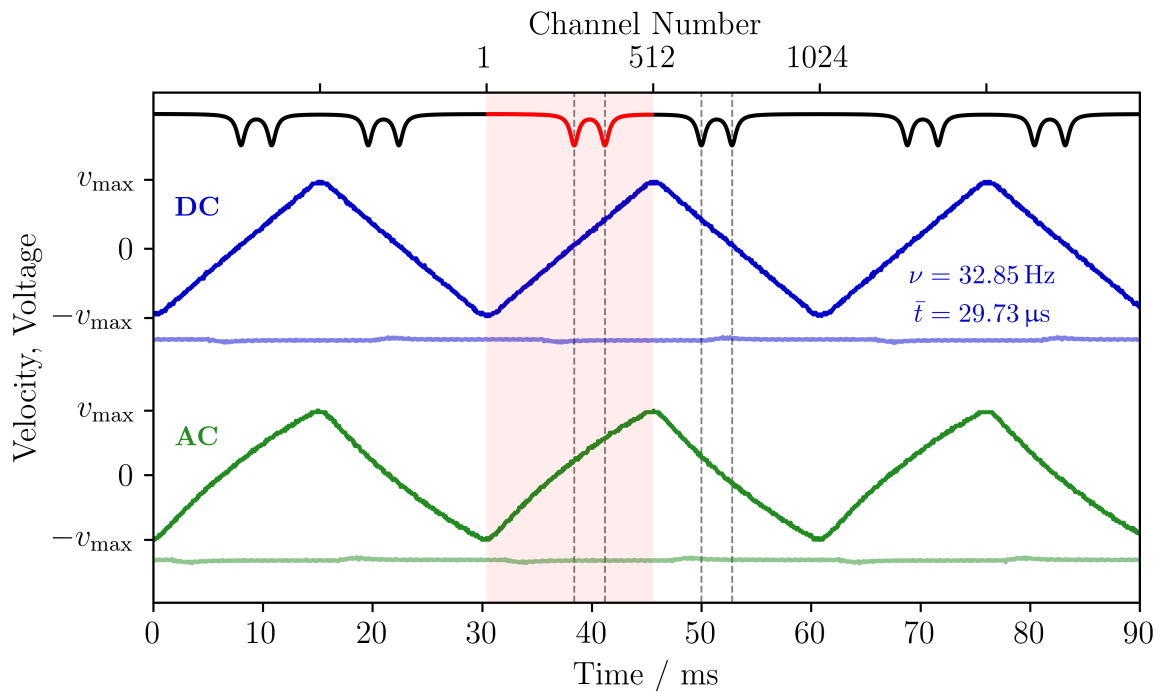


Figure 3.4: DC and AC voltages measured with an oscilloscope. For an applied voltage of 0 V the source is not moving, i.e. about to turn its direction. Maximum velocities are reached when the source is in the centre position between the two inversion points. The spectrum is measured twice in one periodic motion of the source (channels 1 to 1024) and has to be folded by adding the counts in channel 1 and 1024, 2 and 1023, etc. The resulting spectrum is shown in red.

The radioactive source used in the set-up was supplied by RitVerc and labelled MCo7.124 by them. It contains ^{57}Co in a rhodium matrix with an activity of $50 \text{ mCi} = 1850 \text{ MBq}$ and a natural line width of $1.2(1) \text{ mm s}^{-1}$. The active part has a diameter of 8 mm and is encapsulated by a titanium alloy, with a beryllium window that is transparent for gamma rays. The capsule is screwed onto the velocity drive unit, which is then closed. The housing of the spectrometer also includes a lead shielding to only allow radiation to pass into the direction of the aperture and from there to the sample and detector. The source

is not cooled, i.e. always at room temperature.

In order to protect the user of scattered gamma radiation and additional 5 cm thick lead wall was built next to the cryostat. Additionally, a 1 cm thick steel structure was built to prevent radiation to leak to the other three sides and the top, see Figure 3.5. At all points in the room where the user might be, no excess radiation on top of the background radiation of $0.10(1) \mu\text{Sv h}^{-1}$ could be measured.

3.1.2 Detector Unit

The detector unit houses a scintillating crystal coupled to a photomultiplier tube and all signal-processing electronics in order to convert the attenuated gamma rays into computer readable, digital data. The parts will be explained in the following.

Many different types of detections systems are employed for Mössbauer spectroscopy. The different detector types are summarised in Table 3.1. Ionisation chambers suffer from a high noise level due to very low currents that result from the ionisation events. Geiger-Müller tubes have the disadvantage that at higher count rates the actual value is under-read, which might introduce errors in the experiment. Semiconductor detectors have a very high energy resolution but are very expensive. They are therefore used in gamma spectrometry, where the energy resolution becomes much more relevant than in Mössbauer spectroscopy. This makes scintillators and proportional counters the most widely used detector systems for Mössbauer spectroscopy. The scintillator offers a high luminescence efficiency, chemical inertness and inexpensiveness. Because of their statistical quality, i.e. lowest noise level and therefore fastest spectrum accumulation for Mössbauer spectroscopy, the YAP scintillator (see below) was chosen. [107]

Table 3.1: Comparison of the different systems used for the quantitative detection of gamma radiation.

Type	Effect	Detection	Disadvantage
Scintillator	Photons	PMT	low intrinsic energy resolution
Proportional counter	Ionisation	Current	low intrinsic energy resolution
Ionisation chamber	Ionisation	Current	very low currents can make measurements inaccurate
Geiger-Müller tube	Ionisation	Current	under-reads the actual count rate at higher count rates, detector dead-time follows every ionisation event
Semiconductor detector	Ionisation	Current	degrades over time, expensive

In this spectrometer YAP:Ce (Yttrium Aluminium Perovskite doped with ≈ 0.6 mol-% Cerium) with a diameter of 25.4 mm and a thickness of 0.3 mm is used. The emission in YAP:Ce results from Ce^{3+} 4f-5d transitions with lifetimes of ca. 17 ns [108], which is very short compared to other scintillating crystals [109], allowing for very high temporal resolution. The emission band peaks at 370 nm with various minor side bands that are due to non-equivalent Ce^{3+} centres [108]. It has a relative photoelectron yield of 40 % compared to NaI:Tl but a much faster decay constant of 25 ns compared to 230 ns for NaI:Tl. [109] This number is different from the lifetimes of the excited states due to a second slower process, see Section 2.2.7. Another advantage of YAP:Ce is the fact that it is not hygroscopic in contrast to NaI:Tl and therefore easier to handle. A disadvantage of all scintillator systems is that they are not suitable for a usage in applied magnetic fields because most common photomultiplier tubes are very sensitive to these magnetic fields.

The detector unit of the RCPTM MS-96 Mössbauer spectrometer also includes a circuit board which stores the summed counts of all 1024 available channels until the LabView program fetches the data from the spectrometer, which happens every two minutes. This allows for the continuation of the measurement even if the computer becomes temporarily unavailable, e.g. when software crashes. For writing data from the computer to the detector unit, the power connector is used. It connects via an external circuit board to both the power supply and a USB plug of the computer, thereby allowing transmission of values such as the detector voltage and amplification as well as the current measurement number. The orange and black BNC connectors are left unused in the employed set-up but the orange connector can be used for diagnostics as it outputs the single-channel analyser data, see Figure 3.3.

Lastly, an aperture in front of the detector unit, as can be seen in Figure 3.2, allows for the setting of the opening of the diaphragm through which the gamma rays pass, which is necessary to collimate the gamma rays to remove unwanted broadening of the emission line, see Section 3.2.1.

3.1.3 Cryostat

Being able to do Mössbauer spectroscopy at varying temperatures down to only a few Kelvin has many advantages. It allows for the investigation of temperature-dependent phenomena, such as spin crossover [110], electron hopping [111] or thermally induced valence-tautomeric behavior [112]. To realise the required changes in temperature, usually cryostats cooled by cryogenic liquids are used. In this set-up a JANIS SVT400 cryostat with Mylar windows for optical access was used. Both liquid nitrogen and liquid helium were used as the cooling agent, where temperatures below 80 K are necessary when

the dynamics of the paramagnetic moment, i.e. the spin-lattice relaxation time, of the sample is to be investigated or the sample did not reach a stable state, e.g. incomplete spin crossover, at liquid nitrogen temperatures. Another advantage is that the recoil-free fraction is much closer to unity at 4 K than at 80 K and only then does Mössbauer spectroscopy become somewhat quantitative when simultaneously measuring unknown samples with different temperature dependences of the recoil free fraction.

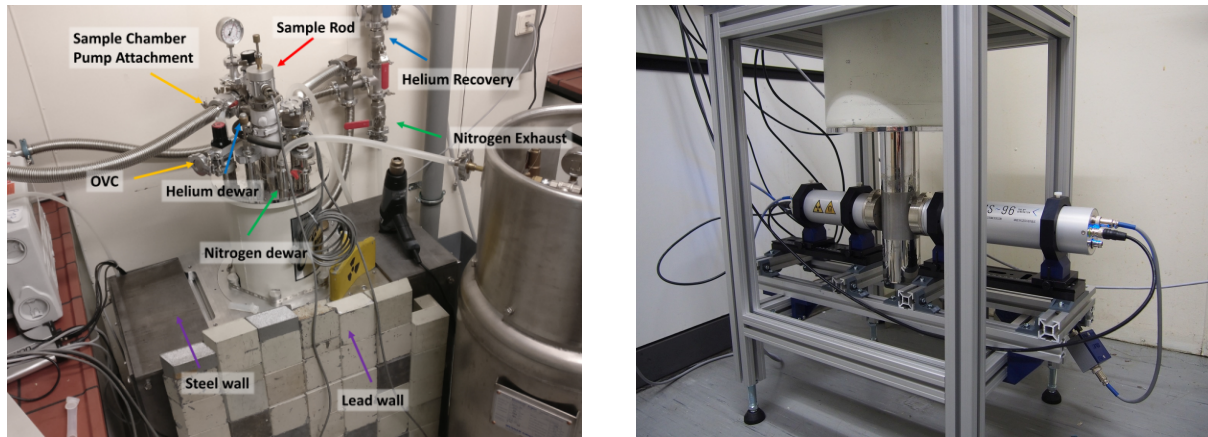


Figure 3.5: Complete set-up of the spectrometer with (left) and without (right) the radiation safety procedures such as the lead wall and steel structures. The cryostat was set up in a way so that easy switching between nitrogen and helium cooling was possible by either using the helium recovery line or the ventilation to recover or remove the evaporated cryogenic gases.

The cryostat was placed on a stand, see Figure 3.5, and the approximate position of the centre of the spectrometer's apertures, i.e. where the gamma radiation is maximal, was estimated based on where the Mylar windows were positioned. The final position of the spectrometer and the sample in the sample holder was then determined by maximizing the count rate on the detector. The rail on which the spectrometer is placed was then attached and the height was adjusted by looking through the Mylar windows without the ^{57}Co source being installed. A fine adjustment of the sample position was achieved by adjusting the length of the sample rod, see Figure 3.10. Due to the used rail system the spectrometer can be easily removed, e.g. for maintenance.

In order to prevent water condensation on the Mylar windows of the cryostat a constant nitrogen gas flow was directed onto the windows.

To control the temperature, a Lakeshore Model 340 Temperature Controller was used and controlled with a self-written LabView program, see Section 3.1.5. For cooling with nitrogen, the needle valve was opened and the pressure difference on both sides of the needle valve, i.e. in the inner cryogenic liquid chamber and the sample chamber, was enough to cool the sample down to liquid nitrogen temperature. Both chambers are

connected via the helium recovery line, leading to the same pressure of the gas in the two chambers, where the presence of liquid nitrogen in one of the chambers is the driving force used to cool the sample. Due to the fact that the liquid scatters the gamma radiation drastically, no measurements were possible at 77 K, where nitrogen is liquid, and the sample was heated to 80 K, where the count rate on the detector increased significantly compared to first test measurements at 77 K. For cooling with liquid helium, the pressure difference is much smaller because of the lower density and an active pumping on the sample chamber was necessary to pull the cold gas past the sample. As the motion of the source is easily disturbed by any outside motion, the vibrations of the pump needed to be dampened, which was achieved by using long and flexible tubes connecting the pump to the cryostat and by placing the pump on a soft surface that dampens the vibrations. Eventually, measurements while pumping on the sample chamber were possible, where the only difference was a slight increase of the line width from 0.426(7) to 0.61(1) mm s⁻¹ measured for ferrocene at 80 K while cooling with helium.

3.1.4 Sample Holder

A new sample holder that can handle pellets of different sizes, powders and liquid samples, had to be designed. The idea was to make the parts that are in direct contact with the sample interchangeable. This design also allows for the sample preparation to take place in a glovebox. Because the attachment to the sample holder was quick and easy, the time the sample has to spend on air could be minimised.

A sample holder was designed, that features a recess with a diameter of 18 mm and a depth of 6 mm for the interchangeable pieces and two holes for a temperature sensor and a heater, see Figure 3.6. First designs were tested by 3D printing them from PLA and it was quickly realised that the design itself allows the desired interchangeability of samples while still offering mechanical stability to be reusable. Measurements at room temperature were possible but PLA does not transfer the heat from the heater to the temperature sensor because of its poor thermal conductivity of $\approx 0.08 \text{ W m}^{-1} \text{ K}^{-1}$ [113], indicating that the sample could also not be heated as it is in thermal contact with both the heater and the sensor. Therefore the sample could not be kept at the desired temperatures when cooling in the cryostat. Subsequently, all parts were made from aluminium which has a much better thermal conductivity of $239 \text{ W m}^{-1} \text{ K}^{-1}$ [114]. Pictures of the three interchangeable parts are shown in Figure 3.12 while the working principle is depicted in Figure 3.6 (B). The sample is always fixed between the two parts, whereas the top part tightly seals the 3D printed liquid sample holder that was made from PETG. Lastly, the parts were secured with a brass plate that was screwed to the sample holder.

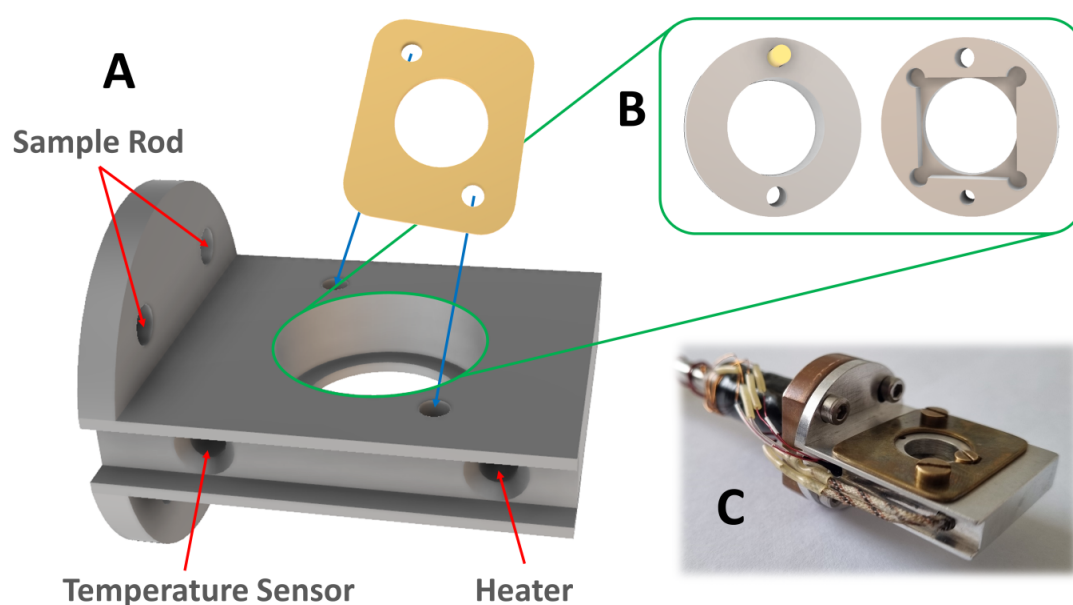


Figure 3.6: Drawing of the sample holder (A) with recesses for the sample compartment shown in the green box (B), the temperature sensor and a heater. (C) Picture of the assembly. A screw through the holes in the bottom of the two parts closes the two pieces in (B) while the brass pin that goes into the upper hole of the part on the right prevents the two pieces from rotating against one another. These pieces are designed for $(10 \times 10) \text{ mm}^2$ samples with a thickness of 1 mm.

Due to the ease of sample preparation and sample recovery, powdered samples in folded weighing paper were used almost exclusively. The sample holder design for this type of sample is shown in Figure 3.6. The sample preparation is explained in more detail in Section 3.2.2.

Before the spectrometer was installed, the height of the sample holder was adjusted by looking through the Mylar windows of the cryostat to place the sample in the centre of the window. The height was adjusted more accurately by maximising the number of counts that reach the detector, see Section 3.2.1

3.1.5 Measurement Computer and Software

In order to control the instrument and analyse the spectra, a measurement computer and appropriate software are required. Here, the LabView program to control the spectrometer was provided by the manufacturer and the LabView program to set and monitor the temperature was self-written for the Lakeshore model 340 temperature controller. Screenshots of the graphical user interfaces of both programs are shown in Figure 3.7.

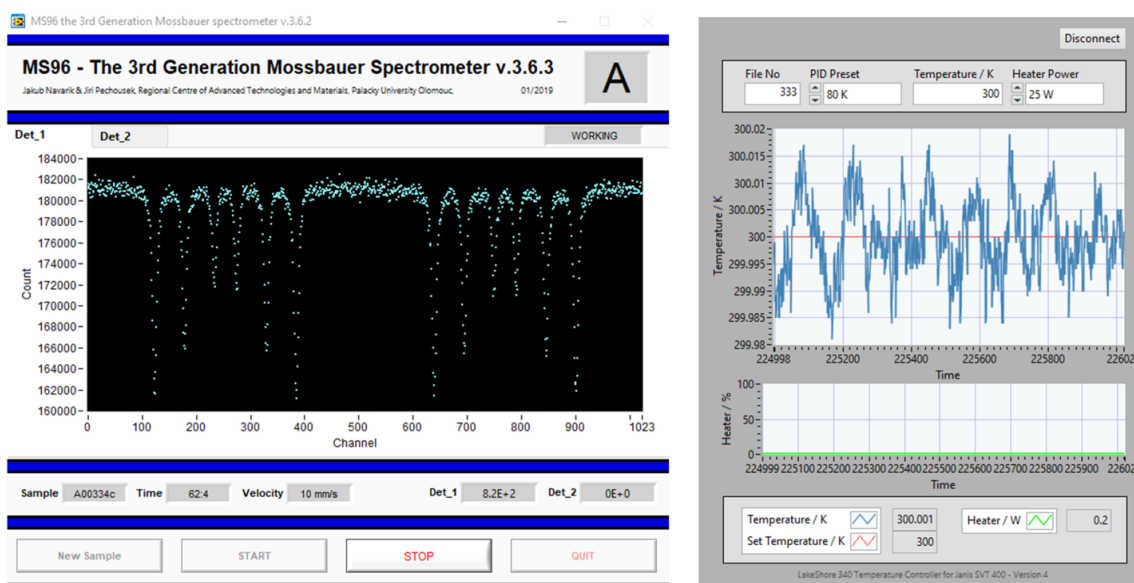


Figure 3.7: Graphical user interfaces of the measurement (left, provided by the manufacturer of the spectrometer) and temperature controller (right, self-written) software. Both programs are written in LabView.

Furthermore, as the instrument software causes the data received from the spectrometer to overwrite the previously fetched data, a python script was written, that always runs in the background and backs up the data. The data analysis was performed in MossWinn

(Version 4.0). The spectrometer-relevant hardware and software will be explained further in the following.

Figure 3.8 depicts the available connections on the computer to the spectrometer. The plugs labelled POWER send the required power to the units and are also used for the detector control, e.g. for setting the voltage of the photomultiplier tube. They are connected to the MIC326 and MIC328 plugs on the drive and detector units, respectively. VEL sends the reference voltage to the Mössbauer drive and DET1 receives the detector signal. START, AI and DET2 are left unused in the set-up. DET2 can be used for a second detector, e.g. to detect conversion electrons simultaneously to the transmission measurement. START and AI would be used to send the period start signal and channel start signal, respectively, but in the used set-up there are no associated connectors on the drive and detector units.

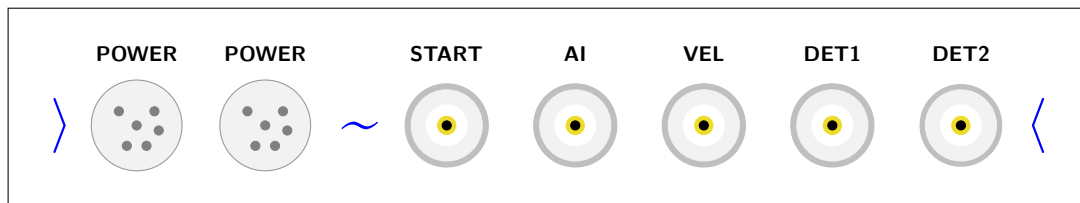


Figure 3.8: Connections on the back side of the measurement computer.

As was mentioned, the LabView program to collect the spectrometer data (see Figure 3.7 left) serves as the interface between the user and the spectrometer. The *New Sample* button opens a new window where the desired maximum velocity in steps of 2 mm s^{-1} up to 30 mm s^{-1} can be set in addition to the metadata, i.e. the spectrometer user, sample owner and notes such as sample name and mass, the set temperature and aperture sizes. A checkmark box serves as a quick way of adding the letter "c" to the sample name to quickly distinguish calibration from research measurements. The measurement number is automatically increased by reading from the calibration file that is updated after every measurement. This file also includes the desired frequency of data fetches and the velocity calibration data. After the measurement is started the LabView program collects the data from the detector in the set intervals and updates the window, i.e. the displayed measurement time, and count rate on the detector, as well as the exported data files that include an encoded LabView-readable file with all data and meta data and two ASCII encoded files that include the meta data and measurement data. The latter of the two ASCII files includes the summed counts per channel for all available channels, i.e. 1024 integer numbers. The velocity axis can be calculated from calibration measurements (Section 3.3.1). The measurement can be stopped at any time.

Since the main instrument control LabView program does not include the option to

control and monitor the temperature, a separate LabView program (see Figure 3.7 right) was written to control the Lakeshore model 340 temperature controller. The measured temperatures are stored every second in a separate file with the current date and time. In order to later unambiguously assign each of the saved temperature curves, the same number was given in the text field *File No* and used as the file name. The desired temperature is set in the field *Temperature / K*. It turned out that the automatic setting of the PID values often leads to temperature drifts and a *PID Preset* was created for cooling with liquid nitrogen, namely $P = 78$, $I = 100$ and $D = 3$ s to get stable temperatures between 80 K and room temperature with the needle valve opened by $1\frac{3}{4}$ rotations. The definition of P , I and D becomes clear from equation (3.1).

$$\text{Heater Output} \propto P \left(\Delta T + I \int \Delta T dt + D \frac{d(\Delta T)}{dt} \right) \quad (3.1)$$

After the temperature and maximum *Heater Power* were set and the needle valve was opened to allow for the cooling to take place, the temperature was logged and usually very stable over the whole measurement, see Figure 3.9.

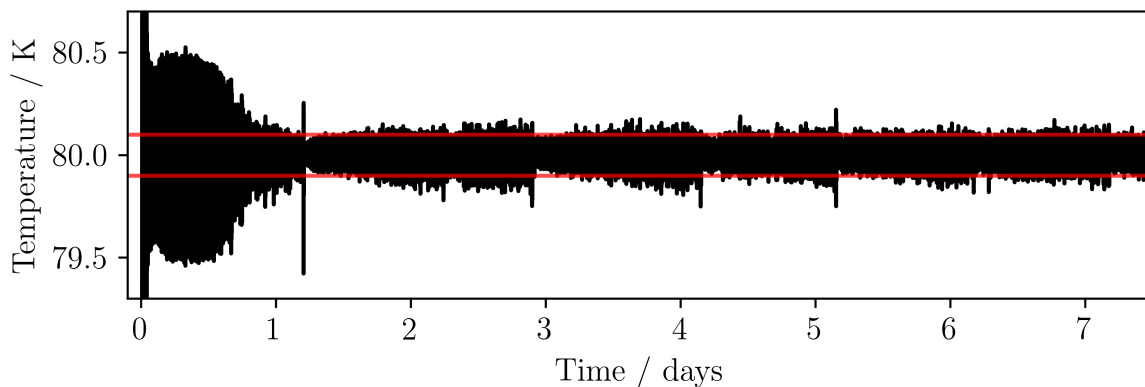


Figure 3.9: Temperature profile during a measurement over the course of eight days. The red lines give the standard deviation $\sigma = 0.1$ K with the mean temperature being 80.000 K. The spikes indicate times when the inner dewar was filled.

As was mentioned, to combine the spectrometer and temperature data, a python script was written. Every three minutes it reads the latest spectrometer file based on the creation date of all files in the spectrometer folder and based on its measurement number, i.e. the file name, finds the respective temperature data file. The script then folds the spectrometer data in the centre, i.e. adds the counts in channel 1 and 1024, 2 and 1023, etc. and plots this folded spectrum. The script also calculates the current signal-to-noise ratio with equations (3.2) and (3.3) with the maximum line intensity I_{\max} , i.e. the lowest

measurement point, and the standard deviation σ , which is calculated for only the first 50 data points ($N = 50$) as it is safe to assume that only baseline, i.e. noise is measured. These already give a good estimate of the overall noise level in the data. The calculation of the standard deviation of the complete data set becomes impossible when automatic fitting of the data fails, e.g. when the number of Gaussian lines, i.e. the signal shape, is unknown and when the noise level is high, i.e. at the beginning of the measurement. The average of the N values is denoted μ .

$$\text{SNR} = \frac{I_{\max}}{\sigma} \quad (3.2)$$

$$\sigma = \sqrt{\frac{\sum(I_i - \mu)^2}{N}} \quad (3.3)$$

For the data analysis the software MossWinn (Version 4.0) was used. Here, a more precise folding of the raw data and calibration of the velocity axis as explained in Section 3.3.1 is undertaken. The spectrum can then be fitted by giving predefined fitting models, such as simple singlet, doublet signals or more advanced models including for example the slow relaxation of the paramagnetic moment of a sample or user-defined models. Then, the starting parameters are set and the least-squares fitting routine can be started. MossWinn always assumes Lorentzian line shapes, unless a model with Gaussian broadening is explicitly selected. The fit and the fitting parameters can then be exported as an ASCII encoded file.

3.2 Measurement and Evaluation of a Spectrum

In this section, the steps needed to record and analyse a Mössbauer spectrum are presented. These consist of the preparation, positioning and measuring of the sample. The influences of different types of samples, the amount of the investigated compound, the position of the sample holder and the setting of the apertures is discussed. Lastly, the execution of the calibration of the velocity axis is presented.

3.2.1 Sample Positioning and Setting of Apertures

Obviously the sample placement is crucial in order to maximize the signal intensity and thereby keeping the measurement time short. Ideally, the sample is in the centre of the gamma ray beam where the whole area of the sample is irradiated. The precise positioning of the sample holder in terms of height and angle was performed by measuring the count rate on the detector for different heights and angles with a sample inserted into the sample

holder. The results of these measurements are shown in Figure 3.10A and B and clearly indicate what the ideal sample placement is and what the influences of deviations of this position are. Moving the sample up and down by ca. 3 mm drops the count rate to about 80 % of its maximum value while rotations of ca. 10° in either direction lead to the same drop in the count rate. Nonetheless, errors of $< 5^\circ$ reduce the count rate on the detector by only $< 2\%$.

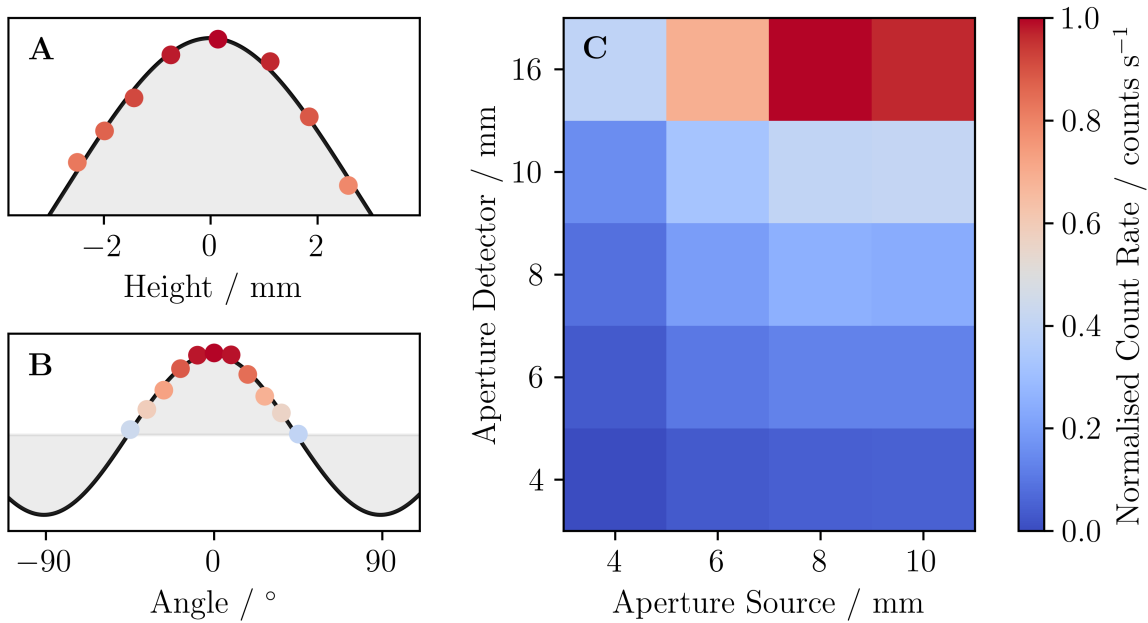


Figure 3.10: Relative count rate in dependence of the relative height (A) and angle (B) of the sample holder. C) Relative count rates for all possible combinations of aperture settings. The respective measurements are shown in Figure A.1 and the fit parameters are given in Figure A.2.

Another crucial aspect in the set-up of the spectrometer is the setting of the apertures that act as a collimator for the gamma rays. As the motion of the source is only in a straight line towards and away from the detector, the Doppler shift of the gamma rays is also only added in this specific direction. For gamma rays that are emitted in an angle θ , see Figure 3.11C, the energy in direction of the gamma rays is only modulated by $v \cos \theta$ with the velocity v of the source. This leads to a Gaussian broadening of the available energies that hit the absorber, thereby broadening the absorption signal. This effect is called cosine smearing and it is increased for larger settings of the apertures as then higher angles θ become accessible. As the source is not a point source but has an active area of 8 mm, the effect is even more drastic than what is depicted in Figure 3.11. Cosine smearing can be easily detected as the baseline of the raw, unfolded spectrum has an underlying cosine function as is depicted in Figure 3.11C. It must be noted that this is

not an actual measurement and is the result of the sum of the measurement where the apertures on the source and detector units were set to 10 and 16 mm, respectively and a cosine function. The actual, untreated measurement is shown in Figure 3.11A, where no cosine smearing, even for the largest apertures, is visible.

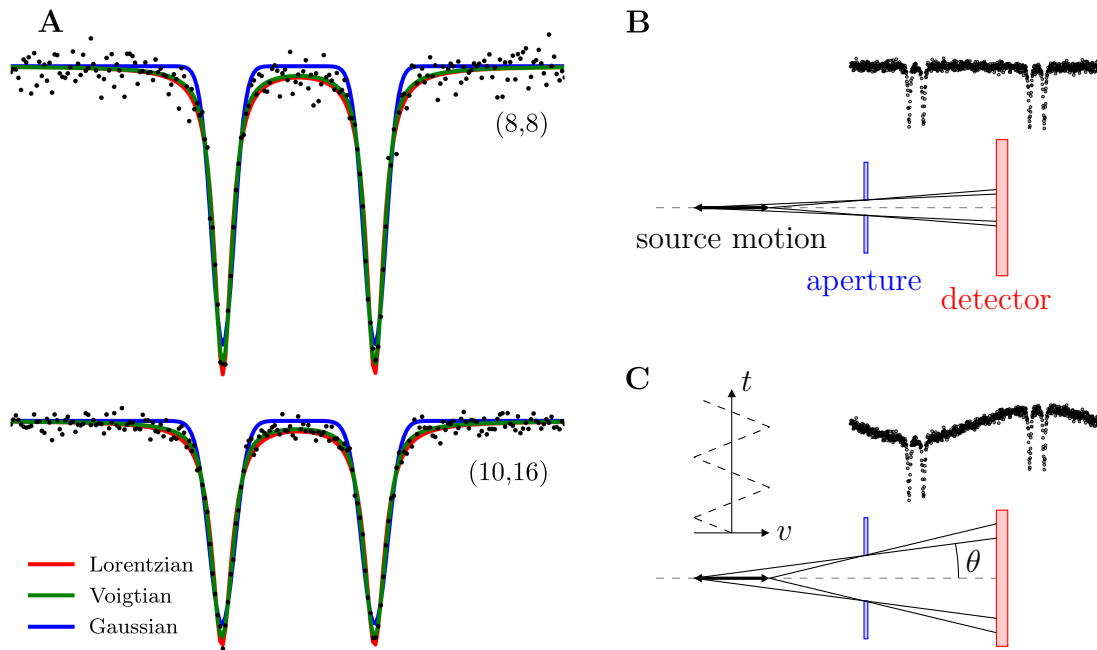


Figure 3.11: A) Line shape analysis of a measurement of ferrocene at 80 with two different aperture settings given in the parentheses in the figure, where the two values depict the diameters of the apertures in millimetres on the source and detector unit, respectively. For the measurement at the top and bottom, the area of the pseudo-Voigtian line consists of 76.1% and 72.6% of the Lorentzian curve, respectively. B) Raw measurement of the (10,16) measurement shown in (A) without any visible cosine smearing and a schematic drawing of the effect of the cosine smearing for small apertures. C) Sum of the raw measurement shown in (B) and a cosine function to show the effect of cosine smearing for large apertures.

As the cosine smearing can be corrected for by folding of the spectrum, the only result it has on the folded signals is a Gaussian broadening. In order to check whether this would be the case in our set-up, a line shape analysis was performed where two measurements with different aperture setting, see Figure 3.11A, were fitted with Lorentzian, Gaussian and pseudo-Voigtian lines, where the latter is the sum of the former two.

$$y_{\text{Voigt}} = \frac{I_{\text{Lorentz}} \Gamma_{\text{Lorentz}}}{2\pi} \left[(x - x_0)^2 + \left(\frac{1}{2} \Gamma_{\text{Lorentz}} \right)^2 \right] + \frac{I_{\text{Gauss}}}{\sqrt{\pi} \Gamma_{\text{Gauss}}} \exp \left[- \left(\frac{x - x_0}{\Gamma_{\text{Gauss}}} \right)^2 \right] \quad (3.4)$$

In the pseudo-Voigtian line profile the intensities I_{Lorentz} and I_{Gauss} are numerically exactly the same as the areas under the respective curves. It becomes obvious that the actual line shape is much closer to a Lorentzian than a Gaussian, even for very large setting of the apertures. By fitting the two experimental spectra with a pseudo-Voigtian function it was estimated that the underlying area consists to 76.1% and 72.6% of a Lorentzian line profile for the small and larger aperture settings, with $\Gamma_{\text{Lorentz}} = 0.38 \text{ mm s}^{-1}$ and $\Gamma_{\text{Gauss}} = 0.20 \text{ mm s}^{-1}$. A Gaussian contribution to the line profile of Mössbauer absorption lines is well known and was extensively studied in the 1970s where it was concluded that unresolved hyperfine splitting, the absorber thickness and vibrations in the building can increase the fraction of the underlying Gaussian [13, 14]. A lineshape analysis for all aperture setting is given in Figure A.3. There, a trend towards higher Gaussian contributions for larger apertures can be seen. The increase of the Gaussian area for higher aperture settings is attributed to a small cosine smearing, which is why smaller aperture settings of 8 mm for both apertures was set, giving a good compromise between the absolute number of counts, i.e. the signal intensity, and the correctness of the line shape. The smaller influence of the source aperture on the count rate is explained by the fact that the sample holder itself acts as a second collimator.

3.2.2 Sample Composition and Preparation

One of the goals in the set-up of the Mössbauer spectrometer was to be able to measure different types of samples, i.e. loose powders, pressed pellets and frozen solutions. Loose powders allow for easy sample preparation and recovery of the compound while pellets are easy to handle and are used also for high-field EPR spectroscopy and SQUID magnetometry in the Van Slageren group, thereby allowing for a complete investigation of a compound with only one sample. Frozen solutions have the advantage that changes in the molecular structure compared to that in a powder or crystal can be investigated via Mössbauer spectroscopy, which is of interest for catalysts that are used in solution. Also, short-range intermolecular interactions, which are often apparent in paramagnetic samples, i.e. exchange interactions as well as ferromagnetic interactions can be eliminated in frozen solutions.

As was mentioned in the previous section, different sample holders were designed to facilitate the use of the mentioned sample types. Solid samples have to be ground to get symmetric lines for quadrupole split signals, i.e. two signals of equal intensity, see Section 2.2.7.5. For loose powders, they were then put into the centre of a $(30 \times 30) \text{ mm}^2$ sheet of weighing paper that was folded twice in both directions to get nine squares of $(10 \times 10) \text{ mm}^2$ each. The paper was then closed to get a $(10 \times 10) \text{ mm}^2$ enclosed sample

that was then secured with Parafilm to stay closed. Pellets with diameters of 8 or 13 mm were put into PTFE tape and pressed with varying pressure, depending on the diameter. Solutions were transferred into the 3D-printed PETG sample holder. Pictures of the prepared samples in the sample holders are also shown in Figure 3.12 (B-D). For air sensitive samples that were to be measured at room temperature, a dry nitrogen gas flow was directed into the inner cryogenic liquid chamber. The sample was in this nitrogen flow by opening the needle valve connecting the sample chamber and the helium reservoir.

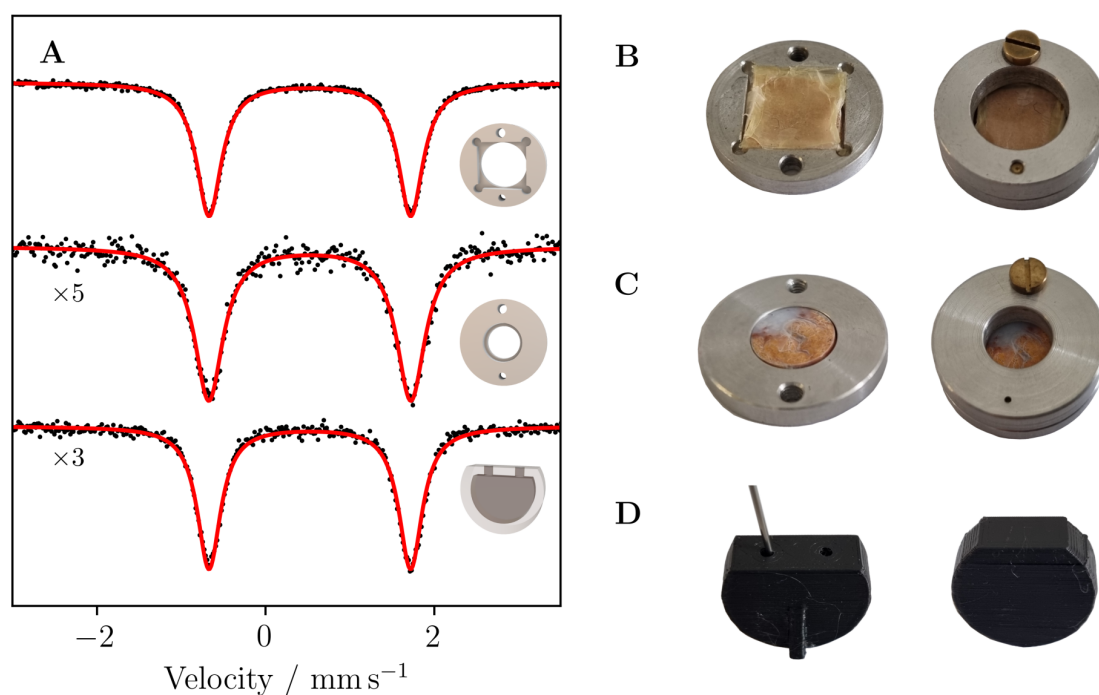


Figure 3.12: A) Measurements of ferrocene at 80 K prepared as a loose powder (top), pressed pellet (middle) and in frozen solution of acetone (bottom). The pictures depict the processes of sample preparation for loose powders (B), pressed pellets (C) and solutions (D), whereas the dim grey area in (A) shows the hollow part of the PETG sample holder. The apertures were set to the same values for all three measurements.

For all of the different types of samples, measurements of ferrocene were performed at 80 K with the same measurement times for all samples to see the effect of the sample preparation on the spectral shape and the signal intensity. For all three samples, typical sample amounts were used, see Table 3.2. They are shown in Figure 3.12A and the fit parameters are given in Table 3.2. From these results it becomes clear that while all measurements give the same fit results for the isomer shift and quadrupole splitting, loose powders have a clear advantage over the two other types of samples. The uncertainty in the fit parameters is smaller because of the higher signal-to-noise ratio, especially compared

to the pressed pellet, which is simply an effect of the sample diameter. Furthermore, loose powder samples allow for much greater sample amounts than solutions due to the limited space in the sample holder and low solubility of many samples. The minor increase of the line width in the measurement of the loose powder compared to the frozen solution does not by itself justify the usage of frozen solutions. The count rate differences are easily explained by the material of the sample holders. PETG transmits gamma rays more easily as the mass attenuation coefficient of most polymers was calculated to $\mu_m \approx 1 \text{ cm}^2 \text{ g}^{-1}$ ($II_0^{-1} = 0.67$ for 5 mm of PLA) for energies of 14.4 keV [115], where similar values were observed experimentally at slightly higher photon energies [116]. The mass attenuation coefficient is larger for halogenated polymers, e.g. for polyvinylchloride a mass absorption coefficient of $\mu_m \approx 10 \text{ cm}^2 \text{ g}^{-1}$ was calculated for 14.4 keV [115]. Aluminium attenuates the gamma rays more efficiently than PETG with $\mu_m \approx 7.5 \text{ cm}^2 \text{ g}^{-1}$ ($II_0^{-1} = 0.25$ for 5 mm of aluminium) at 15 keV [117]. This can also be clearly seen in Section 3.4, where a much higher count rate was measured at the detector for the PLA sample holder than for the aluminium sample holder with the same design. Also, a lower amount of sample for frozen solutions leads to a higher transmission of gamma rays. Furthermore, the hole in the sample holder for pressed pellets has an area of $\pi \cdot (3.5 \text{ mm})^2 \approx 39 \text{ mm}^2$ and the sample holder for loose powders has a much larger area with $\pi \cdot (5 \text{ mm})^2 \approx 79 \text{ mm}^2$.

Table 3.2: Fit parameters for the measurements shown in Figure 3.12A. As the samples were measured at different times, the count rates are calculated to $C_{\text{rel}} = C_t \cdot \exp(t \cdot \ln(2)/t_{1/2})$ with the count rate C_t for the specific measurement and the time t after the installation of the source at which the measurement was taken with the half-life $t_{1/2} = 271.8$ days of ^{57}Co .

	$\delta_{\text{IS}} / \text{mm s}^{-1}$	$\Delta E_{\text{Q}} / \text{mm s}^{-1}$	$\Gamma / \text{mm s}^{-1}$	m / mg	$C_{\text{rel}} / \%$
Powder	0.527(1)	2.392(1)	0.358(2)	53	77
Pellet	0.527(2)	2.396(4)	0.411(6)	62	38
Solution	0.527(1)	2.391(2)	0.336(3)	14	100

3.2.3 Sample Amount

Although a higher amount of sample increases the strength of absorption, and thereby the intensity of the Mössbauer signal, it also attenuates the γ -rays by non-resonant mass absorption, which is caused by Compton scattering and the photo effect. This effect leads to an exponential decrease of the detector signal, i.e. the count rate C

$$C = C_0 e^{-t \cdot \mu_e}, \quad (3.5)$$

with the mass absorption coefficient μ_e in $\text{cm}^2 \text{g}^{-1}$ and the thickness of the absorber t' in g cm^{-2} . It was shown in [118] that the signal-to-noise ratio is proportional to the product of the exponential decay of the count rate and the linear increase of absorption, i.e. an ideal sample amount must exist.

$$\text{SNR} \propto t' e^{-\frac{1}{2} \cdot t' \cdot \mu_e} \quad (3.6)$$

In Figure 3.13 the evolution of the SNR over time for five different sample amounts, i.e. sample thicknesses t' , is shown. In all cases it follows the behaviour $\text{SNR} \propto \sqrt{t}$.

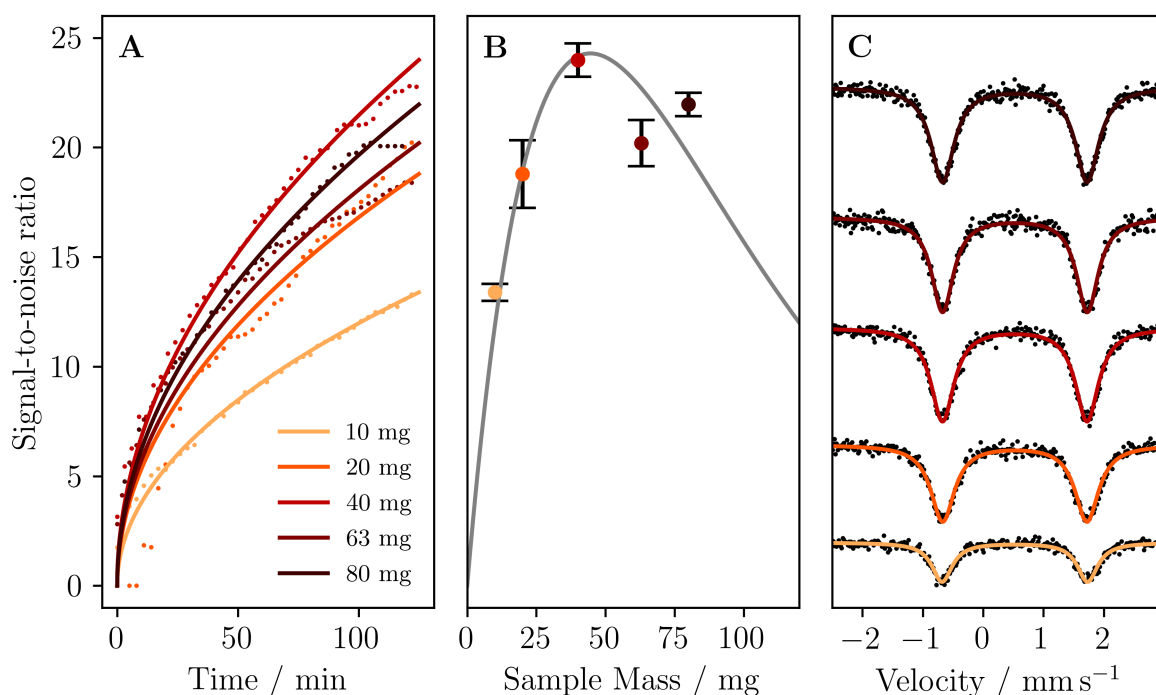


Figure 3.13: A) Signal-to-noise ratios versus measurement time for five samples of ferrocene with different sample amounts measured at 80 K with fits $\text{SNR} = a_i \sqrt{t}$. B) SNR extracted from the fit at $t = 120$ min versus the sample amount with a fit (see text). The error bars show the standard deviation of the data points to the fit in (A). C) Mössbauer spectra of the corresponding samples after 120 min.

When plotting the last value of the fit, i.e. the SNR after the same measurement time for all samples, it becomes clear that for high sample amounts, the SNR starts to decrease, as is predicted in equation 3.6. Due to the limited space in the sample holder the area of all of the samples might not have been the same due to an uneven distribution of the powder in the weighing paper, especially for large sample amounts, which makes the data point for the 80 mg sample unreliable. Still, a trend is clearly visible. The mass absorption coefficient can be calculated from the weighted sums of the coefficients of the

individual atoms. For ferrocene we can calculate $\mu_e = 19.27 \text{ cm}^2 \text{ g}^{-1}$ from the values given in [80, 119]. From the fit in Figure 3.13 we obtain that the area of the γ -rays must be ca. 0.43 cm^2 which fits quite well to the set aperture of 0.8 cm which gives an area of 0.5 cm^2 .

From these results it was estimated that an ^{57}Fe content of $2.12\% \cdot M_{\text{Fe}} \cdot M_{\text{Ferrocene}}^{-1} \cdot 45 \text{ mg} \approx 0.3 \text{ mg}$ is optimal in our set-up. Since the iron content and Mössbauer factor of most samples of interest are much lower than for ferrocene and the 0.3 mg Fe cannot typically be accommodated, we opted for using as much sample as was possible with our sample holder. On the other hand, this shows that for very low iron contents, as is the case for iron species in matrices of other materials, the Mössbauer isotope needs to be enriched in order to obtain realistic measurement times.

3.2.4 Measurement Time

Recording Mössbauer spectra can take substantial time due to the low number of recoil-free absorption processes. In order to unambiguously decide when a measurement is finished, i.e. there is no additional uncertainty in the fitting parameters as a result of a low signal-to-noise ratio due to the low number of resonant absorption processes, the deviation of the fitting parameters in relation to the SNR for different measurements was taken. In Figure 3.14A the deviation of the fitting parameters from the value determined after the measurement was finished and the determined SNR of a measurement of ferrocene at 80 K over the course of the first ten hours of measurement time is plotted.

The SNR was calculated with equations (3.2) and (3.3) with the minimum of the fit being taken as the signal intensity. The SNR was fitted with a square root function $\text{SNR} = a\sqrt{t}$ and the deviations of the fit parameters was calculated by taking the absolute of the difference of the fit parameters at time t and the final measurement's fit.

As can be seen in the figure, the uncertainty in the fit parameters becomes independent of the SNR after about two hours. At that time $\text{SNR} \approx 25$, which is why it was decided that measurements should run until the SNR is larger than 30. In order to realise this, the SNR was calculated regularly in the self-written Python script, see Section 3.1.5. In Figure 3.14B actual measurements are shown for different times t after the measurement was started.

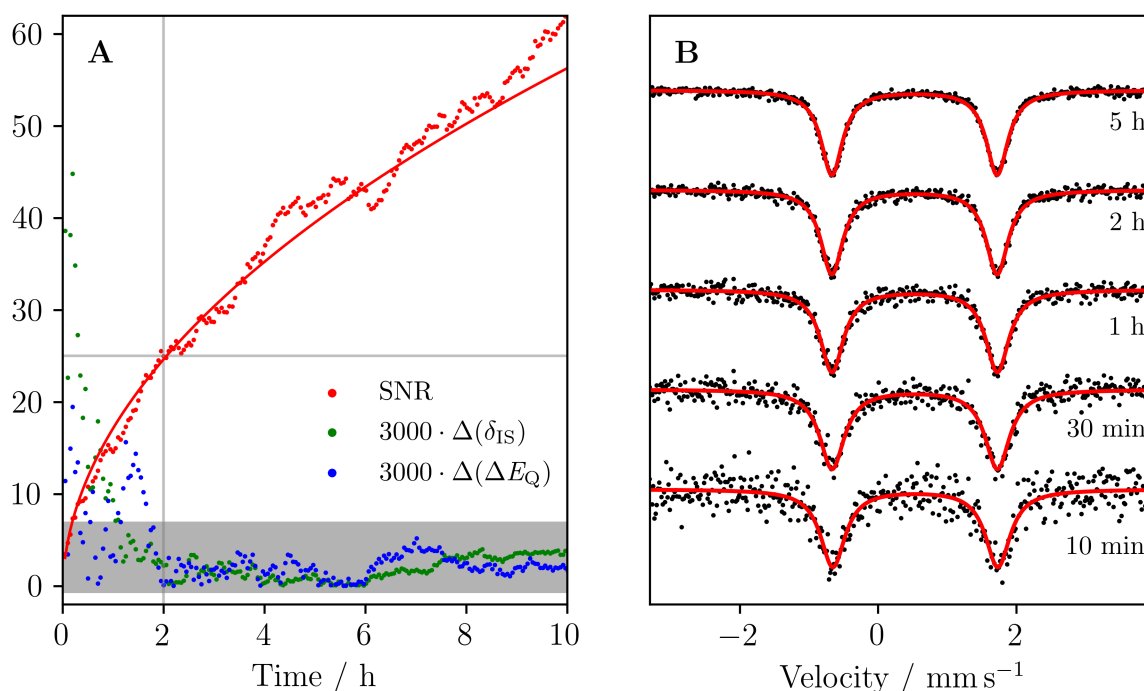


Figure 3.14: A) Signal-to-noise ratios and the absolute deviations of the fit parameters obtained at the given times to the values obtained after the end of the measurement, i.e. $\delta_{\text{IS}} = 0.528(4) \text{ mm s}^{-1}$ and $\Delta E_{\text{Q}} = 2.392(4) \text{ mm s}^{-1}$. For $\text{SNR} > 25$ the fit does not improve for longer measurement times, as is indicated by the grey lines, and the measurement can be stopped. B) Exemplary Mössbauer spectra of ferrocene at 80 K with Lorentzian fits after the specified times.

3.3 Data Analysis

3.3.1 Calibration of the Velocity Axis

The LabView software that was used to record the spectra returns multiple files containing all the experimental parameters known to the spectrometer as well as the raw data. The latter consists of an array of the size of the number of channels, i.e. 1024 data values with the accumulated number of counts detected in the specific channel. In order to translate the channel numbers into the velocity axis, calibration measurements need to be undertaken frequently, e.g. every six months. There are a few requirements for the calibration sample: all fitting parameters such as the isomer shift for the installed ^{57}Co source, as well as the quadrupole and magnetic splittings must be known and the sample should have a strong Mössbauer effect as otherwise the low signal-to-noise ratio prevents a reliable fit or the measurement time becomes very long. Most often, $\alpha\text{-Fe}$ foil is used as the calibration standard. For $\alpha\text{-Fe}$ measured at room temperature with a $^{57}\text{Co}/\text{Rh}$ source, which is also kept at room temperature, these are $\delta_{\text{IS}} = -0.114 \text{ mm s}^{-1}$ and

$B_{\text{hf}} = 33 \text{ T}$. Due to the cubic crystal symmetry of $\alpha\text{-Fe}$, $V_{zz} = 0$ and no quadrupole splitting is observed. The general procedure for the calibration of the velocity axis is shown in Figure 3.15 and explained in the following text.

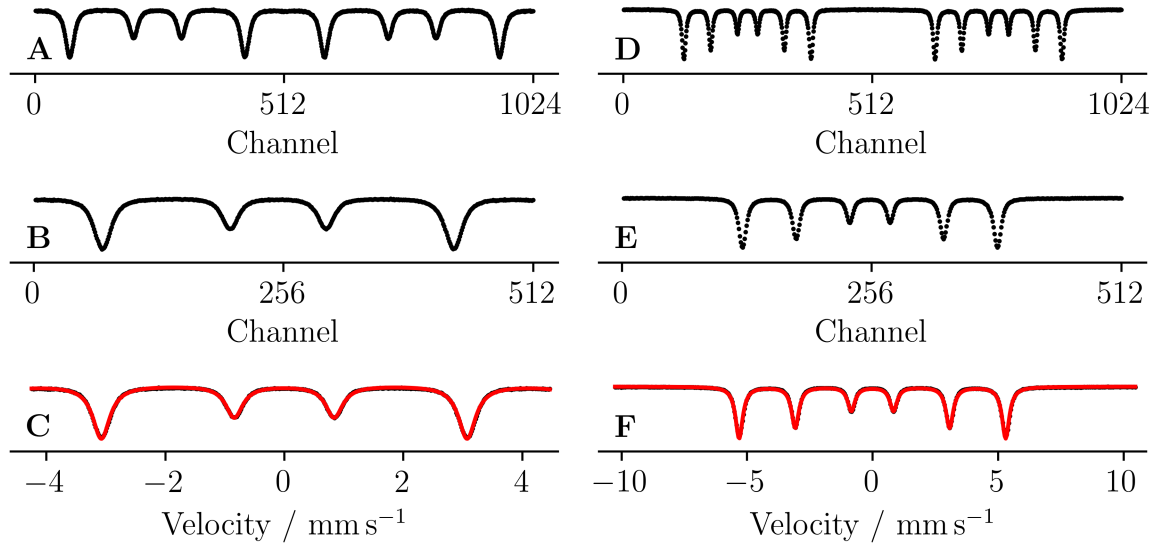


Figure 3.15: Step-by step procedure for the calibration of the velocity axis, as explained in the text, for maximum velocities of ca. 4 mm s^{-1} (A-C) and ca. 10 mm s^{-1} (D-F). In both cases the raw spectrum (A,D) is folded (B,E) and fitted (C,F) with the parameters known for the used calibration sample.

As was shown in Section 2.2.7.6, the distance between the outermost lines can be determined and their centre is known from the isomer shift. Thus, $\alpha\text{-Fe}$ can be used for the calibration of the velocity axis. As described in Section 3.1.1, the raw data includes the spectrum twice as a result of the periodic movement of the source. The first step is to fold the spectrum. In our set-up the data in the channels 513-1024 is reversed, i.e. ordered from high to low Doppler energies. It is easy to assume that the folding point is exactly in the centre of the data but slight time delays in the communication between the velocity drive and detector units can shift this folding point slightly by integer or half-integer values in either direction. The evaluation software MossWinn determines this folding point automatically by determining the value for which the result of subtraction of the spectra on either side of the folding point is minimized. In a next step the folded spectrum is fitted with the fit parameters known for the calibration sample. Again, due to slight timing differences in the communications of the velocity drive and detector units with the computer, i.e. a delay between the start of the counting period in the detector and the movement period in the velocity drive, data might be shifted by a non-integer number of channels. To compensate for this shift, the fit parameter *Delay* in units of

the dwell time (time of counting for each particular channel) is added. By changing this value the spectrum is shifted to either side. The other important added fitting parameter is the maximum velocity which stretches the spectrum to fit the distance of the lines to the expected value. Finally, the whole spectrum is shifted by $\delta_{\text{IS},\alpha\text{-Fe}}$. This procedure is shown in Figure 3.15 (A-C) for a calibration measurement with a maximum velocity of ca. 4 mm s^{-1} and in Figure 3.15 (D-F) for a measurement with a maximum velocity of ca. 10 mm s^{-1} .

3.3.2 Fitting of the Spectrum

When the Mössbauer spectrum of the sample has been recorded and the velocity axis is calibrated, the fitting of the spectrum can commence. For simple spectra that only show an isomer shift and quadrupole splitting, or when the individual lines are well separated, a simple fitting algorithm with the fitting function of the sum of multiple Lorentzian lines can be used. The centre of the lines gives the isomer shift, whereas their distance is equal to the quadrupole splitting. This is basically what specifically written software such as MossWinn does. For each iron component a sub-spectrum is added for which the fitting model can be chosen, e.g. singlets, doublets or magnetically split signals. MossWinn always assumes Lorentzian lines, as expected for most absorption lines and this is adequate for most spectra, even when there is a small amount of inhomogeneous broadening, as was shown in Figure 3.11A. MossWinn also gives the uncertainty in the fit parameters, calculated from the covariance of the determined values. When the spectra become more complicated, good starting values or lower and upper bounds for the fit parameters must be chosen. Here, it is useful to get an idea of the possible isomer shifts and quadrupole splittings of the expected species from other spectroscopic methods. As an example EPR spectroscopy can give an idea of the oxidation state of the iron atom as only Fe^{I} and Fe^{III} show an EPR signal at low microwave frequencies and of the spin state as high-spin and low-spin Fe show different EPR signals, especially at higher microwave frequencies.

3.4 Spectrometer Performance over Time and Source Lifetime

As with all other types of spectroscopy, the spectrometer itself is exposed to environmental changes, such as fluctuations in humidity and temperature, as well as ageing processes. As an example the calibration of the relationship between the applied voltage and velocity might change with time or the detector might lose its sensitivity. One thing that is for certain is that the gamma source intensity decays over time, losing its initial activity. It was observed that the count rate decreased over time quite significantly when measuring

exactly the same sample, e.g. ferrocene for the set-up of the spectrometer or α -Fe for the calibration of the velocity axis. The drop in the count rate over time is shown in Figure 3.16.

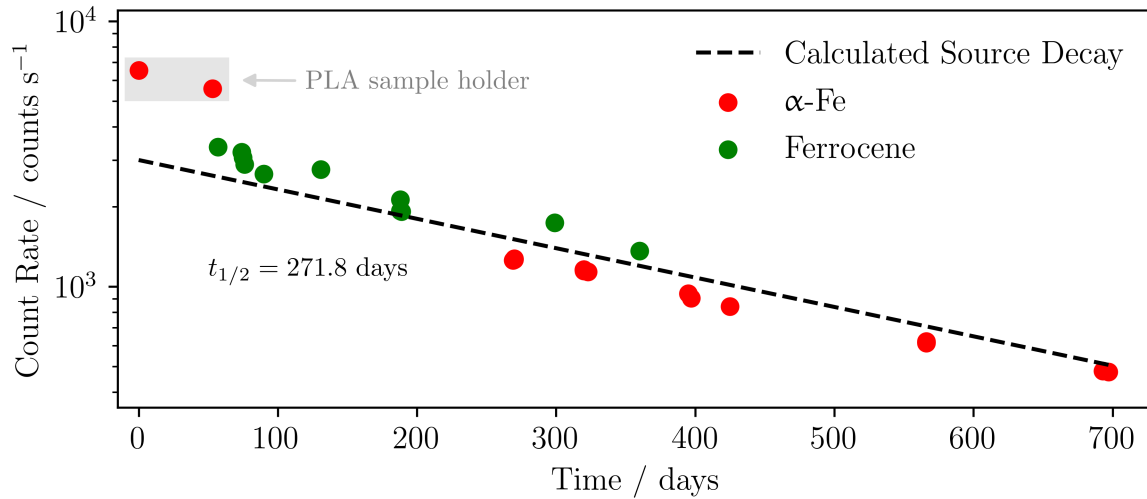


Figure 3.16: Decrease in the count rate over time after the acquisition of the gamma source. The higher count rate in the first two measurements is because a 3D printed PLA sample holder was used to test the design. Afterwards an aluminium sample holder was used. α -Fe shows a lower count rate because the recoil-free fraction is higher and more sample is used, therefore more of the gamma rays are absorbed.

To check for the changes in the calibration of the velocity axis the calibration parameters, see Section 3.3.1, for all calibrations within the first two years of the usage of the spectrometer are given in Table 3.3. Here, virtually no change in any of the parameters occurs, i.e. the velocity calibration does not seem to change within this time.

Table 3.3: Changes over time in the actual velocities and delays between the channel advances in the source and detector in units of the dwell time, i.e. the integration time per channel $\bar{t} = (f \cdot 1024)^{-1} \approx 30 \mu\text{s}$. Both values can be determined by fitting a known standard, e.g. $\alpha\text{-Fe}$.

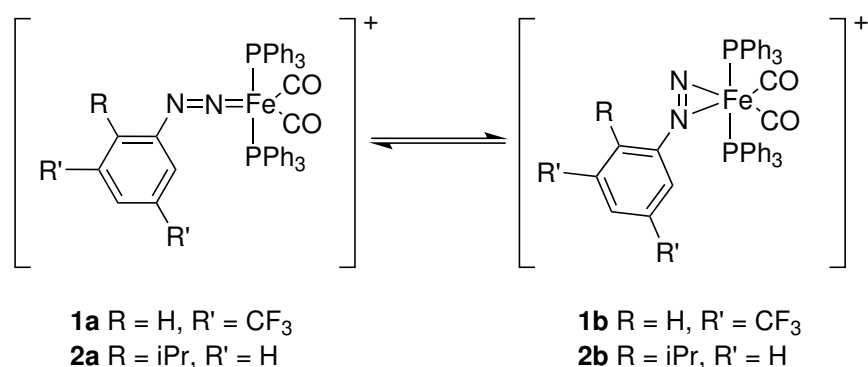
Date	$v_{\text{max}} \approx 4 \text{ mm s}^{-1}$		$v_{\text{max}} \approx 10 \text{ mm s}^{-1}$	
	$v_{\text{max}} / \text{mm s}^{-1}$	Delay / \bar{t}	$v_{\text{max}} / \text{mm s}^{-1}$	Delay / \bar{t}
2019-07	4.3821(4)	0.27(1)	10.4337(9)	-0.13(1)
2019-10	4.3633(4)	-0.23(1)	10.388(1)	-0.10(1)
2020-04	4.370(1)	-0.21(4)	10.413(2)	-0.13(2)
2020-06	4.3712(5)	-0.26(2)	10.408(1)	-0.12(1)
2020-11	4.3731(2)	-0.297(8)	10.4032(2)	-0.124(3)
2021-02	4.361(1)	-0.17(4)	10.382(4)	-0.13(4)
2021-06	4.378(3)	-0.23(9)	10.425(5)	-0.08(4)
2021-08	4.371(2)	-0.35(8)	10.413(3)	-0.16(4)

3.5 Example Measurements

3.5.1 Structure Determination of a Potential Photoswitch

The work presented in this chapter was obtained in close cooperation with Marina Fuhrer (Universität Stuttgart, group of B. Plietker now Technische Universität Dresden) who synthesised the samples and Alexander Waigum (Universität Stuttgart, group of J. van Slageren, under the supervision of the author of this thesis) who performed the theoretical calculations.

Photoswitches are molecules that change their geometric structure and consequently their chemical or physical properties through the irradiation with light. One of the most famous examples for photoswitches are rhodopsins, the membrane-bound photoreceptors that are responsible for vision in the eyes of humans and animals. [120] Potential applications of this type of material lie amongst others in modern electronics, where the different isomers of a molecule immobilised on a semiconductor give different conductivities [121], in changing the properties of liquid crystals by irradiation with light for rewritable ionic circuitries [122], the storage of gases in porous materials by changing the size of the pores as a result of irradiation thereby trapping or releasing the gas [123] or different catalytic activities of the two isomers leading to different products as was shown for azobenzene [124]. See [125] for a broad overview of the topic.



Scheme 2

The compounds depicted in scheme 2 were chosen as it is known that in both compounds an end-on (**1a**, **2a**) and a side-on (**1b**, **2b**) isomer exist, the difference being the binding geometry of the azo group to the iron. From ³¹P-NMR experiments, where the chemical shift of the phosphorus atoms differs for the two isomers, it was determined that the singlet of the phosphorus groups in the end-on configuration is situated at higher chemical shifts than in the side-on isomer. The isomer ratio of end-on to side-on in **2** was determined to 1:5, whereas **1** was shown to be only prevalent in the end-on configuration. Subsequently

Mössbauer spectroscopy was used to further study the materials in their ground states without irradiating the samples. The spectra measured at room temperature are shown in figure 3.17A.

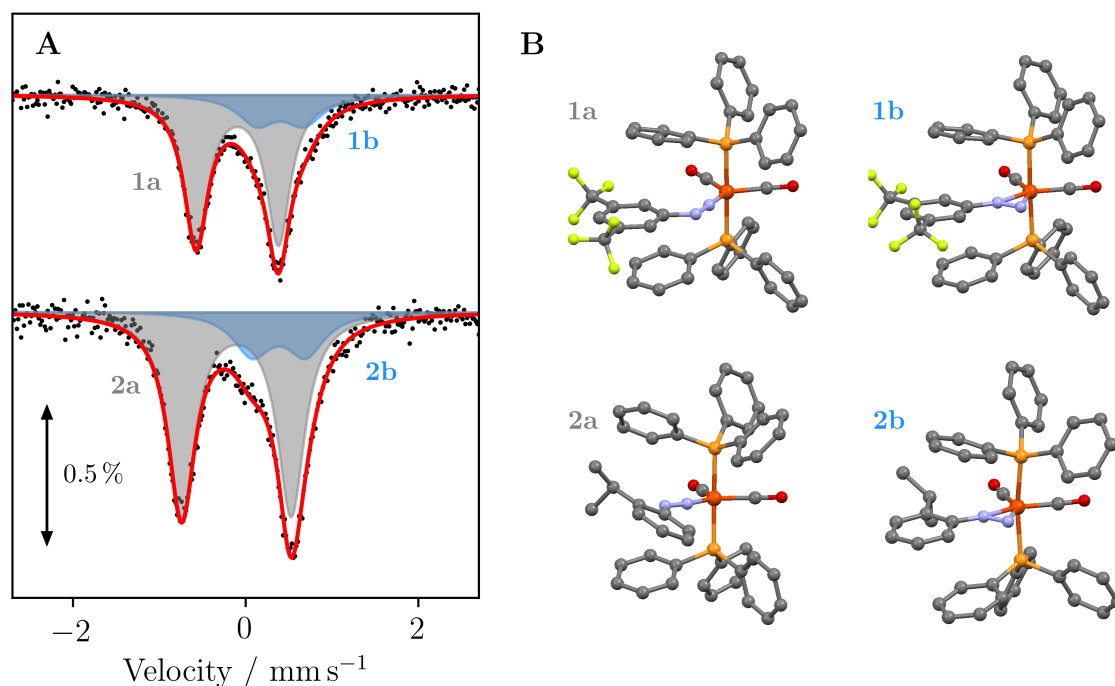


Figure 3.17: (A) Mössbauer data of samples **1** and **2** measured at room temperature with the fit for the end-on and side-on configurations shown in grey and blue, respectively. (B) Computed structures of the different isomers. Atoms are coloured as specified in the CPK colouring convention: carbon (grey), nitrogen (blue), oxygen (red), fluorine (green), phosphorus (orange), iron (dark orange). Hydrogen atoms are omitted for clarity.

The fit parameters are given in Table 3.4 and indicate that both compounds are present in the same isomer ratio as both spectra look remarkably similar with minor differences in the quadrupole splitting for the more intense signal. The isomer shifts indicate a low-spin ($S = 0$) Fe^{II} species for the end-on isomers and a high-spin Fe^{III} species for the side-on isomers. The lower isomer shift for the end-on than for the side-on configuration is consistent with the higher chemical shift for the former in NMR as both are a result of lower d electron density on the iron atom, indicating the iron atom in the end-on isomer to be more electron withdrawing than the side-on isomer. Other iron carbonyl complexes of azo compounds were investigated in the literature and an isomer shift of -0.13 mm s^{-1} and a quadrupole splitting of 0.99 mm s^{-1} were observed for a diamagnetic compound made from benzo[*c*]cinnoline and iron pentacarbonyl investigated in [126], fitting nicely to the values determined for the end-on isomer. Isomer shifts of 0.374 mm s^{-1} and 0.392 mm s^{-1}

and quadrupole splittings of 0.531 mm s^{-1} and 0.668 mm s^{-1} were attributed to a high-spin Fe^{III} species for other azo compounds. [127, 128]

Table 3.4: Comparison of the experimentally determined and computed Mössbauer parameters for samples **1** and **2** with the respective molar fractions x . The errors are given in MossWinn.

	$\delta_{\text{IS}} / \text{mm s}^{-1}$	$\delta_{\text{IS,calc}} / \text{mm s}^{-1}$	$\Delta E_{\text{Q}} / \text{mm s}^{-1}$	$\Delta E_{\text{Q,calc}} / \text{mm s}^{-1}$	$x / \%$
1a	-0.096(2)	-0.09	0.953(3)	-0.83	77(6)
1b	0.40(1)	0.09	0.55(2)	-0.49	23(6)
2a	-0.106(2)	-0.08	1.268(4)	1.00	78(6)
2b	0.38(1)	0.09	0.62(2)	-0.82	22(6)

Although the isomer shift and quadrupole splitting of the end-on isomer indicate a low-spin Fe^{II} species, a trigonal bipyramidal geometry as in the end on configuration would result in an intermediate spin $S = 1$, see figure 3.18. It is assumed that a Jahn-Teller distortion leads to the lowering of one of the singly filled degenerate orbitals leading to a pairing of the spins.

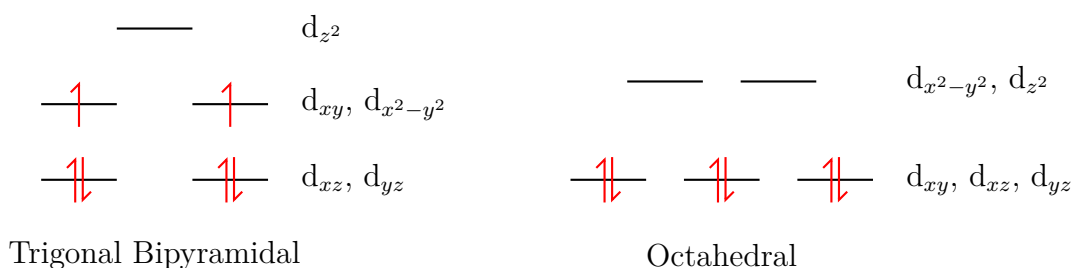


Figure 3.18: Schematic drawing of the energy levels for a d^6 system in trigonal bipyramidal and octahedral geometries.

In order to further elucidate the electronic structure and assess the validity of the analysis of the Mössbauer spectrum, DFT calculations were performed in ORCA (Version 4.2.1). An initial geometry optimisation was performed in TURBOMOLE 7.1 [129] on RI-DFT level [130, 131] with the same basis TZVP [132] as was used in the computation of the Mössbauer parameters for which the functional BP86 [133, 134] with Becke-Johnson-dispersion correction [135] was chosen. Furthermore the property-optimised basis set for iron CP(PPP) [85] was used as it improves the DFT results for the computation of Mössbauer parameters [85]. The electron density as well as the field gradient at the nucleus was calculated with a subroutine in ORCA [85, 136] and the isomer shift was then calculated via equation (3.7) with $\alpha = -0.424 \text{ mm s}^{-1} \text{ au}^3$, $\beta = 7.916 \text{ mm s}^{-1}$ and

$C = 11810 \text{ au}^{-3}$ with a standard deviation of 0.11 mm s^{-1} as determined by a linear fit of computational data of model compounds versus the experimental isomer shifts [137].

$$\delta_{\text{IS}} = \alpha [\rho(0) - C] + \beta \quad (3.7)$$

The input file looks as follows, where *filename.xyz* indicates the file where the coordinates of the geometry-optimised structure are saved.

```
! RKS BP TZVP D3BJ opt TightSCF Grid5 NoFinalGrid SlowConv
%maxcore 1024
%basis NewGTO 26 "CP(PPP)" end
end
%method SpecialGridAtoms 26
SpecialGridIntAcc 7
end
* xyzfile 1 1 filename.xyz
%eprnmr nuclei = all Fe {rho, fgrad}
end
```

The results of the calculations are given in Table 3.4 and fit quite well to the experiment. In both cases the isomer shift is larger in the side-on configuration while the quadrupole splitting decreases, albeit the changes in the calculations are not as drastic as in the experiment when going from the end-on to the side-on isomer. It must be noted that the calculations assume a temperature of $T = 0 \text{ K}$. However, Fe^{II} low-spin species do not show a strong temperature dependence of isomer shift and quadrupole splitting. [138, 139] This means that the second-order doppler shift has the largest effect on the changes with temperature, i.e. the isomer shift is $\approx 0.1 \text{ mm s}^{-1}$ lower at room temperature than it would be at 0 K .

Lastly, because the Mössbauer and initial NMR evaluations gave differing results for the isomer ratios, the ^{31}P -NMR experiments were repeated, see figure 3.19. For **1** only the end-on isomer can be observed, as was the case in the initial NMR measurement. For **2** the NMR spectrum that was measured shortly after dissolving of the compound seemingly contradicts the initial results by showing mostly the end-on isomer. After being in solution for almost a week another NMR spectrum was measured and indeed a shift in the signal intensities can be observed, confirming the initial results. It becomes clear, that the compound behaves differently in the solid state compared to solution.

Another possibility that cannot be excluded is that due to the irradiation with high

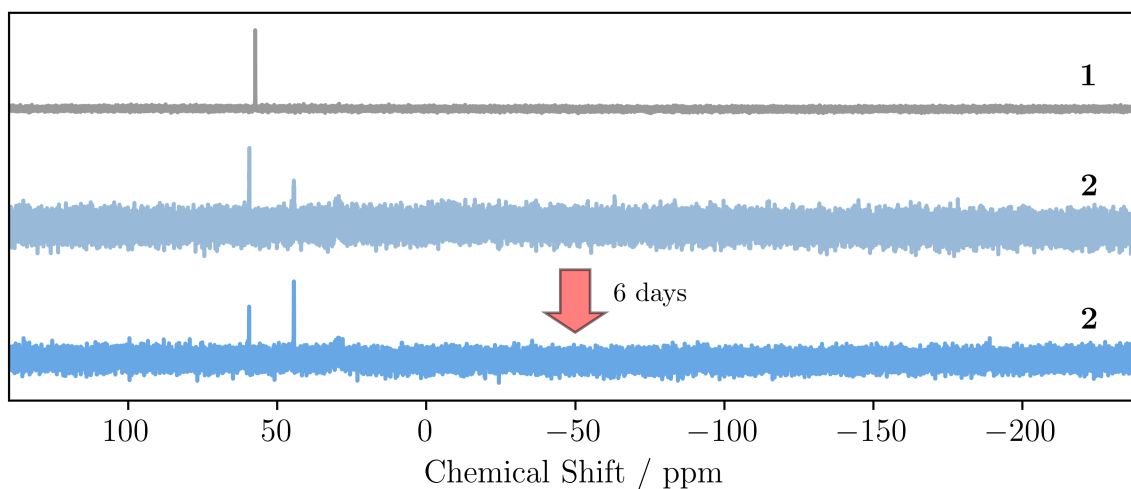


Figure 3.19: ^{31}P -NMR of samples **1** and **2** after the measurement of the Mössbauer spectra. The resonance line due to the end-on isomer is found at larger chemical shifts.

energy gamma rays in the Mössbauer experiment, the energy barrier for the transition between the two isomers could be exceeded during the experiment, giving the equilibrium that is thermodynamically favoured without kinetic effects.

It was confirmed that both configurations of the compound exist and that they can be distinguished with Mössbauer spectroscopy. Further experiments, especially under the irradiation of light must be undertaken to understand the behaviour of the potential photoswitch.

3.5.2 Oxidation States in Synthetic Tochilinite

The results presented in this section were obtained in close cooperation with Robert Bolney (Friedrich-Schiller Universität Jena, group of C. Robl) who synthesised the samples.

The abundance of iron and sulfur in nature and the early days of the earth make the minerals composed of these two elements interesting, as they undoubtedly play an important role in natural biochemical processes. The most famous example is $[\text{FeFe}]$ hydrogenase. In order to understand the formation of these enzymes and life itself it is crucial to understand the formation of the simplest minerals composed of iron and sulfur, e.g. mackinawite (FeS) and tochilinite. A new method to synthesise the latter was developed by Robert Bolney [140] and it is necessary to confirm the successful synthesis and determine the elemental composition. To do so, Mössbauer spectroscopy is a great tool as it allows the determination of oxidation state, spin state, and symmetry of the chemical environment between different iron species and their surroundings from the experimental isomer shift and quadrupole splitting.

Tochilinite was discovered in 1970. Its structure consisting of mackinawite-like and brucite-like layers in an ABAB fashion (see Figure 3.20), was determined shortly after that. [141, 142] The structural formula can be expressed as $6(\text{Fe}_x\text{S}) \cdot 5[\text{Mg}_y\text{Fe}_z(\text{OH})_2]$ with $0.7 \lesssim x \lesssim 1$ and $y+z \approx 1$. [142–144] Because of the iron vacancies in the mackinawite-like substructure, i.e. the iron sulfide layer, some of the iron atoms in the brucite-like layer must be in the +3 oxidation state to compensate the negative net charge of the sulfide layer.

Table 3.5: Differences in the syntheses of the samples **3a-c** with the mixed reactants and their approximate molar ratios in parentheses as well as the atmosphere during the reactions, the reaction temperatures and times. In all cases the powders were mixed at room temperature in the given ratio and stirred in water for the given time at the given temperature. After the reaction was completed all magnetic residues were removed and the resulting powder was washed with organic solvents. [140]

	Reactants	Atmosphere	Solvent	$T / ^\circ\text{C}$	t / days
3a	Fe, S (3:2)	Air	H ₂ O	130	3
3b	Fe, S, Al (5:2:1)	Air	H ₂ O	130	3
3c	Fe, S, Mg, FeO(OH) (6:6:3:1)	N ₂	H ₂ O	160	4

It was shown in [145] that the $\text{Fe}^{\text{III}}/\text{Fe}^{\text{II}}$ ratio is overestimated in Mössbauer spectroscopy by ca. 10%. This was shown by temperature dependent study of basaltic glass where the room temperature ratio is different to that at 10 K. For very low temperatures, similar recoil-free fractions for the two oxidation states approaching unity are expected, giving the best estimation of the true ratios. In [145], $\text{Fe}^{\text{III}}/\text{Fe}^{\text{II}} = 1$ is assumed to be true at 10 K but no further measurements were undertaken to prove this statement. By increasing the temperatures, the area attributed to the Fe^{III} species increased more strongly than that for the Fe^{II} species. A correction factor of 1.125(68) for the Fe^{III} content was suggested and the areas of the Fe^{II} species determined from the Mössbauer measurements would have to be multiplied by this factor. Others have reported that the room temperature $\text{Fe}^{\text{III}}/\text{Fe}^{\text{II}}$ ratio determined by Mössbauer is the same as was determined chemically while at the same time stating that the latter method is erroneous. [146] In this work, the given ratios are taken directly from the areas in the Mössbauer experiment.

Here, three samples with differing synthetic routes, as given in Table 3.5, resulting in different elemental compositions are investigated via Mössbauer spectroscopy. An alternative method to determine the ratios of the four different iron species, namely Fe^{II} in mackinawite-like layers, Fe^{III} in mackinawite-like layers, Fe^{II} in brucite-like layers and Fe^{III} in brucite-like layers, ICP-AES was used and the determined values are given in

Table 3.6. This analysis was done by assuming that all atoms other than iron are in their typical oxidation states of -2 (O,S), $+1$ (H), $+2$ (Mg) and $+3$ (Al) while assuming that the iron compensates for the excess charge, giving it an average oxidation state between $+2$ and $+3$.

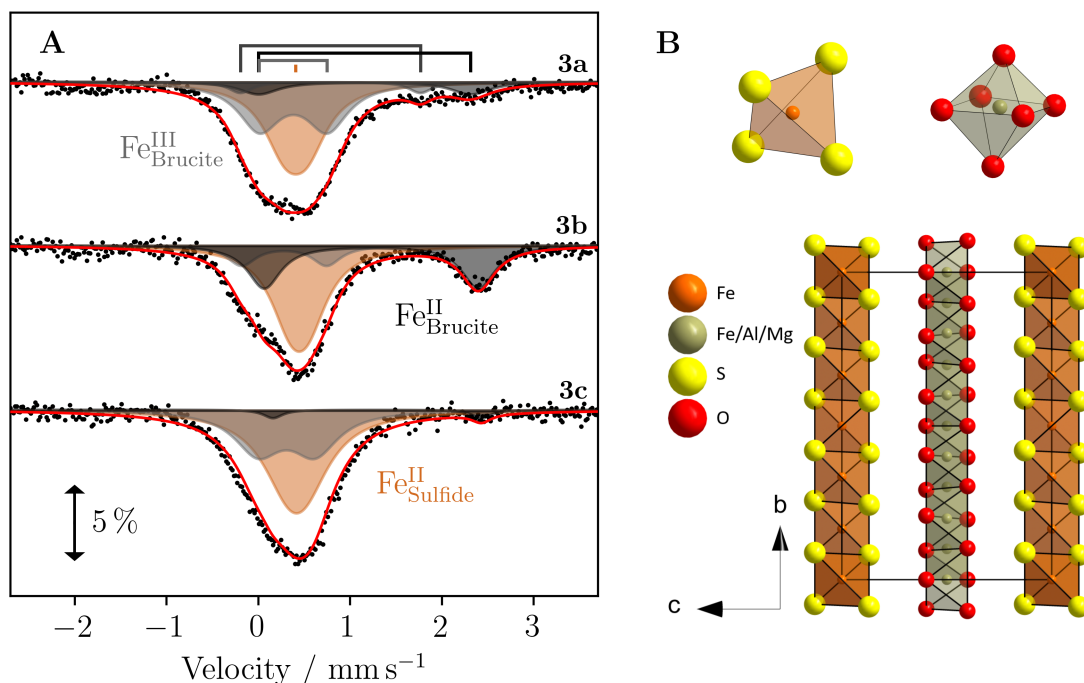


Figure 3.20: (A) Mössbauer data of samples **3a-c** measured at room temperature with the fit for Fe^{II} in $\frac{2}{\infty}\{[\text{FeS}_{4/4}]\}$ tetraheders (orange), Fe^{II} in $\frac{2}{\infty}\{[\text{Fe}(\text{OH})_{6/3}]\}$ octahedrons (dark grey) and Fe^{III} in $\frac{2}{\infty}\{[\text{Fe}(\text{OH})_{6/3}]^+\}$ octahedrons (grey). (B) Crystal structure of tochilinite taken from [141] with the two clearly distinguishable iron sulfide (mackinawite-like) and Fe/Al/Mg oxide (brucite-like) layers. Atoms are coloured as specified in the CPK colouring convention: iron (dark orange), sulfur (yellow), oxygen (red), varying atoms (grey). Hydrogen atoms are omitted for clarity.

The Mössbauer spectra of the three samples **3a-c** are shown in Figure 3.20A and the fit parameters are given in Table 3.6. They consist of at least three sets of signals, all of which are split into two lines by the quadrupole splitting.

For mackinawite, which is purely composed of iron sulfide layers, only one of these signals is observed, i.e. a single line centred at 0.2 mm s^{-1} at 4.2 K. [147] For synthetic mackinawite an isomer shift of 0.37 mm s^{-1} was found at room temperature. [32, 148, 149] Due to the line being split by exactly the strength of an applied magnetic field, it was concluded that there is no internal magnetic field in mackinawite, i.e. the iron atoms must be in a low-spin ($S = 0$) state or the d electrons must be delocalised in the Fe-Fe plane [147]. In tetrahedral symmetry an intermediate-spin ($S = 1$) or high-spin ($S = 2$)

state seem more likely although Jahn-Teller distortion might stabilise the low-spin state. Others have suggested that the absence of the internal field results from itinerant spin fluctuations. [150] The slightly higher isomer shifts observed for the iron atoms in the mackinawite-like layer in tochilinite compared to those in pure mackinawite might arise from an expansion of the unit cell [151] or the iron deficiency in the tetraeders, which leads to different Fe-S distances, thereby influencing the isomer shift. [142]

The second set of signals, i.e. the lines which are split by $\Delta E_Q > 1.9 \text{ mm s}^{-1}$, can be attributed to Fe^{II} in the brucite-like layers. The observed isomer shift and quadrupole splitting of Fe^{II} in both layers fit well to literature values for tochilinite of 0.45(1), 1.12(1) and 0.87(2) mm s^{-1} for the isomer shifts and 0.16(2), 2.38(2) and 1.88(4) mm s^{-1} for the quadrupole splittings in the sulfide layer and the two different species in the brucite-like layer, respectively. [152] This still leaves some of the signals unassigned, i.e. those labelled $\text{Fe}_{\text{Brucite}}^{\text{III}}$ in Table 3.6.

As was already mentioned, a result of the iron deficiency in the sulfide layers is that some of the iron in the brucite-like layers must be Fe^{III} to compensate the negative charge. For higher oxidation states, lower isomer shifts are expected, see Section 2.2.7. As a result of that, Fe^{III} usually has a lower isomer shift than Fe^{II} but for both oxidation states the isomer shift increases with the spin state.

Table 3.6: Fit parameters for the Mössbauer measurements shown in Figure 3.20 for the different iron species. The errors in the isomer shift δ_{IS} , the quadrupole splitting ΔE_Q , the linewidth Γ and the molar fraction x_{MB} are given by MossWinn. The error for the molar fraction x_{EA} that was determined by elemental analysis is estimated.

		$\delta_{\text{IS}} / \text{mm s}^{-1}$	$\Delta E_Q / \text{mm s}^{-1}$	$\Gamma / \text{mm s}^{-1}$	$x_{\text{EA}} / \%$	$x_{\text{MB}} / \%$
3a	$\text{Fe}_{\text{Sulfide}}^{\text{II}}$	0.41(1)	0.24(4)	0.56(9)	50(5)	46(5)
	$\text{Fe}_{\text{Brucite},1}^{\text{II}}$	1.16(2)	2.31(3)	0.53(5)	5(5)	10(3)
	$\text{Fe}_{\text{Brucite},2}^{\text{II}}$	0.79(2)	1.96(3)	0.32(5)	5(5)	5(3)
	$\text{Fe}_{\text{Brucite}}^{\text{III}}$	0.38(5)	0.74(5)	0.55(4)	45(5)	38(5)
3b	$\text{Fe}_{\text{Sulfide}}^{\text{II}}$	0.45(1)	0.19(1)	0.54(4)	58(5)	55(5)
	$\text{Fe}_{\text{Brucite}}^{\text{II}}$	1.23(2)	2.33(4)	0.44(2)	40(5)	32(5)
	$\text{Fe}_{\text{Brucite}}^{\text{III}}$	0.28(1)	0.93(3)	0.38(4)	2(5)	13(5)
3c	$\text{Fe}_{\text{Sulfide}}^{\text{II}}$	0.42(1)	0.18(2)	0.70(5)	69(5)	59(5)
	$\text{Fe}_{\text{Brucite}}^{\text{II}}$	1.30(3)	2.27(5)	0.26(7)	2(5)	3(3)
	$\text{Fe}_{\text{Brucite}}^{\text{III}}$	0.31(1)	0.63(3)	0.62(3)	29(5)	38(5)

The best fit for all three measurements in Figure 3.20 is obtained by adding a further quadrupole split signal on top of the two or three signals that have been discussed so

far. These signals have isomer shifts of $\approx 0.3 \text{ mm s}^{-1}$ and quadrupole splittings of $\approx 0.6 - 0.9 \text{ mm s}^{-1}$. Fe^{III} in hydroxide octahedrons in the brucite-like layers of Valleriite shows isomer shifts of $0.36(1) \text{ mm s}^{-1}$ and quadrupole splittings of $0.62(2) \text{ mm s}^{-1}$. [152] The quadrupole splittings reported here are slightly higher, which might arise from a slight distortion of the octahedrons in tochilinite compared to valleriite but the assignment is still valid.

In comparison, a singlet centred in the range of $0.3\text{-}0.5 \text{ mm s}^{-1}$ would be expected for high-spin ($S = 5/2$) Fe^{III} , i.e. the $\text{Fe}_{\text{Brucite}}^{\text{III}}$ species must be in the low-spin state. [79, 152, 153] In octahedral sites there should be a significant quadrupole splitting for low-spin Fe^{III} , due to the non-isotropic distribution of electron density in the d orbitals around the nucleus, showing that the Fe^{III} cannot be in the mackinawite-like layer.

It was shown that the three synthetic tochilinite samples are composed of different amounts of Fe^{II} and Fe^{III} in tetrahedral and octahedral sites by comparing carefully to literature known substances. This helps in identifying the compounds that were synthesised in a completely new way, allowing for a better understanding of the formation of this type of material both in a laboratory and in nature.

3.5.3 Temperature-Induced Spin Crossover

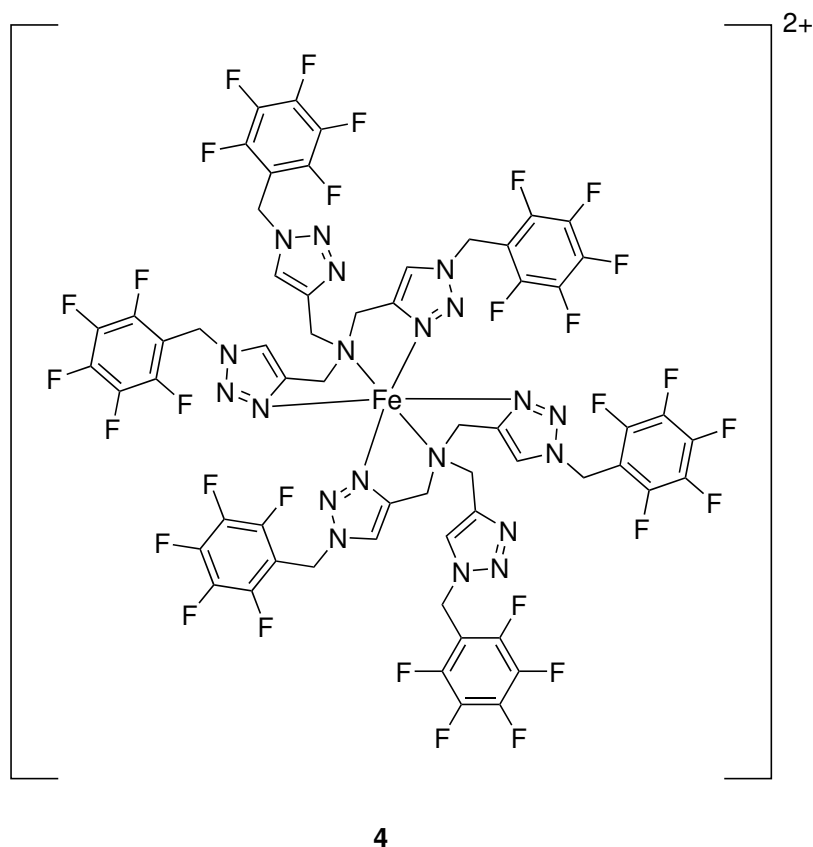
The work presented in this subsection was performed in close cooperation with Maite Nößler (Freie Universität Berlin) who synthesised the compounds and David Hunger (Universität Stuttgart, group of J. van Slageren) and Felix Reichert (Universität Stuttgart, group of J. van Slageren, under the supervision of the author of this thesis) who did the magnetometric investigations of the samples and helped with the Mössbauer measurements. The results of this chapter were published in [154].

Spin crossover, i.e. the gradual transition of a compound from a low-spin to a high-spin state by increasing the temperature, has been known since the 1930s [155] and was further investigated for cobalt and iron complexes in the 1960s [156] where magnetometry and Mössbauer spectroscopy were some of the first tools to explain the phenomenon [157].

More recently the research of spin crossover complexes was directed towards a wide range of possible applications [158] where supramolecular spin crossover materials are considered as candidates for data storage, sensors and molecular switches due to their predictable behaviour. [159] A recent highlight is addressing such particles on a surface by scanning tunneling microscopy, i.e. reading the spin state of molecules adsorbed on the surface, further paving the way for the usage of the phenomenon in applications. [160]

As was mentioned in the previous section, Mössbauer spectroscopy is a great tool to investigate the changes of the spin state on the iron atom as a result of external stimuli,

e.g. by changes in temperature or pressure as well as through irradiation with light. In this section, spin transitions of the iron compound **4** are investigated in a temperature range from 80 K to room temperature. The chemical structure is given in scheme 3, where the positive charge is compensated by two $[\text{BF}_4]^-$ anions.



Scheme 3

The Mössbauer measurement of **4** is shown in Figure 3.21. A spin crossover is clearly visible through the appearance of a second set of lines when going down in temperature. Between 170 K and 240 K both the high-spin species, depicted in blue, and the low-spin species, depicted in green, coexist.

The high-spin molar fraction x_{HS} was determined from the ratio of the areas of the fits for the two spin species and the result is shown in Figure 3.21B. As the recoil-free fraction of the two species is not necessarily the same and the low signal-to-noise ratio gives an uncertainty in the fits, a rather large error for x_{HS} was estimated. It was shown by Slichter and Drickamer in [161] that the high-spin molar fraction can be calculated from the equilibrium condition $\left(\frac{\partial G}{\partial x_{\text{HS}}}\right)_{p,T} = 0$ with the enthalpy and entropy changes for

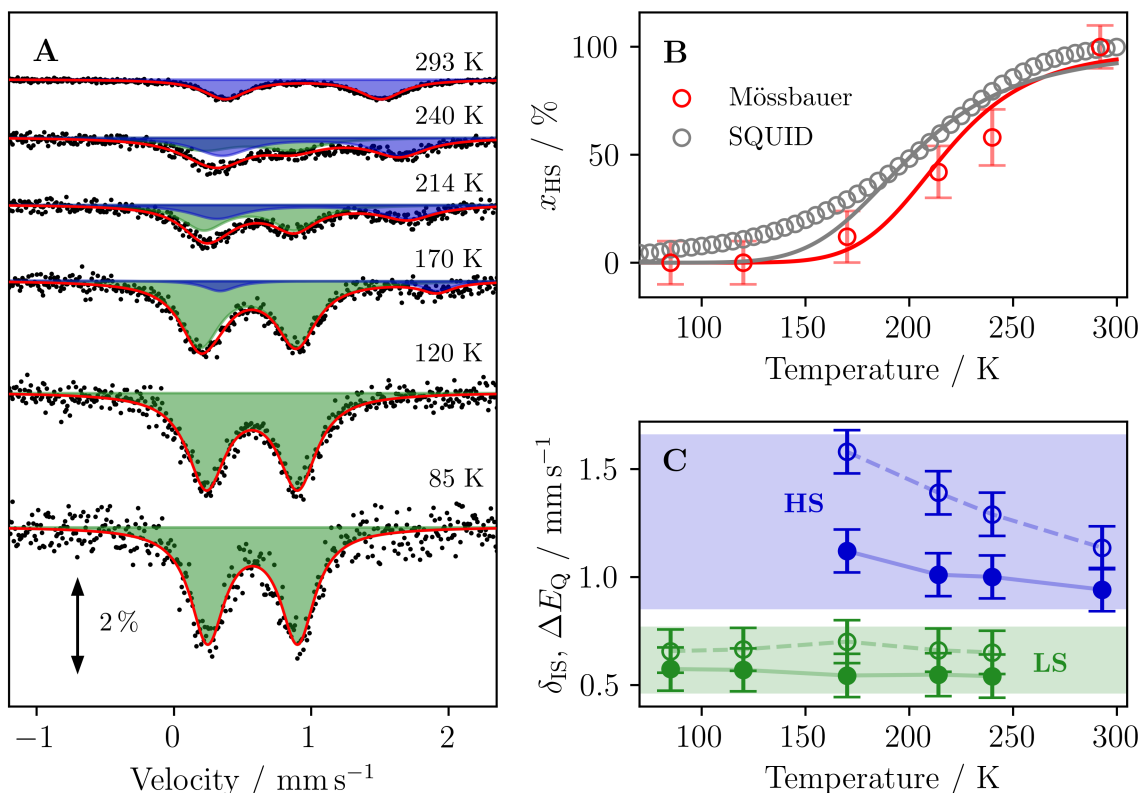


Figure 3.21: (A) Mössbauer measurements of **4** at different temperatures where a spin crossover is clearly visible. (B) High-spin molar fractions as determined from Mössbauer spectroscopy (red) and SQUID magnetometry (grey) versus the temperature fitted with equation (3.8). (C) Temperature dependence of the isomer shift (solid lines, filled circles) and quadrupole splitting (dashed lines, open circles).

the transition ΔH and ΔS , respectively, to

$$\ln\left(\frac{1-x_{\text{HS}}}{x_{\text{HS}}}\right) = \frac{\Delta H + \Gamma_{\text{SD}}(1-2x_{\text{HS}})}{k_{\text{B}}N_{\text{A}}T} - \frac{\Delta S}{k_{\text{B}}N_{\text{A}}} \quad (3.8)$$

with the cooperativity Γ_{SD} . The phenomenological parameter Γ_{SD} describes how strongly the individual molecules interact. Positive values indicate that a spin can decrease its energy by undergoing a spin transition to the majority spin state, i.e. the spin crossover becomes abrupt for large positive values. For negative values of Γ_{SD} a more gradual spin crossover is observed. More specifically, if $\Gamma_{\text{SD}} < 2RT_{1/2}$, where $T_{1/2}$ is the temperature for which $x_{\text{HS}} = 0.5$, the spin conversion is gradual, for $\Gamma_{\text{SD}} = 2RT_{1/2}$ the transition is abrupt and in the case $\Gamma_{\text{SD}} > 2RT_{1/2}$ the transition shows temperature hysteresis. [162] Compounds with $\Gamma_{\text{SD}} < 0$ are labelled antiferromagnetic and show a gentle rise of the high-spin

molar fraction. [163] In literature, values up to 5 kJ mol^{-1} have been reported for Γ_{SD} . [163–165]

Other models that describe the spin crossover behaviour also exist, such as the Sorai and Seki model (assumes regions of molecules of the same spin-state) [166], the Ising-like model (takes the degenerate energy levels in a new Hamiltonian into account) [167] and the atom-phonon coupling model (extension of the Sorai and Seki model that tries to explain the origin of the interaction parameter) [168, 169]. A brief overview of all models is given in [170].

The red line in Figure 3.21B results from a fit of the data in the mentioned fashion, i.e. by calculating the left side of equation (3.9) for Γ_{SD} in the range from -10 to 10 kJ mol^{-1} , giving an array of values for each Γ_{SD} . All of these data sets were plotted against the temperature and fit with a line. The covariance in the fit parameters was the smallest for $\Gamma_{\text{SD}} = 0 \text{ kJ mol}^{-1}$, which shows that the molecules do not interact with each other. This also gives $\Delta H = 18(2) \text{ kJ mol}^{-1}$ and $\Delta S = 83(13) \text{ J K}^{-1} \text{ mol}^{-1}$. $x_{\text{HS,Fit}}$ can then be determined by finding the value for which equation (3.9) holds true with the obtained parameters, e.g. by bringing everything on one side of the equation and finding the zero crossings for each temperature.

$$k_{\text{B}}N_{\text{A}}T \ln \left(\frac{1 - x_{\text{HS}}}{x_{\text{HS}}} \right) - \Gamma_{\text{SD}}(1 - 2x_{\text{HS}}) = \Delta H - T\Delta S \quad (3.9)$$

The small value for the cooperativity is expected for intermolecular distances $> 3.5 \text{ \AA}$ or when solvent molecules hinder the required intermolecular interaction. [171] For stronger intermolecular interactions, i.e. larger values for Γ_{SD} , the spin crossover would happen in a tighter temperature range.

This data fits to the published high-spin molar fractions determined from magnetic susceptibility measurements, see Figure 3.21, where the high-spin molar fraction is slightly higher than that determined from the Mössbauer measurements. [154] This may be because the recoil-free fraction of high-spin Fe^{II} is slightly lower than that of low-spin Fe^{II} . [172]

The high-spin fraction shows high isomer shifts and quadrupole splittings, where the latter show a strong increase for lower temperatures. The low-spin fraction shows much lower values for both the isomer shift and quadrupole splitting where neither shows a clear temperature dependence, see figure 3.21C. This behaviour is also observed in literature. The quadrupole splitting in low-spin iron(II) compounds ($S = 0$) is usually $\Delta E_{\text{Q}} < 0.8 \text{ mm s}^{-1}$ [138, 139, 173–175] and shows no temperature dependence [138, 139] while high-spin compounds show much higher quadrupole splittings and a stronger tem-

Table 3.7: Fit parameters for the measurements depicted in figure 3.21. The errors given for the high-spin molar fraction x_{HS} are the sum of the error given by MossWinn and an additional five percentage points resulting from the poor resolution of the data.

T / K	High-Spin Fraction		Low-Spin Fraction		$x_{\text{HS}} / \%$
	$\delta_{\text{IS}} / \text{mm s}^{-1}$	$\Delta E_{\text{Q}} / \text{mm s}^{-1}$	$\delta_{\text{IS}} / \text{mm s}^{-1}$	$\Delta E_{\text{Q}} / \text{mm s}^{-1}$	
292	0.941(2)	1.135(3)	-	-	100(5)
240	1.00(1)	1.29(2)	0.54(1)	0.65(3)	58(8)
214	1.01(1)	1.39(3)	0.547(7)	0.66(2)	42(7)
170	1.12(1)	1.58(3)	0.543(3)	0.700(5)	12(7)
120	-	-	0.569(2)	0.664(5)	0(5)
85	-	-	0.573(3)	0.656(6)	0(5)

perature dependence of the same [95]. The temperature dependence of the isomer shift can be explained by the second-order Doppler shift.

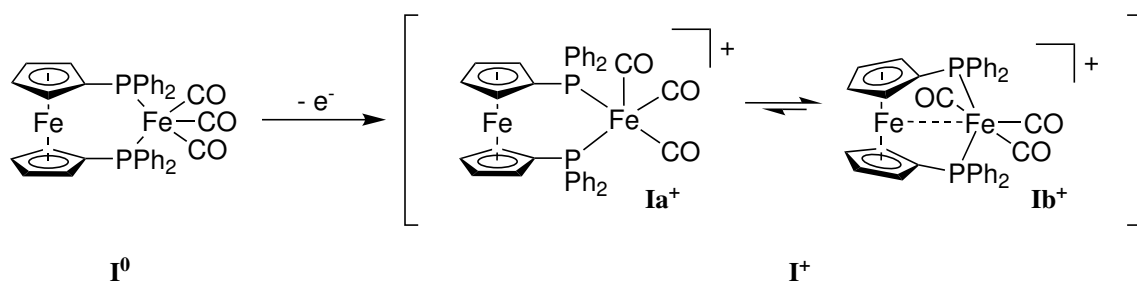
It was shown that the investigated sample shows a clear Fe^{II} spin crossover in the temperature range from 80 to 290 K without significant cooperativity.

4 The Electronic and Geometric Structure of a Probe Molecule

The results presented in this Chapter were obtained in close cooperation with Marc Schnierle (Universität Stuttgart, group of M.R. Ringenberg) who synthesised the samples, Felix Ehrlich (Universität Stuttgart, group of J. van Slageren, under the supervision of the author of this thesis) who measured the MCD spectra and helped with the analysis, Kim-Isabelle Mehnert (Universität Stuttgart, group of J. van Slageren, under the supervision of the author of this thesis) who helped with the measurements and analysis of the Mössbauer spectra, Alena M. Sheveleva (University of Manchester, group of F. Tuna) who carried out the ENDOR and HYSCORE measurements and Lukas Burkhardt (Universität Paderborn, group of M. Bauer) who performed the X-Ray measurements. The results have been published in [176].

Depletion of resources and the search for alternative fuels have driven research towards finding better and cheaper catalysts. Nature has been using iron as a catalyst due to its bioavailability even in the early days of the earth. To this day bimetallic complexes, e.g. in [FeFe] hydrogenase, play an important role in nature and consequently iron complexes have been used as catalytic species in the current research, where humankind is trying to imitate nature. [177–179] Self-evidently, iron is becoming one of the most heavily studied transition metals as the active site in catalytic systems. [180–185] Non-innocent ligands, such as CO and CN^- , facilitate rapid charge distribution away from and to the active site, thereby allowing for multielectron transfer reactions. Charge separation processes are important in reactions with small molecules, e.g. H_2 and O_2 .

Another concept that is used in nature is the confinement of all reaction partners and the catalysts, as is the case in enzymes. There, the reagent only fits into the structure of the part of the enzyme where the active site is located, which drastically increases the selectivity of the reaction. Such confinement effects can be mimicked by using porous structures, where the pore size influences the activity and selectivity. [10] Although it is possible to simply have both the reagents and the catalyst in the pores, it is advantageous to chemically immobilise the catalyst to force the reaction to take place in the pores, for a higher reproducibility and the possibility to selectively add co-catalysts in close vicinity to the active species. This means that the catalyst of interest must allow for an easy modification to enable the chemical immobilisation, e.g. via click chemistry.



Scheme 4: Chemical structure of the probe molecule in its neutral state and for both isomers in the oxidised form.

All of the mentioned aspects make the molecule $(\text{dppf})\text{Fe}(\text{CO})_3$ (\mathbf{I}^0 , $\text{dppf} = 1,1'$ -Bis(diphenylphosphino)ferrocene), see Scheme 4 and Figure A.4, a potential candidate for the catalysis of the hydrogen evolution reaction (HER, $2 \text{H}^+ + 2 \text{e}^- \rightarrow \text{H}_2$) both inside and outside of a pore. The ferrocene moiety allows for the functionalisation of the compound with an alkyne or azide group to enable the click reaction to immobilise the catalyst. Furthermore, the molecule possesses many spectroscopic handles, allowing for a multitechnique investigation of the behaviour of the catalyst both inside and of the pores. The paramagnetic state of the oxidised species allows for advanced magnetic resonance methods, the presence of iron atoms allows for the investigation with Mössbauer spectroscopy and the carbonyl ligands are a great marker to observe changes involving the carbonyl iron atom.

The first aim of the Thesis project was the chemical immobilisation of the probe molecule \mathbf{I} in mesopores via click reaction to investigate the behaviour of the immobilised catalyst. To achieve this goal, a high catalytic activity of the molecule is not important as it only acts as a probe molecule to investigate the influence of the immobilisation and interactions with the porous framework. For the immobilisation the molecule was planned to be functionalised at the ferrocene ring to attach an alkyne group to allow the attachment into azide-functionalised pores. To this end we first need to understand the parent compound, where the interplay of the catalytic activity and the electronic structure of the compound are of interest, making it the other of the two main research goals in this Chapter. As the HER involves both the neutral and the oxidised form of the catalyst, in this Chapter both species are investigated. To do so, multiple experimental techniques that give information on the electronic and geometric structure, e.g. magnetic circular dichroism (MCD), X-Ray emission (XES), Mössbauer and electron paramagnetic resonance (EPR) spectroscopies as well as SQUID magnetometry are used to investigate \mathbf{I} and the open-shell oxidised species \mathbf{I}^+ ($\text{BAr}_4^{\text{F}-}$) ($\text{BAr}_4^{\text{F}-} = \text{tetrakis}(3,5-$

bis(trifluoromethyl)phenyl)borate).

Preliminary results published in [12] indicate the formation of two isomers through oxidation, as observed via EPR. They show a temperature dependent ratio with the Mössbauer spectrum indicating the presence of only two different iron species at 80 K. This behaviour was not further investigated. Infrared spectroscopy shows an increase of energy of the CO vibrations, suggesting that the oxidation takes place on the carbonyl iron. In the following a more complete investigation of the molecule with respect to its electronic and geometric structure in regard to the immobilisation into mesoporous structures is presented. The previous results are expanded with those obtained from pulsed EPR, MCD and X-ray spectroscopies as well as SQUID magnetometry.

4.1 Catalytic Behaviour of the Iron Compound

The catalytic activity of the probe molecule **I** for the hydrogen evolution reaction



can be determined from cyclic voltammetry measurements when adding a proton source, i.e. a strong acid. The voltammograms are shown in Figure 4.1A.

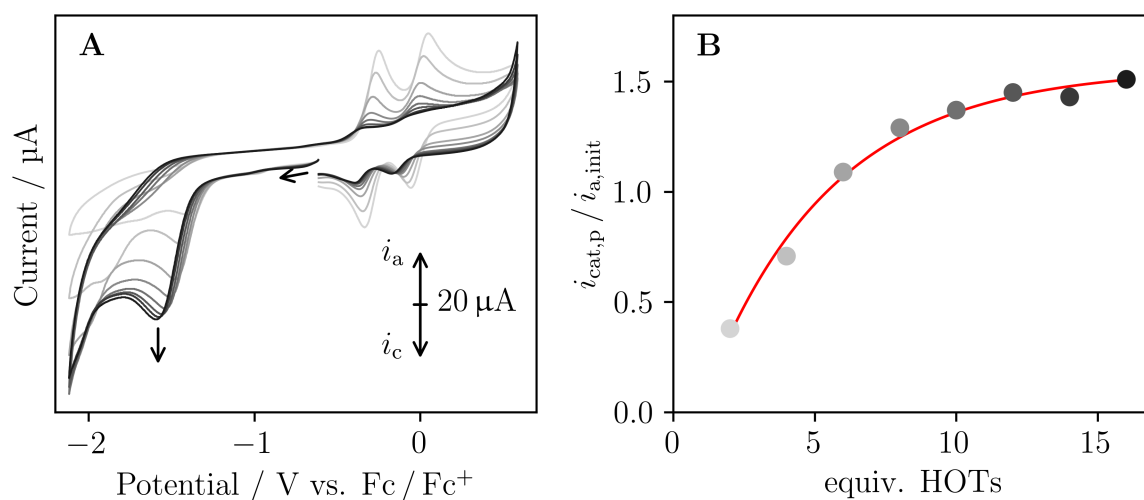


Figure 4.1: A) Cyclic voltammetry measurements of **I** with increasing amounts of *p*-toluenesulfonic acid (HOTs). B) Ratio of the catalytic and initial currents as a function of the amount of added HOTs. The red line is intended only as a guide.

The initial measurement, i.e. before adding *p*-toluenesulfonic acid (HOTs), shows an irreversible anodic wave at +0.5 V which is attributed to the oxidation of the dppf ligand.

By adding HOTs, a new reduction wave at -1.6 V appears that monotonically increases with the number of HOTs equivalents, see Figure 4.1B. It is attributed to the catalytic proton reduction. Simultaneously, a decrease of the peak currents of the previously present anodic oxidation waves can be observed. The rate constant k of the hydrogen evolution reaction can be calculated from this data with Equation 4.1 with the universal gas constant R , the temperature T , the Faraday constant F and the scan rate v . [186] The constant 4.481 results from the numerical solution of the diffusion equations and the number of electrons that are involved in the process.

$$\frac{i_{\text{cat,p}}}{i_{\text{a,init}}} = 4.481 \sqrt{\frac{RTk}{Fv}} \quad (4.1)$$

With the catalytic peak current $i_{\text{cat,p}}$ at a potential of ca. -1.6 V and the peak current of the initial oxidation wave $i_{\text{a,init}}$ at a potential of ca. -0.2 V the rate constant can be calculated to be $k_{\text{I}} \approx 0.5 \text{ s}^{-1}$. In comparison, much higher rates are achieved for the hydrogen evolution reaction, both in nature, $k_{[\text{FeFe}] \text{ hydrogenase}} \approx 700 \text{ s}^{-1}$ [187], and for molecular systems, $k_{[\text{Ni}(\text{PPh}_2\text{N}^{\text{Ph}})_2](\text{BF}_4)_2} \approx 33000 \text{ s}^{-1}$ [188].

Although the observed rate is very slow, it proves that the complex can be used as a catalyst for production of hydrogen. In order to design better catalysts it is important to understand the interplay of the electronic and geometric structure and the catalytic activity of the compound. In the following sections, a multitechnique experimental study of the neutral and oxidised species of **I** is presented.

4.2 Magnetic Circular Dichroism Spectroscopy

In addition to UV/Vis spectroscopy, magnetic circular dichroism (MCD) spectroscopy is a powerful tool to investigate the electronic structure of transition metal compounds. In the former, purely the absorption of light in the visible and ultraviolet regions is measured, while in MCD the relative absorption of left and right circular polarised light in a magnetic field is the measured quantity. This makes the MCD effect a signed quantity, thereby increasing the effective resolution. The transitions that can be observed in an MCD spectrum arise from the different mechanisms (A -, B - and C -terms), see also Section 2.2.4. C -terms only exist in paramagnetic compounds and are typically of much stronger intensity than the other terms at low temperatures and strong applied magnetic fields, making MCD spectroscopy especially powerful for open-shell systems.

The MCD spectrum of the diamagnetic compound **I**⁰ is shown in Figure 4.2. It shows two signals of opposite sign in the region around 27000 cm^{-1} (Figure 4.2A, Table 4.1).

In order to determine the origin of these signals, spectra at variable temperature (Figure 4.2C) and applied magnetic field (Figure 4.2D) were measured.

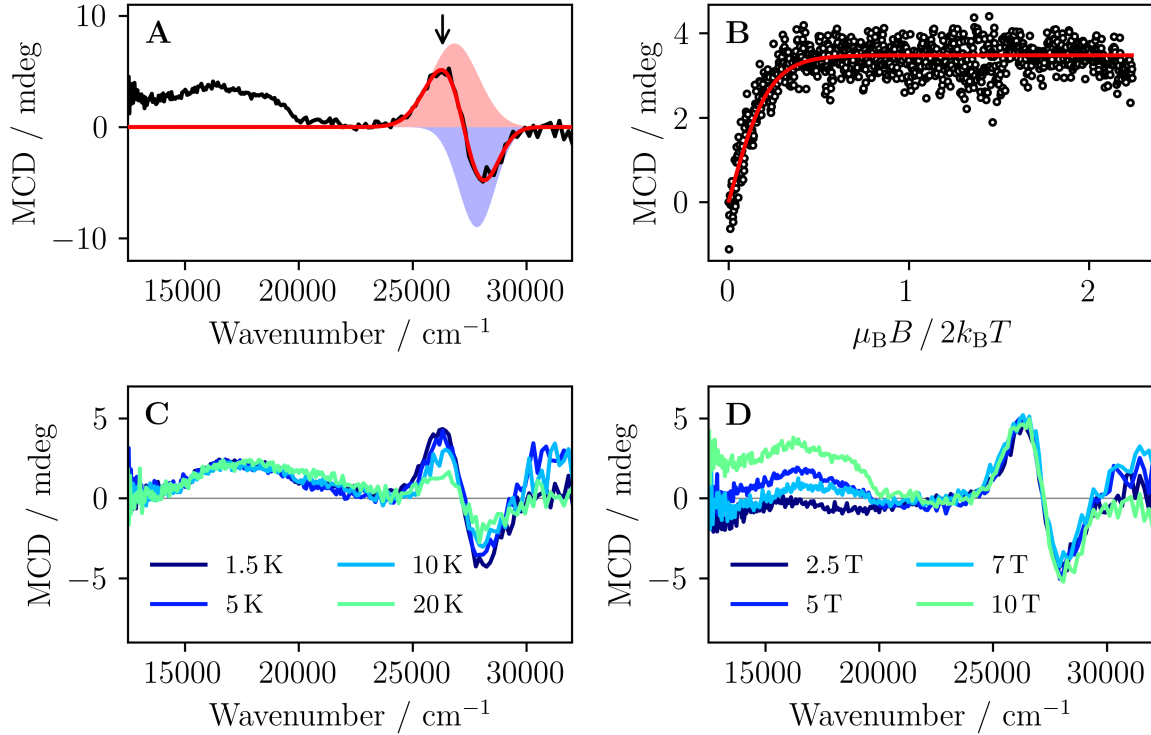


Figure 4.2: A) MCD spectrum of **I** in Fluorolube measured at 1.5 K and 10 T with the spectral fit shown in red. B) MCD intensity as measured during a magnetic field sweep at a wavelength of 380 nm up to 10 T and back to zero field at 1.5 K in units of the reduced magnetic field B/T with the best fit (see Equation (4.2), $S = 5/2$, $g_{\text{iso}} = 2.0$, $T = 2.2$ K). C) Variable temperature MCD spectra at 5 T. D) Variable field MCD spectra at 1.5 K.

Since only signals arising from C terms show a temperature and field dependence and both signals show a clear increase in intensity for lower temperatures, it was concluded that indeed a non-degenerate ground state must exist, i.e. the signals must arise from a C -term. The fact that no field dependence is observed can be explained with the field sweep from 0 to 10 T shown in Figure 4.2B measured at 1.5 K and a wavelength of 380 nm. At applied fields $B > 2$ T the signal intensity reaches a plateau and no change in the spectra is expected for these magnetic fields. By fitting the signal intensity with Equation 4.2 the spin of the system can be determined. [189] This function is applicable for $S > 1/2$ systems with small zero-field splitting and $S = 1/2$ systems.

$$\Delta A = h\nu K \left[\frac{2S+1}{2S} \coth\left(\frac{(2S+1)g\mu_B B}{k_B T}\right) - \frac{1}{2S} \coth\left(\frac{g\mu_B B}{k_B T}\right) \right] \quad (4.2)$$

For the signal in the MCD spectrum of \mathbf{I}^0 a spin $S = 5/2$ was determined that can be attributed to a high-spin Fe^{III} impurity. Although the temperature was set to 1.5 K at the sample holder, a temperature of 2.2 K was necessary in the fit, likely resulting from a heating of the sample by constant irradiation during the experiment.

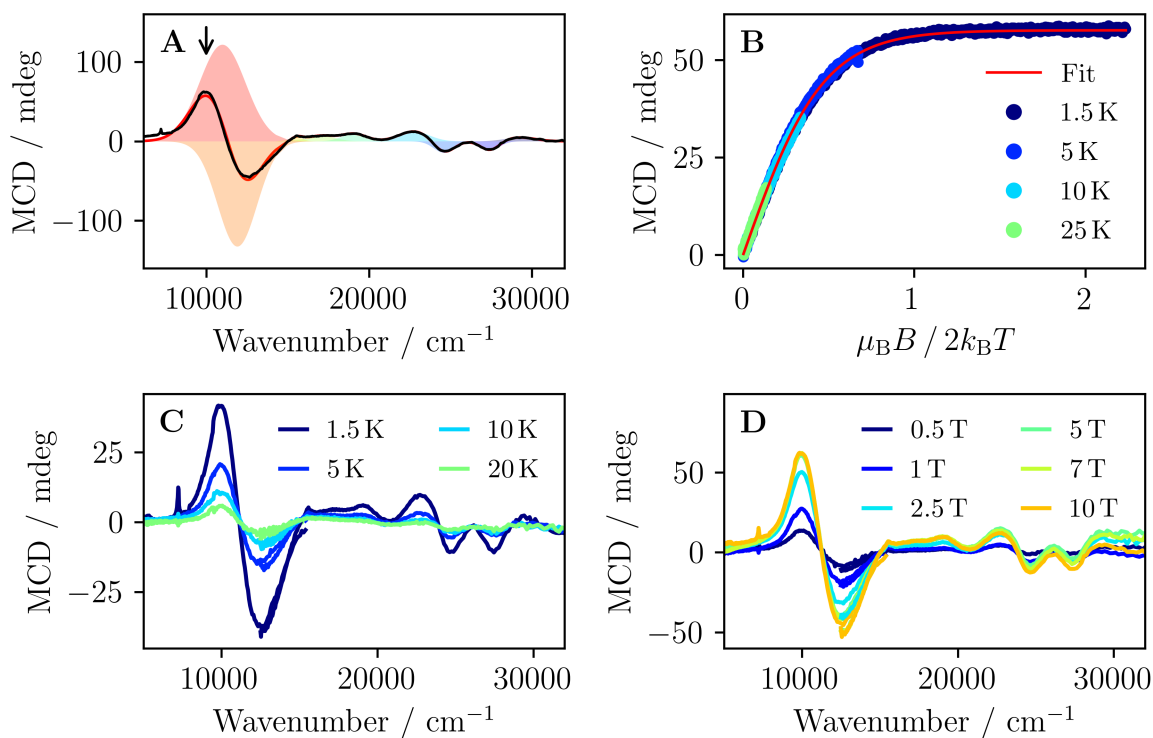


Figure 4.3: A) MCD spectrum of \mathbf{I}^+ in Fluorolube at 1.5 K and 10 T with the spectral fit shown in red. B) MCD intensity as a function of the ratio of Zeeman to thermal energy at different temperatures as indicated in the Figure between 0 and 10 T with the best fit (see Equation (4.2), $S = 1/2$, $g_{\text{iso}} = 2.02$, $T = 2.8 \text{ K}$). C) Variable temperature MCD spectra measured at 2.5 T. D) Variable field spectra measured at 1.5 K.

In contrast, the MCD spectrum of \mathbf{I}^+ shows both a higher number of signals and a higher overall signal intensity. Figure 4.3 shows two intense signals of opposite sign in the near infra-red region at $\tilde{\nu} \approx 10000 \text{ cm}^{-1}$ and weaker signals in the visible range (Table 4.1). Signals at energies similar to those of the former features were previously observed in UV/vis/NIR spectroelectrochemistry and an assignment to a metal-to-metal charge transfer transition was based on time-dependent DFT calculations. [12] These calculations revealed that the electron density is transferred from the ferrocene iron to the carbonyl iron, making it an intervalence charge transfer. This agrees with the expectation that metal-based transitions show higher MCD intensities than ligand-centred transitions. The fit of the field-sweep strongly suggests the spin to be $S = 1/2$ without significant spin-

spin interactions (Figure 4.3B) and the variable temperature (Figure 4.3C) and variable field (Figure 4.3D) spectra prove that all observed signals arise from C -terms due to their temperature and field dependence.

In order to confirm the preliminary results of the oxidation locus to be on the carbonyl iron, the Fe^{III} compound $[\text{Fc}]^+(\text{BAr}_4^{\text{F}})^-$ was measured for comparison. The spectrum shown in Figure 4.4 is vastly different from those of I^0 and I^+ . It displays an intense signal with a fine structure due to vibronic coupling to the totally symmetric metal-ligand vibration. [190] This transition that shows clear C -term like behaviour (Figure 4.4B and C) has previously been observed in MCD [191] and high-resolution matrix spectroscopy experiments [190, 192]. It was assigned to charge transfer from the π -orbitals of the cyclopentadienyl ring to the iron ion.

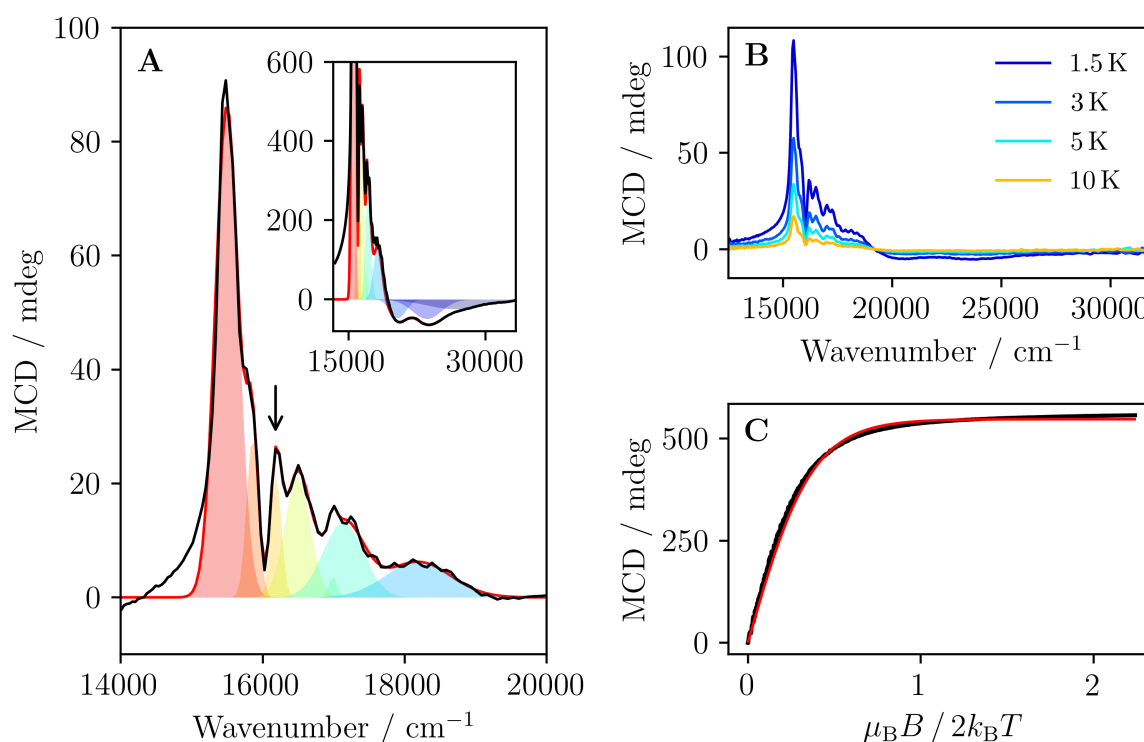


Figure 4.4: A) MCD spectrum of $[\text{Fc}]^+$ measured at 1.5 K and 0.1 T with the spectral fit shown in red. B) Variable temperature spectra measured at 0.1 T. C) Field sweep from 0 to 10 T at 16181 cm^{-1} with fit (see Equation (4.2), $S = 1/2$, $g_{\text{iso}} = 3.61$, $T = 4.0 \text{ K}$).

A comparison of all spectra is depicted in Figure 4.5 and all observed transitions are given in Table 4.1. It becomes clear that all spectra are qualitatively very different from each other, possibly confirming the preliminary result of the oxidation to take place on

the carbonyl iron, as mentioned in the introduction of this Chapter.

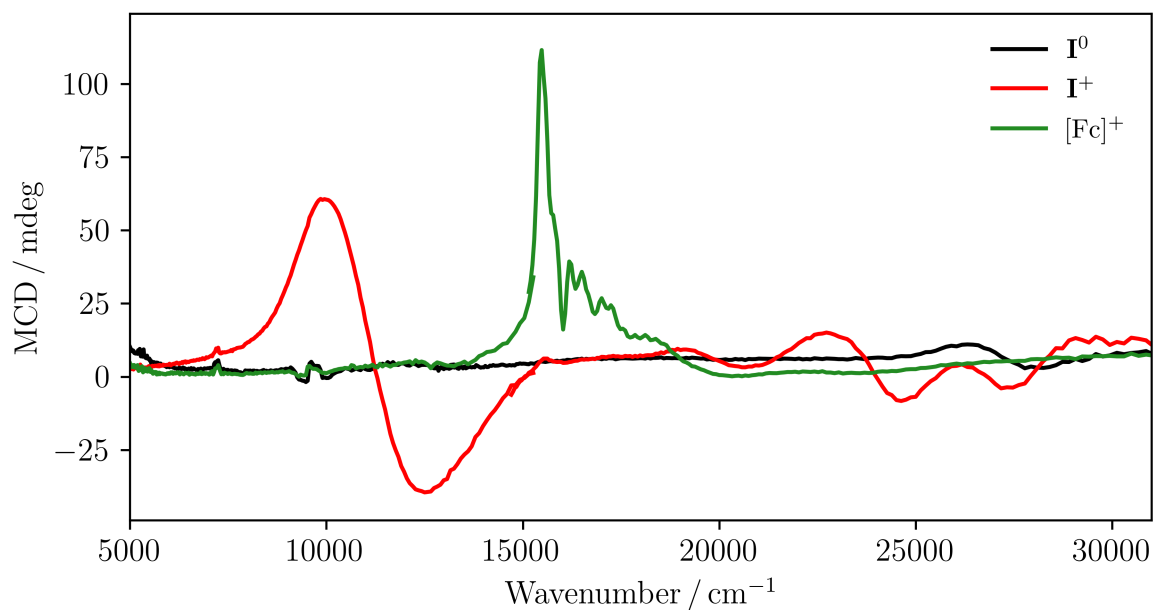


Figure 4.5: MCD spectra of \mathbf{I}^0 , \mathbf{I}^+ and $[\text{Fc}]^+$ measured in Fluorolube at 1.5 K and fields of 5 T (\mathbf{I}^0 and \mathbf{I}^+) and 0.1 T ($[\text{Fc}]^+$).

MCD spectra on low-spin Fe^{I} are rare, but spectra of $[\text{FeCl}(\text{PP})]$ with a diphosphino ligand have been reported. [193] For this compound, the signals in the NIR region were assigned to d-d transitions, making a comparison with compound \mathbf{I}^+ difficult, as the reported origin of the bands is different.

In conclusion the MCD spectra suggest the oxidation to take place on the carbonyl iron but further experiments were performed to confirm these results.

Table 4.1: Energies and signs of the observed transitions.

$\tilde{\nu}_{\mathbf{I}^0} / \text{cm}^{-1}$	$\tilde{\nu}_{\mathbf{I}^+} / \text{cm}^{-1}$	$\tilde{\nu}_{[\text{Fc}]^+} / \text{cm}^{-1}$
26832 (+)	10202 (+)	15496 (+)
27817 (−)	12196 (−)	15852 (+)
	15603 (+)	16186 (+)
	17010 (+)	16487 (+)
	19090 (+)	16985 (+)
	22768 (+)	17133 (+)
	24599 (−)	18186 (+)
	27421 (−)	20415 (−)
	29223 (+)	23574 (−)
		26686 (−)

4.3 X-Ray Absorption and Emission Spectroscopy

4.3.1 Core-to-Core and Valence-to-Core X-Ray Emission Spectroscopy

X-ray emission (XES) spectroscopy can give detailed knowledge about the electronic structure of molecules. The immediate surrounding of the central atom, i.e. bond lengths and coordination geometry can be investigated with X-ray absorption near edge structure (XANES) measurements. Compared to other methods, such as EPR, MCD and Mössbauer spectroscopy that primarily or exclusively probe the transition metal, XES can give more information on the ligand framework (by comparing the valence-to-core (VtC) spectra, that show high sensitivity to changes in the environment, to calculations, as was done in [194]) and the metal centre, especially for reaction intermediates. [195] In order to probe further from the central atom than the first coordination sphere, advanced pulsed magnetic resonance techniques such as ENDOR and ESEEM would be required but they are still limited to paramagnetic molecules and those nuclei that couple to the unpaired electron. In XES a 1s core electron is removed from the atom under investigation by high-energy X-rays and the photons emitted during the electron decay back to the empty 1s orbital are detected. The most prominent transitions found in transition metal complexes are explained in Section 2.2.5. Generally, the technique is subdivided into core-to-core (CtC) and valence-to-core XES, depending on whether the decaying electron stems from an orbital from the metal centre or one with predominantly ligand character. XES has been shown to be sensitive towards the spin and oxidation state of the metal as well as to the ligand identity, ligand ionization and the bond-lengths in the first coordination sphere

around the metal centre. [194]

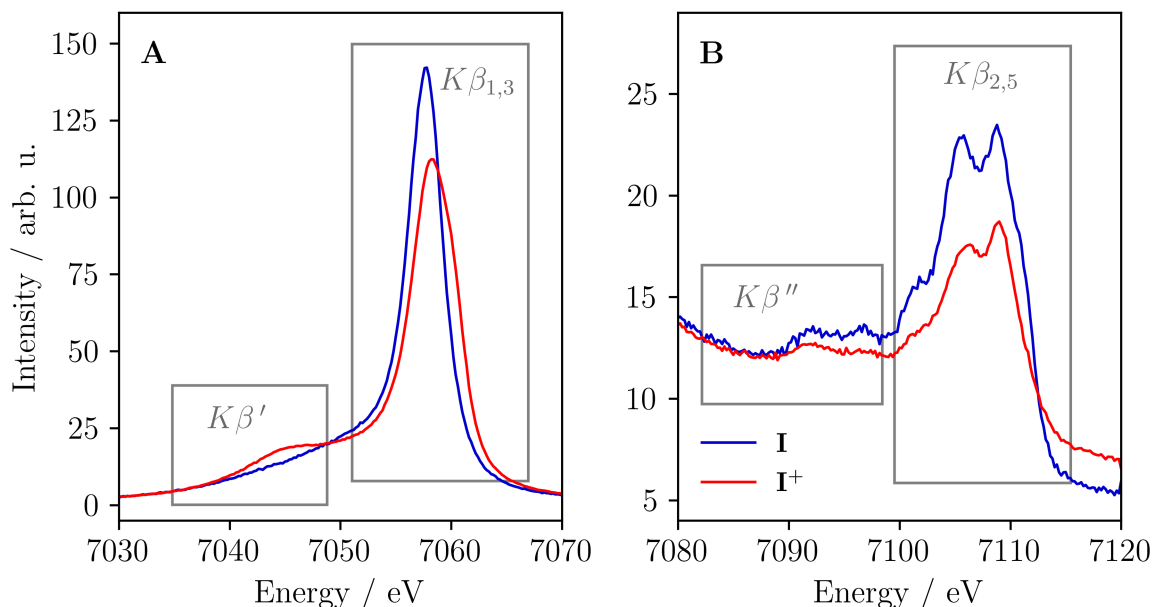


Figure 4.6: CtC (A) and VtC (B) regions of the XES spectrum of \mathbf{I}^0 and \mathbf{I}^+ .

The CtC and VtC XES spectra of powders of \mathbf{I}^0 and \mathbf{I}^+ are depicted in Figure 4.6. For both samples, the typical XES pattern is observed. The CtC region at lower energies (Figure 4.6A) shows an intense $K\beta_{1,3}$ mainline with a weaker shoulder at lower energies, the $K\beta'$ region. The increase of the splitting of the two lines as well as the increase in intensity of the latter in the oxidised species stems from the higher electron spin compared to the diamagnetic \mathbf{I}^0 . This can be explained with increased 3p-3d exchange interaction for higher electron spins, see Section 2.2.5. The appearance of the high-energy shoulder at ca. 7061 eV after oxidation could result from the formation of an Fe^{I} or Fe^{III} species in \mathbf{I}^+ but the HERFD-XANES spectrum measured at 7060.2 eV (see next Section) does not resemble that of either the Fe^{I} or Fe^{III} reference compound and rather that of the neutral compound \mathbf{I}^0 . Furthermore, the distance of the mainline in \mathbf{I}^0 and the shoulder in \mathbf{I}^+ is $\Delta E \approx 2.4$ eV, which is larger than the value reported for the system $\text{Fc}/[\text{Fc}]^+$, suggesting that the shoulder does not appear due to the formation of an Fe^{III} species. The shoulder may instead result from a slight shift of the transition energy in the ferrocene iron due to weak Fe-Fe interactions. This leads to the conclusion that the spin is not primarily located on the ferrocene iron in \mathbf{I}^+ , thereby backing the results from the MCD spectra of the oxidation to take place on the carbonyl iron.

The VtC region (Figure 4.6 (B)) shows a similar pattern as the CtC region, i.e. an

intense mainline and a weaker shoulder at lower energies. The main difference in the two spectra of \mathbf{I}^0 and \mathbf{I}^+ is the absence of the shoulder at 7111 eV in the oxidised species. Features at energies above 7110 eV typically arise from 3d-1s transitions while features below these energies are due to transitions from ligand orbitals that mix with iron 4p orbitals. [196] In the $\text{Fc}/[\text{Fc}]^+$ system the high-energy lines are missing due to the lack of 3d-4p hybridization in ferrocene. [197, 198] In comparison, iron carbonyls do show these hybridizations, again suggesting that the change in the XES spectra arises from a change on the iron carbonyl. Possibly, the lower 3d occupancy due to the electron withdrawing character of the CO ligands reduces the number of 3d-1s transitions, decreasing the intensity of the high-energy shoulder.

4.3.2 High Energy Resolution Fluorescence-Detected X-Ray Absorption Near Edge Structure

Another element-specific type of spectroscopy to determine the local electronic structure is X-ray absorption near-edge structure (XANES). By detecting the absorption spectrum indirectly via the intensity of the X-ray emission, the linewidth can be greatly reduced because the linewidth no longer depends on the short core hole lifetime, but on the lifetime of the valence hole. [199] This technique is called high energy resolution fluorescence detected XANES (HERFD-XANES). [200, 201] HERFD-XANES spectra of powders of \mathbf{I}^0 , \mathbf{I}^+ , $\text{Fe}_2(\text{CO})_9$ [202], $\text{FeBr}(\text{dpbz})$ ($\text{dpbz} = 1,2\text{-bis-(diphenylphosphino)-benzol}$) [203], dppf [198] and $[\text{Fc}]^+$ [198] are shown in Figure 4.7.

In HERFD-XANES the edge and pre-edge regions are of most interest. Here, the spectrum of \mathbf{I}^0 possesses a lot of similarities with $[\text{Fe}(\text{CpPPh}_2)_2]$ (dppf) with both showing an intense feature at ca. 7122 eV arising from 4p transitions. The pre-edge features at 7113.3 and 7115.0 eV can also be found in $\text{Fe}_2(\text{CO})_9$ and dppf , respectively. Also, no peak at 7111.6 eV, reported for dppf^+ , can be observed. [198] This confirms the oxidation states of the iron atoms in the diamagnetic \mathbf{I}^0 to be 0 and +2. The higher intensity of the pre-edge features of the two reference compounds can be explained by the higher relative iron concentration, leading to self-absorption effects.

The separation of the mainline in the CtC spectrum allows for site-selective measurements of the HERFD-XANES spectra. The spectrum measured at the low-energy shoulder shows an intense 4p feature in the edge region and two pre-edge signals. The latter were also observed for $[\text{Fc}]^+$ and derivatives of the same [197, 198] but also for $\text{FeBr}(\text{dpbz})$, a low-spin Fe^{I} compound [203]. While the spectrum measured at the low-energy shoulder does share similarities to both Fe^{I} and Fe^{III} species, the transition energies and intensities of the pre-edge and edge features are closer to those of the Fe^{I} compound. This observa-

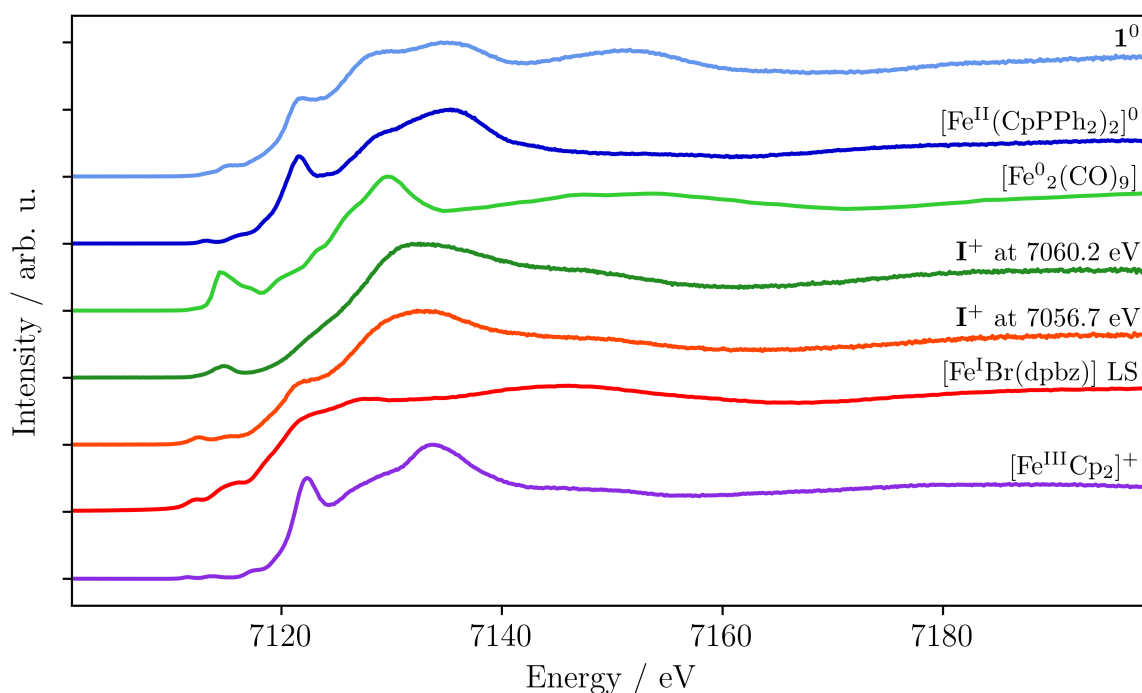


Figure 4.7: HERFD-XANES spectra of \mathbf{I}^0 , \mathbf{I}^+ and other iron compounds with known oxidation states ranging from 0 to +3. The spectra of \mathbf{I}^+ were measured at two different emission energies corresponding to the high- and low-energy sides of the CtC-XES mainline shown in Figure 4.6 (A).

tion also agrees with the conclusions drawn from the CtC and VtC spectra, namely that the oxidation takes place on the carbonyl iron, making it an Fe^{I} species. The spectrum measured on the high-energy side of the CtC mainline does not show close similarities to any of the spectra of the reference compounds. The pre-edge features are closest to those of the neutral compound \mathbf{I}^0 , suggesting that the oxidation does indeed only take place on one of the iron atoms and that a part of the spectrum and therefore the electronic structure remains unchanged.

X-ray absorption and emission spectroscopy thus confirms the results of the analysis from the MCD spectra that the oxidation takes place on the carbonyl iron.

4.4 Mössbauer Spectroscopy

Mössbauer spectroscopy is a great tool to investigate iron atoms and their immediate surroundings. It relies on the absorption of gamma rays by the ^{57}Fe nuclei in the sample. The isomer shift and quadrupole splitting, the two most important fit parameters, depend primarily on the oxidation state and symmetry of the charges surrounding the nucleus, see Section 2.2.7 for further details. This makes Mössbauer spectroscopy very

powerful for the determination of the oxidation locus and in distinguishing the two isomers introduced at the beginning of the Chapter and in Scheme 4. Furthermore, it allows for the measurement of spin-lattice relaxation rates on the order of the Mössbauer time scale, i.e. in the nanosecond regime. Due to a very fast relaxation of the paramagnetic moment without an applied magnetic field of many open-shell systems, other methods such as pulsed EPR spectroscopy and ac SQUID magnetometry do not allow the experimental determination of the zero-field relaxation behaviour of potential single-molecule magnets (SMMs). In this context, ferrocenium derivatives were named potential SMMs after studying of their relaxation behaviour with all of the given methods. [204] This is a further motivation to use Mössbauer spectroscopy in the study of the open-shell system \mathbf{I}^+ .

Mössbauer spectra of \mathbf{I}^0 , \mathbf{I}^+ and reference compounds with similar structures and known oxidation states are shown in Figure 4.8. Firstly, a clear trend of the isomer shift to higher values for higher oxidation states can be observed. The s-electron density at the nucleus decreases with higher numbers of d-electrons as they shield the nucleus from the charges of the electrons in the 4s orbital. Additionally, a higher electron spin further increases the isomer shift. The oxidation states of 0 and +2 in \mathbf{I}^0 are confirmed by comparing the isomer shifts and quadrupole splitting to those of dppf and $[(\text{PPh}_3)_2\text{Fe}(\text{CO})_3]$ (see also Table 4.2). They agree with reported values of $\delta_{\text{IS}} = 0.51$ and -0.05 mm s^{-1} and $\Delta E_{\text{Q}} = 2.33$ and 2.18 mm s^{-1} for the ferrocene and the carbonyl iron in \mathbf{I}^0 , respectively. [205] The slightly higher isomer shifts may be due to a different source material that has another baseline emission energy.

The spectrum of \mathbf{I}^+ is much more complicated with at least three quadrupole-split signals. The outermost lines with $\delta_{\text{IS}} \approx 0.5 \text{ mm s}^{-1}$ and $\Delta E_{\text{Q}} \approx 2.3 \text{ mm s}^{-1}$ are very similar to those attributed to Fe^{II} in \mathbf{I}^0 . This suggests a minimal influence of the oxidation of the ferrocene iron ions.

To aid the assignment of the signals in the centre of the spectrum, variable temperature spectra (Figure 4.9A) were recorded, since fluid solution EPR measurements revealed that at low temperatures only one isomer (see Section 4) is present. Indeed, the spectra contain fewer contributions at low temperatures. Below 50 K only two doublets are visible with isomer shifts of ca. 0.1 mm s^{-1} and 0.5 mm s^{-1} and quadrupole splittings 0.5 mm s^{-1} and 2.3 mm s^{-1} . The former of each parameters are assigned to Fe^{I} and the latter due to its similarity to ferrocene and dppf to the ferrocene iron in \mathbf{Ib}^+ .

This leaves only one doublet in the room temperature spectrum unassigned. It was assigned to the carbonyl iron of the isomer that only exists at elevated temperatures. The different isomer shifts and quadrupole splittings of the carbonyl iron nuclei in the two

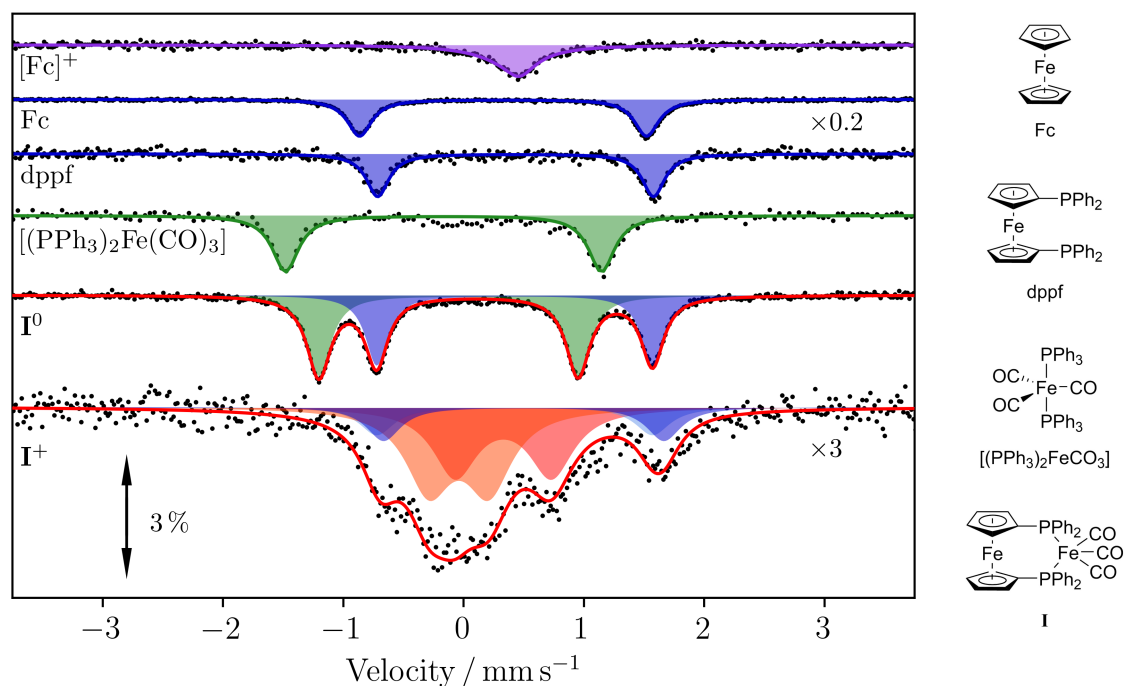


Figure 4.8: Room temperature Mössbauer spectra of \mathbf{I}^0 , \mathbf{I}^+ and reference compounds with fits. The colours are chosen based on the oxidation states of 0 (green), +1 (red), +2 (blue) and +3 (violet).

isomers may be explained with the different geometries that are depicted in Scheme 4. The different geometries of the isomers are known from DFT calculations. [12]

The fit parameters for the variable temperature spectra depicted in Figure 4.9A for \mathbf{Ia}^+ and \mathbf{Ib}^+ are given in Tables A.1 and A.2, respectively, as well as in Table 4.2. The amount of \mathbf{Ib}^+ increases from 55% at room temperature to 93% at 50 K. Below 10 K only that isomer exists, see also Table A.3. Furthermore, the isomer shift only increases slightly for lower temperatures, which is due to the second-order Doppler shift. The quadrupole splitting does not increase for either of the iron atoms. This is also observed for example for ferrocene that shows a quadrupole splitting of 2.39 mm s^{-1} at 80 K and room temperature and isomer shifts of 0.52 and 0.43 mm s^{-1} at 80 K and room temperature, respectively. This behaviour is also known in literature for other low-spin Fe^{II} compounds [138, 139] Literature data for low-spin Fe^{I} for similar, molecular systems only exists for measurements at room temperature. $[\text{Fe}(\text{nacnac})^-(\text{CO})_3]$, where $\text{nacnac} = \text{N,N}'\text{-bis}(2,4\text{-diisopropylphenyl})\text{-}1,3\text{-diketiminate}$, has an isomer shift of 0.12 mm s^{-1} and a quadrupole splitting of 0.77 mm s^{-1} . [206] Those values are comparable but nonetheless different to those of \mathbf{I}^+ , likely because of the difference in the ligands nacnac and dppf .

Table 4.2: Fitting parameters of the Mössbauer spectra shown in Figure 4.8. The errors in the relative amounts of the areas in \mathbf{I}^+ is estimated.

	Ox. State	$\delta_{\text{IS}} / \text{mm s}^{-1}$	$\Delta E_{\text{Q}} / \text{mm s}^{-1}$	$x / \%$
$[\text{Fc}]^+$	+3	0.417(7)	0	100
Fc	+2	0.524(7)	2.398(7)	100
dppf	+2	0.43(1)	2.29(1)	100
$[(\text{PPh}_3)_2\text{Fe}(\text{CO})_3]$	0	-0.166(7)	2.627(7)	100
\mathbf{I}^0	+2	0.424(7)	2.294(7)	45(1)
\mathbf{I}^0	0	-0.125(7)	2.155(7)	55(1)
\mathbf{Ia}^+	+2	0.42(1)	2.29(1)	11(5)
\mathbf{Ia}^+	+1	0.33(1)	0.80(1)	34(5)
\mathbf{Ib}^+	+2	0.50(1)	2.33(1)	13(5)
\mathbf{Ib}^+	+1	-0.04(1)	0.50(1)	42(5)

The Mössbauer spectrum of $[\text{Fc}]^+$ in Figure 4.8 vastly differs from that of the other compounds as it consists of only one singlet. This behaviour is known to result from slow relaxation of the magnetic moment in the paramagnetic compound, albeit not slow enough to show the typical sextet (see Section 2.2.7). [204, 207, 208] This leads to the singlet at room temperature even when $V_{zz} \neq 0$, due to a broadening of the $\pm 1/2 \rightarrow \pm 3/2$ transition due to slow relaxation. [98] At low temperatures, magnetic splitting into a sextet can be observed, due to the increase of the spin-lattice relaxation time, i.e. the hyperfine field becomes relatively stable on the Mössbauer timescale. Figure 4.9B shows that this behaviour is indeed observed for the ferrocenium ion. The fit parameters for $[\text{Fc}]^+$ are given in Table 4.3. They show an increase in the spin-lattice relaxation time for lower temperatures with a hyperfine field typical for Fe^{III} and slightly increasing isomer shifts due to the second-order Doppler shift.

The Mössbauer spectra of the paramagnetic \mathbf{I}^+ down to 3 K (Figure 4.9A) do not show a magnetic splitting into six lines. Instead, they show an increase of the linewidth below 7 K that can be attributed to a slowly relaxing magnetic moment, as is the case for $[\text{Fc}]^+$. It can not be excluded that this effect results from the boiling of helium that is pumped through the sample chamber, potentially leading to vibrations of the sample rod, thereby modulating the Doppler shift of the gamma rays. In order to minimise the effect of vibrations and increase the comparability of different measurements, the experimental set-up was kept the same in all measurements in Figure 4.9, i.e. the pump was running for all measurements of \mathbf{I}^+ and $[\text{Fc}]^+$. In order to further investigate the linewidth increase,

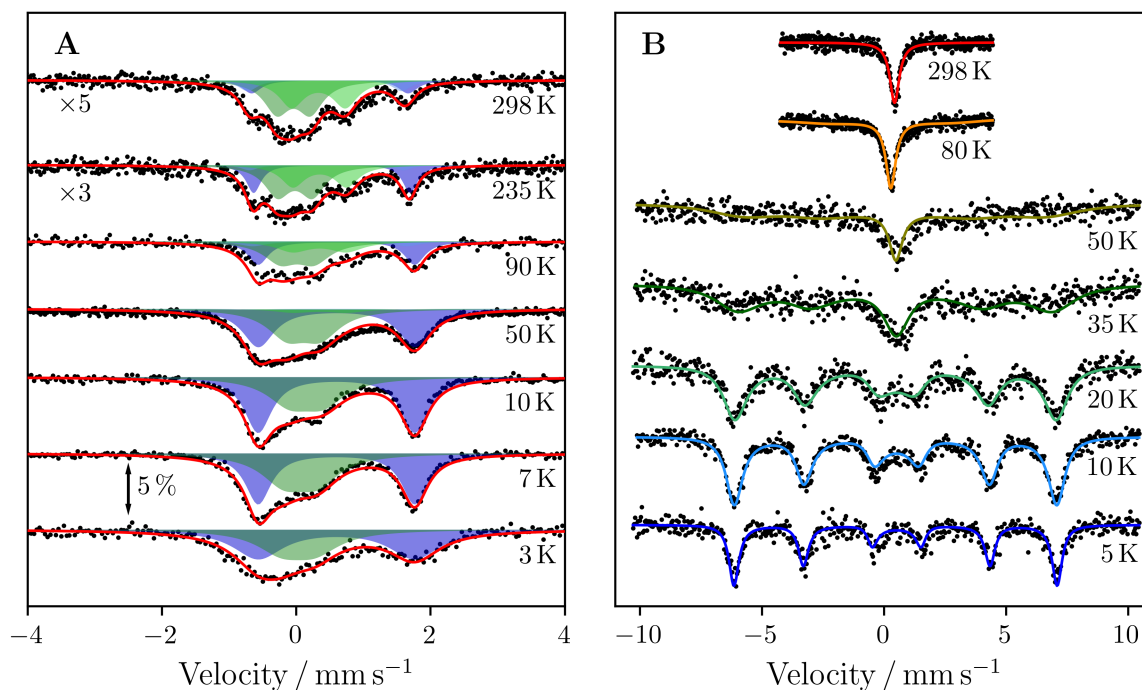


Figure 4.9: Variable temperature spectra of I^+ (A) and $[\text{Fc}]^+$ (B). In (A) the signals attributed to the carbonyl Fe^{I} are shown in green, those of the ferrocene Fe^{II} are shown in blue. The colours of the signals attributed to the Ia^+ isomer are lighter and those of Ib^+ are darker.

the Blume-Tjon model [98] for slowly relaxing magnetic moments was used to fit the data measured at 7 K and 3 K, see Figure 4.10. For the fit of the measurement at 7 K the magnetic hyperfine field was kept constant at $B_{\text{hf}} = 0 \text{ T}$ and the electric field gradients for the two iron species were determined to be $V_{zz} = 4.6 \cdot 10^{-21} \text{ V m}^{-2}$ and $V_{zz} = 1.0 \cdot 10^{-21} \text{ V m}^{-2}$ for the ferrocene and carbonyl iron, respectively. The asymmetry parameter of the electric field gradient was determined to $\eta = -5$ for both iron species. These values were used to determine the hyperfine field and jump rates of the magnetic moments, i.e. the spin-lattice relaxation times, at 3 K, which were determined to be $B_{\text{hf}} = 5 \text{ T}$, $T_{1, \text{carbonyl iron}} = 100(50) \text{ ns}$ and $T_{1, \text{ferrocene iron}} = 0.6(1) \text{ ns}$, assuming that the line width increase from cooling down results only from the slow relaxation of the magnetic moments. The non-zero relaxation rates for both iron ions indicate that spin density resides on both ions, suggesting an Fe-Fe interaction. The small change in isomer shift and quadrupole splitting during the oxidation indicates that this interaction is rather weak, albeit does not exclude this type of interaction. These results prove the value of Mössbauer spectroscopy where a site-specific relaxation rate of the order of nanoseconds can be determined.

Mössbauer spectroscopy confirms the previous results of the oxidation to take place on

Table 4.3: Fit parameters derived from the Blume-Tjon fit of the measurements of $[\text{Fc}]^+$ shown in Figure 4.9B. At all temperatures $B_{\text{hf}} = 41.2 \text{ T}$, $V_{zz} = -0.28 \cdot 10^{-21} \text{ V m}^{-2}$ and $\eta = 0.9$ were used in the fits.

T / K	$\delta_{\text{IS}} / \text{mm s}^{-1}$	T_1 / ns
298	0.42(1)	< 20
80	0.46(1)	< 20
50	0.47(1)	23(3)
35	0.49(1)	30(12)
20	0.50(1)	70(10)
10	0.50(1)	105(4)
5	0.50(1)	175(2)

the carbonyl iron, giving Fe^{I} and Fe^{II} ions in the oxidised state. It was confirmed that two isomers in a temperature dependent ratio exist. Furthermore, a slow relaxation of the paramagnetic moment of I^+ is observed at 3 K in zero-field. The relaxation behaviour in an applied magnetic field was further investigated via EPR spectroscopy and SQUID magnetometry and is discussed in the following.

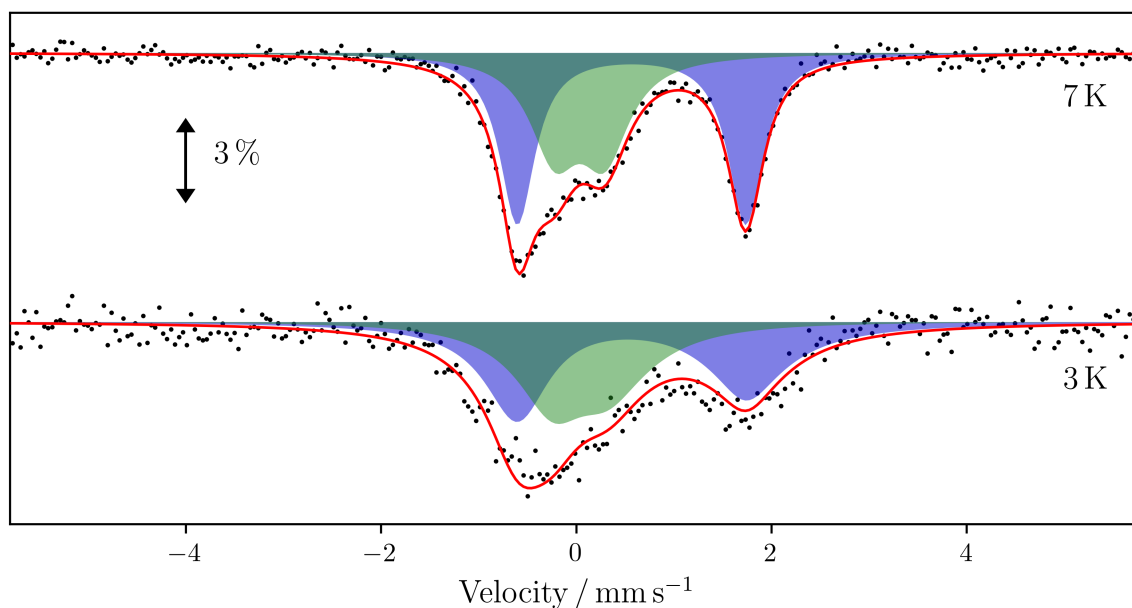


Figure 4.10: Fits of the measurements of I^+ at 3 and 7 K with the Blume-Tjon model.

4.5 Electron Paramagnetic Resonance Spectroscopy

Electron paramagnetic resonance (EPR) spectroscopy is a great tool to investigate paramagnetic complexes in different oxidation states, as the EPR signal strongly depends on the spin of the system of interest, and on the immediate surrounding of the location of the unpaired electrons through the hyperfine interaction to nearby nuclei. Although the results presented in the previous sections revealed oxidation states of 0 on the carbonyl iron and +2 on the ferrocene iron for the neutral species with the oxidation taking place predominantly on the carbonyl iron, giving oxidation states of +1 and +2, the low catalytic activity is still unanswered. Furthermore, stable systems with unpaired electrons might be used as single-molecule magnets (SMMs) and quantum bits if they show residual magnetisation in zero-field and long spin coherence times, respectively, see also Section 2.1. I^+ is indeed a field-induced SMM but the relaxation behaviour is still poorly understood. Pulsed EPR spectroscopy and ac SQUID magnetometry are great techniques to investigate spin-lattice relaxation and to shed light on the relaxation mechanisms.

4.5.1 The Static Electronic Structure of the Molecule

The most important parameters that can be determined by EPR for an open-shell system are the g and hyperfine A tensors, giving information on the symmetry of the system and the distances of surrounding nuclei. The distances of coupling nuclei can be extracted

from the the axial component of the hyperfine tensor that can be precisely determined for example via ENDOR and HYSCORE experiments. Another important parameter, especially for SMMs are the zero-field splitting parameters D and E for $S > 1/2$ and spin-spin interactions. All of these values can be determined from the measurement of the absorption of microwaves in different frequency and field regions. The separation of the absorption signals for the different components of the g tensor, i.e. g_{xx} , g_{yy} and g_{zz} , is dependent on the applied field while the hyperfine coupling is field-independent. Therefore, low microwave frequencies (X-Band, $\nu_{\text{MW}} \approx 9.5$ GHz) are best suited for the determination of the A tensor and g_{iso} . High frequencies (high-field EPR (HF-EPR), $\nu_{\text{MW}} > 100$ GHz) are more powerful for the determination of the individual components of the g tensor and for the determination of the zero-field splitting parameters D and E .

The X-Band spectrum of \mathbf{I}^+ in solution at room temperature is shown in Figure 4.11. It shows two signals with $g_{\text{iso}} \approx 2.05$ and $g_{\text{iso}} \approx 2.02$, each of which is composed of three lines in a 1:2:1 ratio. The two signals are attributed to the existence of the two isomers that were also seen in the Mössbauer spectrum of \mathbf{I}^+ and have been previously reported in literature. The ratio of the two isomers has also been shown to be temperature dependent in EPR, where \mathbf{Ib}^+ (green in Figure 4.11) was predominant at low temperatures. [12] The signal shape result from hyperfine coupling of the electron spin to two equivalent nuclei with $I = 1/2$ for both nuclei. Here, $A_{\text{iso}} \approx 71$ and 37 MHz are determined for \mathbf{Ia}^+ and \mathbf{Ib}^+ , respectively.

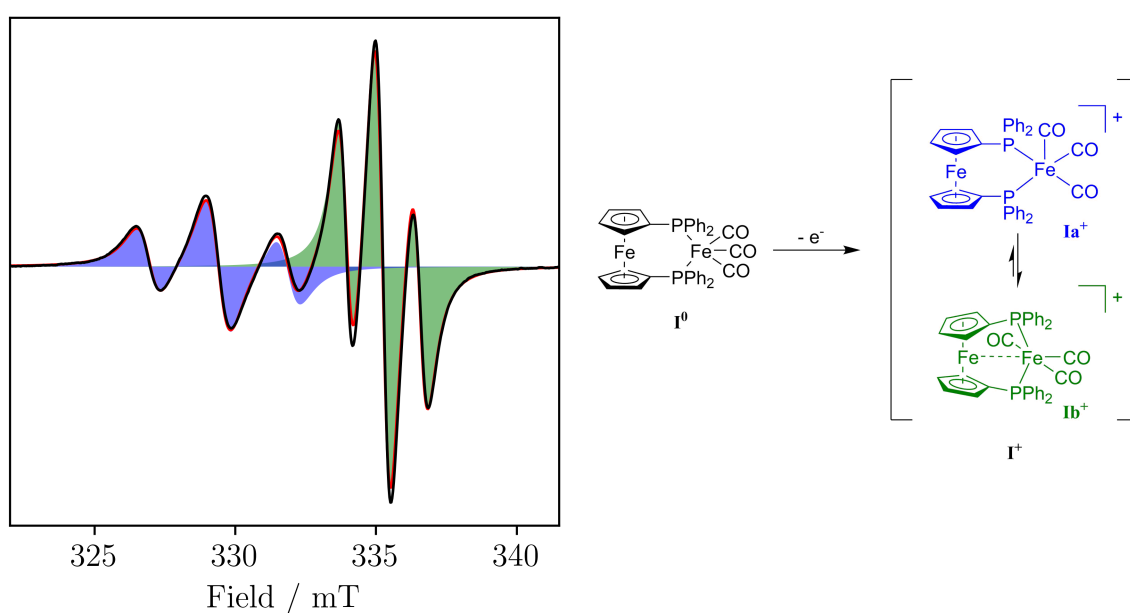


Figure 4.11: EPR spectrum of \mathbf{I}^+ measured at 9.46 GHz in a solution of DCM:toluene (1:1) showing the presence of two isomers. The fit parameters are given in Table 4.4.

The only nuclei in \mathbf{I}^+ with a nuclear spin $I = 1/2$ are ^1H that are too far away to justify such a strong coupling to the unpaired electron, ^{13}C of which there are three bound to the iron where the unpaired electron is located and also the low natural amount of the spin-bearing isotope excludes the coupling to these carbon atoms, leaving only ^{31}P of which there are two. The different g_{iso} and coupling strengths to the phosphorus atoms can be explained with the different geometries and coupling mechanisms, e.g. the strength of dipolar interaction only depends on the distance of the coupling spins. A_{iso} is decreased for less electron density on the spin-bearing nucleus. The higher chemical stability, especially at low temperatures, lower g_{iso} and A_{iso} of \mathbf{Ib}^+ are explained by a delocalisation of the unpaired electron over both iron atoms, stabilising the open-shell configuration and lowering the electron density on the carbonyl iron. [12] In literature, EPR spectra of Fe^{I} carbonyls have been reported with similar values for g and A , e.g. $g_{\text{iso}} = 2.052$ and $A_{\text{iso}} = 22.6$ MHz for $[\text{Fe}(\mathbf{P2})(\text{CO})_3]$, where $\mathbf{P2} = 3,4\text{-dimethyl-3',4'-bis-(diphenylphosphino)-tetrathiafulvalene}$ [209] and $g_{\text{iso}} = 2.0433$, $A_{\text{iso},^1\text{H}} = 63$ MHz for $[\text{H}_2\text{Fe}_2(\text{CO})_7]^+$ [210]. The lower g value of the isomer \mathbf{Ib}^+ compared to the compounds in literature further support the hypothesis of weak Fe-Fe interactions that change the spin-orbit coupling, which in turn increases g_{iso} .

In comparison, $[\text{Fe}]^+$ ($S = 1/2$) shows g values of $g_{\parallel} \approx 3.5$ and $g_{\perp} \approx 1.7$ [204] and high-spin Fe^{III} ($S = 5/2$) systems show $g_{xx} = g_{yy} = g_{zz} \approx 2$ and $D \leq 300$ GHz. [211–216] Fe^{II} ($S = 2$) systems typically show rhombic g tensors with all components close to $g = 2$ but a large number of signals at high microwave frequencies ($\nu_{\text{MW}} > 100$ GHz) due to many allowed transitions between the spin microstates and D up to 400 GHz. [216, 217] At low microwave frequencies ($\nu_{\text{MW}} \approx 10$ GHz) non-Kramers systems are typically EPR silent.

The EPR spectra and simulations of the same of \mathbf{I}^+ in glassy frozen solutions at two different microwave frequencies are shown in Figure 4.12. Due to the immobility of the molecule in the frozen solvent, the individual components of the g tensor and dipolar couplings to the surrounding nuclei can be resolved. Following the convention that $g_{zz} > g_{yy} > g_{xx}$, the hyperfine couplings in these orientations, that are independent of the orientations in the molecule (z is not necessarily the axis of highest symmetry in the molecule), can be determined. A_{zz} and A_{yy} can be easily read from the X-Band spectrum (Figure 4.12A) and A_{xx} could then be calculated from $A_{\text{iso}} = 1/3(A_{xx} + A_{yy} + A_{zz})$. Here, all hyperfine values were obtained from electron-nuclear double resonance (ENDOR) measurements that directly probe the hyperfine tensor giving a higher accuracy because NMR transitions within the spin states at constant applied magnetic fields are measured, giving a much more precise estimate of the individual components of the A tensor, see

Section 4.5.3. Furthermore, A_{iso} might change with temperature, excluding the calculation of A_{xx} here. All simulation parameters are given in Table 4.4. The absence of resolved hyperfine coupling in the g_{zz} component in the spectrum measured at 35 GHz is most likely due to g strain that inhomogeneously broadens the EPR line so that the hyperfine coupling is not resolved.

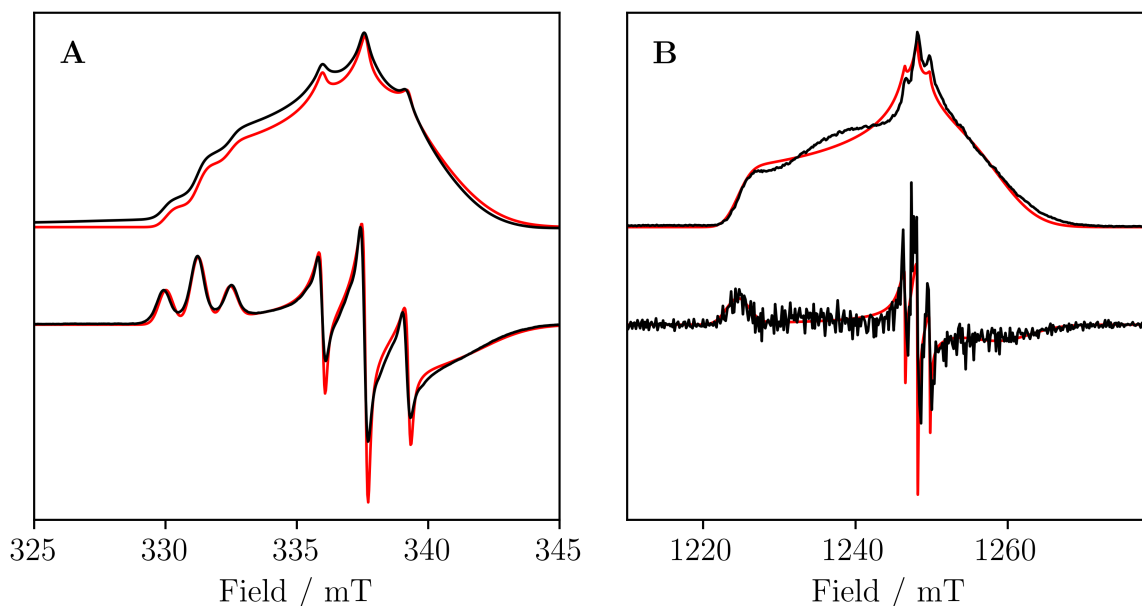


Figure 4.12: EPR spectra of I^+ in frozen solutions in DCM:toluene (1:1) and concentrations of 1 mmol l^{-1} measured at 9 K and 9.46 GHz (A) and 10 K and 35 GHz (B). The simulation parameters are given in Table 4.4.

All EPR spectra measured so far suggest the electron spin to be $S = 1/2$ or at least having the $m_S = \pm 1/2$ state to be lowest in energy due to the fact that the g values are close to that of the free electron $g_e \approx 2.0023$ for both frequencies with no additional signals being visible. To prove the spin state to be $S = 1/2$, which would be expected for a d^7 system in trigonal bipyramidal symmetry, high-field EPR spectra were measured, see Figure 4.13. Furthermore, the components of the g tensor are better resolved at higher magnetic fields. For $S > 1/2$, transitions between the $\pm m_S$ states, e.g. from $m_S = -1/2$ to $m_S = -3/2$, would be expected. As there are no transitions apart from those attributed to those within the $m_S = \pm 1/2$ Kramers doublet, it can be concluded that either $S = 1/2$ or the zero-field splitting parameter $D \gg 2\nu_{\text{MW, max}} = 750 \text{ GHz}$. Also, the high applied magnetic fields lead to the strongest separation of the components of the g tensor, giving the most reliable estimate of g_{xx} , g_{yy} and g_{zz} , see Table 4.4. Lastly, the low rhombicity of the g tensor leads to the assumption of a very low spin-orbit coupling, i.e. a $[\text{Ar}]3d^54s^2$ ground state electron configuration, further strengthening the hypothesis of the oxidation

state to be +1.

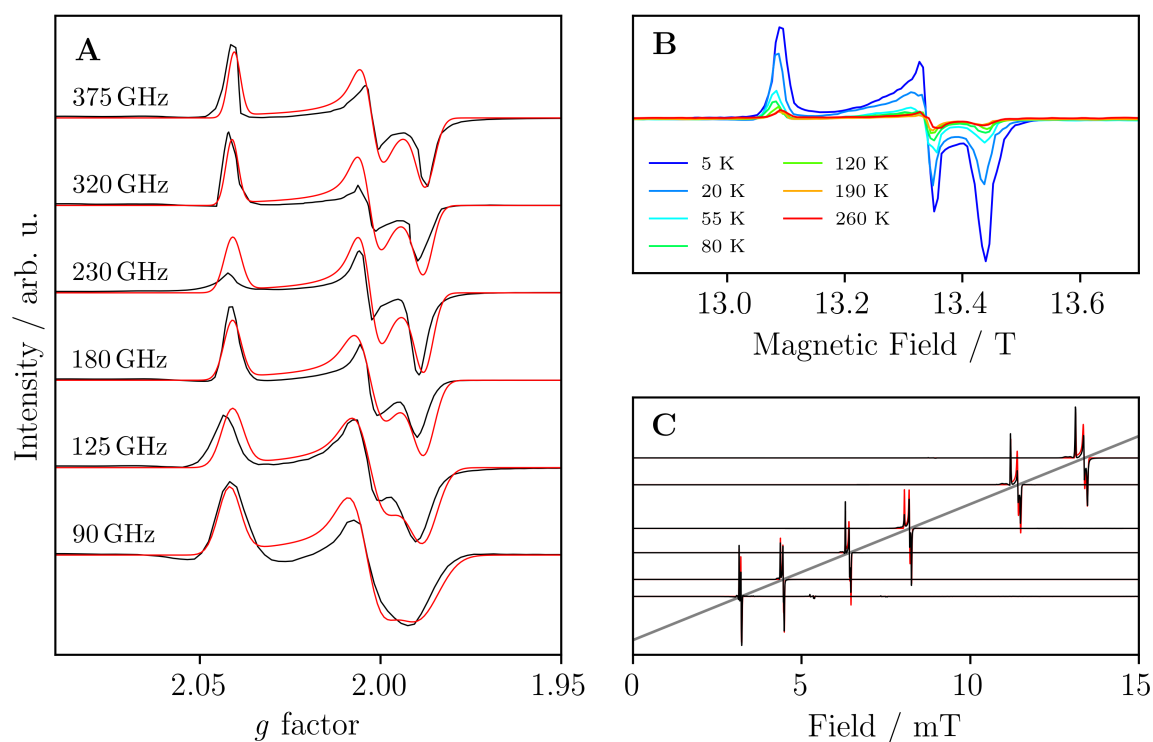


Figure 4.13: A) HFEPR spectra of a powder pellet of I^+ at 5 K and different microwave frequencies. B) HFEPR spectra measured at 375 GHz and different temperatures. C) HFEPR spectra over the full field-range at 10 K and variable microwave frequencies. The frequencies are the same as in (A) and the grey line shows $g = 2$.

EPR spectroscopy proves the presence of two isomers at room temperature with only one existing at low temperatures which was also observed in Mössbauer spectroscopy. It also confirms a spin state of $S = 1/2$, an oxidation state of +1 on the carbonyl iron and no considerable spin density on the ferrocene iron. The coupling of the electron spin to the two phosphorus atoms directly attached to the carbonyl iron where most of the spin density must reside could be observed as well.

Table 4.4: Simulation parameters for the simulations shown in Figures 4.11 (Solution, X-Band), 4.12 (Frozen solution, X- and Q-Band) and 4.13 (Powder, HFEPR).

	Ia ⁺ (Solution)	Ib ⁺ (Solution)	Ib ⁺ (Frozen solution)	Ib ⁺ (Powder)
g_{xx}			1.9850	1.9910
g_{yy}			2.0035	2.0060
g_{zz}			2.0420	2.0460
g_{iso}	2.0524	2.0166	2.0102	2.0143
A_{xx} / MHz			38.6	
A_{yy} / MHz			46.0	
A_{zz} / MHz			33.9	
A_{iso} / MHz	71	37	39.5	

4.5.2 Spin Dynamics of the Molecule from Pulsed EPR

In order to carry out advanced methods of pulsed EPR, such as ENDOR and HYSCORE to further investigate the hyperfine tensor and thereby the orientations and distances of coupling nuclei, the molecule must possess sufficiently long spin-lattice and spin-spin relaxation times, i.e. much longer than the pulse sequences. Hence, the phase-memory time T_M should be of the order of microseconds or longer. The spin-lattice relaxation time T_1 and the phase-memory time T_M can be determined with the inversion-recovery experiment and the Hahn-echo sequence, respectively. The relaxation times were measured at field positions corresponding to purely the g_{zz} and g_{yy} components, labelled Pos. 1 and Pos. 2, respectively, in Figure 4.14A. The individual decay curves measured at Pos. 2 are shown in Figure 4.14C and Figure 4.14D and the extracted relaxation times are given in Figure 4.14B and in Tables A.4 and A.5.

The spin-lattice relaxation times T_1 decrease with increasing temperatures, following the expected temperature-dependent behaviour. This can be explained as the Raman process (see Section 2.1.8 for an explanation of the relaxation mechanisms) becomes the dominant relaxation pathway for elevated temperatures. Orbach processes do not play a role for $S = 1/2$ systems as no real intermediate energy level exists in the system. Quantum tunnelling only occurs at very low magnetic fields for $S = 1/2$. The data can be fit reasonably well with

$$T_1^{-1} = c_{\text{direct}}T + c_{\text{Raman}}T^{n_{\text{Raman}}} \quad (4.3)$$

with the parameters given in Table 4.5, see Figure A.6. They show that the relaxation

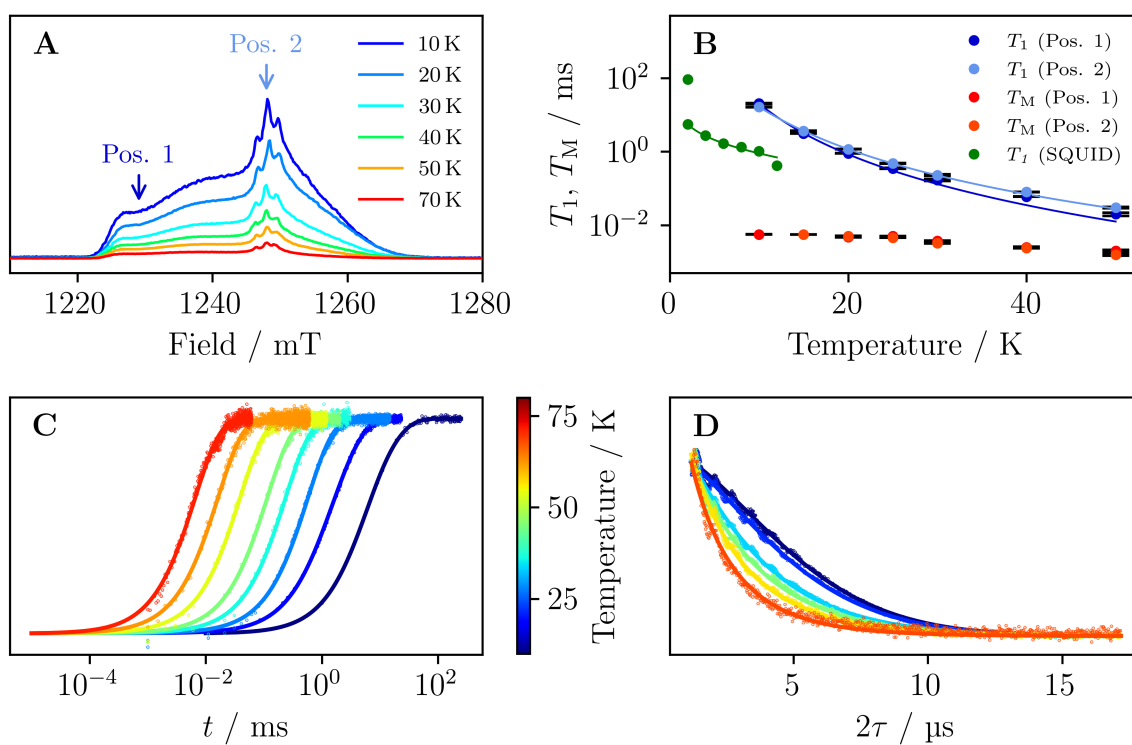


Figure 4.14: A) Variable temperature EPR spectra of I^+ in a 1 mmol l⁻¹ DCM:toluene (1:1) solution at a microwave frequency of 35 GHz. B) Spin-lattice relaxation times T_1 from EPR and SQUID (1250 mT) and phase-memory times T_M . Echo decays from the inversion-recovery (C) and Hahn-echo experiments (D) measured at Pos. 1.

happens only via a Raman process for g_{yy} and a Raman and direct process for g_{zz} . This may be due to the anisotropic nature of lattice vibrations that need to allow for the relaxation of the spin in direction of the excitation. This phonon density of states may be different for the different orientations in the molecule, prohibiting direct processes in certain directions. The fit function for the relaxation times determined from ac SQUID measurements show that the direct process is much more important at lower temperatures. Data on the spin-lattice relaxation of Fe^I compounds is non-existent in literature and predominantly high-spin Fe^{III} are reported on with much faster relaxation times (< 1 ms at 4 K in an Fe₃ cluster [218] and ≈ 1 μ s at 4 K in iron porphyrins [219]) and a much stronger decrease of T_1 with increasing temperatures due to the additional, faster Orbach relaxation process.

Table 4.5: Fit parameters for the direct and Raman processes of the spin-lattice relaxation times shown in Figures 4.14 and A.6 with Equation 4.3.

	$c_{\text{direct}} / \text{s}^{-1} \text{K}^{-1}$	$c_{\text{Raman}} / \text{s}^{-1} \text{K}^{-n_{\text{Raman}}}$	n_{Raman}
Pos. 1	0.0(5)	$1.3(8) \cdot 10^{-3}$	4.6(2)
Pos. 2	1.28(8)	$3.7(3) \cdot 10^{-3}$	4.11(3)
SQUID	88(8)	0.5(5)	3(2)

Figure 4.14B also shows spin-lattice relaxation times obtained from ac SQUID magnetometry obtained at 1250 mT, i.e. close to those measured with EPR, and variable temperature. The raw data with fits is depicted in Figure 4.15 for the measurements at different temperatures and different applied fields from 0 to 2 T at 1.8 K. The fit parameters are given in Table A.6.

The first observation is that T_1 is much faster in the powder measured with SQUID magnetometry than it is in the frozen solution measured with EPR spectroscopy. A possible reason are increased spin-spin interactions in the powder due to lower distances between the molecules. As the spin relaxation happens through spin-phonon coupling another reason might be a different phonon spectrum in the powder compared to the frozen solution. This hypothesis could be proven by measuring the phonon spectrum of both solids with far-infrared (FIR) spectroscopy. The fact that the Raman coefficients n_{Raman} differ in powder and frozen solution further suggests a different phonon density. The fact that the direct process happens more frequently than the Raman process at lower temperatures is expected and does not necessarily require a different phonon spectrum. Also, Raman processes are more important at higher temperatures and the measurements in the powder might not be at sufficiently high temperatures to confidently determine

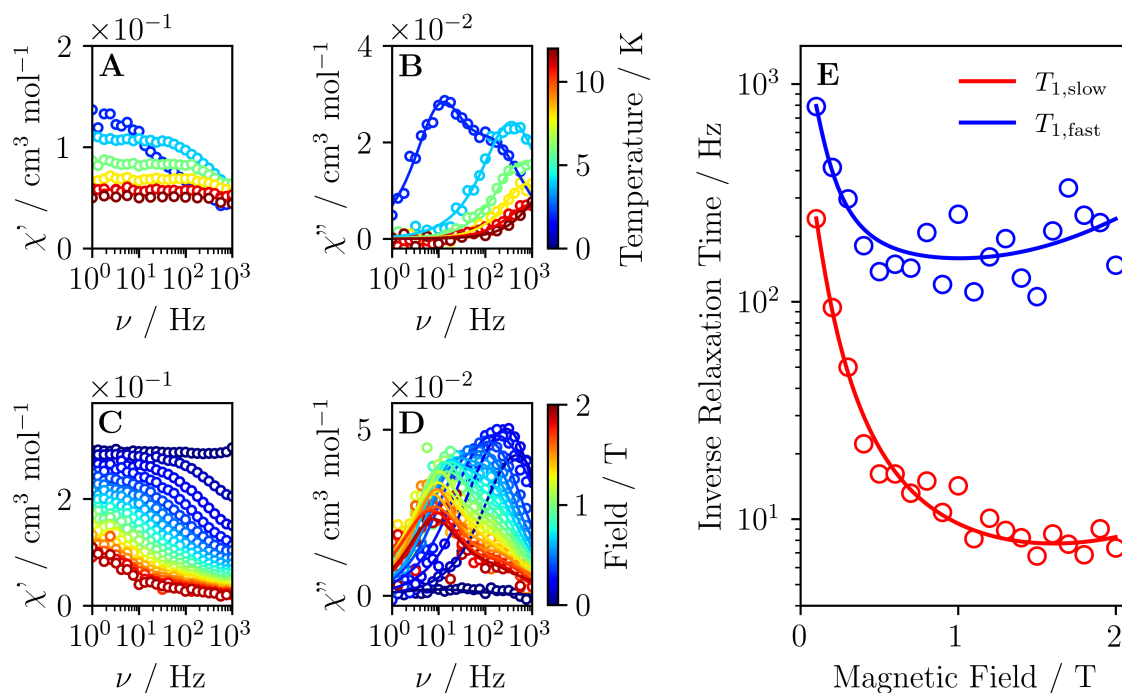


Figure 4.15: A) In-phase susceptibility χ' versus frequency of field modulation ν of \mathbf{I}^+ measured at a bias field of 1250 mT and variable temperatures given by the colourbar on the top right. B) Out-of-phase susceptibility χ'' measured at 1250 mT. C) χ' measured at 1.8 K and variable field as given by the colorbar (bottom right). D) χ'' measured at 1.8 K and variable field. E) Inverse relaxation times extracted from (D) fitted with Equation (4.4).

n_{Raman} , as the process only starts to become relevant at ca. 10 K. From Mössbauer spectroscopy it is known that \mathbf{I}^+ shows $T_1 \approx 100$ ns in zero-field. To further investigate this behaviour, the dependence of the spin-lattice relaxation time on the magnetic field up to 2 T was determined and fitted with a Brons-Van Vleck-like equation

$$\tau^{-1} = cB^4 + d \frac{1 + eB^2}{1 + fB^2} \quad (4.4)$$

with the applied magnetic field B . c parametrises the direct process, e describes the influence of internal fields on the relaxation of interacting spins and f describes the suppression of internal spin-lattice relaxation mechanisms by external fields. [220] Here, $c = 0.2(2) \text{ T}^{-4} \text{ s}^{-1}$, $d = 56(9) \text{ s}^{-1}$, $e = 0.1(1) \text{ T}^{-2}$ and $f = 30(1) \text{ T}^{-2}$. These values suggest a low influence of external fields on the spin-lattice relaxation as they are on the lower end of published data, which, on the other hand, are all for vanadium complexes. [220–222] Another observation from this data is that in zero-field the spin-lattice relaxation time is much faster than what is measurable with the available measurement frequencies,

i.e. $T_1 \ll 1$ ms, underlining the advantage of Mössbauer spectroscopy, where spin-lattice relaxation times on the order of nanoseconds are experimentally accessible.

In summary, the long spin-lattice relaxation and coherence times make \mathbf{I}^+ a field-induced single-molecule magnet and a potential qubit, respectively. Also, they allow for the application of advanced techniques of pulsed EPR, as is shown in the following.

4.5.3 Advanced Pulsed Electron Paramagnetic Resonance Methods

Pulsed EPR allows probing the hyperfine coupling of the electron spin to surrounding nuclei directly, e.g. via electron spin echo envelope modulation (ESEEM), hyperfine sublevel correlation (HYSCORE), which is a two-dimensional ESEEM experiment and electron-nuclear double resonance (ENDOR), see Section 2.2.3. In all of these methods the echo intensity is modulated by the precessing magnetic moment of the nearby nuclei. The intensity and frequency of this modulation gives informations about the distance and type of coupling nuclei.

ESEEM is a relatively simple experiment as it only requires the Hahn-echo pulse sequence that is also used for the measurement of the phase-memory time. The modulation of the echo intensity can be observed for the measurements described in the previous section and is shown also in Figure 4.16A.

As the hyperfine coupling only decreases the echo intensity, a fit through the maxima of the oscillating signal would be correct but in order to determine the oscillation frequency it is sufficient to subtract the original fit and to Fourier transform the data obtained after subtraction of the exponential decay. The results of the Fourier transformations are shown in Figure 4.16C. It has a maximum at ca. 2.75 MHz for all temperatures. The modulation frequency ω_{mod} can be calculated from the hyperfine coupling A and the nuclear Larmor frequency ω_I of the coupling nucleus with Equation (4.5).

$$\omega_{\text{mod}} = |m_S A - \omega_I| \quad (4.5)$$

With $\omega_{I,31\text{P}}/2\pi = 21.51$ MHz and $\omega_{\text{mod}}/2\pi = 2.75$ MHz, $A = 37.5$ MHz and $A = 48.5$ MHz both solve the equation. These values fit to the experimentally determined $A_{xx} = 38.6$ MHz and $A_{yy} = 46.0$ MHz. At Pos. 1 (see Figures 4.14 and A.7) $A = 48.2$ MHz and $A = 37.8$ MHz solve the equation for the observed $\omega_{\text{mod}}/2\pi = 2.60$ MHz where the latter value is close to $A_{zz} = 33.9$ MHz.

The ESEEM experiment can be expanded to the second dimension with the HYSCORE pulse sequence by varying the time between the second and third and between the third and the fourth pulses (Figure 2.19). The signals corresponding to strongly coupled nu-

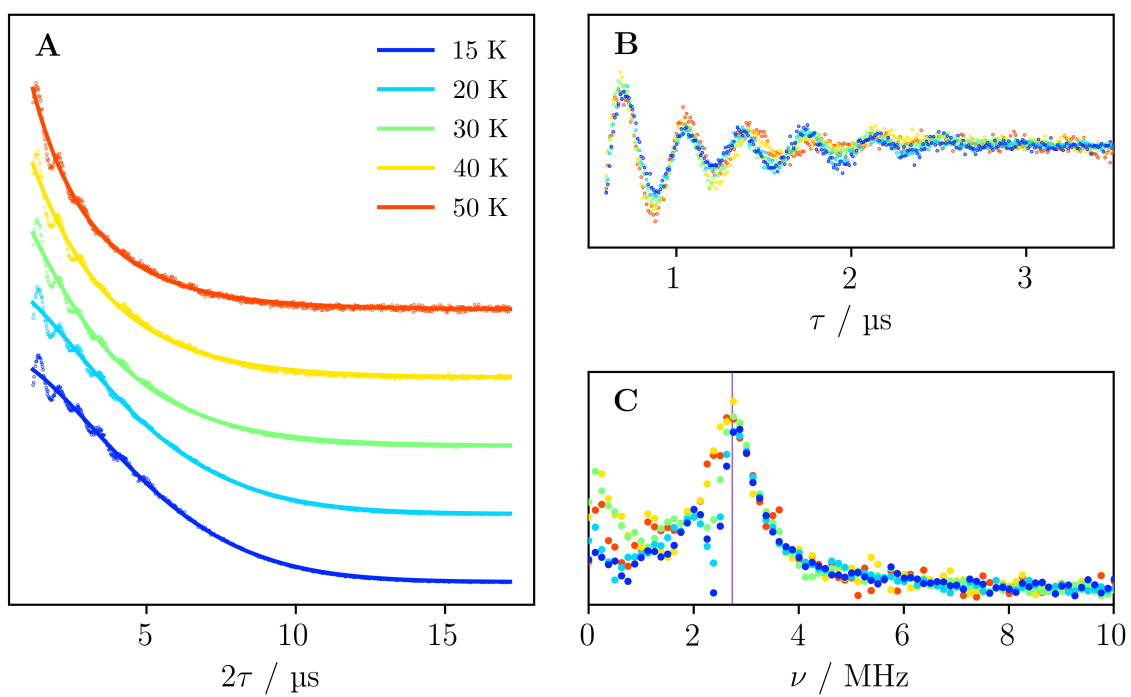


Figure 4.16: A) ESSEM spectra of I^+ obtained at Pos. 2 with the Hahn-echo pulse sequence. B) Modulations after subtraction of the fit. C) Modulation frequencies obtained after Fourier transformation.

clei ($|m_S A| > \omega_I$) are visible in the left quadrant, the signals of weakly coupled nuclei ($|m_S A| < \omega_I$) can be seen in the right quadrant (+, +), see Figure 2.20. A more complete theoretical background can be found in Section 2.2.3.

HYSCORE spectra were measured at field positions corresponding to g_{xx} , g_{yy} and g_{zz} for different pulse lengths to make the ^1H or ^{13}C coupling visible, see Section A.2.3. During longer mixing periods, spins in the $M_S = +1/2$ state decay faster than those in the $M_S = -1/2$ state, leading to a change of the intensity of the individual transitions through influence of the cross polarisation during this mixing period. This effect is also exploited in variable mixing time (VMT) ENDOR, where individual transitions can be saturated and pushed towards negative signal intensities. [223, 224] The coupling to ^1H is therefore only visible for long delay times after the first pulse. One exemplary HYSCORE spectrum of I^+ with a short delay time is shown in Figure 4.17 with simulations for the coupling to hydrogen and carbon atoms. The values for A are given in Table 4.4 and are in accordance to the fits of the ENDOR spectra (see below). The simulation of the ^1H signals fits the measurement with longer delay time much better, because there the signals arising from the coupling to ^1H nuclei are better resolved due to a longer mixing time. This data is shown in Section A.2.3.

The high information content in the HYSCORE spectrum allows for a much more precise determination of the components of the hyperfine tensor, i.e. A_{iso} , T and ρ , see Equation (2.15). The distance between the coupling electron and nuclear spin can then be determined from Equations (2.16), (2.17), (2.18) and (2.19). The distances obtained from HYSCORE (^1H , ^{13}C) and ENDOR (^1H , ^{19}F , ^{31}P) are given in Table 4.6.

The ENDOR spectra of I^+ for fields corresponding to g_{yy} at X-Band and Q-Band frequency are shown in Figure 4.18A and B, respectively. The simulation parameters are given in Table 4.6. For an $S = I = 1/2$ system, signals are centred at $A/2$ and split by $2\omega_I$ in the strong coupling case. For weakly coupled nuclei the signals are centred at ω_I and split by A . As in HYSCORE, signals can therefore be easily attributed to specific nuclei as their field-dependent Larmor frequencies are known.

For I^+ , three coupling nuclei can be identified. All simulation parameters are given in Table 4.6. From the determination of the individual components of the A tensor and under assumption of purely dipolar coupling, the distance between the unpaired electron and the nuclei can be determined.

The coupling to ^{31}P was also observed in the EPR and ESEEM spectra and gives distances of 2.9 Å. In the crystal structure of the neutral compound and the calculated structure of Ib^+ , the Fe-P distance was determined to be 2.3 Å, which is well below that extracted from the ENDOR measurements. [12] This may be because the dipolar

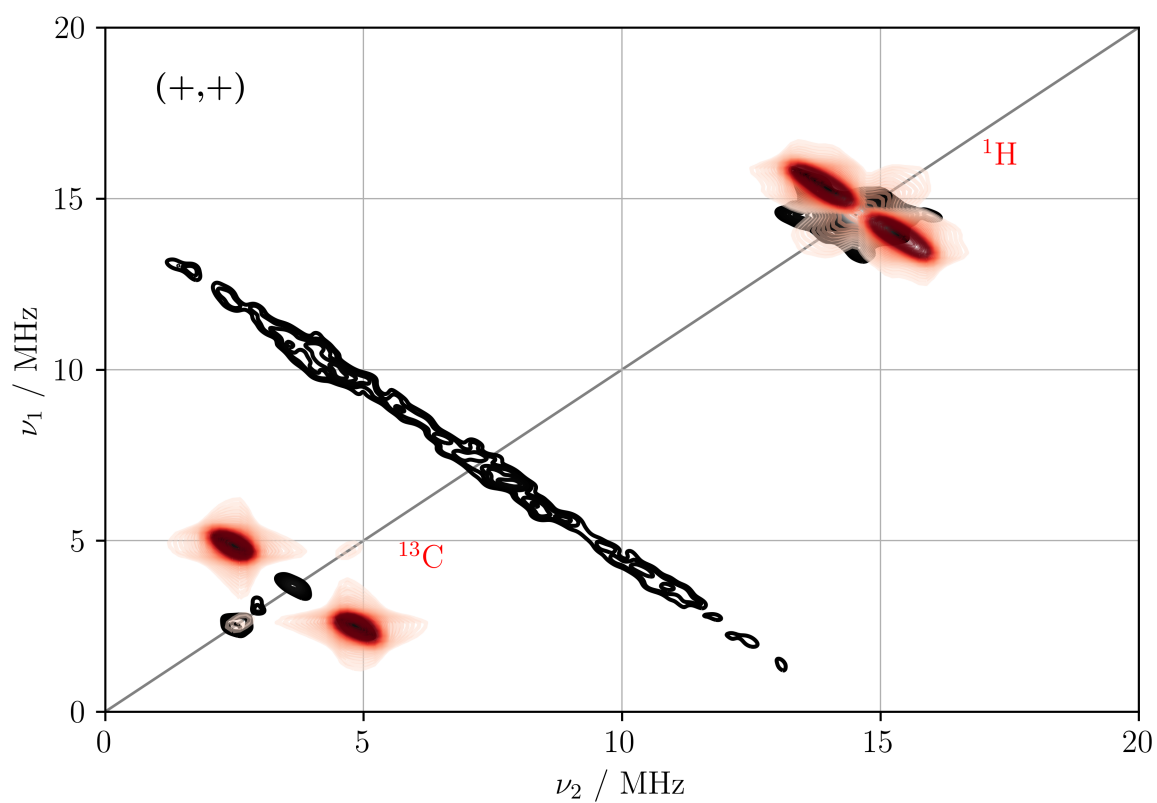


Figure 4.17: (+,+)-quadrant of the HSCORE spectrum of I^+ measured at 10K in a 2 mmol l^{-1} solution in DCM:toluene (1:1) showing the weakly coupled nuclei. Simulation parameters are given in Table 4.6

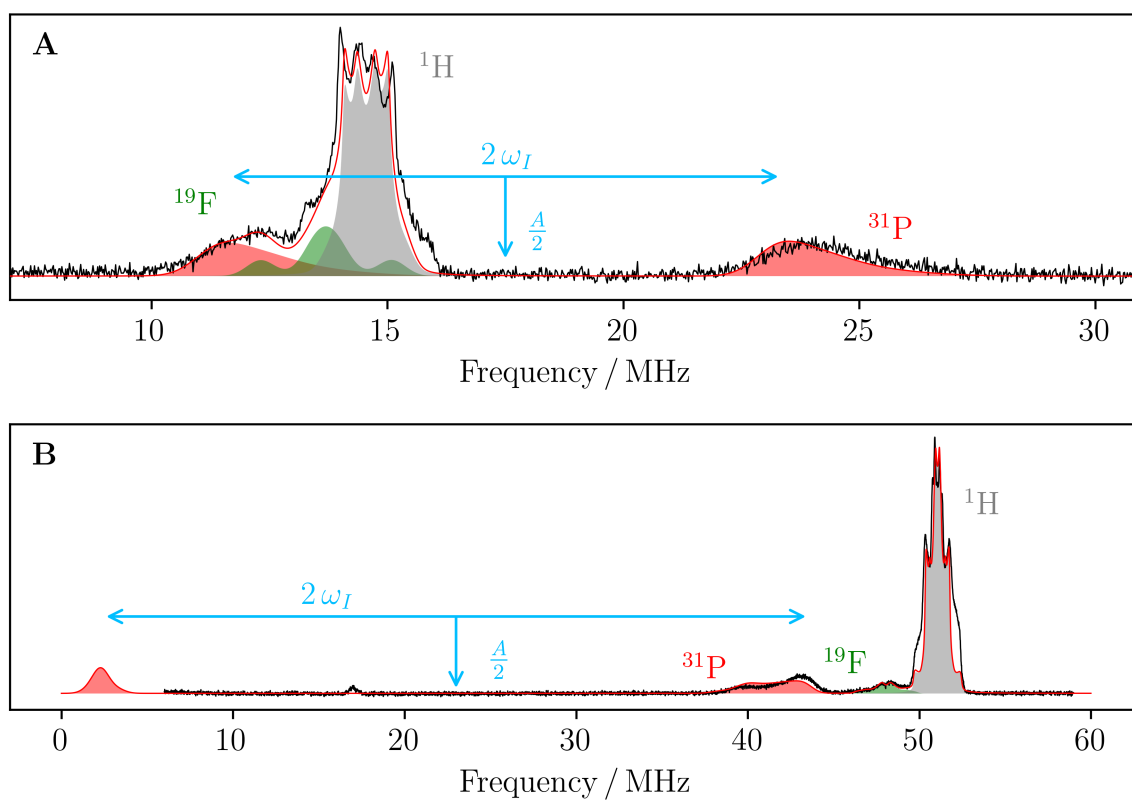


Figure 4.18: ENDOR spectra of I^+ measured at 15 K in a 2 mmol l^{-1} solution in DCM:tol (1:1) at ca. 9.8 GHz (A) and ca. 34 GHz (B). The simulation parameters are given in Table 4.6.

model is not complete and it only explains part of the axial hyperfine interaction. The coupling to ^1H nuclei is expected for most samples but it is usually unresolved due to weak interactions. Here, distances in the range from 3.8-6.8 Å are extracted. Analogous to the Fe-P distances, the distances to coupling ^1H nuclei can be extracted from the crystal structure of \mathbf{I}^0 . There, the closest hydrogen nuclei to the carbonyl iron are those in the PPh_2 phenyl rings with $d = 3.7$ Å and those that are the farthest away have $d = 6.8$ Å. In the calculated structure for \mathbf{Ib}^+ these distances slightly decrease due to a rotation of the phenyl rings and a smaller Fe-Fe distance. The coupling to carbons atoms gives distances of 5.4 Å. In \mathbf{I}^0 and \mathbf{Ib}^+ a range of Fe-C distances exist with carbonyl carbon atoms having the smallest distance of ca. 1.8 Å. Assuming purely dipolar coupling these would be strongly coupled and potentially outside the available measurement range. Other carbon nuclei with distances between 3.5 and 6.0 Å can be found for \mathbf{I}^0 and \mathbf{Ib}^+ in the crystal in calculated structures, respectively. Due to the low natural abundance of ^{13}C is possible that the interaction to all those nuclei is not well resolved. The presence of fluorine atoms is much more interesting as the only fluorine atoms in the sample are from the counter ion $(\text{BAr}_4^{\text{F}})^-$ that is often said to be non-coordinating. With Fe-F distances between 4.1 and 4.4 Å for the three fluorine atoms the counter ion seems to be very closely connected to the catalyst, potentially explaining the low catalytic activity of the compound.

Table 4.6: Simulation parameters for all coupling nuclei observed in the EPR, HYSCORE and ENDOR spectra and the distances calculated with Equation (2.16).

Nucleus	$A_{\text{iso}} / \text{MHz}$	T / MHz	ρ	$d / \text{Å}$
^1H (1)	0	1.40	0	3.84
^1H (2)	0	0.95	0	4.37
^1H (3)	0	0.40	0	5.83
^1H (4)	0	0.25	0	6.82
^{13}C	2.30	0.50	0	5.41
^{19}F (1)	1.20	0.95	0	4.37
^{19}F (2)	1.33	1.08	0	4.19
^{19}F (3)	1.40	1.15	0	4.10
^{31}P (1,2)	39.50	3.25	0.723	2.90

EPR spectroscopy undoubtedly proves the oxidation locus to be on the carbonyl iron, the electron spin to be $S = 1/2$ and field-induced single-molecule magnet behaviour of the system due to long spin relaxation times. The system acts as a potential qubit because of long spin coherence times and the low catalytic activity might be explained from the close

association of the counter ion that sterically hinders the investigated hydrogen evolution reaction.

4.5.4 Immobilisation of the Probe Molecule into the Silica Material SBA-15

As was mentioned at the beginning of the Chapter, the immobilisation of the catalyst into mesopores was to be investigated. Unfortunately, the functionalised molecule is not stable after oxidation with $[\text{Fc}(\text{BAR}_4^{\text{F}})]$ to the EPR active species, i.e. no in-depth analysis of the molecule was possible. This is shown in Figure 4.19. Instead of giving Fe^{I} and Fe^{II} species in a 1:1 ratio, Fe^0 and Fe^{II} species are obtained in a 3:1 ratio due to disproportionation of the oxidised species of the first intermediate along the synthetic route towards the functionalised molecule. The fit parameters are given in Table A.8.

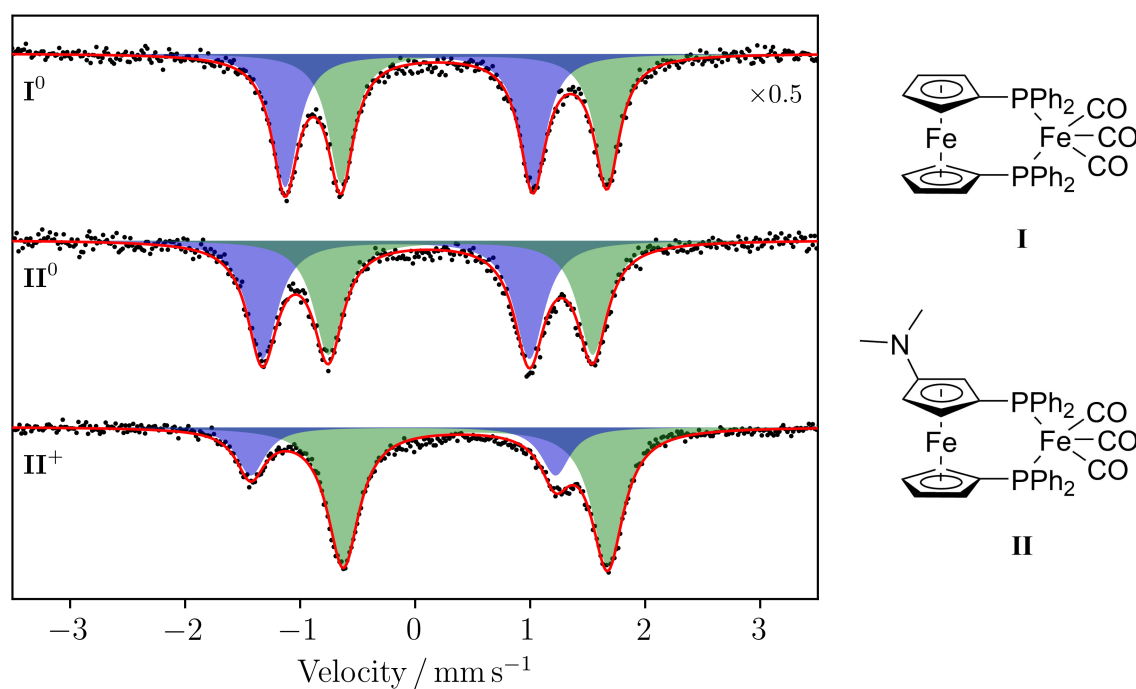
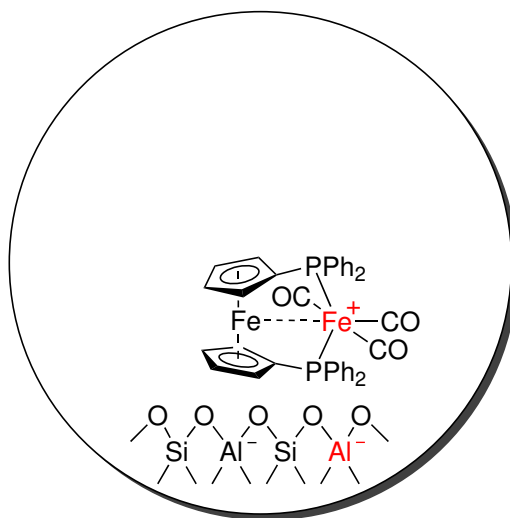


Figure 4.19: Mössbauer spectra of I^0 , the first derivative in the functionalisation of the probe molecule to generate the click-ready species II^0 and its oxidised species II^+ measured at 80 K.

Quite probably, the reaction required for the catalysis would then also not be possible because of the instability of the oxidised species. Alternatively, it was tried to immobilise the oxidised and charged catalyst I^+ by ion pairing to charged aluminium species incorporated into the porous SBA-15 framework (Scheme 5). [225] The ATR-IR spectra of the neutral and oxidised molecule as well as the catalyst in the pores is shown in Figure 4.20A. Figure 4.20B shows the EPR spectrum of the molecule in the pores.

**Scheme 5**

The IR spectrum of the immobilised molecule looks remarkably similar to that of the neutral species, suggesting the reduction of the compound in SBA-15. The difference in the IR spectra is explained by weaker back donation into π^* in the oxidised species, increasing the bond strength. The absence of an EPR signal proves that no open-shell system is apparent in the system. In conclusion, **I** is not suited for catalysis in pores due to the low stability of the oxidised species that is of importance during redox reactions. Hence, it was decided to use the organic radical TEMPO as a simpler and more robust system to investigate the behaviour of immobilised molecules. The results are presented in the next Chapter.

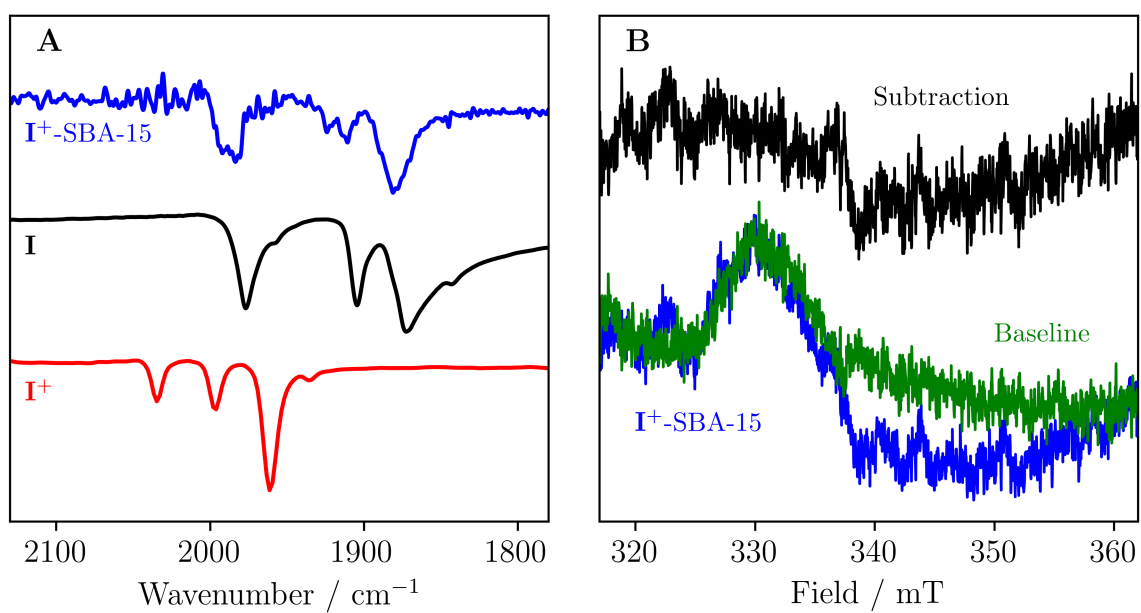


Figure 4.20: ATR-IR (A) and EPR (B) spectra of I^+ in ionic SBA-15 material.

5 Chemically Immobilised Radicals in Mesopores

As was briefly discussed in the previous Chapter, resource depletion has driven research towards finding of new catalysts to achieve higher resource efficiency as well as new and alternative catalysis routes. This Thesis deals with the impact of immobilisation into mesopores on the electronic and geometric structure of a molecule. It was shown in the previous Chapter that the chemical immobilisation of the probe molecule (dppf)Fe(CO)₃ proved impossible in the scope of this work. As an alternative, the radical TEMPO was chosen as it offers multiple functionalisation possibilities. The synthesis of the click-ready derivatives 4-azido-TEMPO and 4-propargyl ether TEMPO have been reported. [45, 46] These allow for the click reaction to take place in the pores under investigation by means of click chemistry. [45, 226–228] TEMPO was shown to be catalytically active in both COFs and metal organic frameworks. [229] Furthermore, TEMPO is a well studied material, making the observed changes in the electronic and geometric structure due to the immobilisation much easier to understand. The molecule has a long history of being used as a spin probe due to its high sensitivity towards rotational mobility in EPR spectroscopy and straightforward means of determining spin-spin distances between two TEMPO radicals by means of pulsed EPR. Thus, it finds application in the structure determination of biomolecules such as large proteins. [50, 230–232] In porous structures, the individual catalyst molecules are statistically distributed in the systems under investigation, making methods such as X-Ray or NMR spectroscopy infeasible as the small differences in the surroundings of the different molecules lead to a broadening of the spectral lines even before immobilisation, which can make it impossible to distinguish the spectral features of the probe molecule from those of the surrounding. Localising the measured property, e.g. the much stronger magnetic moments of the electron spins, on a few atoms makes it possible to understand the effect of the immobilisation on the electronic and geometric structure.

In this Chapter, the organic radical TEMPO is presented both in its unfunctionalised and click-ready forms as well as immobilised in the porous materials, including covalent organic frameworks (COFs), SBA-15 and ordered mesoporous carbon (OMC). The work presented in this chapter was carried out in close cooperation with Sebastian Emmerling (Max-Planck-Institut für Festkörperforschung, Stuttgart, group of B. Lotsch) who synthesised the COFs, Ann-Katrin Beurer (Universität Stuttgart, group of Y. Traa) who synthesised the SBA-15 materials, Charlotte Vogler (Universität Stuttgart, group of S. Naumann) who synthesised the mesoporous carbon material, Florian Diehl (Universität Stuttgart, group of J. van Slageren, under the supervision of the author of this thesis)

who helped with the investigation of the COFs and Lukas Bauder (Universität Stuttgart, group of J. van Slageren, under the supervision of the author of this thesis) who helped with the investigation of the SBA-15 materials. The DEER measurements on the functionalised COFs presented at the end of the chapter were performed by Edmund Little (University of Manchester, group of F. Tuna).

In the following sections, the advantages of the TEMPO radical are presented in more detail (Section 5.1) and the electronic structure of TEMPO and its click-ready derivatives, as determined via continuous wave and pulsed EPR, is shown (Section 5.2). Subsequently, the immobilisation into the different porous materials (COF, SBA-15 and OMC in Sections 5.3, 5.4 and 5.5, respectively) is given and the changes in the electronic and geometric structure due to the immobilisation are highlighted.

5.1 Why TEMPO? The Advantages of the Organic Radical as a Probe Molecule

The stable organic radical TEMPO has numerous advantages over most other paramagnetic compounds for the research goals of this Thesis. First of all the narrow EPR linewidths mean that an EPR signal can be observed even for small amounts of spins, which is expected after the immobilisation in the porous materials. This is an advantage especially compared to transition metals, where unresolved hyperfine splittings and shorter lifetimes of the excited spin states substantially broaden the absorption lines. Furthermore, the unique hyperfine splitting pattern from the coupling to one nitrogen nucleus make the EPR signal easily distinguishable from that of other organic radicals. This is of advantage particularly for low numbers of radicals since most spurious background signals are single-line absorption spectra of paramagnetic impurities with g values close to g_e . Most importantly, the EPR signal of TEMPO is sensitive to the mobility of the molecule and distances to nearby electron spins, see Figure 5.1 that visualises the dependence of the EPR spectrum on the exchange frequency and the rotational correlation time. The two parameters therefore give a very good understanding of the mobility of immobilised catalysts inside mesopores, potentially explaining the catalytic behaviour of similar catalysts.

TEMPO is a very well studied organic radical both in terms of its electronic and geometric structure [16, 47, 233, 234] and its applications in synthesis for the catalytic oxidation of alcohols [17, 18, 49, 235]. It was shown that the unpaired electron is located in the p_z orbital of the nitrogen nucleus that is perpendicular to the CCNO plane. The unpaired electron resides mainly in this p_z orbital. [47, 233] Contrary to the convention of $g_{zz} \geq g_{yy} \geq g_{xx}$ for systems where the orientation of the g tensor in the molecule is

unknown, for TEMPO it is g_{xx} that has the largest value. Because of the orientation of the orbital that carries the unpaired electron in z direction and the dipolar nature of the coupling between the electron spin and the nitrogen nucleus, A_{zz} is much larger than the other two components of the A tensor. For purely dipolar coupling and the unpaired electron being positioned in the nitrogen p_z orbital, an axial A tensor would be expected. Due to the weak hyperfine coupling in x and y these hyperfine values can not be determined accurately from EPR spectra, where the splitting is unresolved. The influence of the surrounding of the molecule on A_{zz} has also been well studied [21, 48], making it useful as a probe for the immediate surrounding of the catalysts, potentially indicating whether or not the radical is collapsed to the pore wall or pointing to the centre of the pore.

This extensive knowledge about the radical and its relatively simple chemical functionalisation make it one of the most common spin labels used to investigate the structure of proteins. [19, 20, 50, 236–238] To do so, the radicals are attached to the protein in known positions and the spin-spin distances are measured with double electron-electron resonance (DEER) spectroscopy, a pulsed EPR technique. [19, 20, 237, 238]

These attributes make TEMPO the perfect probe molecule to investigate the behaviour of catalysts in porous structures. In the next Sections, the electronic and geometric structure of TEMPO and its click-ready derivatives and the influence of the immobilisation in the pores on the electronic structure and the mobility of the TEMPO radical are presented. The static electronic structure was investigated with continuous wave EPR and the spin relaxation was determined with pulsed EPR. Finally, the TEMPO-TEMPO distances as determined from DEER spectroscopy are presented.

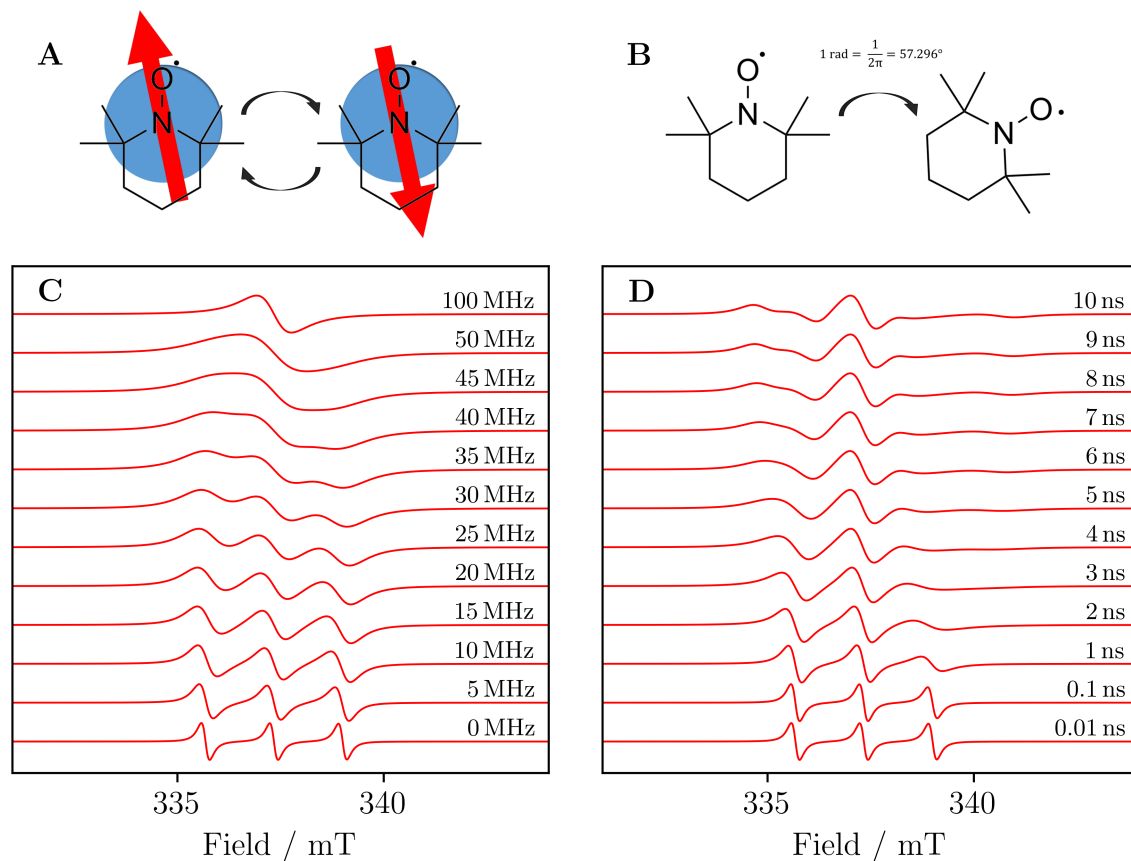
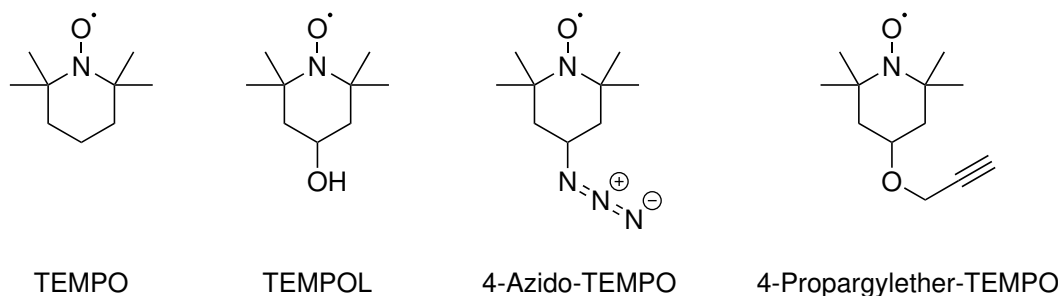


Figure 5.1: Visualisation of the influences of the exchange interaction, i.e. the frequency of spin exchange between two neighbouring molecules, depicted in the sketch in (A), and the rotational correlation time t_{corr} , i.e. the time it takes for the molecule to rotate by one radian as depicted in (B) on the EPR spectrum of the TEMPO radical. The EPR spectra for different exchange interaction strengths are shown in (C) and the EPR spectra for different rotational correlation times are shown in (D). All simulations are performed with the chili function in EasySpin with the parameters $g_{xx} = 2.009$, $g_{yy} = 2.006$, $g_{zz} = 2.002$ and an anisotropic hyperfine interaction to the nitrogen nucleus of $A_{xx} = A_{yy} = 20 \text{ MHz}$, $A_{zz} = 100 \text{ MHz}$. In all cases the natural, Lorentzian linewidth is $\Gamma_L = 0.2 \text{ mT}$ and the microwave frequency is set to $\nu_{\text{MW}} = 9.47 \text{ GHz}$.

5.2 The Electronic Structure of TEMPO and its Click-Ready Derivatives

The aim of this Chapter is to examine the changes in the electronic structure of the radical that result from the chemical immobilisation into mesopores. The first step was to investigate the influence of the functionalisation of the molecule. In the following, the electronic structures (Section 5.2.1), mobilities in different matrices (Section 5.2.2) and spin dynamics (Section 5.2.3) of the radicals TEMPO, TEMPOL and the click-ready derivatives 4-azido-TEMPO and 4-propargyl ether TEMPO are presented. Herein, the variation in the g and A tensors as well as the spin dynamics of the functionalised compound in respect to TEMPO give a better understanding of how the chemical alteration affects the electronic structure. The chemical structures of the four compounds are shown in Scheme 6.



Scheme 6: Chemical structures of the derivatives of TEMPO investigated in this Section.

The syntheses of the azide- and alkyne-functionalised derivatives are known from literature and given in Section 6.2.

5.2.1 The Static Electronic Structure - The g and Hyperfine Tensors

EPR spectroscopy is a very powerful tool to investigate open-shell molecules and was used almost exclusively in the determination of the electronic structure of the paramagnetic compounds of interest in this Chapter. The most important parameters that can be obtained from the simulation of EPR spectra are the components of the g and A tensors that give an idea of the localisation of the unpaired electron, as well as the linewidths and lineshapes that give an indication of the mobility of the molecule and the strengths of interactions of the electron spin with the immediate surrounding of the paramagnetic molecules. The resolution of the g tensor is the highest at large microwave frequencies and magnetic fields, while the components of the A tensor are often unresolved at these high magnetic fields due to increased linewidths due to faster spin relaxation in high magnetic fields. The EPR spectra of TEMPO in frozen solutions at X-Band and Q-Band frequency

as well as TEMPO in polystyrene measured at 320 GHz are shown in Figure 5.2 to show some of the advantages of the different available frequency ranges in EPR spectroscopy. In the available HFEPR set-up, it was not possible to measure frozen solutions and polystyrene was chosen as the diamagnetic matrix to measure the magnetically diluted sample. High microwave frequencies allow for a precise determination of the g tensor while low microwave frequencies allow for a more accurate determination of the A tensor due to smaller linewidths. The simulation parameters are given in Table 5.1.

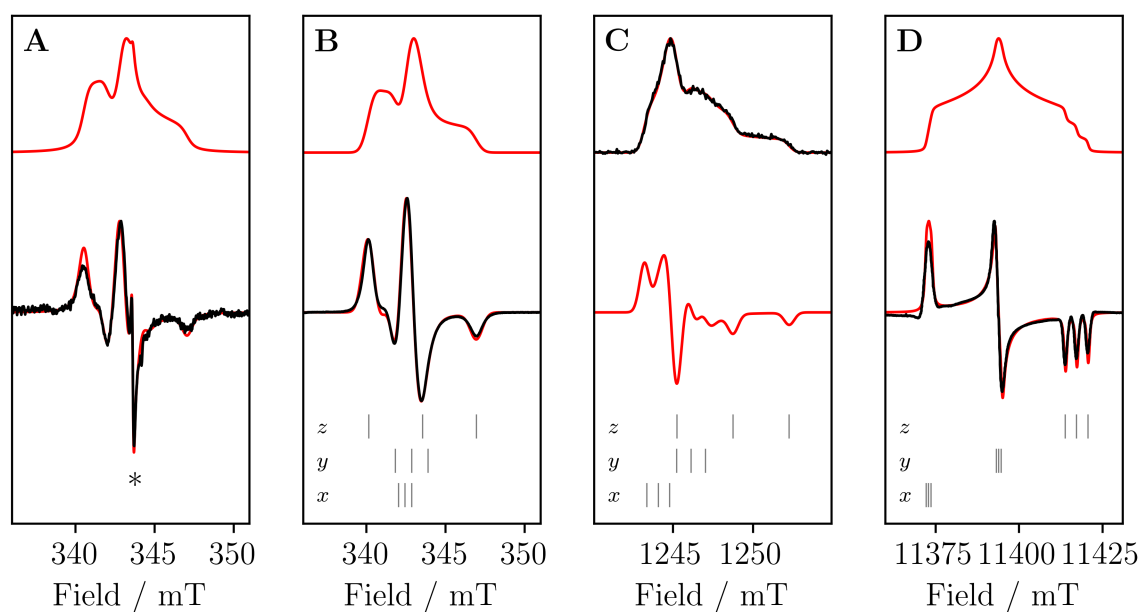


Figure 5.2: A) EPR spectra (black) of TEMPO in a $10 \mu\text{mol l}^{-1}$ frozen solution in DCM:toluene (1:1) at 140 K and 9.63 GHz with dpph ($g = 2.0036$, marked with an asterisk) powder in a sealed tube immersed into the solution. B) EPR spectrum of TEMPO in a 1 mmol l^{-1} frozen solution in DCM:toluene (1:1) at 140 K and 9.63 GHz. C) EPR spectrum of TEMPO in a 1 mmol l^{-1} frozen solution in DCM:toluene (1:1) at 7 K and 35 GHz. D) EPR spectrum of TEMPO in a $100 \mu\text{mol g}^{-1}$ droplet of polystyrene at 70 K at 320 GHz (D). The simulation (red) parameters are given in Table 5.1.

As even small uncertainties in the magnetic fields have a big influence on the determined g values, it is best practice to use a relative method to determine the components of the g tensor, e.g. in a simultaneous measurement of the unknown sample and a reference compound with known g values such as the organic radical dpph. [239] This measurement is shown in Figure 5.2A. As g_{zz} can be determined with the highest precision due to the unambiguous attribution of the three signals resulting from the large hyperfine interaction with the nitrogen nucleus, the spectra for the other frequencies were field corrected to give $g_{zz} = 2.0025$ as was determined in the measurement with dpph at X-Band. This allows

the interpretation of the relative changes of the g tensor components. From the simulation parameters given in Table 5.1 it becomes clear that there is a small dependence of g_{xx} on the magnetic field. The difference corresponds to a shift of the resonance frequency by ca. 0.2 mT in X-Band which is larger than the experimental accuracy. This change could be due to the temperature or magnetic field. In literature, slight increases of g_{xx} and slight decreases of g_{zz} are reported for lower temperatures through the temperature dependence of the oxygen vibrations. [240] Another important influence on the spectrum is the matrix, especially the dielectric constant of the same, making comparisons of the spectra difficult. [21]

Additionally, the hyperfine tensor changes with frequency. A_{iso} decreases slightly from 45.4 MHz at X-Band to 45.0 MHz at 320 GHz but as the hyperfine splitting is unresolved at high magnetic fields, it is impossible to determine these values precisely and only the upper limit to A is available. Assuming that the error in A is 0.1 MHz at ca. 10 GHz and 1 MHz above 100 GHz, the two values for A_{iso} are the same within experimental certainty. In literature, the dependence of A on the temperature, frequency and matrix are discussed and are of similar magnitude as observed here. [21, 47, 240] Nonetheless, the most reliable change is that of the lineshape. At low magnetic fields, the line is of Gaussian shape, indicating underlying unresolved hyperfine coupling to the surrounding hydrogen nuclei. Since this splitting is smaller at higher fields, relative to the natural linewidth, it has a less important contribution and a more Lorentzian lineshape can be observed. In order to better resolve the A tensor, ENDOR spectroscopy would be very helpful.

Table 5.1: Simulation parameters of the spectra shown in Figure 5.2.

	9.63 GHz	35 GHz	320 GHz
g_{xx}	2.0090(5)	2.0100(5)	2.0103(1)
g_{yy}	2.0066(5)	2.0067(5)	2.0066(1)
g_{zz}	2.0025(5)	2.0025(5)	2.0025(1)
A_{xx} / MHz	11.9(1)	20.0(1)	< 20(1)
A_{yy} / MHz	28.9(1)	25.3(1)	< 20(1)
A_{zz} / MHz	95.3(1)	98.0(1)	95(1)
$\Delta B_{\text{pp,G}}$ / mT	0.76(5)	0.63(5)	0.50(5)
$\Delta B_{\text{pp,L}}$ / mT	0	0	0.40(5)

In order to further investigate the influence of the polarity of the matrix, especially to understand the differences of immobilised TEMPO in COFs and SBA-15, a sample of

TEMPOL immobilised in trehalose was prepared by dissolving both solids in the desired ratio in water and letting the solvent evaporate while stirring. A molecular dilution is possible as the hydrogen bonds between TEMPOL and water are replaced with hydrogen bonds to the OH-groups in trehalose. [16] The room temperature EPR spectra of the different dilutions of TEMPOL in the sugar are shown in Figure 5.3, the simulation parameters are given in Table 5.2.

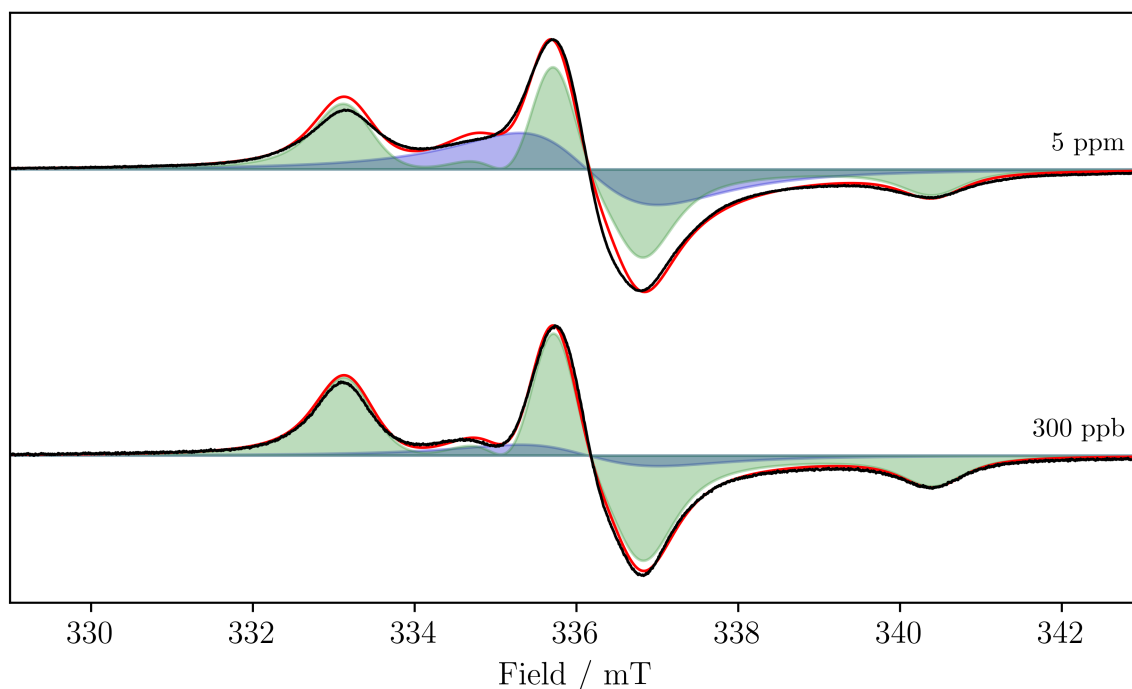


Figure 5.3: Room temperature EPR spectra of TEMPOL in trehalose at two different mass concentrations of TEMPOL (black) and simulations (red) with the two subspectra in green and blue.

The decrease in g_{xx} compared to the measurement of TEMPOL in frozen solution in DCM:toluene can be explained by residual water (determined to be ca. 7% when drying at a reduced pressure of 1 mbar [241]) in the TEMPOL-Trehalose sample as the mixture ($\epsilon_{\text{mixture}} = x_1\epsilon_1 + x_2\epsilon_2$) of DCM ($\epsilon' = 8.7$ at 1.8 MHz [242]) and toluene ($\epsilon' = 2.4$ at 1 MHz [243]) has a very similar dielectric constant as trehalose ($\epsilon' = 4$ at 1 MHz [244]). A higher permittivity leads to lower g_{xx} and higher A_{zz} as the electron density is pulled away from the nitrogen nucleus towards the oxygen atom. [21, 245] The increase in the hyperfine interaction can be explained through an increase of the spin density on the nitrogen nucleus which in turn happens because of a decrease of the energy of the oxygen p_z orbital with respect to the nitrogen p_z orbital energy in a polar surrounding. This results in an increased nitrogen character of the antibonding orbital with the unpaired electron, i.e. more spin

density on the nitrogen nucleus and an increased hyperfine coupling strength. Both of the mentioned trends are observed in TEMPOL-Trehalose. Furthermore, it was necessary to include a second spin system in the simulation of the 300 ppb sample. This indicates higher local concentrations of the radical than assumed for a homogeneous distribution of the molecules, leading to an exchange-broadened line that does not show hyperfine splitting. This second spin system is even better visible in the 5 ppm sample that clearly has a much broader linewidth. This becomes especially obvious in the shoulder at ca. 335 mT.

Table 5.2: Simulation parameters of the X-Band EPR spectra of TEMPOL-Trehalose at mass concentrations of 5 ppm and 300 ppb (g g^{-1}) of the radical measured at room temperature.

	5 ppm	300 ppb
g_{xx}	2.0088(5)	
g_{yy}	2.0075(5)	
g_{zz}	2.0025(5)	
A_{xx} / MHz	16.0(1)	
A_{yy} / MHz	20.0(1)	
A_{zz} / MHz	101.5(1)	
$\Delta B_{\text{pp,G},1} / \text{mT}$	0.38(5)	
$\Delta B_{\text{pp,L},1} / \text{mT}$	0.42(5)	
$\Delta B_{\text{pp,G},2} / \text{mT}$	0.0	
$\Delta B_{\text{pp,L},2} / \text{mT}$	1.50(5)	
$x_1 / \%$	63(5)	87(5)

In order to investigate the influence of the functional groups that allow for the click reaction to take place on the EPR spectrum and therefore the electronic structure of the radical, EPR spectra were measured of samples of TEMPO, TEMPOL, 4-azido-TEMPO and 4-propargyl ether TEMPO in liquid and frozen solutions at concentrations (see the caption of Figure 5.4) where the exchange interaction is negligible, compare Section 5.2.2. All spectra are shown in Figure 5.4 and the simulation parameters are given in Table 5.3. All samples were measured in a double resonator first with and then without dpph powder in the second cavity, which allows a more precise determination of the g values without an overlapping dpph signal in the latter case since both cavities are tuned simultaneously and no retuning of the microwave to the resonator is necessary for a subsequent measurement. The measurement without dpph then allows for a more precise simulation of the spectrum.

Most notably, g_{xx} , A_{xx} and A_{zz} increase in the functionalised radicals compared to

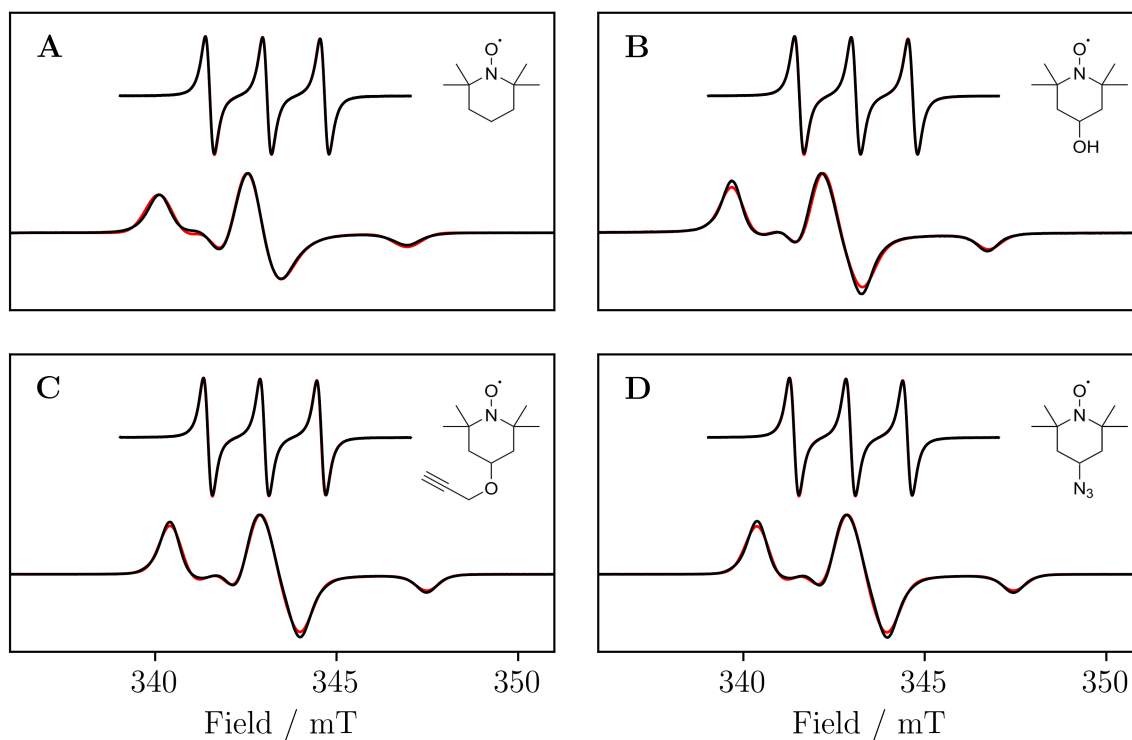


Figure 5.4: EPR spectra of TEMPO (1 mmol l⁻¹) (A), TEMPOL (0.2 mmol l⁻¹) (B), 4-propargyl ether TEMPO (1 mmol l⁻¹) (C) and 4-azido-TEMPO (1 mmol l⁻¹) (D) in DCM:toluene (1:1) at room temperature (top) and 140 K (bottom). The simulation (red) parameters are given in Table 5.3.

TEMPO, whereas g_{zz} and A_{yy} decrease, making the g tensor more rhombic and the A tensor more axial in the X-Band measurements. This trend cannot be observed in the spectra of the same compounds at 35 GHz and 7 K in frozen solutions in DCM:toluene (1:1) (Table A.9). It is unclear whether the compounds have a different temperature dependence of the principal values of the g and A tensors as they are all the same within experimental error. Neither spectrum could be reproduced with the simulation parameters obtained at the other microwave frequency. As these changes are very small in any case this behaviour was not further investigated and instead the mobility and exchange interaction of the molecule was focused on.

Table 5.3: Fit parameters of the TEMPO derivatives measured at X-Band. The principal values of the g and A tensor were determined from the measurement in frozen solution (DCM:toluene (1:1)) at 140 K, g_{iso} , A_{iso} and t_{corr} were determined from the fluid solution measurements at room temperature. The difference in g_{iso} and A_{iso} and the respective averages of the individual values can be explained with the temperature dependence of these values.

	TEMPO	TEMPOL	4-Propargyl ether TEMPO	4-Azido- TEMPO
g_{xx}	2.0090(5)	2.0095(5)	2.0097(5)	2.0097(5)
g_{yy}	2.0066(5)	2.0064(5)	2.0064(5)	2.0064(5)
g_{zz}	2.0025(5)	2.0024(5)	2.0022(5)	2.0022(5)
g_{iso}	2.0062(5)	2.0062(5)	2.0062(5)	2.0063(5)
A_{xx} / MHz	11.9(1)	19.9(1)	19.1(1)	19.1(1)
A_{yy} / MHz	28.9(1)	20.3(1)	19.3(1)	19.3(1)
A_{zz} / MHz	95.3(1)	98.7(1)	98.5(1)	98.5(1)
A_{iso} / MHz	44.4(1)	43.9(1)	43.8(1)	43.8(1)
$\Delta B_{\text{pp,G,140K}}$ / mT	0.76(5)	0.49(5)	0.58(5)	0.63(5)
$\Delta B_{\text{pp,L140K}}$ / mT	0	0.23(5)	0.10(5)	0.07(5)
$\Delta B_{\text{pp,G,RT}}$ / mT	0.11(5)	0.10(5)	0.10(5)	0.12(5)
$\Delta B_{\text{pp,L,RT}}$ / mT	0.20(5)	0.20(5)	0.20(5)	0.20(5)
t_{corr} / ps	12.6(1)	12.6(1)	12.6(1)	12.6(1)

5.2.2 The Mobility of the Radical in different Matrices as a Model for Chemically Immobilised Species

In order to better understand the behaviour of TEMPO radicals in different matrices at various concentrations, samples were prepared in solution (toluene), frozen solution (DCM:toluene) and polymer matrix (polystyrene). Figure 5.5 shows the EPR spectra of highly mobile TEMPO in toluene at room temperature and X-Band frequency.

The simulations (see Table 5.4) give a clear answer to how the exchange interaction and mobility of the individual molecules depend on the concentration, i.e. the average TEMPO-TEMPO distance. The distances between the molecules are calculated with Equation 5.1 under the assumption that every molecule occupies the volume of a sphere with sphere-packing of 74 % [246] of the total volume. From the known number of molecules and the volume of the solution, the radius of these spheres can be calculated.

$$R_{\text{sphere}} = \sqrt[3]{\frac{3}{4\pi} V_{\text{sphere}}} \quad \text{with} \quad V_{\text{sphere}} = \frac{74.048 \%}{N_{\text{A}} \cdot c} \quad (5.1)$$

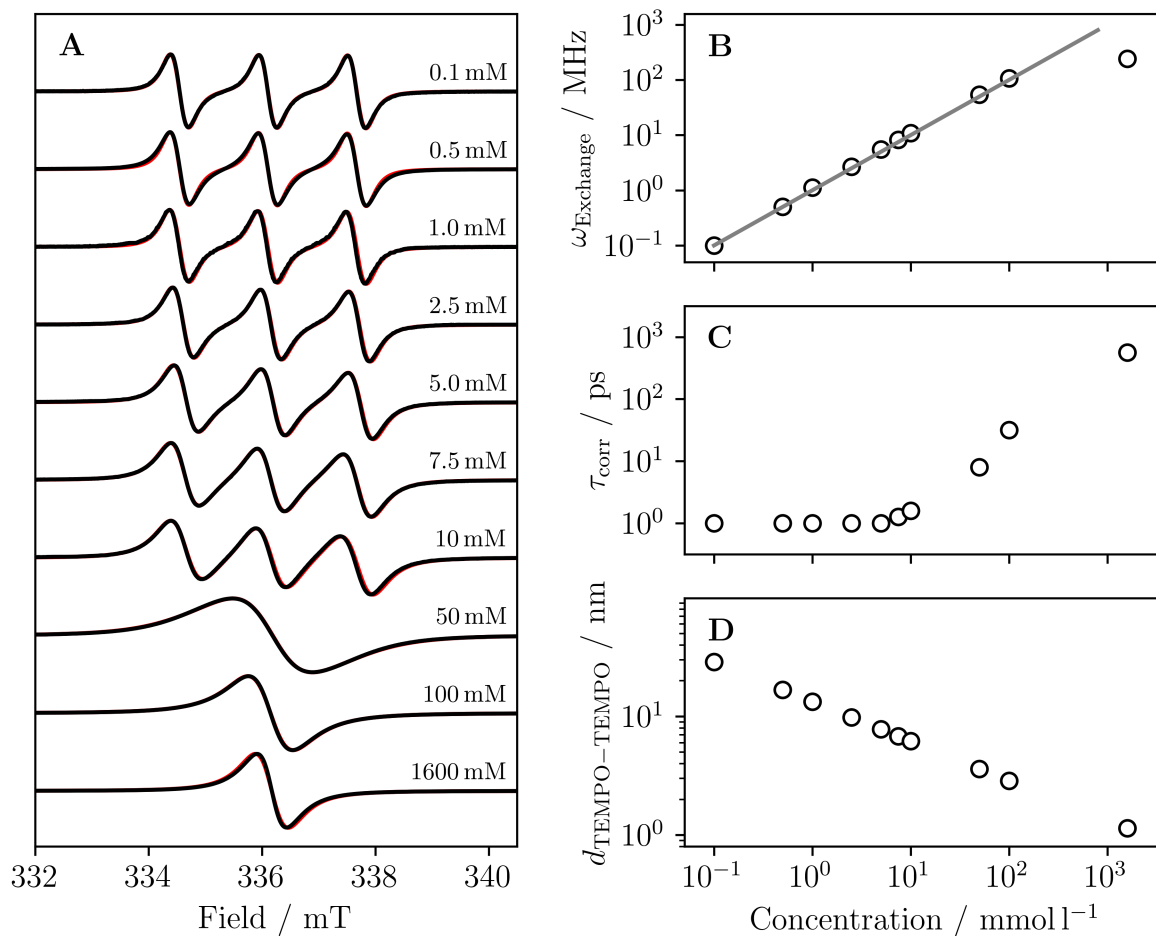


Figure 5.5: Room temperature X-Band EPR spectra of TEMPO in toluene at different concentrations with the varying simulation parameters exchange coupling strength ν_{Exchange} , rotational correlation time τ_{corr} and the average distance between the molecules for each concentration.

The exchange interaction increases for higher concentrations and leads to a broadening of the spectrum as the radical-bearing orbitals overlap more frequently since molecules have to travel smaller distances when the average TEMPO-TEMPO distance is smaller. At a certain point a higher exchange frequency does not lead to a further increase of the linewidth. At that point, the hyperfine interaction of the electron spin with the nitrogen nucleus is averaged out due to the fast flipping of the electron spin. The three lines start to collapse into one and the linewidth decreases. At a certain point the linewidth does not further decrease. This happens when the natural linewidth due to the lifetime of the state (determined by T_2) is reached. Then, an increase in the exchange frequency can not be observed experimentally. Additionally, a decrease of the mobility can be seen in the increased rotational correlation time, i.e. how long it takes a molecule to rotate by one

radian. For TEMPO $\tau_{\text{corr}} < 1$ ps can not be observed experimentally as X-Band frequency as the spectrum does not change above these high rotational mobilities.

Table 5.4: Simulation parameters for the different concentration of TEMPO in toluene at room temperature shown in Figure 5.5. For all concentrations $g_{xx} = 2.0101(5)$, $g_{yy} = 2.0066(5)$, $g_{zz} = 2.0025(5)$, $A_{xx} = 12.4(1)$ MHz, $A_{yy} = 24.7(1)$ MHz, $A_{zz} = 94.7(1)$ MHz.

$c / \text{mmol l}^{-1}$	$\nu_{\text{Exchange}} / \text{MHz}$	$\tau_{\text{corr}} / \text{ps}$
0.1	0.1(1)	< 1
0.5	0.5(1)	< 1
1.0	1.1(1)	< 1
2.5	2.7(1)	< 1
5.0	5.5(1)	< 1
7.5	8.3(1)	1.3(1)
10	10.9(1)	1.6(1)
50	53.9(1)	7.9(1)
100	106.8(1)	31.6(1)
1600	241.0(1)	562.3(1)

The fact that the exchange interaction depends strongly on the rotational mobility of the molecules can be seen in Figure 5.6 where EPR spectra of frozen solutions of TEMPO in DCM:toluene (1:1) measured at 140 K are shown.

At $c = 60 \text{ mmol l}^{-1}$ only a partial broadening of the powder-like spectrum can be observed in the glassy solid matrix, whereas in solution the hyperfine-split EPR lines collapsed into one broad line already at $c = 50 \text{ mmol l}^{-1}$. Another matrix material that was studied here is polystyrene. The EPR spectra of polystyrene films with different mass fractions of TEMPO are shown in Figure 5.7.

With densities $\rho_{\text{polystyrene}} \approx 1$, a concentration of 1 wt.-% corresponds to a molarity of 65 mmol l^{-1} . For similar concentration the mobility in solutions is much higher than in a polystyrene matrix. Nonetheless a much higher mobility in polystyrene than in frozen solution is observed. This is not a new finding and the mobility of molecules in polystyrene matrices is well-studied. [247–249] The simulations could be improved by adding a second species with just one broad line, indicative of an exchange-broadened TEMPO signal that is the result of high local concentration due to a inhomogeneous distribution of radicals in the matrix. It is likely that this aggregation happened after the dropcasting as a homogeneous distribution is expected in solution, especially at 60°C , at which temperature the films were prepared.

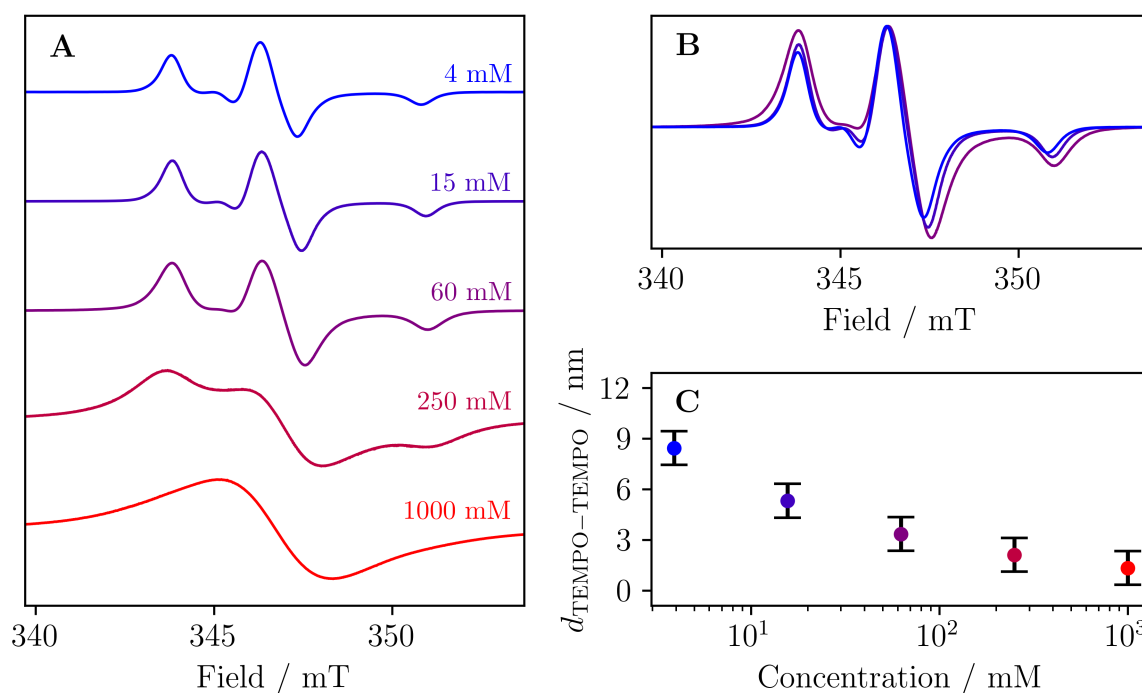


Figure 5.6: EPR spectra of TEMPO in frozen solutions of DCM:toluene (1:1) measured at 140 K in different concentrations.

The exchange interactions were also studied by means of SQUID magnetometry, where spin-spin interactions lead to a decrease of the susceptibility-temperature product compared to the interaction-free value $\chi T = 0.375 \text{ K cm}^3 \text{ mol}^{-1}$ that is expected from the Curie law for a $g = 2$ and $S = 1/2$ system in CGS units, where the natural constants are approximately equal to $1/8 \text{ K cm}^3 \text{ mol}^{-1}$, see Equation (5.2).

$$\chi T = \frac{\mu_B^2}{3k_B} g^2 S(S+1) \approx \frac{1}{8} g^2 S(S+1) \quad (5.2)$$

Such a decrease of χT going towards lower temperature can be observed in Figure 5.8 where a TEMPOL pellet and the film of TEMPO with a mass concentration of 10 wt.-% in polystyrene show a much gentler rise for χT than the film with a mass concentration of 1 wt.-%. Due to the high diamagnetic susceptibility of the heavily diluted sample, the paramagnetic moment is buried in the much higher diamagnetic moment of the matrix above ca. 20 K. This makes SQUID magnetometry not very useful for the analysis of diluted samples as is the goal in this thesis. Nonetheless, the exchange interaction is visible in SQUID magnetometry.

In this Section, the dependence of the electronic structure of TEMPO in different matrices was studied. The line shape gave some information on the dynamics of the

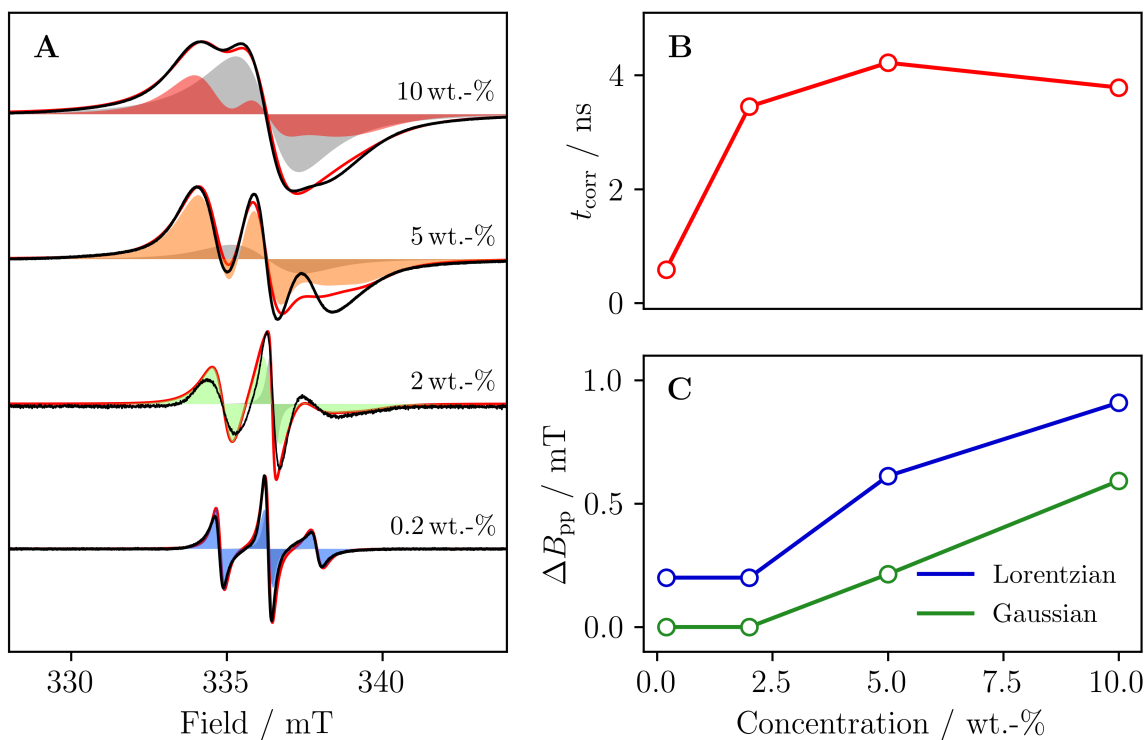


Figure 5.7: A) EPR spectra (black) and simulations (red) of TEMPO in polystyrene at different concentrations of TEMPO measured at room temperature. B) Rotational correlation times versus the concentrations. C) Linewidths of the mobile species in dependence of the concentration. The simulation parameters for both the mobile species (colored) and the exchange-broadened species (grey) are given in Table 5.5.

system. More detailed information about the dynamics can be obtained from pulsed EPR spectroscopy, as described in the next Section.

Table 5.5: Simulation parameters for TEMPO in Polystyrene with $g_{xx} = 2.0095(5)$, $g_{yy} = 2.0065(5)$, $g_{zz} = 2.0025(5)$, $A_{xx} = 5.0(1)$ MHz, $A_{yy} = 30.0(1)$ MHz, $A_{zz} = 96.0(1)$ MHz for all simulations.

	0.2 wt.-%	2 wt.-%	5 wt.-%	10 wt.-%
$t_{\text{corr}} / \text{ns}$	0.6(1)	3.5(1)	4.2(1)	3.8(1)
$\Delta B_{\text{pp,G}} / \text{mT}$	0	0	0.20(5)	0.60(5)
$\Delta B_{\text{pp,L}} / \text{mT}$	0.20(5)	0.20(5)	0.60(5)	0.90(5)
$x_{\text{TEMPO,exchange}} / \%$	14(5)	5(5)	22(5)	61(5)
$\Delta B_{\text{pp,exchange,G}} / \text{mT}$	0	0	1.30(5)	0
$\Delta B_{\text{pp,exchange,L}} / \text{mT}$	0.20(5)	0.20(5)	1.50(5)	2.00(5)

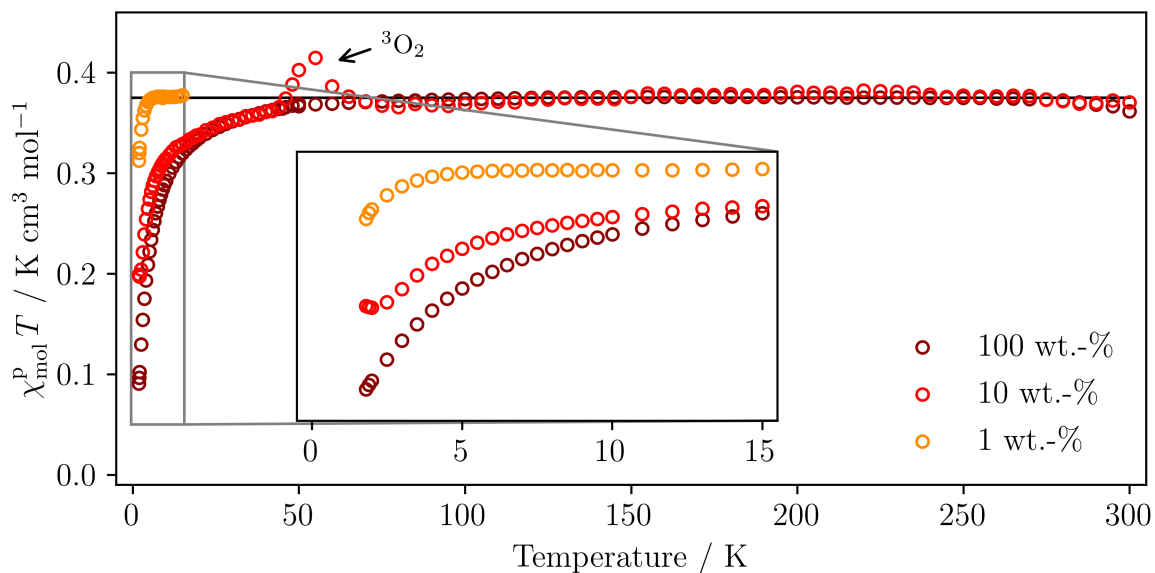


Figure 5.8: Temperature-susceptibility product for three TEMPO samples (powder pellet and dilutions in polystyrene) measured at magnetic fields of 1000 Oe between 1.8 and 50 K and 10000 Oe between 40 and 300 K.

5.2.3 The Spin Dynamics of TEMPO and its Derivatives

The spin dynamics, especially the spin-lattice relaxation T_1 can give insight into the interaction of the radical with its immediate surrounding, i.e. the matrix, since T_1 is influenced by the spin-spin distances as well as vibrational and rotational motion of the molecule which are heavily determined by the porous framework. The phase-memory time T_M is strongly dependent on the presence of nearby magnetic moments, e.g. other open-shell molecules or nuclear spins. In a first step, the field and temperature dependence of T_1 and the phase-memory time T_M are investigated in frozen solution to later compare the values to those obtained for the immobilised radical. In the following, measurements for 4-azido-TEMPO are presented in detail. All other measurements, simulations and fit parameters for TEMPO, TEMPOL, 4-propargyl ether TEMPO and TEMPOL in trehalose are discussed here and the data is given in the appendix (Section A.3.3).

Orientation dependence

Figure 5.9 shows the Q-Band EPR spectrum and relaxation times of 4-azido-TEMPO at three field positions, corresponding to g_{zz} (Pos. 3), both g_{yy} and g_{zz} (Pos. 2) and a mixture of all three principal values (Pos. 1). The relaxation in z direction is much slower than in the other two directions. This is counter-intuitive since $A_{zz} \gg A_{xx} \approx A_{yy}$ and hyperfine interaction and spin-orbit coupling are the two most important mechanisms that couple the spin states to orbital states, leading to spin relaxation, whereas the latter plays a limited role in organic radicals. [250, 251] Nonetheless, a slower relaxation for g_{zz} was also observed for TEMPONE in glassy frozen solutions in [252] where it was concluded that the relaxation rate indeed does not depend on the modulation of the hyperfine interaction through vibrations based on single-crystal measurements. Due to small changes by deuteration, the proton hyperfine interaction from the methyl groups was also excluded as the origin of the orientation dependence of T_1 . Instead the modulation of g anisotropy via vibrations was reported to be the origin of the orientation dependence of the relaxation rate. This is explained by two mechanisms. Firstly, a large number of vibrations of the C_2NO unit exist, allowing relaxation in the xy plane. Secondly, for magnetic fields in the xy plane, spin-orbit coupling mixes excited states into the p_z orbital, where the unpaired electron partially resides. Vibrations in this plane therefore modulate the spin-orbit coupling strength, causing relaxation. [252] No dependence of T_M on the field was observed here or in literature.

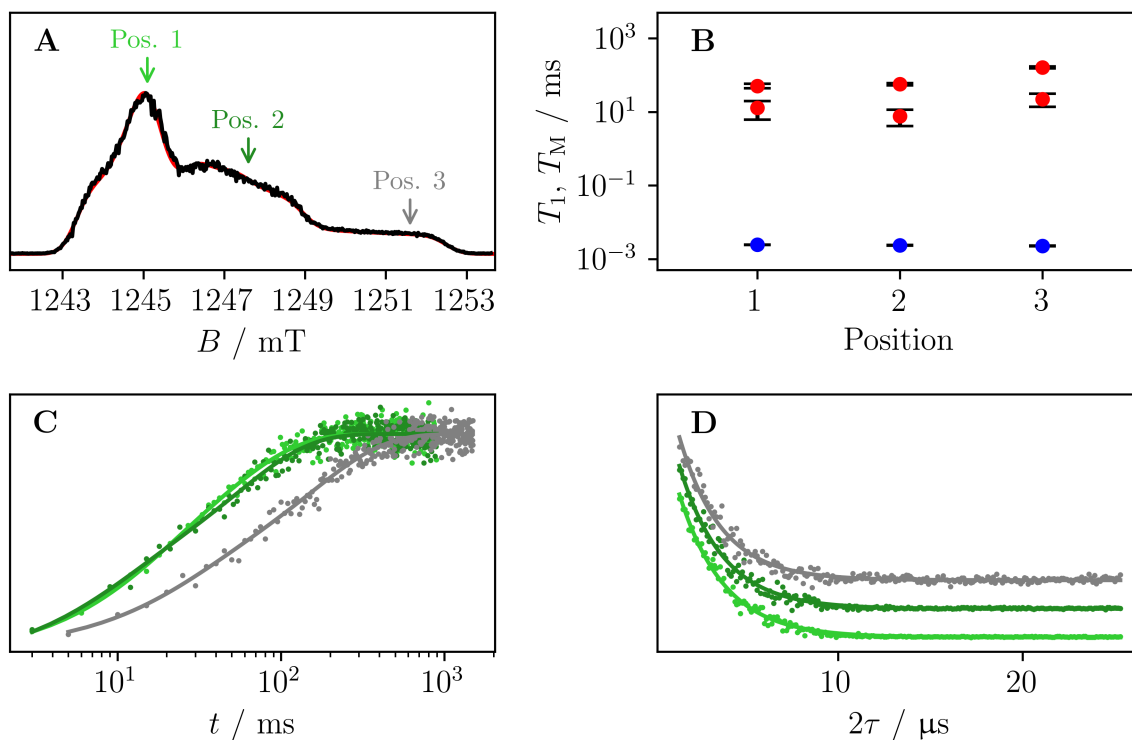


Figure 5.9: A) Echo detected EPR spectrum. B) Spin-lattice relaxation times for the fast and slow processes (red) and phase-memory times (blue) at three field positions. C) Inversion recovery decay curves. D) Hahn-echo decays. All measurements were done for 4-azido-TEMPO in a 1 mmol l^{-1} solution in DCM:toluene (1:1) at 7 K and 35 GHz.

Temperature dependence

Figure 5.10 shows the temperature dependence of T_1 and T_M and the values are given in Table A.12. The spin-lattice relaxation time decreases for increasing temperatures, as is expected because all the different relaxation pathways of direct, Raman and local mode vibrations lead to faster relaxation at higher temperatures, see Equation (5.3). [15, 253–256]

$$T_1^{-1} = c_{\text{direct}}T + c_{\text{Raman}}T^{n_{\text{Raman}}} + c_{\text{local}} \frac{e^{-\Delta_{\text{local}}T^{-1}}}{(e^{-\Delta_{\text{local}}T^{-1}} - 1)^2} \quad (5.3)$$

Direct processes are important at low temperatures, where the phonons required for two-phonon processes (Raman, Orbach) are not available. The theory behind Raman relaxation was developed for ionic centres in crystalline lattices [257] and local mode vibrations were introduced later. [253] The latter are used for the explanation of the temperature-dependence of the spin-lattice relaxation rate in molecules. The pathway for

Table 5.6: Spin-lattice relaxation times T_1 and phase-memory times T_M for three magnetic fields for 4-azido-TEMPO measured at 35 GHz and 7 K in a 1 mmol l⁻¹ frozen solution of DCM:toluene (1:1).

Pos.	g	$T_{1,\text{slow}} / \text{ms}$	$T_{1,\text{fast}} / \text{ms}$	$x_{T_{1,\text{slow}}} / \%$	$T_M / \mu\text{s}$
1	x, y, z	51(7)	13(7)	64(14)	2.43(3)
2	y, z	56(4)	8(4)	67(7)	2.35(4)
3	z	160(10)	22(9)	70(5)	2.27(5)

Raman relaxation proceeds via a virtual state through a two-phonon process. As more phonon states are populated at increasing temperatures it becomes more likely for two phonons to exist with exactly the energy difference of the excited Zeeman state for the relaxation to take place. The local mode relaxation is also a two-phonon process but it involves localised vibrations with frequencies above the Debye frequency as compared to lattice modes, i.e. phonons, in the Raman model.

For the temperature dependence of the phase-memory time no clear trend can be observed. T_M increases from 10 K to 30 K and then slowly decreases for higher temperatures, The echo intensity decreases monoexponentially at all temperatures. In literature, the temperature dependence of the phase-memory time for increasing temperatures is explained by rotations of the methyl groups in nitroxyl radicals with activation barriers of ca. 2 kcal mol⁻¹ in water:glycerol. [22] The temperature dependence below this maximum in T_M is attributed to the dynamics of the glassy solid (e.g. rotation of the methyl group and lattice vibrations in the whole molecule which lead to oscillating magnetic fields that influence spin relaxation) as observed in toluene with a decrease of T_M below ca. 40 K [23] and ethanol [24] where a maximum of T_M was observed at ca. 20 K. For the latter, this phenomenon was assumed to be related to the modulation of the dipolar coupling between electron spins through lattice vibrations and not because of the methyl groups of the nitroxyl radical or the solvent. The vibrations apparently appear due to coupling of the electron spins to lattice boson peak excitations, that can only be observed in glassy matrices. [24]

The relaxation times for all compounds investigated in this section follow the same trends as was observed for 4-azido-TEMPO and the results are shown in Figure 5.11. The spin-lattice relaxation time decreases approximately exponentially with temperature and the phase-memory time increases when going from 7 K to ca. 20 K and then drops for $T > 40$ K. The most important observations are that the spin-lattice relaxation time of TEMPOL immobilised in trehalose follows a monoexponential decay in the inversion recovery experiment, as is expected for a relatively uniform distribution of molecules in

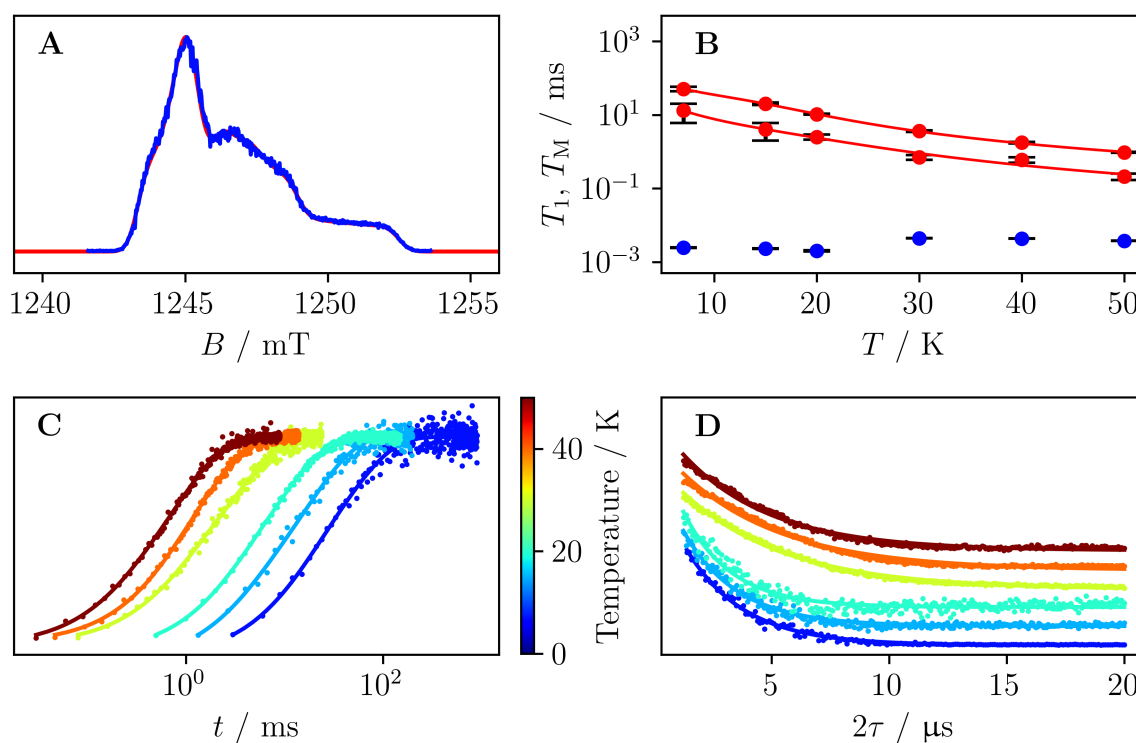


Figure 5.10: A) EPR spectrum (blue) and simulation (red) of 4-azido-TEMPO (1 mmol l^{-1} in DCM:toluene (1:1)) measured at 35 GHz and 7 K. B) Temperature dependence of the relaxation times T_1 (red) and T_M (blue) measured at peak intensity (see Figure 5.11 for a zoom on the individual relaxation processes and a comparison to the other TEMPO derivatives). Inversion recovery (C) and Hahn-echo (D) decay curves.

the matrix, but it is also faster by almost an order of magnitude compared to TEMPO in a frozen solution in DCM:toluene. This could be explained by the strong interactions of trehalose with TEMPOL via hydrogen bonds, compared to the organic solvents DCM and toluene. The hydrogen bonds that quite probably also exist to the NO oxygen would drastically alter the vibrations at the location of the radical, influencing T_1 relaxation, although it might not necessarily decrease T_1 . Surrounding ^1H nuclei could also explain the decrease in T_M .

The temperature dependence of T_1 was fitted with Equation (5.3), see Figure 5.10 and those in Section A.3.3. The fit parameters are given in Table 5.7. The data suggests that the direct process is only important for the click-ready derivatives 4-azido-TEMPO and 4-propargyl ether TEMPO. For TEMPO the local mode relaxation pathway is dominant and the spin in TEMPOL relaxes preferably via a Raman process. The relatively large number of parameters compared to the number of data points and the experimental error make the fit parameters rather unreliable due to overparameterisation. On the other

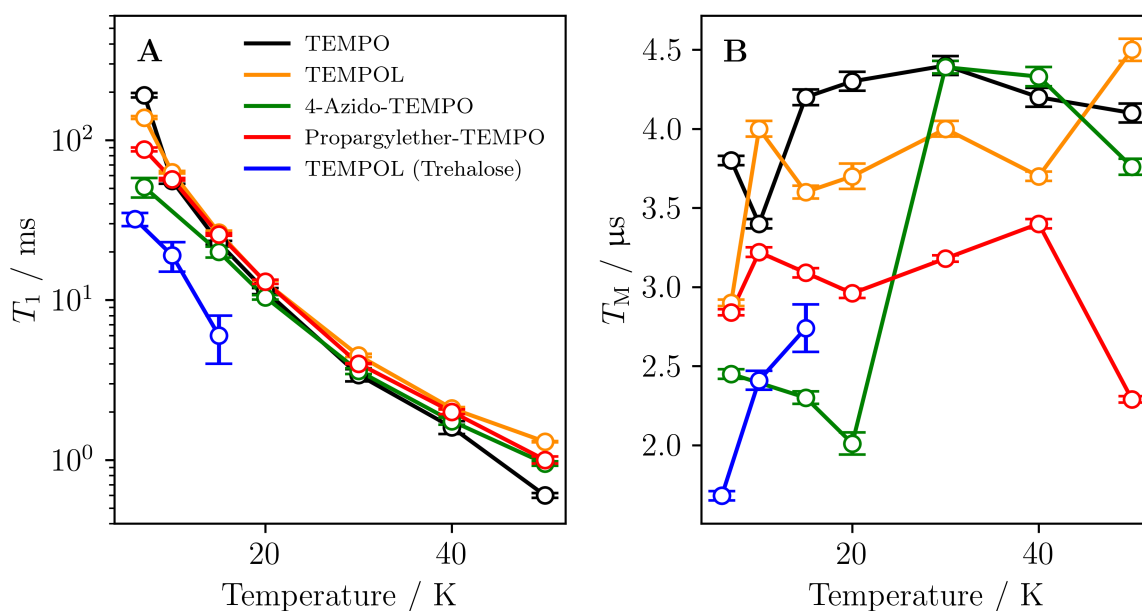


Figure 5.11: A) Temperature dependence of the slower of the process of the spin-lattice relaxation times extracted from the biexponential echo decay curves B) Phase-memory times from the monoexponential echo decay of the derivatives of TEMPO.

hand, fits where relaxation processes were omitted did not converge. Nonetheless, values similar to those reported in literature are found. For TEMPO and TEMPOL values of $c_{\text{Raman}} \approx 0.5 \text{ s}^{-1} \text{ K}^{-2}$, $c_{\text{local}} \approx 4 \cdot 10^6 \text{ s}^{-1}$ and $\Delta E_{\text{local}} \approx 1000 \text{ K}$ were observed in solutions in toluene near the melting point. [15]. Others have reported $c_{\text{Raman}} \approx 0.06 \text{ s}^{-1} \text{ K}^{-2.6}$ and only a Raman process up to 80 K for TEMPO in glassy ethanol. [255]

The largest difference in relaxation times is for the lowest temperatures, where long relaxation times are either due to the Raman and local mode relaxation pathways not being relevant or a different phonon spectrum that decreases the number of available phonons for relaxation. Further conclusions are unreliable based on these data sets alone.

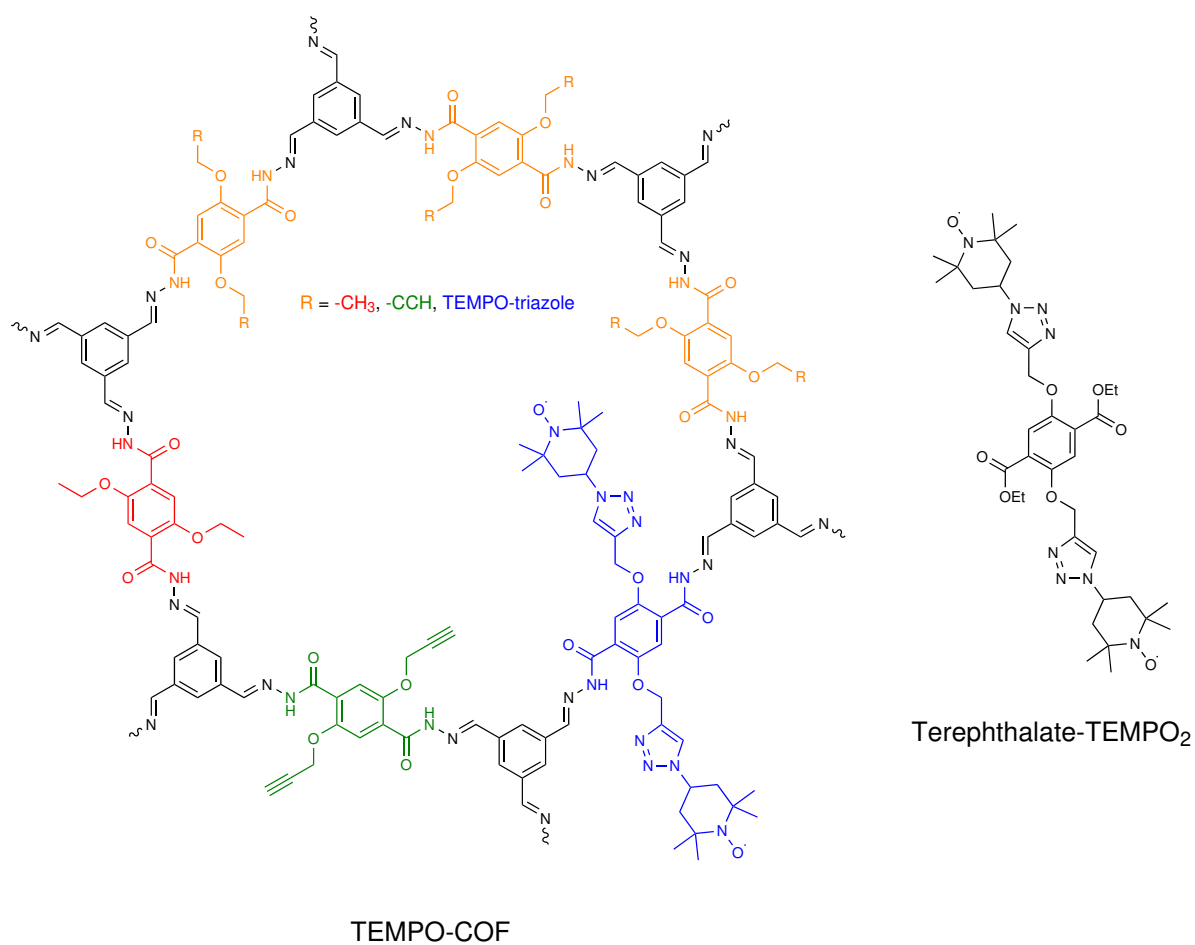
The results presented in this Section give a solid basis for the interpretation of the measurements of TEMPO immobilised in porous structures. It was shown that the g and A tensors as well as the spin relaxation times are only weakly influenced by the functionalisation and the electronic structure remains almost unchanged. It was shown that the matrix does have a rather large influence on the EPR spectrum itself as well as the spin dynamics. Here, mostly the polarity and viscosity of the matrix affect both the electronic structure and spin relaxation. The results for TEMPO in COFs are presented in the next Section.

Table 5.7: Fits of the temperature dependence of T_1 for the slow and fast processes of relaxation, see Equation (5.3). a: TEMPO, b: TEMPOL, c: 4-Azido-TEMPO, d: 4-Propargyl ether TEMPO. The errors are very large due to the low number of data points and the extracted values are only meant as a trend within the investigated compounds.

	$c_{\text{direct}} / \text{s}^{-1} \text{K}^{-1}$	$c_{\text{Raman}} / \text{s}^{-1} \text{K}^{-n_{\text{Raman}}}$	n_{Raman}	$c_{\text{local}} / \text{s}^{-1}$	$\Delta_{\text{local}} / \text{K}$
a_{slow}	0(9)	0(1)	2.1(1)	200(1500)	25(22)
a_{fast}	0(9)	0(1)	2.0(1)	258(1500)	16(22)
b_{slow}	0.0(4)	0.10(9)	2.2(3)	6000(6000)	150(80)
b_{fast}	0.0(4)	0.50(9)	2.2(3)	0(6000)	150(81)
c_{slow}	3(6)	0(2)	2.0(1)	4000(5000)	93(8)
c_{fast}	4(5)	2(2)	1.7(1)	28000(6000)	129(8)
d_{slow}	1.62(1)	$0(1) \cdot 10^{-7}$	6(4)	1300(400)	69(4)
d_{fast}	6.71(1)	$0(1) \cdot 10^{-7}$	3(3)	6240(450)	72(4)

5.3 TEMPO in Covalent Organic Frameworks

In the following, the immobilisation of TEMPO into covalent organic frameworks (COFs) of four different concentrations of alkyne is presented with the aim to assess the influence of immobilization on the electronic structure and geometric dynamics by means of (pulsed) EPR measurements. The COFs were prepared by reacting TFB (TFB = 1,3,5-triformylbenzene, black in Scheme 7) with varying ratios of DETH (DETH = 2,5-diethoxyterephthalohydrazide, red in Scheme 7) and DPTH (DPTH = 2,5-bis(prop-2-yn-1-yloxy)-terephthalohydrazide, green in Scheme 7). [258] The expected chemical structure of the immobilised radical in the investigated COF is shown in Scheme 7. The samples are labelled in the way that the number in the subscript gives the percentage of DPTH in the DPTH/DETH mixture, e.g. in TEMPO-COF_{10%} 10% of DETH was replaced with DPTH. In order to investigate potential spin-spin interactions, terephthalate-TEMPO₂, also shown in Scheme 7, was synthesised and investigated as a model system.



Scheme 7: Chemical structures of TEMPO-COF and Terephthalate-TEMPO₂.

5.3.1 The Synthetic Procedure to Immobilise the Organic Radical

The immobilisation of radicals into pores must fulfil certain criteria. The immobilisation reaction must be quantitative, reliable and must not lead to degradation of the radical or the porous material. The copper(I)-catalyzed azide-alkyne cycloaddition, the so-called click reaction, is widely used to link an azide to an alkyne group through the formation of a triazole ring. [42, 101, 259, 260] Typically, copper(II) is used which is reduced with sodium ascorbate in situ to generate the catalytically active copper(I) species. Here, this approach could not be used as the reducing agent also reduces the organic radical TEMPO, see Figure A.21. Instead, different catalytic systems were tested. $(\text{MeCN})_4\text{Cu(I)PF}_6$ [261] did not lead to the successful formation of the triazole ring while $[\text{CuBr}(\text{PPh}_3)_3]$ [262] did. However, higher yields after the same reaction time were observed for the system copper(I) iodide, TBTA (TBTA = tris((1-benzyl-4-triazolyl)methyl)amine), triethylamine in either THF or toluene. The underlying reason for this behaviour was not further investigated and the last mentioned catalytic system was used for all click reactions presented in this work, giving quantitative conversions, see Section 6.2. As will be seen in the next Sections, remaining Cu(II) interacts with the magnetic moments of the TEMPO radical and potentially also interferes with catalytic processes. It was therefore tried to immobilise the catalyst with spin-free transition metals, e.g. a ruthenium complex, namely Carbonyl(dihydrido)tris(triphenylphosphine)ruthenium(II). [263] The synthesis of Terephthalate-TEMPO₂ was possible although the mass spectrum shows a lower purity than for the copper catalysed reaction, see Figure A.34. For the immobilisation reaction in the COF, it was observed from the EPR spectrum (Figure A.15), which is the sum of mobile (unclicked) and powder-like (immobilised) species, that residual TEMPO could not be washed out of the pores. This may be because the ruthenium catalyst disturbs the structure of the COF by disrupting the stacking of the layers. This would decrease the effective pore diameter, potentially trapping mobile species within the framework.

5.3.2 Spin-Spin Interactions in the Model Compound

Because of short TEMPO-TEMPO-distances in the COF due to the direct connection to the same bridging benzene ring, the influence of the same was investigated outside of the porous structure by also synthesising Terephthalate-TEMPO₂. Both EPR spectroscopy and SQUID magnetometry are very well suited to study interactions of nearby spins. The EPR spectra of Terephthalate-TEMPO₂ in liquid and frozen solution as well as the susceptibility-temperature product measured with SQUID magnetometry are shown in Figure 5.12. In EPR broader linewidths compared to those in TEMPO and its derivatives at similar concentrations can be observed. To prove that this line broadening is not due to

intermolecular interactions, the solution was diluted by a factor of 10000 and the spectrum still shows substantial line broadening, see Figure A.22 and Table A.16. This broadening results from the decreased mobility of the large molecule compared to 4-Azido-TEMPO, as can be seen in Figure A.16, where no increased spin-spin interactions are visible in the diluted sample in the temperature-susceptibility product.

Figure 5.12 also depicts the susceptibility-temperature product versus the temperature for two different samples of Terephthalate-TEMPO₂, one of which was purified by column chromatography and the other one was measured after only drying under vacuum, with the mass spectrum confirming the compound to be pure. The former compound shows an anti-ferromagnetic coupling of the spins with $J = -38 \text{ cm}^{-1}$ and an additional paramagnetic contribution of $\chi T = 0.06 \text{ K cm}^3 \text{ mol}^{-1}$ that is attributed to 14% of the total number of molecules where TEMPO was clicked to only one side of the terephthalate. For the sample that was prepared in THF a ferromagnetic coupling of $J = 2.3 \text{ cm}^{-1}$ and no impurities are observed. The latter sample was then also investigated with pulsed EPR, see next Sections. Both simulations were done with $g_{\text{iso}} = 2.006$. The different magnetic behaviours of samples of the same compound is known in literature where for example two different phases (dimers and chains) exist in dpph [264] and where temperature and solvent have an influence on whether the interaction is ferromagnetic or anti-ferromagnetic [265].

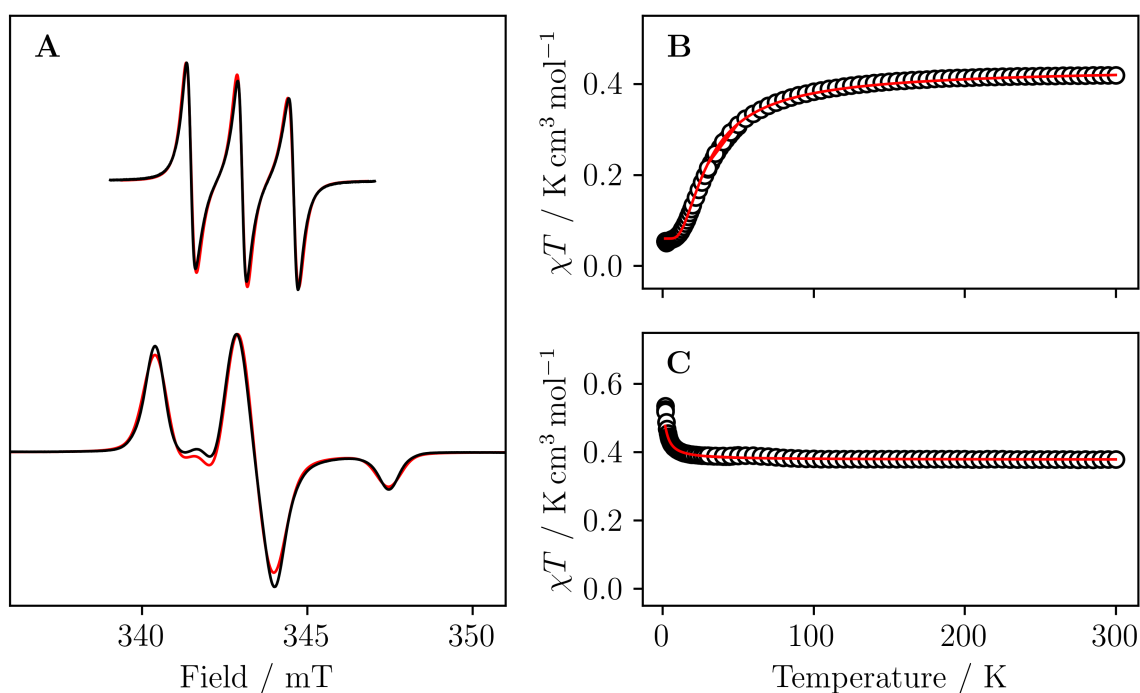


Figure 5.12: A) X-Band EPR spectrum of Terephthalate-TEMPO₂ in solution (1 mmol l⁻¹ in DCM:toluene (1:1)) at room temperature (top) and 140 K (bottom) with simulations (red). The simulation parameters are given in Table A.15. Susceptibility-temperature products of the compound synthesised in toluene after column chromatography in DCM:ethyl acetate (B) and directly after the reaction in THF (C). The simulation parameters are given in the text.

5.3.3 The Electronic Structure of immobilised TEMPO probed by Continuous Wave Electron Paramagnetic Resonance

As was mentioned at the beginning of this Chapter, the EPR signal of TEMPO is very sensitive to the mobility of the molecule. A broadening of the linewidths of TEMPO in mesopores was attributed to slow motion and exchange interaction but neither a quantitative estimate of these parameters nor a proof of chemical immobilisation was given. [266] Figure 5.13 shows the EPR signals of chemically immobilised TEMPO radicals and those that are physisorbed on the surface or in the pores of the material. The clicked sample was prepared as is explained in Section 6.2 and the other one was prepared by using excess TEMPO and no catalyst with stirring of the suspension for the same amount of time. Both materials were filtered and washed in the same manner and then dried under reduced pressure. The EPR signals are vastly different showing broad signals for the immobilised TEMPO and a fast-motion, solution like, EPR spectrum of the sample where clicking was impossible. The mobility most likely arises from leftover solvent that

cannot be removed under reduced pressure. The mobility of the radical in the pores is crucial as chemical reaction could not take place if the reagents were stuck to the pore walls. The position of guest molecules in pores was determined to be dependent on the polarity of the porous framework and the mobile molecules, while the molecules are predominantly located close to the pore wall. [267] The additional signal marked with an asterisk is due to impurities in the EPR tube that can also be seen in measurements of a clean and empty quartz tube.

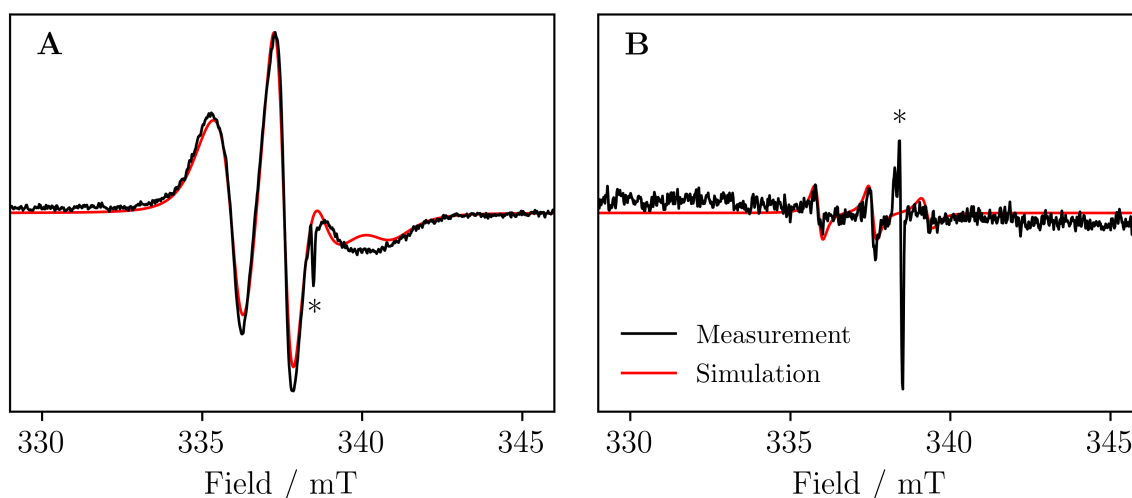


Figure 5.13: Room temperature EPR signals and simulations (red) of chemisorbed (A) and physisorbed (B) TEMPO in COF_{10%}. The simulation parameters are given in Table 5.8.

Table 5.8 lists the simulation parameters, showing that the difference in the EPR line-shape between chemisorbed and physisorbed species can be attributed to predominantly a decrease in the mobility due to the attachment to the pore walls. This is manifested in an increase of the rotational correlation time t_{corr} by an order of magnitude compared to the mobility of freely moving TEMPO in the pores and by three orders of magnitude compared to TEMPO in low concentrated solutions.

Figure 5.14 shows variable temperature EPR spectra of TEMPO-COF_{10%} measured at X-Band. Two important results can be obtained from this data. Firstly, the linewidth increases below 20 K, secondly a second set of signals at field values between 280 and 330 mT appears that could be attributed to a copper(II) species. The line broadening can be easily explained with the decrease in the phase-memory time, i.e. also in T_2 , that increases the natural linewidth, see Equation 5.4. [268]

$$T_2 = \frac{h}{\sqrt{3}\pi g \mu_B \Delta B_{\text{pp}}} \quad (5.4)$$

Table 5.8: Simulation parameters for chemisorbed and physisorbed TEMPO in COF_{10%} as shown in Figures 5.13 and 5.14B.

	Chemisorption		Physisorption
	10 K	RT	RT
g_{xx}	2.0097(5)	2.0094(5)	2.0094(5)
g_{yy}	2.0065(5)	2.0055(5)	2.0055(5)
g_{zz}	2.0022(5)	2.0026(5)	2.0026(5)
A_{xx} / MHz	19.0(1)	16.6(1)	16.6(1)
A_{yy} / MHz	19.0(1)	25.0(1)	25.0(1)
A_{zz} / MHz	102.0(1)	100.8(1)	100.8
$\Delta B_{pp,G}$ / mT	0.70(5)	0	0
$\Delta B_{pp,L}$ / mT	0.50(5)	0.22(5)	0.20(5)
t_{corr} / ns	-	4.63(2)	0.50(2)

This decrease in T_2 can be observed for all investigated samples in the previous Section and also for both TEMPO-COF and Terephthalate-TEMPO₂, see next Section. The presence of the copper(II) signal can be explained with the catalyst for the click reaction that remained in the porous framework even after washing of the sample in an aqueous EDTA (EDTA = 2,2',2'',2'''-(ethane-1,2-diylidinitrilo)tetraacetate) solution for a week. This may be explained by strong adhesion of the charged copper ions to the nitrogen atoms in the porous framework providing many binding sites for positively charged species. The larger value for A_{zz} can be explained to coordination to a surrounding with higher dielectric constants, indicating at least a partial interaction with the pore wall. [21]

In order to better understand the origin of the line broadening in the EPR spectra of TEMPO-COF_{10%} compared to TEMPO in frozen solution, COFs with different amounts of the alkyne functionalised building block were prepared, giving samples with 0.2, 2 and 20 % of functionalisation. Figure 5.15 shows the X-Band EPR spectra of these three samples measured at room temperature and 140 K.

The samples with different amounts of functionalisation show similar EPR spectra as TEMPO-COF_{10%}, indicating similar g and A values with comparable mobilities of the radical in the pores. For the lowest concentration, the line shape is significantly different to that of TEMPO immobilised at comparable concentrations in frozen solutions or solid matrices. This observation can be explained with a slightly higher mobility of the radical in the pores, leading to a line broadening due to an incomplete averaging of the g and A tensors. At higher concentrations the line shape does not change significantly and only

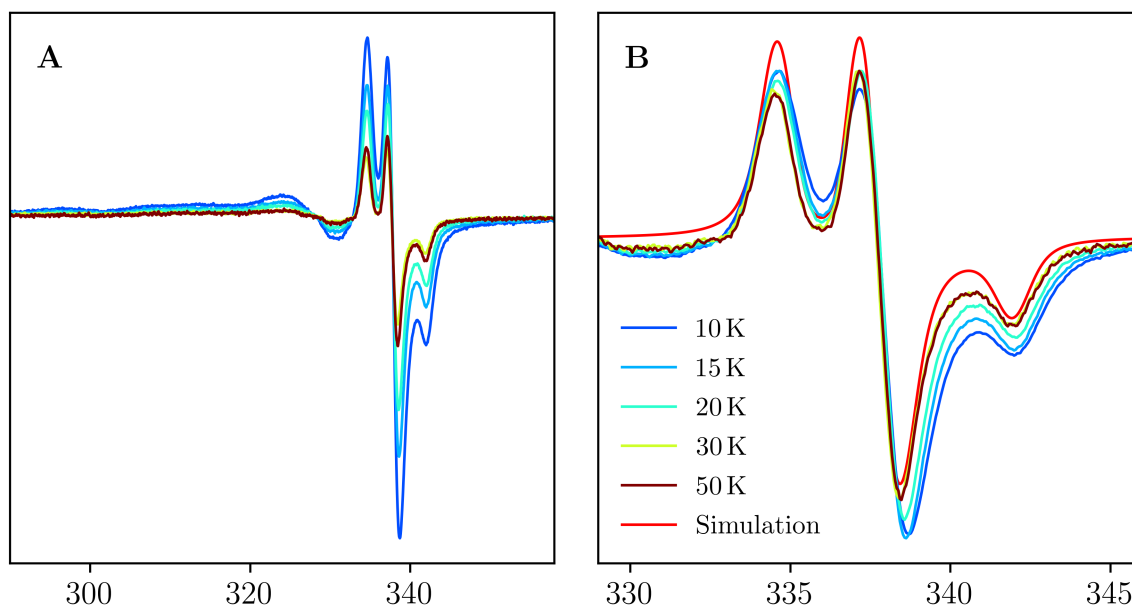


Figure 5.14: Variable temperature X-Band EPR spectra of TEMPO-COF_{10%} as measured (A) and after normalisation (B). The signals at magnetic fields below ca. 330 mT in (A) are attributed to leftover copper(II) species from the click reaction.

broadens slightly. This behaviour must arise from increased radical-radical interactions. Cooling down to 140 K gives an EPR spectrum of an immobile TEMPO species. This may be because remaining solvent that could not be removed from the pores even after drying in vacuum freezes, hindering the motion of the radical. Hyperfine interaction strength very close to values observed for TEMPO in DCM:toluene indicate that the TEMPO radical does not interact strongly with partially charged species as that would increase A_{zz} , as discussed in the previous Section. Especially interaction of the radical to the nitrogen and oxygen atoms in the pore wall can therefore be excluded, compare also to the behaviour of TEMPO in SBA-15 in the next Section.

Additionally, HFEPR spectra of TEMPO, the TEMPO derivatives 4-azido-TEMPO and 4-propargylether-TEMPO as well as Terephthalate-TEMPO₂ in polystyrene ($c = 0.1 \text{ mmol g}^{-1}$), TEMPO-COF_{0.2%} and TEMPO-COF_{2%} were measured. Figure 5.16 shows the data and a simulation for all spectra of samples without considerable exchange interaction.

The HFEPR spectra of TEMPO, 4-azido-TEMPO and 4-propargylether-TEMPO are the same within experimental accuracy. They all have the same g and A tensors with slightly different linewidths that can be attributed to imperfect distribution of molecules in polystyrene as that would lead to a variation in radical distances, giving broader lines

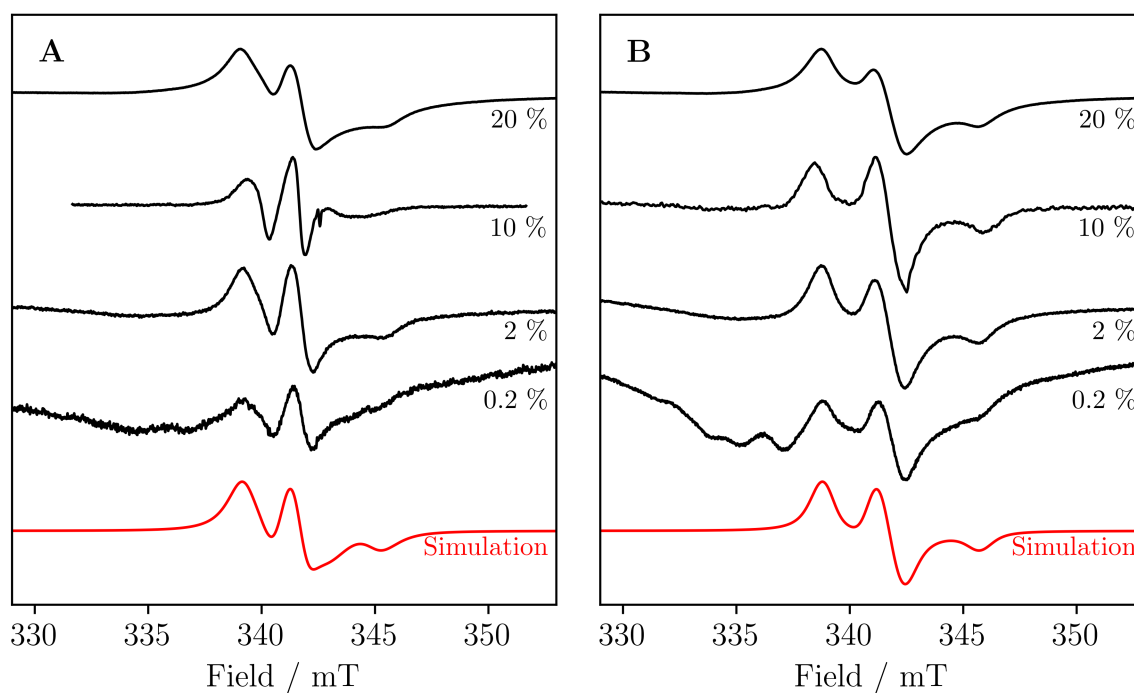


Figure 5.15: X-Band EPR spectra of TEMPO-COF_{0.2%}, TEMPO-COF_{2%}, TEMPO-COF_{10%} and TEMPO-COF_{20%} measured (black) at room temperature (A) and 140 K (B) as well as simulations (red). The simulation parameters are $g_{xx} = 2.0097$, $g_{yy} = 2.0064$ and $g_{zz} = 2.0022$, $A_{xx} = A_{yy} = 20$ MHz and $A_{zz} = 96$ MHz. The room temperature spectra were simulated with rotational correlation times $t_{\text{corr}} = 10$ ns.

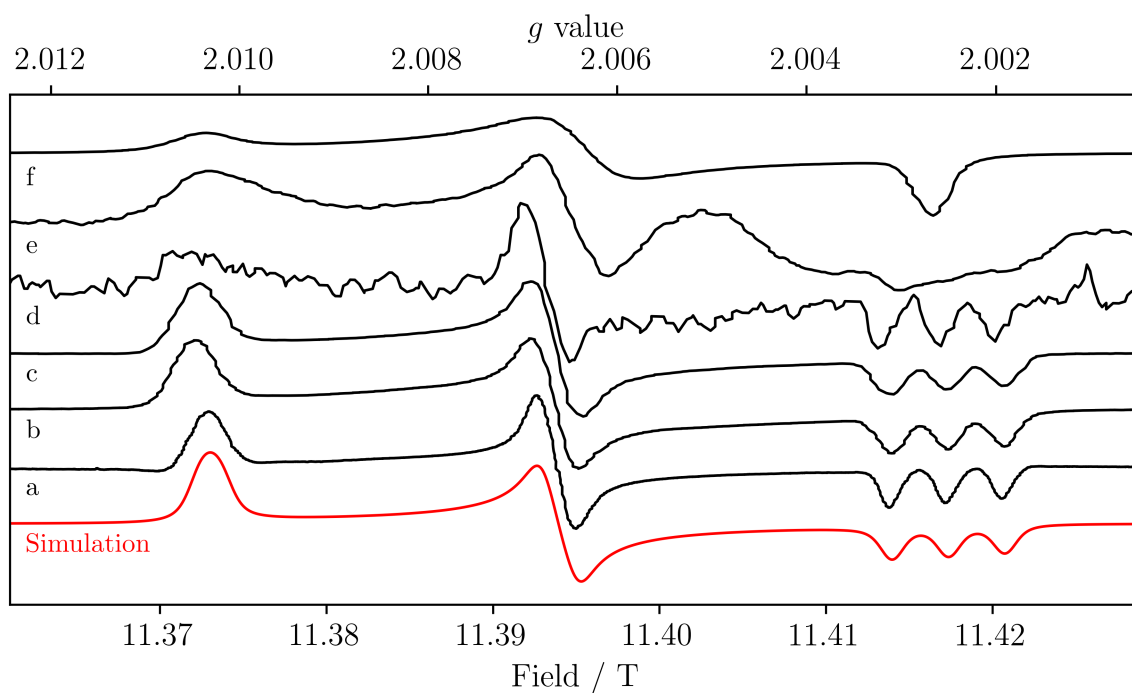


Figure 5.16: HFEPR spectra measured at 70 K and 320 GHz of TEMPO (a), 4-azido-TEMPO (b), 4-propargylether-TEMPO (c) in polystyrene ($c = 0.1 \text{ mmol g}^{-1}$), TEMPO-COF_{0.2%} (d), TEMPO-COF_{2%} (e) and Terephthalate-TEMPO₂ in polystyrene ($c = 0.1 \text{ mmol g}^{-1}$) (f) as well as a simulation with $g_{xx} = 2.0103$, $g_{yy} = 2.0066$, $g_{zz} = 2.0025$, $A_{xx} = A_{yy} = 20 \text{ MHz}$ and $A_{zz} = 95, \text{MHz}$.

for those species that are in close proximity to other radicals. This inhomogeneous distribution of radical in polystyrene is also the reason for the lack of hyperfine splitting A_{zz} in Terephthalate-TEMPO₂ in polystyrene. The X-Band room temperature EPR spectrum of the same sample also does not show hyperfine splitting. This is interesting since Terephthalate-TEMPO₂ in 1 mmol⁻¹ solution does show hyperfine splitting and the polystyrene sample was prepared from the same solution of which the spectra in Figure 5.12 were measured. Since A_{zz} was already known and the individual components of the g tensor can still be read from the spectrum, no new sample was prepared. The HFEPR spectrum of TEMPO-COF_{0.2%} is very similar to those of the radicals in polystyrene with the same values in the g and A tensors. The sample with a higher concentration of TEMPO does show considerable line broadening, especially for g_{zz} , indicating that weak exchange interactions are prevalent. The X-Band EPR spectra of TEMPO-COF_{2%} do not indicate an increased hyperfine interaction, confirming that any line broadening is only due to exchange interaction.

In summary, the g and A tensors are not influenced by the immobilisation and only steric demand and decreased radical distances compared to homogeneous liquid solutions of comparable concentrations lead to a line broadening in the EPR spectrum. It can therefore be concluded that the electronic structure is the same with and without immobilisation in the pores.

5.3.4 Spin Relaxation of TEMPO in COFs

TEMPO in COFs and the model compound Terephthalate-TEMPO₂ were investigated with pulsed EPR in order to determine the influence of the pore wall on the spin dynamics. Here, especially the spin-lattice relaxation time T_1 is of interest as it is directly influenced by the surrounding, i.e. the lattice.

As a first step, the influence of the close association of the TEMPO radicals through the bridge in the pore wall was investigated. Figure 5.17 shows the echo detected EPR spectrum and the extracted spin relaxation times of Terephthalate-TEMPO₂. Table A.17 lists the relaxation times. T_1 decreases from ca. 4 ms at 7 K to ca. 0.3 ms at 50 K while T_M increases from ca. 3.7 μ s at 7 K to ca. 6.9 μ s at 15 K from where it decreases to ca. 5.1 μ s at 50 K.

The spin-lattice relaxation times are smaller by an order of magnitude than for any of the molecules with only one attached TEMPO radical investigated in this thesis. This behaviour may be explained either by decreased TEMPO-TEMPO distances compared to the previously investigated solutions or a change in the phonon spectrum in Terephthalate-TEMPO₂ compared to the free molecule. The fact that the phase-memory times of

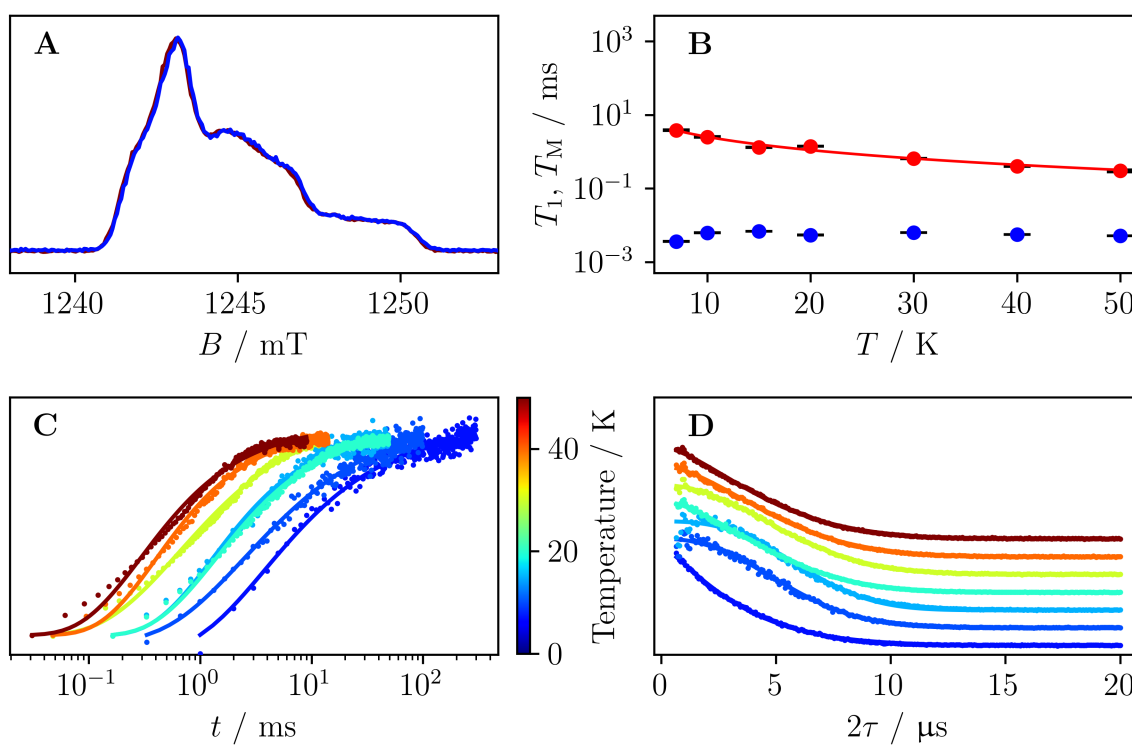


Figure 5.17: A) EPR spectrum of Terephthalate-TEMPO₂ measured at 35 GHz and 7 K (blue) and 50 K (red) in a frozen solution of DCM:toluene (1 mmol l⁻¹). B) Temperature dependence of the spin-lattice relaxation times T_1 (red) and phase-memory times T_M (blue) extracted from the inversion recovery (C) and Hahn echo experiments (D).

Terephthalate-TEMPO₂ do not decrease compared to 4-azido-TEMPO shows that the shorter spin-spin distance does at least not influence T_M , suggesting also a limited influence of the radical distance on T_1 . The more likely explanation for the decrease in T_1 is therefore the different phonon spectra of Terephthalate-TEMPO₂ and the other molecules. The fit of the temperature dependence of T_1 (Table 5.9) suggests that the different relaxation times indeed stem from different phonon spectra with very different contributions of the individual relaxation pathways. Especially the local mode relaxation play a subordinate role in Terephthalate-TEMPO₂ compared to the other radicals (Table 5.7).

Table 5.9: Fits of the temperature dependence of the spin-lattice relaxation time with direct, Raman and local mode relaxation processes. These values must be taken with caution only few data points were available for the fit with a high number of parameters, especially at higher temperatures, where the local vibration modes start to occur.

$c_{\text{direct}} / \text{s}^{-1} \text{K}^{-1}$	$c_{\text{Raman}} / \text{s}^{-1} \text{K}^{-n_{\text{Raman}}}$	n_{Raman}	$c_{\text{local}} / \text{s}^{-1}$	$\Delta E_{\text{local}} / \text{K}$
30(80)	0(30)	2.0(2)	50(100)	130(50)

Another interesting change compared to the unclicked TEMPO radicals is that the echo decay in the inversion recovery experiment follows a stretched exponential. This is known for a continuous distribution of relaxation times, i.e. a range of spin-lattice relaxation times. [269, 270] It can be explained by irregular TEMPO-TEMPO distances from molecules where only one TEMPO radical is attached to and the limited solubility of Terephthalate-TEMPO₂ in DCM:toluene, giving locally varying spin concentrations.

The spin dynamics were also investigated for TEMPO immobilised in the COFs with different amounts of alkyne functionalisation. The EPR spectrum and relaxation times of TEMPO-COF_{10%} are shown in Figure 5.18.

The material was dried under vacuum after the click reaction and was measured without further dilution as a powder. It gives the typical powder-like EPR spectrum of TEMPO, albeit with slightly higher linewidths than what was observed for the 1 mmol l⁻¹ solutions of the TEMPO derivatives. With an alkyne concentration of ca 0.1 mmol g⁻¹ in COF_{10%} the amount of TEMPO radicals per unit volume is very similar to that in the frozen solutions but the molecules are not as evenly distributed in the pores, as can be seen in the DEER measurement shown in the next Section, giving higher local concentrations. These higher concentrations increase the linewidth and also decrease both relaxation times T_1 and T_M by a factor of ca. 10 compared to Terephthalate-TEMPO₂. Since it was unclear whether this behaviour stems from an increased mobility in the pores compared to the sample in frozen solution (see Figures 5.6A and 5.15), that were assumed to be

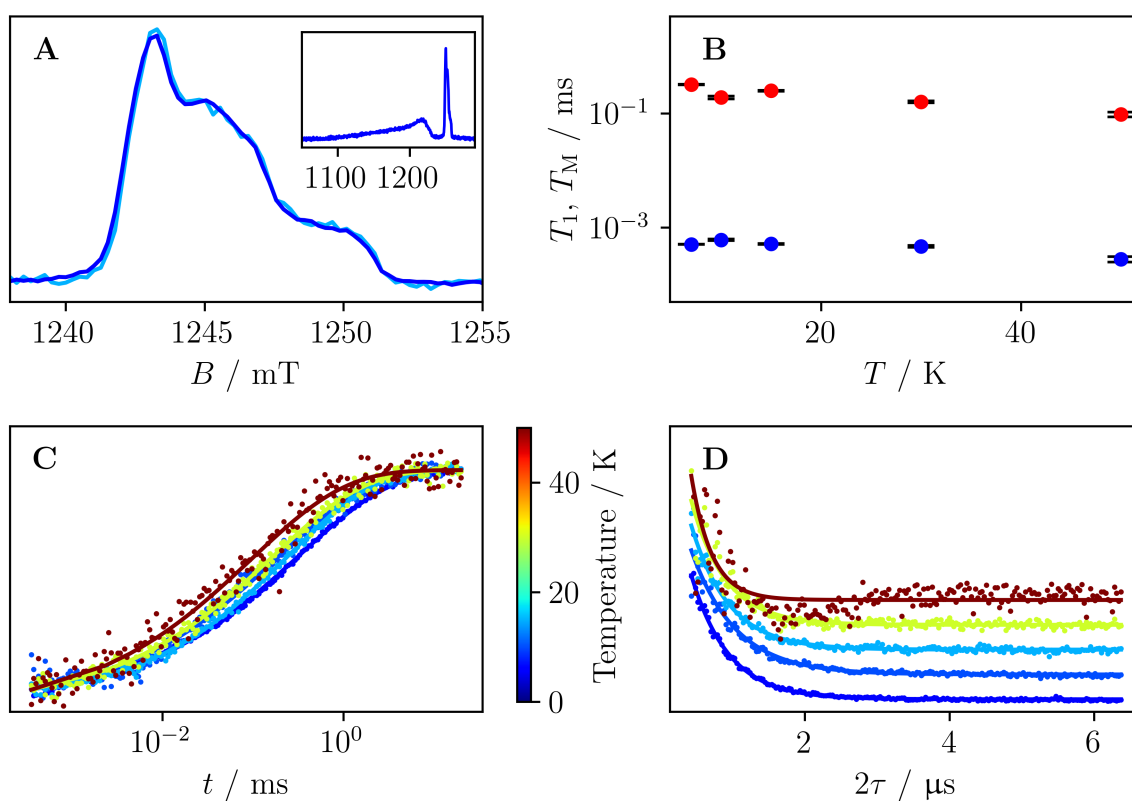


Figure 5.18: A) EPR spectrum of TEMPO-COF_{10%} measured at 35 GHz and 7 K (dark blue) and 15 K (light blue) with the inset showing a larger field sweep. B) Spin-lattice relaxation times T_1 (red) and phase-memory times T_M (blue) extracted from the inversion recovery (C) and Hahn echo experiments (D).

free of residual solvent, the sample was also submerged in toluene to fill the pores. This sample was also measured and the results are given in Figure A.23 and Table A.19. The extracted relaxation times are the same within experimental certainty, suggesting that the pores were not empty in the dried sample and solvent remained even after drying under vacuum.

Table 5.10: Dependence of the spin relaxation times T_1 and T_M and the exponents k of the stretched exponential function of the differently concentrated TEMPO-COF samples.

	T / K	T_1 / ms	k_{T_1}	$T_M / \mu\text{s}$
0.2	6	1.7(1)	1	0.23(2)
2	10	0.78(2)	0.327(4)	0.574(7)
10	6	0.093(3)	1	0.390(6)

From Figure 5.18A it can also be seen that a lot of paramagnetic copper remains in the pores even after washing with an aqueous EDTA solution. These ions may be interacting with the pore wall more strongly than with EDTA or the chelating ligand is too big to fit into the pores. It is likely that additional magnetic moments in the sample influence the spin relaxation, as T_M is very similar for all TEMPO concentrations in the COFs as seen in Table 5.10 and Figures A.24 and A.25. It is likely that the residual copper that could not be washed out leads to a fast relaxation time. The residual amount of copper seems to be independent of the amount of used copper in the synthesis, as seen in Figure 5.19. This may be because the paramagnetic copper preferably binds to a limited number of available nitrogen or oxygen sites in the COF. As the number of these sites are the same in all COFs the influence of them should be of similar magnitude, giving comparable spin-lattice relaxation times. All of the copper ions that did not bind to the pore wall might have been removed in the washing process. The ratio between the TEMPO spectra in Figure 5.19 as taken from the raw data is not the same as the ratio expected from the number of alkyne functionalised sites. This may be because the shorter phase-memory time leads to weaker echo intensities after the same time τ in the Hahn echo sequences.

In summary, TEMPO-COF_{2%} has the longest phase-memory time because of the weaker TEMPO-copper interactions than in TEMPO-COF_{2%} and weaker TEMPO-TEMPO interactions than in TEMPO-COF_{10%}, making it the best sample to measure the TEMPO-TEMPO distances with DEER spectroscopy, where long phase-memory times are required to most confidently determine radical distances.

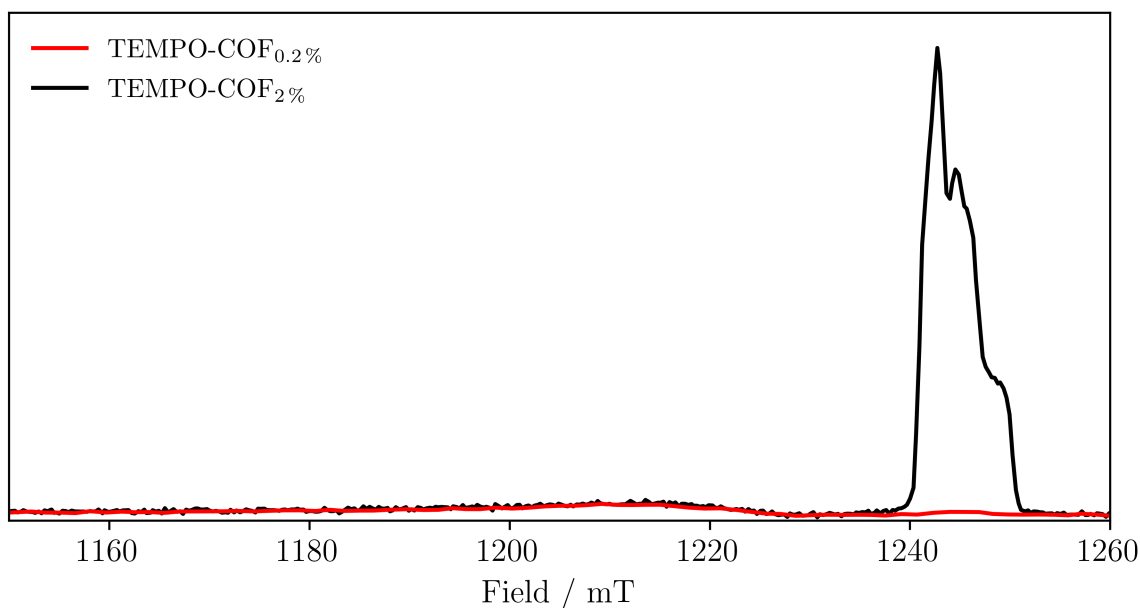


Figure 5.19: EPR spectra of TEMPO-COF_{0.2%} (red) and TEMPO-COF_{2%} (black) measured at 35 GHz and 6 and 10 K, respectively.

5.3.5 Radical Distances in the COF from Double Electron-Electron Resonance Spectroscopy

Although the EPR measurements give insight into the mobility and distance distribution of spin in the porous framework, the pulsed EPR technique double electron-electron resonance (DEER) spectroscopy gives the distance distribution directly. The distance information is gained from the modulation of the echo intensity in the four-pulse experiment, see Section 2.2.3. This so-called DEER trace is shown in Figure 5.20B with the fit from which the distribution of spins is extracted, see Figure 5.20A. Figure 5.20C shows the structure of the COF and the extracted distances relative to the centre TEMPO radical in this dimension.

Interestingly, no distances $d < 1.8$ nm are observed although the layers of the COF should have distances of ca. 0.4 nm, potentially allowing smaller spin-spin distances. [258, 271–273] The absence of such short distances is also consistent with the EPR spectrum of TEMPO (compare Figure 5.6) that would show substantial broadening even for immobile molecules at these small distances. From a force-field geometry optimisation of TEMPO-COF and Terephthalate-TEMPO₂ different radical-radical distances were obtained. They are in the range from 1.6 nm for molecules that are both bent towards the bridging wall and 2.5 nm for molecules pointing to the centre of the pore. The experiment seemingly confirms the two TEMPO molecules to point away from the pore wall and towards the

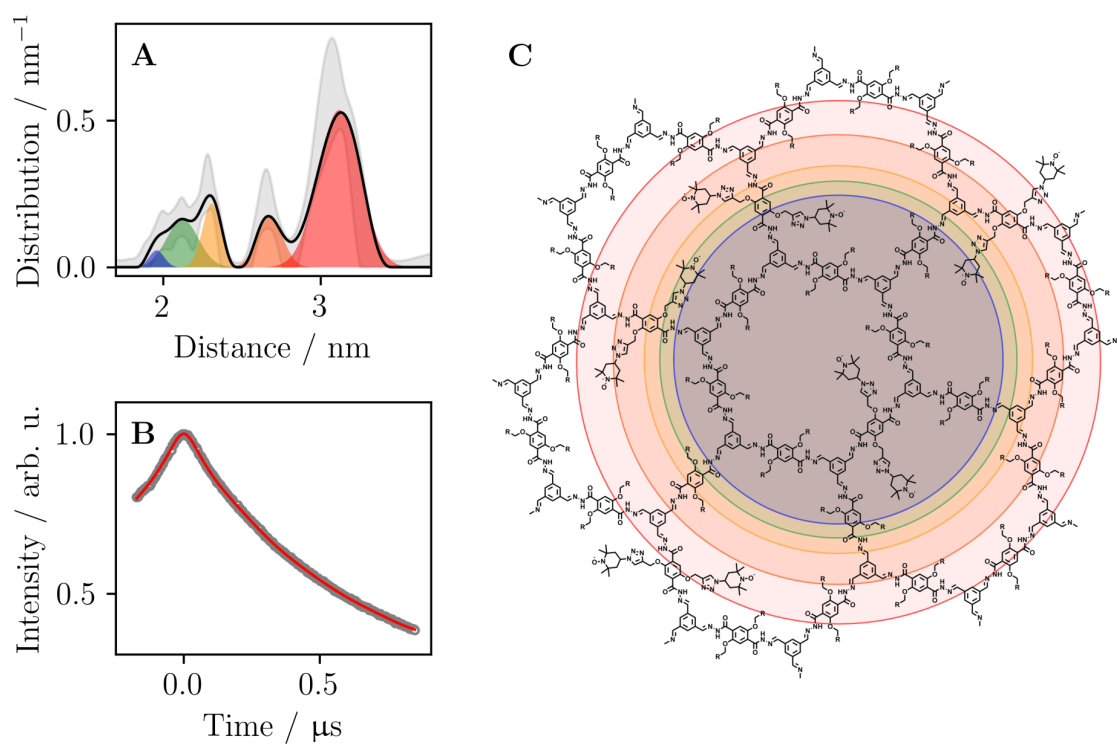


Figure 5.20: A) Results of the DEER experiment of TEMPO-COF_{2%} showing the distance distribution of the TEMPO radicals. B) The DEER trace with fit. C) Structure of the porous framework.

centre of the pore. Distances above 2.5 nm can be explained by interaction with radicals in nearby pores with the most intense peak resulting from the pore diameter of ca. 3.6 nm, proving at least a short-range order of the porous structure.

5.4 TEMPO in the Porous Silica Material SBA-15

The mesoporous silica material SBA-15 [55] has been widely used as a porous framework in environmental adsorption [274, 275], advanced optics [276, 277] and most importantly catalysis [56, 58, 278]. Here, the dynamics of the organic radical TEMPO in mesoporous silica is investigated with EPR spectroscopy. The immobilisation of TEMPO was performed with the click reaction of 4-propargylether and azide-functionalised SBA-15 which was prepared with the reagent AzPTES (AzPTES = 3-azidopropyltriethoxysilane). [57] Five samples were prepared from the same silica material containing 0.387 mmol azide groups per gram of material, as was determined with elemental analysis. Molar ratios of 0.1, 1, 10 or 100 % of alkyne-functionalised TEMPO were added to a suspension of the material and after two hours of stirring that allow a distribution of the radical into the pores, the catalyst for the click reaction was added, see Section 6.2. Additionally a sample with an excess of 4-propargylether-TEMPO without the catalyst was prepared to compare chemi- and physisorbed species.

5.4.1 Synthetic Procedure to Immobilise the Radical in Azide-Functionalised SBA-15

The success of the chemical immobilisation of 4-propargylether-TEMPO into azide-functionalised SBA-15 was followed with IR spectroscopy, where the azide vibration must disappear after the formation of the triazole ring. The vibration has energies of ca. 2100 cm^{-1} as can be seen in Figure 5.21 that does indeed show a decrease of the intensity of the azide vibration for higher amounts of TEMPO.

Additionally the residual amount of copper catalyst was measured with ICP-OES, see Table 5.11, where a substantial amount of copper could be determined in the material after the click reaction even though the material was washed with EDTA solution multiple times. Compared to TEMPO-COF (see previous Section) no copper(II) signal could be observed in the EPR measurements of TEMPO in SBA-15. This is most likely due to copper staying in the +1 oxidation state that is EPR silent.

As is the case for TEMPO-COF, a significant difference in the EPR spectra of the chemisorbed and physisorbed TEMPO radicals can be observed, see Figure 5.22. The air dried sample without added catalyst shows a mobile species in residual solvent that cannot be linked to the pore walls. After drying carefully at pressures below 10^{-8} mbar,

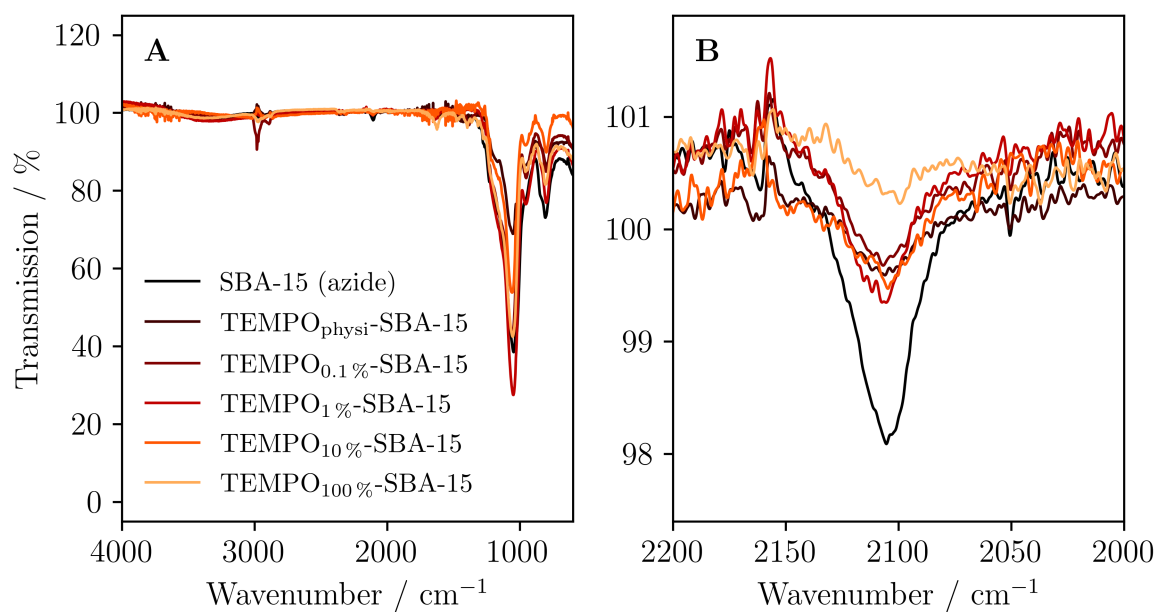


Figure 5.21: ATR-IR spectra of the investigated TEMPO-SBA-15 samples.

Table 5.11: Results of the ICP-OES measurements to determine the amount of copper in the SBA-15 material after the click reaction. 1 ppm is equal to 1 μg copper per 1 g of SBA-15 material.

	SBA-15 material	TEMPO-SBA-15 _{0.1%}
$\chi_{\text{Cu},1}$ / ppm	-1	231
$\chi_{\text{Cu},2}$ / ppm	-12	236
$\bar{\chi}_{\text{Cu}}$ / ppm	-6(6)	234(3)

the solvent is removed and the radical remains in the pores but must be stuck to the pore walls, allowing no mobility. The sample where catalyst was added does not show a mobile species in EPR even when the solvent is not removed by just air drying the material.

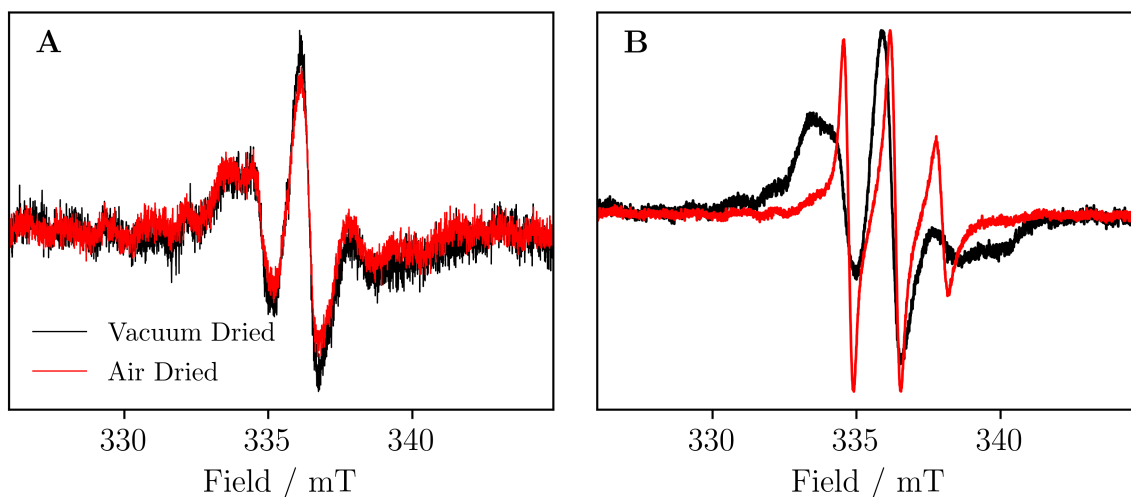


Figure 5.22: Room temperature EPR spectra of 1% 4-propargylether-TEMPO in SBA-15 with (A, chemisorbed) and without (B, physisorbed) the addition of catalyst. The samples were dried on air or under reduced pressures of ca. 10^{-8} mbar.

5.4.2 The Electronic Structure Probed with Continuous Wave Electron Paramagnetic Resonance

The influence of the TEMPO concentration was also investigated for SBA-15. Instead of changing the number of functionalised sites in the porous framework, as was done in the COFs, the amount of 4-propargylether-TEMPO was adjusted. Figure 5.23 shows the X-Band EPR spectra of the four different concentration of TEMPO that were immobilised in SBA-15.

The sample with the lowest TEMPO concentration did not show an EPR signal at room temperature (Figure 5.23A) and only the impurity signal of the quartz tube at 10 K (Figure 5.23B) is visible. This is unexpected as the sample with ten times the amount of TEMPO shows a rather intense EPR signal at 10 K, indicating that the sensitivity for the detection of the lowest concentration of TEMPO is experimentally given. This indicates that the reaction yield is very low, possibly due to a low amount of used catalyst and a decreasing probability of coincidence of TEMPO, the catalyst and the azide group in SBA-15. For all other concentrations the EPR spectra show a mobile species at room temperature with low mobility (Table 5.12) and a powder-like spectrum at 10 K.

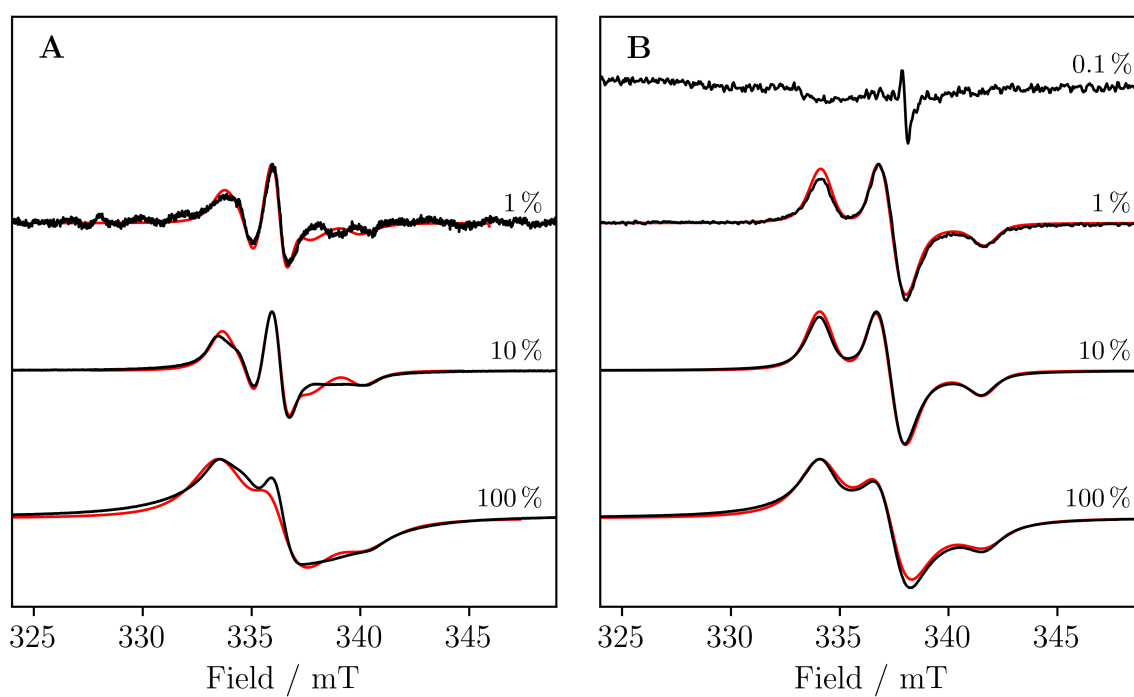


Figure 5.23: EPR spectra and simulations (red) of TEMPO-SBA-15 measured at room temperature (A) and 10 K (B) for different concentrations of the immobilised radical. The simulation parameters are given in Table 5.12.

This observation could be explained with a lower mobility for lower temperatures or by freezing of residual solvent, hindering the motion of the radical below the melting point of the solvent. Increased concentrations lead to lower mobilities at room temperature and increased exchange broadening for both temperatures. The much higher value for A_{zz} is due to a much higher dielectric constant of the surrounding in silica compared to organic solvents, where experimentally differences of ca. 8 MHz were observed. [21] This indicates a significant influence of the polar pore wall, suggesting at least a partial collapse of the radical to the same.

Table 5.12: Simulation parameters for the EPR measurements of TEMPO-SBA-15 shown in Figure 5.23.

	RT			10 K		
	1 %	10 %	100 %	1 %	10 %	100 %
g_{xx}	2.0097(5)	2.0097(5)	2.0097(5)	2.0097(5)	2.0097(5)	2.0097(5)
g_{yy}	2.0065(5)	2.0065(5)	2.0065(5)	2.0065(5)	2.0065(5)	2.0065(5)
g_{zz}	2.0022(5)	2.0022(5)	2.0022(5)	2.0022(5)	2.0022(5)	2.0022(5)
A_{xx} / MHz	19.0(1)	19.0(1)	19.0(1)	19.0(1)	19.0(1)	19.0(1)
A_{yy} / MHz	19.0(1)	19.0(1)	19.0(1)	19.0(1)	19.0(1)	19.0(1)
A_{zz} / MHz	104.5(1)	104.5(1)	104.5(1)	104.5(1)	103.5(1)	105.0(1)
$\Delta B_{\text{pp,G}}$ / mT	0.07(5)	0.00(5)	0.00(5)	0.75(5)	0.81(5)	0.61(5)
$\Delta B_{\text{pp,L}}$ / mT	0.30(5)	0.42(5)	1.52(5)	0.45(5)	0.54(5)	1.30(5)
t_{corr} / ns	6.0(2)	7.2(2)	9.0(2)			

5.4.3 The Spin Dynamics of TEMPO in SBA-15 as determined with Pulsed Electron Paramagnetic Resonance

To investigate the influence of the pore wall on the spin dynamics, the spin-lattice and spin-spin relaxation times were measured. Unfortunately no spin echo could be observed for the samples with very high TEMPO concentration, possibly due to too strong inter-radical interactions that decrease T_M to values below the time required in the Hahn-echo sequence. No spin echo could be observed for the samples with very low TEMPO concentration either, likely due to the low absolute number of spins below the detection limit of the spectrometer. The measurements on the TEMPO_{10%}-SBA-15 sample are shown in Figure 5.24.

The measurements of the spin-lattice relaxation time give a biexponential relaxation rate with a slow and a fast process, see Table 5.13. The Hahn-echo sequence shows a

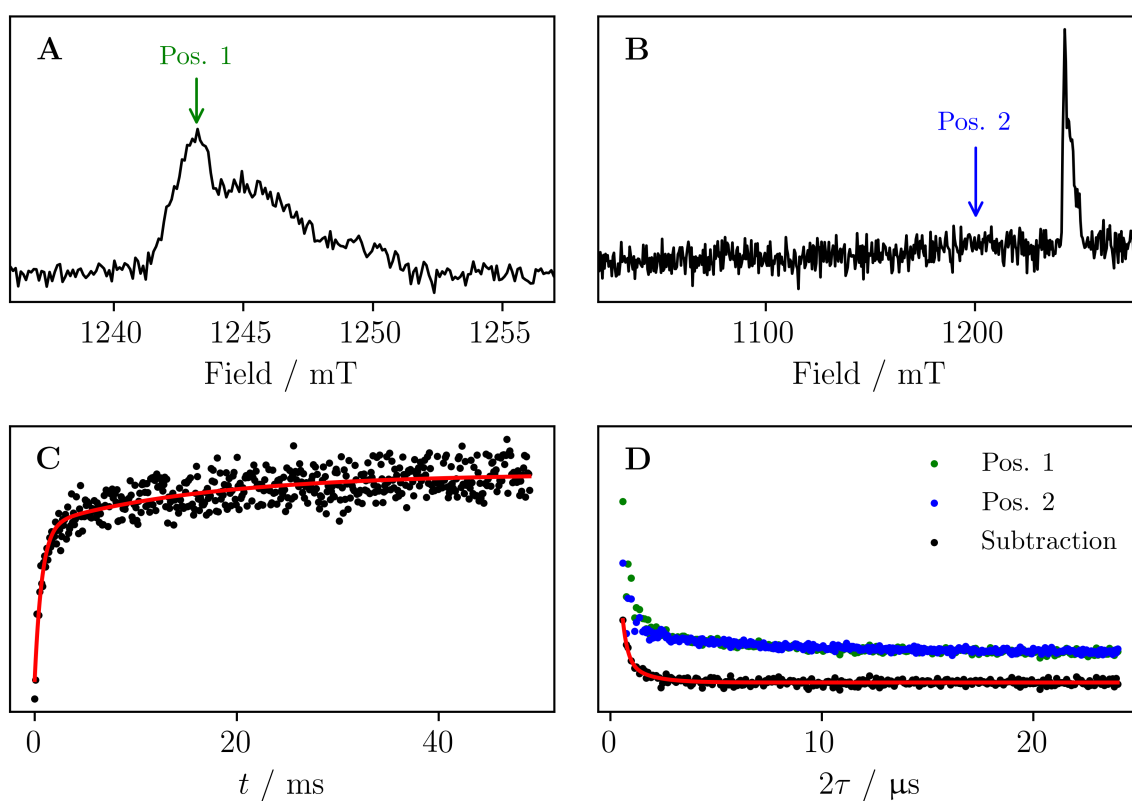


Figure 5.24: EPR spectrum of TEMPO_{10%}-SBA-15 measured at 35 GHz in the $g \approx 2$ region (A) and the region where a Cu(II) signal would be expected (B). Inversion-recovery (C) and Hahn-echo decays (D), where the latter was measured on- and off-resonance to remove the spectrometer background. All measurements were performed at 6 K. The fit parameters are given in Table 5.13.

long coherence time that is also apparent when measuring at magnetic fields where no EPR transition is observed, i.e. off-resonance. This decay is attributed to cavity ringing, i.e. the decay of the pulse power in the resonator after the microwave is switched off. This phenomenon was investigated in literature for quickly changing resonator lengths in Fabry-Pérot cavities. [279] A quickly changing frequency, as is the case at the edges of a pulse should have the same effect as a change in the geometry of the resonator. After subtraction of the background, the echo decay could be fit with a biexponential decay with predominantly a fast process with $T_M = 230$ ns. This is much faster than that for the TEMPO derivatives in frozen solutions and in the COF. The most likely explanation is the high number of surrounding spins of the ^1H nuclei at the pore wall. As was already seen in the X-Band EPR spectra, there are no substantial amounts of Cu(II) species in the sample, so that cannot be the reason for the fast echo decay.

Table 5.13: TEMPO_{10%}-SBA-15.

	$T_{1,\text{slow}} / \text{ms}$	$T_{1,\text{fast}} / \text{ms}$	$x_{T_{1,\text{slow}}} / \%$	$T_{M,\text{slow}} / \mu\text{s}$	$T_{M,\text{fast}} / \mu\text{s}$	$x_{T_{M,\text{slow}}} / \%$
6 K	16(3)	0.71(8)	25(2)	1.1(3)	0.23(5)	6(6)

The immobilisation of TEMPO in SBA-15 was shown to be successful. It was proven that physisorbed and chemisorbed species can be distinguished and that a partial collapse of the TEMPO radical to the pore takes place. A very fast relaxation of the excited spin was observed which may be due to the interaction with the pore wall.

5.5 Clicking into Ordered Mesoporous Carbon

As a last porous material, ordered mesoporous carbon (OMC) was chosen. This material is prepared by self-assembly of triblock polyethers and subsequent thermopolymerization and carbonization at elevated temperatures of ca. 700 °C. [61] By functionalising the polymer building blocks with azide groups, click chemistry can be enabled. Here, 4-propargylether-TEMPO was immobilised in the pores (21 mmol of azide per gram of material, as determined from elemental analysis) through the copper catalysed click reaction. Figure 5.25 shows the X-Band EPR spectrum of the radical immobilised in OMC.

The spectrum can be simulated with contributions of different TEMPO species with the same g tensor but different linewidths, see Table 5.14. This may be due to an irregular spacing of the azide groups in the pores, giving a broad range of radical distances, i.e. different exchange interaction strengths. Although species with weak intermolecular interactions exist, the main contribution is from radicals with nearby TEMPO molecules. This may be from a preferential clicking at the pore entrances which in turn might block

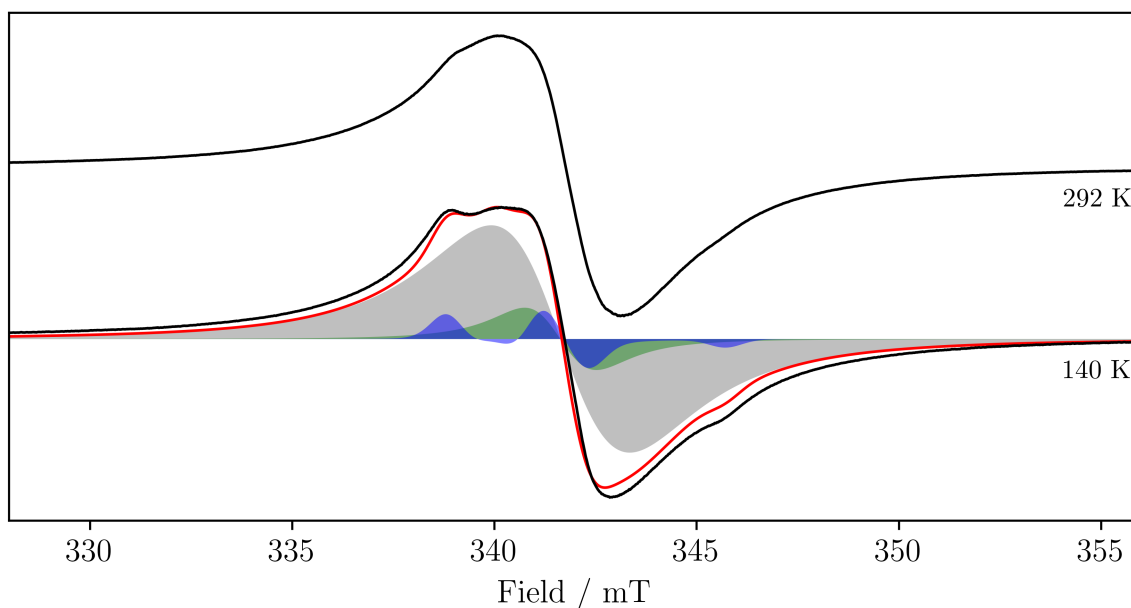


Figure 5.25: X-Band EPR spectra of TEMPO-OMC measured at room temperature and 140 K (black) with simulations of the individual components showing different ranges of exchange interaction (coloured) and their sum (red).

other molecules from entering the pores. Alternatively, the azide groups might be located preferably at the pore entrances. As was also seen for TEMPO in COFs and SBA-15, a temperature decrease leads to a slight sharpening of the lines due to decreased mobility of the immobilised molecules, potentially due to leftover solvent that freezes at these temperatures.

Table 5.14: Parameters for the simulations shown in Figure 5.25. $g_{xx} = 2.0097(5)$, $g_{yy} = 2.0064(5)$ and $g_{zz} = 2.0022(5)$ for all individual simulations and $A_{xx} = A_{yy} = 20.0(1)$ MHz and $A_{zz} = 96.0(1)$, MHz for the simulation shown in blue and $A_{xx} = A_{yy} = A_{zz} = 0$ MHz for the other two simulations in green and grey.

	blue	green	grey
$\Delta B_{pp,G} / \text{mT}$	0.70(5)	0.00(5)	1.00(5)
$\Delta B_{pp,L} / \text{mT}$	0.10(5)	1.50(5)	3.00(5)
$x / \%$	3(3)	6(3)	91(5)

A concentration series might give further insight into the observed behaviour through possible changes in the relative areas of the individual components of the EPR spectrum. Unfortunately, no pulsed EPR measurements could be performed as no spin echo was visible. Nonetheless, the successful immobilisation of TEMPO into OMC was shown.

6 Experimental Section

6.1 Experimental Techniques and Sample Preparation

6.1.1 Continuous-Wave EPR spectroscopy

X-Band EPR Spectra were recorded on a Bruker EMX spectrometer with two different resonators, a 4102ST resonator for measurements down to 4 K with liquid helium and a 4105DR double resonator for measurements down to 140 K with liquid nitrogen or for measurements with another sample in the second cavity for more precise determination of the g value without overlapping signals. The Q values of the resonators are 2500 (4102ST, TE_{102}) and 3000 (4105DR, TE_{104}). The microwave magnetic field B_1 can be calculated with Equation (6.1) with the conversion factors $C_{4102ST} = 1.4 \text{ G W}^{-0.5}$ and $C_{4105DR} = 0.6 \text{ G W}^{-0.5}$. [280]

$$B_1 = C \cdot \sqrt{P} \quad (6.1)$$

The modulation amplitude and phase of both resonators were calibrated regularly and magnetic field shifts (ca. -0.57 mT) were determined by regularly measuring dp_{pp} with known resonance fields for given microwave frequencies. Also a Magnettech MiniScope MS 400 spectrometer was used, for which field shifts of ca. $+1.26 \text{ mT}$ were determined by measuring dp_{pp}. Samples were measured in quartz tubes by Wilmad-LabGlass (4 mm O.D., 3 mm I.D.). All samples were centred in the cavity for the highest signal-to-noise ratio. The modulation amplitude was set to $B_{\text{mod}} < 1/3 \Delta B_{\text{pp}}$ in order not to over-modulate and the microwave power was set to not saturate the transition. The time constant and conversion time were set to ca. 40 ms for all measurements and the receiver gain was set so that the detector level did not exceed ca. 80 % of its maximum level.

HFEPR spectra were measured on a home-built spectrometer. [281] Samples were measured as pressed pellets with a diameter of 5 mm. The modulation amplitude was set so that the spectra were not over-modulated and the spectra were phase-corrected after the measurement by measuring the original and 90° phase-shifted signal. The spectra were field-corrected by multiplying the sweep speed in T min^{-1} with the offset 0.03 min. The offset was determined from the average difference in resonance fields for sweeps to higher and lower fields at the same microwave frequency.

All spectra were simulated with the EasySpin (Versions 5.2.28 and 5.2.33) [282] toolbox in MatLab (Version R2019b).

Experimental errors are estimated to $\Delta g = 0.005$ (0.001), $\Delta A = 0.1$ MHz (1 MHz), $\Delta t_{\text{corr}} = 2$ ns and $\Delta\Delta B_{\text{pp}} = 0.01$ mT (0.1 mT) for microwave frequencies of ca. 10 GHz (> 100 GHz). These values were determined by repetition measurements of identical samples.

6.1.2 Pulsed EPR spectroscopy

Q-Band (35 GHz) spectra, inversion-recovery and Hahn-echo experiments were measured on a home-built spectrometer. [283] Samples were measured in quartz tubes by Wilmad-LabGlass (2 mm O.D., 1 mm I.D.). Pulse lengths of the 90° and 180° pulses were chosen to 20 and 40 ns, respectively for the measurements on (dppf)Fe(CO)₃ and 40 and 80 ns, respectively for the measurements of the nitroxyl radicals. Repetition times were chosen to be approximately five times as long as the spin-lattice relaxation time and τ was set to 300 ns for the measurement of spectra and in the inversion-recovery experiments.

X-Band ENDOR and HYSCORE as well as Q-Band (ca. 34 GHz) ENDOR and DEER spectra were measured on a Bruker Elexsys 580 spectrometer at the National EPR Facility at the University of Manchester by Edmund Little and Alena Sheveleva (University of Manchester, group of Floriana Tuna).

In the HYSCORE experiment the pulse lengths were set to $t_{\frac{\pi}{2}} = 16$ ns and $t_{\pi} = 30$ ns and the delay between the two first pulses was set to 136 ns.

In the ENDOR experiment at X-Band (Q-Band) the microwave pulse lengths were set to $t_{\frac{\pi}{2}} = 128$ ns (200 ns) and $t_{\pi} = 256$ ns (400 ns), the selection pulse length was $t_{\text{sel}} = 256$ ns (400 ns). The radio pulse length was set to 12 μ s (12 μ s) and the mixing time to 14 μ s (14 μ s). The time between the pulses was set to 500 ns (1 μ s).

In the DEER experiment, the pulse lengths were set to $t_{\frac{\pi}{2}} = 28$ ns, $t_{\pi} = 56$ ns and $t_{\text{pump}} = 36$ ns. The time between the first two pulses was set to 240 ns and the time between the inverted echo and the third pulse to 1600 ns.

All spectra were simulated with the EasySpin (Versions 5.2.28 and 5.2.33) [282] toolbox in MatLab (Version R2019b). Fitting of echo decay curves was done in Python (Version 3.8) with the SciPy toolbox. [284]

Experimental errors are estimated to $\Delta g = 0.003$, $\Delta A = 0.3$ MHz, and $\Delta\Delta B_{\text{pp}} = 0.03$ mT for microwave frequencies of ca. 35 GHz. These values were determined by repetition measurements of identical samples.

6.1.3 Mössbauer spectroscopy

All spectra were recorded on a homemade Mössbauer spectrometer based on a RCPTM MS-96 spectrometer and a Janis SVT400 bath cryostat. The spectrometer was equipped with a Ritverc ^{57}Co in Rh-matrix source with an initial activity of 50 mCi (MCo7.124). All spectra are referenced against $\alpha\text{-Fe}$ measured at room temperature in regular intervals. For most of the measurements liquid nitrogen was used as cooling agent without pumping of the sample chamber. The spectra were fitted in MossWinn 4.01. Samples were prepared by packing finely ground powder in weighing paper that was then folded and closed with parafilm.

Experimental errors were determined to $\Delta\delta_{\text{IS}} = 0.1 \text{ mm s}^{-1}$, $\Delta\Delta E_{\text{Q}} = 0.1 \text{ mm s}^{-1}$ and $\Delta\Gamma = 0.1 \text{ mm s}^{-1}$. These values were determined by repetition measurements of identical samples.

6.1.4 MCD spectroscopy

MCD spectra were measured on a homemade spectrometer based on a Aviv 42CD spectrometer and an Oxford Instruments 10T Spectromag optical cryomagnet. [285, 286] Samples were prepared by mixing the ground powder sample and fluorolube® oil. Spectra were measured at positive and negative fields and subtracted from one another to obtain the MCD spectrum.

6.1.5 SQUID magnetometry

Measurements were performed on a MPMS3 magnetometer by Quantum Design from 1.8 to 300 K and magnetic fields up to 70 kOe. Samples were prepared by either pressing a ground powder to a pellet with a diameter of 5 mm or by dropcasting a droplet of a solution of polystyrene (ca. 30 g l^{-1}) and the radical in toluene onto a microscope slide. The sample was then inserted into a plastic straw where it was fixated. Due to the fast sublimation of TEMPO, special care had to be taken for measurements on solids, i.e. the actual amount of TEMPO may differ from the weighed in value. The measured magnetic moments μ were corrected for impurities μ_{imp} and the diamagnetic contribution $\chi_{\text{mol}}^{\text{d}}$ of the sample and sample holder to obtain the paramagnetic susceptibility $\chi_{\text{mol}}^{\text{p}}$ for each magnetic field H with the molar mass M and sample mass m .

$$\chi_{\text{mol}}^{\text{p}} = \frac{\mu - \mu_{\text{imp}}}{H} \cdot \frac{M}{m} - \chi_{\text{mol}}^{\text{d}} \cdot \frac{M}{m} \quad (6.2)$$

The magnetic moment of the impurity can be estimated from measurements at the same

temperatures for different fields. The diamagnetic contribution can be estimated either from Pascal's constants (giving the diamagnetic contribution for each atom and functional group) [287] or by correcting the temperature-susceptibility product to a straight line at high temperatures as long as it is known that spins do not interact in that temperature range and that no spin-crossover exists in the sample.

6.1.6 Cyclic Voltammetry

Cyclic voltammetry was measured in acetonitrile with 0.1 M tbaPF₆ and 0.02 M tbaBArF₄. Glassy carbon (WE), Pt (CE) and Ag (quasi reference) were chose as electrode materials with ferrocene as an internal standard.

6.1.7 ATR-IR Spectroscopy

ATR-IR spectra of powder samples were measured on a Nicolet iS5 by Thermo Fischer Scientific.

6.1.8 X-Ray Emission Spectroscopy

X-ray emission spectra were measured by Lukas Burkhardt (Universität Paderborn, group of M. Bauer) at the ID26 beamline of European Synchrotron Radiation Facility (ESRF), as described in [196].

6.1.9 NMR Spectroscopy

¹H NMR spectra were recorded on a Bruker Ascend 400 at 400 MHz. They were evaluated in MestReNova (Version 9.0.1) and referenced against the residual solvent peak of the deuterated solvent CDCl₃. [288] Paramagnetic samples were reduced with phenyl hydrazine before the measurements. [289]

6.1.10 Elemental Analysis

ICP-OES spectra were measured by Heike Fingerle (Institute für Technische Chemie, Universität Stuttgart) on a Vista-MPX, CCD simultaneous ICP-OES by Varian in aqueous solution.

6.1.11 Mass Spectrometry

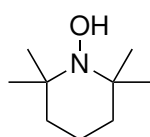
mass spectra were measured on a Bruker Micro-TOF Q spectrometer with the ESI technique by the analytics division (Institute für Organische Chemie, Universität Stuttgart)

6.1.12 Visualisation

All plots were made with the Matplotlib toolbox in Python (Version 3.8). [290]. 2D chemical structures were drawn in ChemDraw Professional 16.0, 3D chemical structures were visualised with Mercury (Version 3.10.3).

6.2 Syntheses

2,2,6,6-Tetramethylpiperidin-1-ol

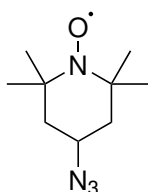


TEMPO-H
C₉H₁₉NO
157.26

The synthesis was performed as is described in [291]: (2,2,6,6-Tetramethylpiperidin-1-yl)oxyl (100 mg, 0.6 mmol, 1 eq) and an excess of (+)-sodium L-ascorbate (300 mg, 1 mmol, 1.7 eq) were dissolved in water (3 ml). The solution was stirred for 2 h, filtered and washed with water. The obtained solid was then dissolved in diethyl ether (2 ml) and volatiles were removed under reduced pressure. The product (60 mg, 38 %) was obtained as a white powder.

FT-IR (ATR): $\tilde{\nu} = 3435, 3005, 2978, 2968, 2927, 2869, 2846, 1467, 1402, 1381, 1360, 1340, 1293, 1236, 1206, 1183, 1131, 1046, 1027, 999, 959, 937, 870, 782, 728, 694 \text{ cm}^{-1}$

4-Azido-(2,2,6,6-tetramethylpiperidin-1-yl)oxyl



4-Azido-TEMPO
C₉H₁₇N₄O•
197.26

The synthesis was performed as is described in [45]: A mixture of demineralised water (2.5 ml) and toluene (2.5 ml) was cooled to 0 °C and sodium azide (550 mg, 13.5 mmol, 4.6 eq) was added. Subsequently, triflic anhydride (0.85 ml, 5.2 mmol, 1.77 eq) was added dropwise and the solution was stirred for 18 h with the temperature increasing slowly to room temperature. Then, a saturated sodium hydrocarbonate solution was added slowly until gas evolution ceased. The product was extracted with toluene (2 × 8 ml) and then

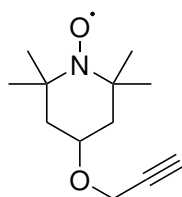
dried with anhydrous sodium sulfate. Due to its explosiveness in the dried form and lower vapour pressure of the triflyl azide compared to toluene, the mixture was not concentrated under vacuum and no further purification was undertaken.

The triflyl azide solution from the first step was added to a mixture of 4-amino-TEMPO (540 mg, 2.93 mmol, 1 eq), sodium bicarbonate (1 g, 1.2 mmol, 4.1 eq) and copper sulfate (50 mg, 0.3 mmol, 0.11 eq) in water (4 ml) and the suspension was stirred at room temperature for 3 h. The mixture was then washed with saturated sodium bicarbonate solution (8 ml) and extracted with ethyl acetate (2×10 ml). The combined organic phases were dried with sodium sulfate and the solvent was evaporated under vacuum. The product was purified by flash column chromatography (silica, hexane:ethyl acetate (3:1), $R_f = 0.75$). The product (363 mg, 1.8 mmol, 63 %) was obtained as orange crystals.

MS (ESI): m/z calc. for $C_9H_{17}N_4O$ $[M + Na]^+$: 220.13; found: 220.13.

1H NMR (400 MHz, $CDCl_3$) $\delta = 1.07$ (s, 6H), 1.13 (s, 6H), 1.46 (t, $J = 12.3$, 2H), 1.73 – 1.81 (m, 2H), 3.50 (tt, $J = 12.3$, 4.1, 1H) ppm.

4-Propargyl ether (2,2,6,6-tetramethylpiperidin-1-yl)oxyl



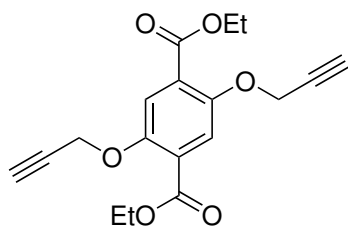
4-Propargylether-TEMPO

$C_{12}H_{20}NO_2$
210.30

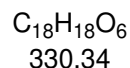
The synthesis was performed similarly to what is described in [46]: Sodium hydride suspension (60 % in mineral oil, 850 mg, 22 mmol, 1.26 eq) was added to dry dimethylformamide at room temperature. After cooling to 0 °C, 4-hydroxy-TEMPO (3 g, 17.4 mmol, 1 eq) was added slowly and the mixture was stirred for 30 min, after which propargyl bromide (80 wt.-% in toluene, 2 ml, 22 mmol, 1.26 eq) was added dropwise. The mixture was then stirred at room temperature for 3 h. After adding water (100 ml) and extracting with ethyl acetate (5×50 ml), the organic phases were washed with water (10×50 ml) and dried over magnesium sulfate. The solvent was removed under reduced pressure and the product was purified by column chromatography (silica, hexane:ethyl acetate (9:1), $R_f = 0.37$). The product (2.47 g, 11.7 mmol, 68 %) was obtained as orange crystals.

MS (ESI): m/z calc. for $C_{12}H_{20}NO_2$ $[M + Na]^+$: 233.14; found: 233.14.

1H NMR (400 MHz, $CDCl_3$) $\delta = 1.11$ (s, 6H), 1.17 (s, 6H), 1.41 – 1.52 (m, 2H), 1.83 – 1.92 (m, 2H), 2.32 (t, $J = 2.4$, 1H), 3.72 – 3.81 (m, 1H), 4.07 (d, $J = 2.4$, 2H) ppm.

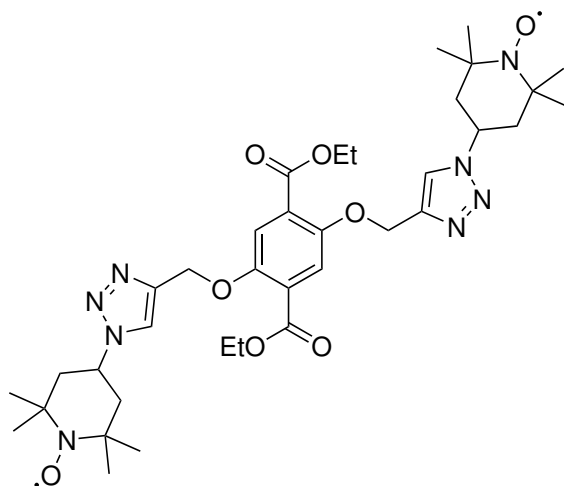
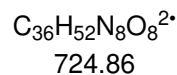
Diethyl 2,5-bis(prop-2-yn-1-yloxy)terephthalate

Terephthalate-Alkyne



The synthesis was performed as is described in [292]: A solution of diethyl 2,5-dihydroxyterephthalate (771 mg, 3.0 mmol, 1 eq), propargyl bromide (80 wt.-% in toluene, 1 ml, 11 mmol, 3.7 eq) and potassium carbonate (2.23 g, 15.1 mmol, 5 eq) in dry acetone (30 ml) was refluxed over night. The suspension was filtered and washed with acetone. The solvent was then removed under reduced pressure. After dissolution in chloroform (40 ml), washing with water (3 × 30 ml) and drying over sodium sulfate, the solvent was again removed under reduced pressure. The product (912 mg, 91 %) was obtained as a light yellow powder.

^1H NMR (400 MHz, CDCl_3): δ 1.40 (t, $J = 7.2$, 6H), 2.53 (t, $J = 2.4$, 2H), 4.39 (q, $J = 7.2$, 4H), 4.76 (d, $J = 2.4$, 4H), 7.56 (s, 2H) ppm.

Diethyl 2,5-bis((1-(2,2,6,6-tetramethylpiperidin-4-yl)oxyl-1H-1,2,3-triazol-4-yl)methoxy)terephthalateTerephthalate-TEMPO₂**Copper catalysed click reaction**

To a solution of 4-azido-TEMPO (150 mg, 0.8 mmol, 2.5 eq), terephthalate-alkyne (100 mg, 0.3 mmol, 1 eq), copper(I) iodide (3 mg, 0.02 mmol, 0.05 eq) and tris((1-benzyl-4-triazolyl)-

methyl)amine (10 mg, 0.02 mmol, 0.05 eq) in dry tetrahydrofuran (30 ml), triethylamine (90 μl , 0.726 g cm^{-3} , 0.6 mmol, 2 eq) was added. The solution was stirred for 4 days. The product precipitated and was then purified by filtration and washing with diethylether (20 ml). The product (210 mg, 96 %, before drying) was obtained as a light yellow powder.

MS (ESI): m/z calc. for $\text{C}_{36}\text{H}_{52}\text{N}_8\text{O}_8^2$ $[\text{M} + \text{H}]^+$: 725.40; found: 725.40.

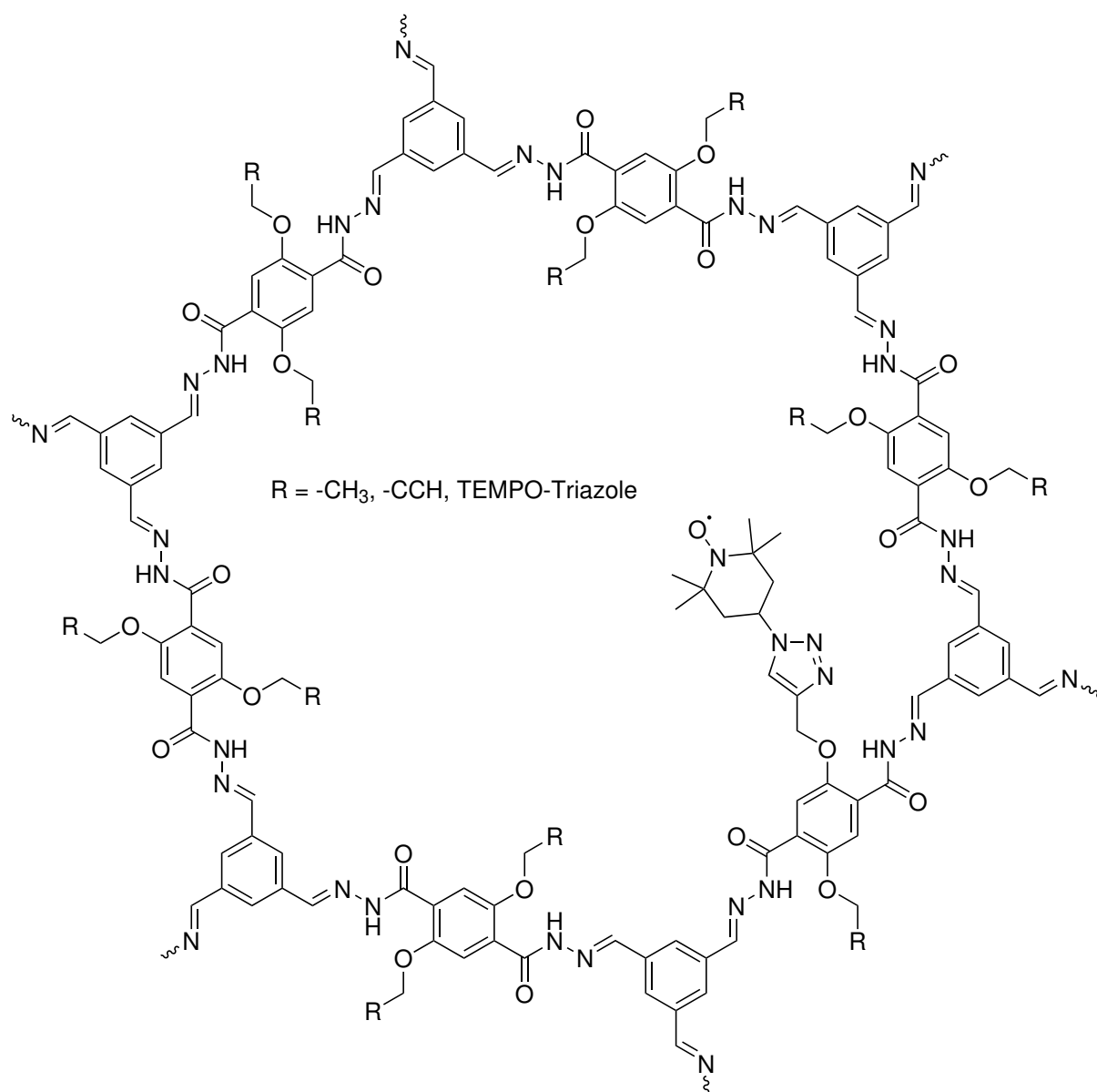
^1H NMR (400 MHz, CDCl_3) δ = 1.17 (s, 24H), 1.28 (t, J = 7.2, 6H), 1.85 – 2.03 (m, 8H), 4.27 (q, J = 7.2, 4H), 4.77 (tt, J = 12.3, 4.1, 2H), 5.17 (s, 4H), 7.45 (s, 2H), 7.63 (s, 2H) ppm.

Ruthenium catalysed click reaction

Carbonyl(dihydrido)tris(triphenylphosphine)ruthenium(II) (1.6 mg, 1.7 μmol , 0.05 eq), 4-azido-TEMPO (19.1 mg, 96.8 μmol , 2.73 eq) and terephthalate-alkyne (11.7 mg, 35.4 μmol , 1 eq) were dissolved in dry tetrahydrofuran (4 ml). The solution was stirred for two weeks at 60 °C. The precipitate was filtered and washed with tetrahydrofuran (3×10 ml). After drying under reduced pressure, the product (9 mg, 35 %) was obtained as a light yellow powder.

MS (ESI): m/z calc. for $\text{C}_{36}\text{H}_{52}\text{N}_8\text{O}_8^2$ $[\text{M} + \text{Na}]^+$: 747.38; found: 747.38.

TEMPO-COF

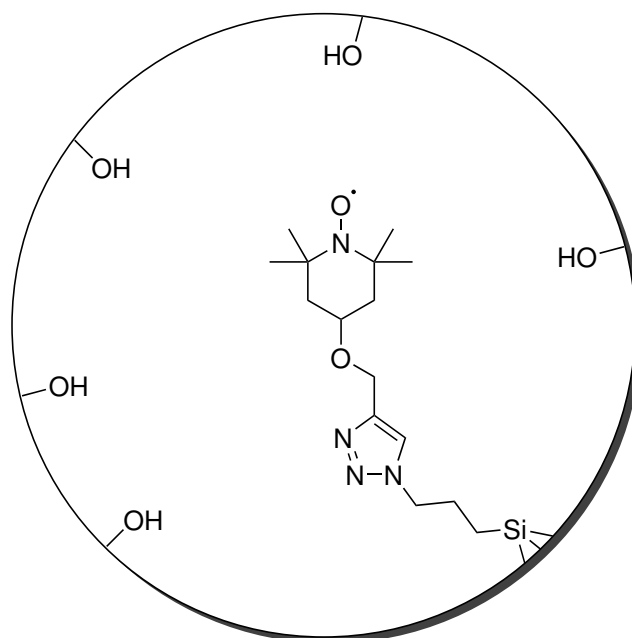


To a suspension of the respective covalent organic framework, 4-azido-TEMPO, copper(I) iodide and tris((1-benzyl-4-triazolyl)methyl)amine in dry toluene (3 ml), triethylamine was added and the solution was lightly stirred for two weeks. The solid product was centrifuged and washed with tetrahydrofuran (3 × 5 ml), water (3 × 5 ml), dichloromethane (3 × 5 ml) and acetone (3 × 5 ml). Between each of the washing steps, the solvent was removed after centrifuging by decantation. The solid was then stirred in an aqueous solution of sodium hydroxide (pH = 8) and tetrasodium 2,2',2'',2'''-(ethane-1,2-diyl)dinitrilo)tetraacetate (3 ml, 1.5 g l⁻¹), centrifuged and washed again with the men-

tioned solvents in the same manner. The product was obtained as a brownish powder.

- TEMPO-COF_{0.2%}: COF_{0.2%} (15.6 mg, 0.16 μmol alkyne, 1 eq), 4-Azido-TEMPO (1.1 mg, 5.6 μmol , 35 eq), CuI (1.2 mg, 6.3 μmol , 39 eq), TBTA (1.3 mg, 2.5 μmol , 15.6 eq), NEt₃ (100 μl , 0.726 g cm⁻³, 717.5 μmol , 4484 eq)
- TEMPO-COF_{2%}: COF_{2%} (15.7 mg, 1.61 μmol alkyne, 1 eq), 4-Azido-TEMPO (2.1 mg, 10.6 μmol , 6.6 eq), CuI (2.6 mg, 13.7 μmol , 8.5 eq), TBTA (2.6 mg, 4.9 μmol , 3.0 eq), NEt₃ (100 μl , 0.726 g cm⁻³, 717.5 μmol , 445 eq)
- TEMPO-COF_{10%}: COF_{10%} (14.9 mg, 7.59 μmol alkyne, 1 eq), 4-Azido-TEMPO (4.1 mg, 20.8 μmol , 2.7 eq), CuI (0.7 mg, 3.7 μmol , 0.5 eq), TBTA (1.8 mg, 3.4 μmol , 0.4 eq), NEt₃ (2 μl , 0.726 g cm⁻³, 14.3 μmol , 1.9 eq)
- TEMPO-COF_{20%}: COF_{20%} (15.5 mg, 15.72 μmol alkyne, 1 eq), 4-Azido-TEMPO (4.5 mg, 22.8 μmol , 1.5 eq), CuI (5.7 mg, 30.0 μmol , 1.9 eq), TBTA (4.5 mg, 8.5 μmol , 0.5 eq), NEt₃ (100 μl , 0.726 g cm⁻³, 717.5 μmol , 45.6 eq)

TEMPO-SBA-15



A suspension of the SBA-15 material (0.387 mmol of azide per g of material) and 4-propargyl ether TEMPO, in dry toluene (5 ml) was stirred for two hours at room temperature. Then, a suspension of copper(I) iodide, tris((1-benzyl-4-triazolyl)methyl)amine

and triethylamine in toluene was added and the solution was lightly stirred for one week at room temperature. The solid product was centrifuged and washed with toluene (3×5 ml), n-hexane (3×5 ml), acetone (3×5 ml), an aqueous solution of tetrasodium 2,2',2'',2'''-(ethane-1,2-diyldinitrilo)tetraacetate (3 ml, 1.5 g l^{-1}), demin. water (3×5 ml) and acetone (3×5 ml). Between each of the washing steps, the solvent was removed after centrifuging by decantation. The solid was then dried under vacuum. The product was obtained as a white powder.

- TEMPO_{0.1%}-SBA-15: SBA-15 (30.8 mg, 12 μmol azide, 1 eq), 4-Propargyl ether TEMPO (0.002 mg, 0.01 μmol , 0.001 eq), CuI (0.001 mg, 0.007 μmol , 0.0006 eq), TBTA (0.004 mg, 0.007 μmol , 0.0006 eq), NEt₃ (0.008 μl , 0.726 g cm^{-3} , 0.05 μmol , 0.004 eq)
- TEMPO_{1%}-SBA-15: SBA-15 (29.6 mg, 11 μmol azide, 1 eq), 4-Propargyl ether TEMPO (0.024 mg, 0.11 μmol , 0.01 eq), CuI (0.014 mg, 0.073 μmol , 0.007 eq), TBTA (0.041 mg, 0.073 μmol , 0.007 eq), NEt₃ (0.076 μl , 0.726 g cm^{-3} , 0.55 μmol , 0.05 eq)
- TEMPO_{10%}-SBA-15: SBA-15 (29.0 mg, 11 μmol azide, 1 eq), 4-Propargyl ether TEMPO (0.240 mg, 1.14 μmol , 0.10 eq), CuI (0.138 mg, 0.725 μmol , 0.07 eq), TBTA (0.410 mg, 0.730 μmol , 0.07 eq), NEt₃ (0.762 μl , 0.726 g cm^{-3} , 5.47 μmol , 0.50 eq)
- TEMPO_{100%}-SBA-15: SBA-15 (31 mg, 12 μmol azide, 1 eq), 4-Propargyl ether TEMPO (4.0 mg, 19.0 μmol , 1.6 eq), CuI (0.9 mg, 5.0 μmol , 0.42 eq), TBTA (0.5 mg, 1.0 μmol , 0.08 eq), NEt₃ (3.3 μl , 0.726 g cm^{-3} , 24 μmol , 2.0 eq)

TEMPO-OMC

To a suspension of the ordered mesoporous carbon material (20.4 mg, 0.97 μmol azide, 1 eq), 4-propargyl ether TEMPO (2.3 mg, 10.9 μmol , 11.2 eq), copper(I) iodide (2.2 mg, 11.6 μmol , 11.9 eq) and tris((1-benzyl-4-triazolyl)methyl)amine (2.9 mg, 5.5 μmol , 5.7 eq) in dry toluene (3 ml), triethylamine (50 μl , 0.726 g cm^{-3} , 358.8 μmol , 370 eq) was added and the solution was lightly stirred for two weeks. The solid product was centrifuged and washed with acetone (3×2 ml), an aqueous solution of tetrasodium 2,2',2'',2'''-(ethane-1,2-diyldinitrilo)tetraacetate (3×2 ml, 1.5 g l^{-1}), water (3×2 ml) and acetone (3×2 ml). Between each of the washing steps, the solvent was removed after centrifuging by decantation. The product was obtained as a black powder after drying in vacuum.

References

- [1] E. I. Solomon, A. Decker, N. Lehnert, *Proc. Natl. Acad. Sci.* **2003**, *100*, 3589–3594, DOI 10.1073/pnas.0336792100.
- [2] S. P. de Visser, D. Kumar, *Iron-Containing Enzymes*, Royal Society of Chemistry, Cambridge, **2011**, DOI 10.1039/9781849732987.
- [3] C. Madden, M. D. Vaughn, I. Díez-Pérez, K. A. Brown, P. W. King, D. Gust, A. L. Moore, T. A. Moore, *J. Am. Chem. Soc.* **2012**, *134*, 1577–1582, DOI 10.1021/ja207461t.
- [4] J. M. Hawkins, T. J. N. Watson, *Angew. Chem. Int. Ed.* **2004**, *43*, 3224–3228, DOI 10.1002/anie.200330072.
- [5] *Handbook of transition metal polymerization catalysts*, Wiley, Hoboken, N.J, **2010**, DOI 10.1002/9780470504437.
- [6] C. A. Busacca, D. R. Fandrick, J. J. Song, C. H. Senanayake, *Adv. Synth. Catal.* **2011**, *353*, 1825–1864, DOI 10.1002/adsc.201100488.
- [7] C. M. Kalamaras, A. M. Efstathiou, *Conf. Paper Energy* **2013**, *2013*, 1–9, DOI 10.1155/2013/690627.
- [8] B. Khezri, A. C. Fisher, M. Pumera, *J. Mater. Chem. A* **2017**, *5*, 8230–8246, DOI 10.1039/C6TA09875D.
- [9] S. Nitopi, E. Bertheussen, S. B. Scott, X. Liu, A. K. Engstfeld, S. Horch, B. Seger, I. E. L. Stephens, K. Chan, C. Hahn, J. K. Nørskov, T. F. Jaramillo, I. Chorkendorff, *Chem. Rev.* **2019**, *119*, 7610–7672, DOI 10.1021/acs.chemrev.8b00705.
- [10] V. Mouarrawis, R. Plessius, J. I. van der Vlugt, J. N. H. Reek, *Front. Chem.* **2018**, *6*, 623, DOI 10.3389/fchem.2018.00623.
- [11] M. R. Buchmeiser, *ChemCatChem* **2021**, *13*, 785–786, DOI 10.1002/cctc.202001941.
- [12] M. R. Ringenberg, F. Wittkamp, U.-P. Apfel, W. Kaim, *Inorg. Chem.* **2017**, *56*, 7501–7511, DOI 10.1021/acs.inorgchem.7b00957.
- [13] M. J. Evans, P. J. Black, *Aust. J. Phys.* **1970**, *3*, 2167–2177, DOI 10.1088/0022-3719/3/10/020.
- [14] G. K. Wertheim, M. A. Butler, K. W. West, D. N. E. Buchanan, *Rev. Sci. Instrum.* **1974**, *45*, 1369–1371, DOI 10.1063/1.1686503.
- [15] H. Sato, S. E. Bottle, J. P. Blinco, A. S. Micallef, G. R. Eaton, S. S. Eaton, *J. Magn. Reson.* **2008**, *191*, 66–77, DOI 10.1016/j.jmr.2007.12.003.
- [16] A. Clark, J. Sedhom, H. Elajaili, G. R. Eaton, S. S. Eaton, *Concepts Magn. Reson. A* **2016**, *45A*, e21423, DOI 10.1002/cmra.21423.
- [17] T. Okada, T. Asawa, Y. Sugiyama, M. Kirihara, T. Iwai, Y. Kimura, *Synlett* **2014**, *25*, 596–598, DOI 10.1055/s-0033-1340483.

- [18] X.-Q. Li, C. Zhang, *Synthesis* **2009**, *2009*, 1163–1169, DOI 10.1055/s-0028-1087850.
- [19] S. A. Shelke, S. T. Sigurdsson, *Eur. J. Org. Chem.* **2012**, *2012*, 2291–2301, DOI 10.1002/ejoc.201101434.
- [20] I. D. Sahu, R. M. McCarrick, G. A. Lorigan, *Biochemistry* **2013**, *52*, 5967–5984, DOI 10.1021/bi400834a.
- [21] R. Owenius, M. Engström, M. Lindgren, M. Huber, *J. Phys. Chem. A* **2001**, *105*, 10967–10977, DOI 10.1021/jp0116914.
- [22] K. Nakagawa, M. B. Candelaria, W. W. Chik, S. S. Eaton, G. R. Eaton, *J. Magn. Reson.* **1992**, *98*, 81–91, DOI 10.1016/0022-2364(92)90111-J.
- [23] K. B. Konov, A. A. Knyazev, Y. G. Galyametdinov, N. P. Isaev, L. V. Kulik, *Appl. Magn. Reson.* **2013**, *44*, 949–966, DOI 10.1007/s00723-013-0464-8.
- [24] M. Kveder, M. Jokić, B. Rakvin, *J. Chem. Phys.* **2011**, *134*, 044531, DOI 10.1063/1.3533798.
- [25] S. von Kugelgen, M. D. Krzyaniak, M. Gu, D. Puggioni, J. M. Rondinelli, M. R. Wasielewski, D. E. Freedman, *J. Am. Chem. Soc.* **2021**, *143*, 8069–8077, DOI 10.1021/jacs.1c02417.
- [26] E. Drobner, H. Huber, G. Wächtershäuser, D. Rose, K. O. Stetter, *Nature* **1990**, *346*, 742–744, DOI 10.1038/346742a0.
- [27] G. Wächtershäuser, *Prog. Biophys. molec. Biol.* **1992**, *58*, 85–201, DOI 10.1016/0079-6107(92)90022-X.
- [28] G. Wächtershäuser, *Science* **2000**, *289*, 1307–1308, DOI 10.1126/science.289.5483.1307.
- [29] M. Dörr, J. Kässbohrer, R. Grunert, G. Kreisel, W. A. Brand, R. A. Werner, H. Geilmann, C. Apfel, C. Robl, W. Weigand, *Angew. Chem. Int. Ed.* **2003**, *42*, 1540–1543, DOI 10.1002/anie.200250371.
- [30] H. Raanan, S. Poudel, D. H. Pike, V. Nanda, P. G. Falkowski, *Proc. Natl. Acad. Sci.* **2020**, *117*, 7193–7199, DOI 10.1073/pnas.1914982117.
- [31] D. D. Sasselov, J. P. Grotzinger, J. D. Sutherland, *Sci. Adv.* **2020**, *6*, eaax3419, DOI 10.1126/sciadv.aax3419.
- [32] R. Bolney, M. Grosch, M. Winkler, J. van Slageren, W. Weigand, C. Robl, *RSC Adv.* **2021**, *11*, 32464–32475, DOI 10.1039/d1ra03705f.
- [33] P. R. Smith, A. S. Bingham, J. R. Swartz, *Int. J. Hydrog. Energy* **2012**, *37*, 2977–2983, DOI 10.1016/j.ijhydene.2011.03.172.
- [34] W. Lubitz, H. Ogata, O. Rüdiger, E. Reijerse, *Chem. Rev.* **2014**, *114*, 4081–4148, DOI 10.1021/cr4005814.
- [35] J. Huang, A. Jones, T. D. Waite, Y. Chen, X. Huang, K. M. Rosso, A. Kappler, M. Mansor, P. G. Tratnyek, H. Zhang, *Chem. Rev.* **2021**, *121*, 8161–8233, DOI 10.1021/acs.chemrev.0c01286.

- [36] S. B. Singh in *Enzymes in Food Technology, Vol. 45*, (Ed.: M. Kuddus), Springer Singapore, Singapore, **2018**, pp. 143–165, DOI 10.1007/978-981-13-1933-4_8.
- [37] J. C. Védrine, *ChemSusChem* **2019**, *12*, 577–588, DOI 10.1002/cssc.201802248.
- [38] J. D. Hayler, D. K. Leahy, E. M. Simmons, *Organometallics* **2019**, *38*, 36–46, DOI 10.1021/acs.organomet.8b00566.
- [39] L. O. Mark, M. C. Cendejas, I. Hermans, *ChemSusChem* **2020**, *13*, 5808–5836, DOI 10.1002/cssc.202001905.
- [40] G. Lloyd, R. S. Forgan, *Reactivity in Confined Spaces*, Royal Society of Chemistry, Cambridge, **2021**, DOI 10.1039/9781788019705.
- [41] R. Huisgen, *Proc. Chem. Soc.* **1961**, 357, DOI 10.1039/PS9610000357.
- [42] V. V. Rostovtsev, L. G. Green, V. V. Fokin, K. B. Sharpless, *Angew. Chem. Int. Ed. Engl.* **2002**, *41*, 2596–2599, DOI 10.1002/1522-3773(20020715)41:14<2596::AID-ANIE2596>3.0.CO;2-4.
- [43] R. A. Evans, *Aust. J. Chem.* **2007**, *60*, 384, DOI 10.1071/CH06457.
- [44] M. Meldal, C. W. Tornøe, *Chem. Rev.* **2008**, *108*, 2952–3015, DOI 10.1021/cr0783479.
- [45] W. Bi, Y. Bi, X. Gao, P. Li, S. Hou, Y. Zhang, C. Bammert, S. Jockusch, T. D. Legalley, K. Michael Gibson, L. Bi, *Bioorg. Med. Chem.* **2017**, *25*, 2545–2568, DOI 10.1016/j.bmc.2017.03.033.
- [46] M. J. Moure, A. Eletsky, Q. Gao, L. C. Morris, J.-Y. Yang, D. Chapla, Y. Zhao, C. Zong, I. J. Amster, K. W. Moremen, G.-J. Boons, J. H. Prestegard, *ACS Chem. Biol.* **2018**, *13*, 2560–2567, DOI 10.1021/acscchembio.8b00511.
- [47] A. I. Smirnov, T. I. Smirnova, P. D. Morse, *Biophys. J.* **1995**, *68*, 2350–2360, DOI 10.1016/S0006-3495(95)80417-0.
- [48] I. G. Shenderovich, Z. Kecki, I. Wawer, G. S. Denisov, *Spectrosc. Lett.* **1997**, *30*, 1515–1523, DOI 10.1080/00387019708006741.
- [49] T. Vogler, A. Studer, *Synthesis* **2008**, *2008*, 1979–1993, DOI 10.1055/s-2008-1078445.
- [50] D. B. Gophane, S. T. Sigurdsson, *Beilstein J. Org. Chem.* **2015**, *11*, 219–227, DOI 10.3762/bjoc.11.24.
- [51] A. P. Côté, A. I. Benin, N. W. Ockwig, M. O’Keeffe, A. J. Matzger, O. M. Yaghi, *Science* **2005**, *310*, 1166–1170, DOI 10.1126/science.1120411.
- [52] X. Feng, X. Ding, D. Jiang, *Chem. Soc. Rev.* **2012**, *41*, 6010–6022, DOI 10.1039/C2CS35157A.
- [53] S.-Y. Ding, W. Wang, *Chem. Soc. Rev.* **2013**, *42*, 548–568, DOI 10.1039/C2CS35072F.
- [54] N. Huang, P. Wang, D. Jiang, *Nat. Rev. Mater.* **2016**, *1*, 6010, DOI 10.1038/natrevmats.2016.68.
- [55] D. Zhao, J. Feng, Q. Huo, N. Melosh, G. H. Fredrickson, B. F. Chmelka, G. D. Stucky, *Science* **1998**, *279*, 548–552, DOI 10.1126/science.279.5350.548.

- [56] R. Huirache-Acuña, R. Nava, C. L. Peza-Ledesma, J. Lara-Romero, G. Alonso-Núñez, B. Pawelec, E. M. Rivera-Muñoz, *Materials* **2013**, *6*, 4139–4167, DOI 10.3390/ma6094139.
- [57] B. Malvi, B. R. Sarkar, D. Pati, R. Mathew, T. G. Ajithkumar, S. Sen Gupta, *J. Mater. Chem.* **2009**, *19*, 1409, DOI 10.1039/B815350G.
- [58] P. Verma, Y. Kuwahara, K. Mori, R. Raja, H. Yamashita, *Nanoscale* **2020**, *12*, 11333–11363, DOI 10.1039/D0NR00732C.
- [59] W. Teng, Z. Wu, J. Fan, W.-x. Zhang, D. Zhao, *J. Mater. Chem. A* **2015**, *3*, 19168–19176, DOI 10.1039/C5TA05320J.
- [60] P. Zhang, L. Wang, S. Yang, J. A. Schott, X. Liu, S. M. Mahurin, C. Huang, Y. Zhang, P. F. Fulvio, M. F. Chisholm, S. Dai, *Nat. Commun.* **2017**, *8*, 15020, DOI 10.1038/ncomms15020.
- [61] F. Markus, C. Vogler, J. R. Bruckner, S. Naumann, *ACS Appl. Nano Mater.* **2021**, *4*, 3486–3492, DOI 10.1021/acsanm.0c03467.
- [62] *EPR spectroscopy: Fundamentals and methods*, (Eds.: D. Goldfarb, S. Stoll), Wiley, Chichester, West Sussex, **2018**.
- [63] T. Prisner, M. Rohrer, F. MacMillan, *Annu. Rev. Phys. Chem.* **2001**, *52*, 279–313, DOI 10.1146/annurev.physchem.52.1.279.
- [64] A. Schweiger, G. Jeschke, *Principles of pulse electron paramagnetic resonance*, Reprinted., Oxford Univ. Press, Oxford, **2005**.
- [65] A. Bencini, D. Gatteschi, *Electron Paramagnetic Resonance of Exchange Coupled Systems*, Springer Berlin Heidelberg, Berlin, Heidelberg, **1990**, DOI 10.1007/978-3-642-74599-7.
- [66] P. Atkins, *Molecular quantum mechanics: An introduction to quantum chemistry*, Oxford University Press, London, **1970**.
- [67] J. N. Molin, K. M. Salichov, K. I. Zamaraev, *Spin exchange: Principles and applications in chemistry and biology*, Springer, Berlin and Heidelberg, **1980**.
- [68] H. A. Atwater, *Am. J. Phys.* **1969**, *37*, 836–837, DOI 10.1119/1.1975863.
- [69] G. R. Eaton, S. S. Eaton, D. P. Barr, R. T. Weber, *Quantitative EPR*, Springer, Wien, **2010**.
- [70] *Distance Measurements in Biological Systems by EPR*, (Ed.: L. J. Berliner), Kluwer Academic Publishers, Boston, MA, **2002**, DOI 10.1007/b111467.
- [71] G. Jeschke, V. Chechik, P. Ionita, A. Godt, H. Zimmermann, J. Banham, C. R. Timmel, D. Hilger, H. Jung, *Appl. Magn. Reson.* **2006**, *30*, 473–498, DOI 10.1007/BF03166213.
- [72] G. Jeschke, *Annu. Rev. Phys. Chem.* **2012**, *63*, 419–446, DOI 10.1146/annurev-physchem-032511-143716.
- [73] P. J. Stephens, *J. Chem. Phys.* **1970**, *52*, 3489, DOI 10.1063/1.1673514.

- [74] W. R. Mason, *A practical guide to magnetic circular dichroism spectroscopy*, Wiley-Interscience, Hoboken, N.J., **2007**.
- [75] M. Bauer, *Phys. Chem. Chem. Phys.* **2014**, *16*, 13827–13837, DOI 10.1039/C4CP00904E.
- [76] J. A. van Bokhoven, C. Lamberti, *X-Ray Absorption and X-Ray Emission Spectroscopy*, John Wiley & Sons, Ltd, Chichester, UK, **2016**, DOI 10.1002/9781118844243.
- [77] J. Clarke, A. I. Braginski, *The SQUID Handbook*, Wiley, **2004**, DOI 10.1002/3527603646.
- [78] M. Buchner, K. Höfler, B. Henne, V. Ney, A. Ney, *J. Appl. Phys.* **2018**, *124*, 161101, DOI 10.1063/1.5045299.
- [79] P. Gütlich, *Z. Anorg. Allg. Chem.* **2012**, *638*, 15–43, DOI 10.1002/zaac.201100416.
- [80] P. Gütlich, E. Bill, A. X. Trautwein, *Mössbauer Spectroscopy and Transition Metal Chemistry*, Springer Berlin Heidelberg, Berlin, Heidelberg, **2011**, DOI 10.1007/978-3-540-88428-6.
- [81] J. Konijn, E. Lingeman, *Nucl. Instrum. Methods* **1971**, *94*, 389–390, DOI 10.1016/0029-554X(71)90597-0.
- [82] C. J. da Silva, A. Iwahara, D. S. Moreira, J. U. Delgado, R. S. Gomes, *Appl. Radiat. Isot.* **2012**, *70*, 1924–1926, DOI 10.1016/j.apradiso.2012.02.038.
- [83] V. A. Morozov, N. V. Morozova, T. Badica, G. Cata-Danil, D. Ghita, I. V. Popescu, *Nucl. Instrum. Methods Phys. Res. A: Accel. Spectrom. Detect. Assoc. Equip.* **2006**, *566*, 448–451, DOI 10.1016/j.nima.2006.06.059.
- [84] W. R. Leo, *Techniques for Nuclear and Particle Physics Experiments: A How-to Approach*, 1st ed., Springer Berlin Heidelberg, Berlin/Heidelberg, **1994**.
- [85] F. Neese, *Inorganica Chim. Acta* **2002**, *337*, 181–192, DOI 10.1016/S0020-1693(02)01031-9.
- [86] O. C. Kistner, A. W. Sunyar, *Phys. Rev. Lett.* **1960**, *4*, 412–415, DOI 10.1103/PhysRevLett.4.412.
- [87] B. D. Josephson, *Phys. Rev. Lett.* **1960**, *4*, 341–342, DOI 10.1103/PhysRevLett.4.341.
- [88] K. N. Shrivastava, *Phys. Rev. B* **1970**, *1*, 955–956, DOI 10.1103/PhysRevB.1.955.
- [89] K. N. Shrivastava, *Hyperfine Interact.* **1985**, *26*, 817–843, DOI 10.1007/BF02354640.
- [90] R. Ingalls, *Phys. Rev.* **1964**, *133*, A787–A795, DOI 10.1103/PhysRev.133.A787.
- [91] C. K. Jørgensen, J. B. Neilands, R. S. Nyholm, D. Reinen, R. J. P. Williams, *Structure and Bonding*, Springer, Berlin and Heidelberg, **1967**, DOI 10.1007/BFb0118871.
- [92] A. J. Nozik, M. Kaplan, *Phys. Rev.* **1967**, *159*, 273–276, DOI 10.1103/PhysRev.159.273.
- [93] R. Bersohn, R. G. Shulman, *J. Chem. Phys.* **1966**, *45*, 2298–2303, DOI 10.1063/1.1727924.

- [94] M. Weissbluth, J. E. Maling, *J. Chem. Phys.* **1967**, *47*, 4166–4172, DOI 10.1063/1.1701594.
- [95] P. B. Merrithew, P. G. Rasmussen, D. H. Vincent, *Inorg. Chem.* **1971**, *10*, 1401–1406, DOI 10.1021/ic50101a017.
- [96] D. C. Cook, *Z. Naturforsch. A* **1996**, *51*, 368–372, DOI 10.1515/zna-1996-5-610.
- [97] G. Höhler, J. H. Kühn, T. Müller, J. Trümper, A. Ruckenstein, P. Wölffe, F. Steiner, R. Röhlberger, *Nuclear Condensed Matter Physics with Synchrotron Radiation, Vol. 208*, Springer Berlin Heidelberg, Berlin, Heidelberg, **2005**, DOI 10.1007/b86125.
- [98] M. Blume, J. A. Tjon, *Phys. Rev.* **1968**, *165*, 446–456, DOI 10.1103/PhysRev.165.446.
- [99] H. H. Wickman, M. P. Klein, D. A. Shirley, *Phys. Rev.* **1966**, *152*, 345–357, DOI 10.1103/PhysRev.152.345.
- [100] H. C. Kolb, M. G. Finn, K. B. Sharpless, *Angew. Chem. Int. Ed. Engl.* **2001**, *40*, 2004–2021, DOI 10.1002/1521-3773(20010601)40:11<2004::AID-ANIE2004>3.0.CO;2-5.
- [101] F. Himo, T. Lovell, R. Hilgraf, V. V. Rostovtsev, L. Noodleman, K. B. Sharpless, V. V. Fokin, *J. Am. Chem. Soc.* **2005**, *127*, 210–216, DOI 10.1021/ja0471525.
- [102] J. E. Moses, A. D. Moorhouse, *Chem. Soc. Rev.* **2007**, *36*, 1249–1262, DOI 10.1039/b613014n.
- [103] R. V. Morris, G. Klingelhöfer, C. Schröder, D. S. Rodionov, A. Yen, D. W. Ming, P. A. de Souza, I. Fleischer, T. Wdowiak, R. Gellert, B. Bernhardt, E. N. Evlanov, B. Zubkov, J. Foh, U. Bonnes, E. Kankeleit, P. Gütlich, F. Renz, S. W. Squyres, R. E. Arvidson, *J. Geophys. Res.* **2006**, *111*, n/a–n/a, DOI 10.1029/2005JE002584.
- [104] G. Klingelhöfer, R. V. Morris, B. Bernhardt, C. Schröder, D. S. Rodionov, P. A. de Souza, A. Yen, R. Gellert, E. N. Evlanov, B. Zubkov, J. Foh, U. Bonnes, E. Kankeleit, P. Gütlich, D. W. Ming, F. Renz, T. Wdowiak, S. W. Squyres, R. E. Arvidson, *Science* **2004**, *306*, 1740–1745, DOI 10.1126/science.1104653.
- [105] R. V. Pound, G. A. Rebka, *Phys. Rev. Lett.* **1959**, *3*, 439–441, DOI 10.1103/PhysRevLett.3.439.
- [106] R. L. Mössbauer, *Z. Phys.* **1958**, *151*, 124–143, DOI 10.1007/BF01344210.
- [107] A. L. Kholmetskii, M. Mashlan, K. Nomura, O. V. Misevich, A. R. Lopatik, *Czechoslov. J. Phys.* **2001**, *51*, 763–771, DOI 10.1023/A:1017622521098.
- [108] J. A. Mareš, M. Nikl, C. Pédrini, B. Moine, K. Blažek, *Mater. Chem. Phys.* **1992**, *32*, 342–348, DOI 10.1016/0254-0584(92)90178-B.
- [109] S. Baccaro, K. Blažek, F. de Notaristefani, P. Maly, J. Mares, R. Pani, R. Pellegrini, A. Soluri, *Nucl. Instrum. Methods Phys. Res. A: Accel. Spectrom. Detect. Assoc. Equip.* **1995**, *361*, 209–215, DOI 10.1016/0168-9002(95)00016-X.

- [110] J. Tang, J. Sánchez Costa, S. Smulders, G. Molnár, A. Bousseksou, S. J. Teat, Y. Li, G. A. van Albada, P. Gamez, J. Reedijk, *Inorg. Chem.* **2009**, *48*, 2128–2135, DOI 10.1021/ic801973x.
- [111] E. Evangelio, D. Ruiz-Molina, *Eur. J. Inorg. Chem.* **2005**, *2005*, 2957–2971, DOI 10.1002/ejic.200500323.
- [112] A. Rajput, A. K. Sharma, S. K. Barman, D. Koley, M. Steinert, R. Mukherjee, *Inorg. Chem.* **2014**, *53*, 36–48, DOI 10.1021/ic401985d.
- [113] M. S. Barkhad, B. Abu-Jdayil, A. H. I. Mourad, M. Z. Iqbal, *Polymers* **2020**, *12*, DOI 10.3390/polym12092091.
- [114] *Mechanical Engineer's Data Handbook*, Elsevier, **1993**, DOI 10.1016/C2009-0-24207-3.
- [115] R. Mirji, B. Lobo, *Radiat. Phys. Chem.* **2017**, *135*, 32–44, DOI 10.1016/j.radphyschem.2017.03.001.
- [116] M. Savi, D. Villani, M. Andrade, O. Rodrigues, M. Potiens, *Radiat. Phys. Chem.* **2021**, *182*, 109365, DOI 10.1016/j.radphyschem.2021.109365.
- [117] J. W. Allison, *Aust. J. Phys.* **1961**, *14*, 443, DOI 10.1071/PH610443.
- [118] G. J. Long, T. E. Cranshaw, G. Longworth, *Mössbauer Eff. Ref. Data J* **1983**, *6*, 42–49.
- [119] S. Seltzer, J. H. Hubbell, Tables of X-Ray Mass Attenuation Coefficients and Mass Energy-Absorption Coefficients, NIST Standard Reference Database 126, **1995**, DOI 10.18434/T4D01F.
- [120] O. P. Ernst, D. T. Lodowski, M. Elstner, P. Hegemann, L. S. Brown, H. Kandori, *Chem. Rev.* **2014**, *114*, 126–163, DOI 10.1021/cr4003769.
- [121] E. Orgiu, P. Samorì, *Adv. Mater.* **2014**, *26*, 1827–1845, DOI 10.1002/adma.201304695.
- [122] B. Soberats, E. Uchida, M. Yoshio, J. Kagimoto, H. Ohno, T. Kato, *J. Am. Chem. Soc.* **2014**, *136*, 9552–9555, DOI 10.1021/ja5041573.
- [123] J. Park, D. Yuan, K. T. Pham, J.-R. Li, A. Yakovenko, H.-C. Zhou, *J. Am. Chem. Soc.* **2012**, *134*, 99–102, DOI 10.1021/ja209197f.
- [124] R. Dorel, B. L. Feringa, *ChemComm* **2019**, *55*, 6477–6486, DOI 10.1039/C9CC01891C.
- [125] A. Goulet-Hanssens, F. Eisenreich, S. Hecht, *Adv. Mater.* **2020**, *32*, e1905966, DOI 10.1002/adma.201905966.
- [126] R. P. Bennett, *Inorg. Chem.* **1970**, *9*, 2184–2186, DOI 10.1021/ic50091a047.
- [127] V. V. G, V. Sadasivan, S. S. Meena, P. Bhatt in *AIP Conf. Proc.* Pp. 622–626, DOI 10.1063/1.4898308.
- [128] S. Mini, S. S. Meena, P. Bhatt, V. Sadasivan, V. G. Vidya in *AIP Conf. Proc.* Pp. 1011–1012, DOI 10.1063/1.4810575.
- [129] R. Ahlrichs, M. Bär, M. Häser, H. Horn, C. Kölmel, *Chem. Phys. Lett.* **1989**, *162*, 165–169, DOI 10.1016/0009-2614(89)85118-8.

- [130] K. Eichkorn, F. Weigend, O. Treutler, R. Ahlrichs, *Theor. Chem. Acc.* **1997**, *97*, 119–124, DOI 10.1007/s002140050244.
- [131] M. Sierka, A. Hogekamp, R. Ahlrichs, *Theor. Chem. Acc.* **2003**, *118*, 9136–9148, DOI 10.1063/1.1567253.
- [132] A. Schäfer, C. Huber, R. Ahlrichs, *J. Chem. Phys.* **1994**, *100*, 5829–5835, DOI 10.1063/1.467146.
- [133] A. D. Becke, *Phys. Rev. A* **1988**, *38*, 3098–3100, DOI 10.1103/PhysRevA.38.3098.
- [134] Perdew, *Phys. Rev. B* **1986**, *33*, 8822–8824, DOI 10.1103/PhysRevB.33.8822.
- [135] S. Grimme, J. Antony, S. Ehrlich, H. Krieg, *J. Chem. Phys.* **2010**, *132*, 154104, DOI 10.1063/1.3382344.
- [136] S. Sinnecker, L. D. Slep, E. Bill, F. Neese, *Inorg. Chem.* **2005**, *44*, 2245–2254, DOI 10.1021/ic048609e.
- [137] M. Römelt, S. Ye, F. Neese, *Inorg. Chem.* **2009**, *48*, 784–785, DOI 10.1021/ic801535v.
- [138] W. Kerler, W. Neuwirth, E. Fluck, P. Kuhn, B. Zimmermann, *Z. Phys.* **1963**, *173*, 321–346, DOI 10.1007/BF01377831.
- [139] E. Fluck, W. Kerler, W. Neuwirth, *Angew. Chem. Int. Ed. Engl.* **1963**, *2*, 277–287, DOI 10.1002/anie.196302771.
- [140] R. Bolney, Dissertation, Friedrich-Schiller Universität Jena, **2021**.
- [141] N. I. Organova, V. A. Drits, A. L. Dmitrik, *Sov. Phys. Crystallogr.* **1973**, *1973*, 667–671.
- [142] N. I. Organova, V. A. Drits, A. L. Dmitrik, *Am. Mineral.* **1974**, *59*, 190–200.
- [143] Y. Muramatsu, M. Nambu, *J. Japan. Assoc. Min. Petr. Econ. Geol.* **1980**, *75*, 377–384, DOI 10.2465/ganko1941.75.377.
- [144] J. L. Jambor, *Geol. Surv. Can. (Geological Survey of Canada)* **1976**, *Paper 76-1B*, 65–69.
- [145] H. L. Zhang, E. Cottrell, P. A. Solheid, K. A. Kelley, M. M. Hirschmann, *Chem. Geol.* **2018**, *479*, 166–175, DOI 10.1016/j.chemgeo.2018.01.006.
- [146] Y. Minai, T. Tominaga, *Int. J. Appl. Radiat. Isot.* **1982**, *33*, 513–515, DOI 10.1016/0020-708X(82)90004-7.
- [147] D. J. Vaughan, M. S. Ridout, *J. Inorg. Nucl.* **1971**, *33*, 741–746, DOI 10.1016/0022-1902(71)80472-4.
- [148] S. Boursiquot, M. Mullet, M. Abdelmoula, J.-M. Génin, J.-J. Ehrhardt, *Phys. Chem. Miner.* **2001**, *28*, 600–611, DOI 10.1007/s002690100193.
- [149] C. Schröder, M. Wan, I. B. Butler, A. Tait, S. Peiffer, C. A. McCammon, *Minerals* **2020**, *10*, 1090, DOI 10.3390/min10121090.
- [150] K. D. Kwon, K. Refson, S. Bone, R. Qiao, W.-l. Yang, Z. Liu, G. Sposito, *Phys. Rev. B* **2011**, *83*, 1469, DOI 10.1103/PhysRevB.83.064402.

- [151] M. Mashlan, M. Miglierini, P. Schaaf, *Material Research in Atomic Scale by Mössbauer Spectroscopy*, Springer, Dordrecht, **2003**, DOI 10.1007/978-94-010-0151-9.
- [152] N. I. Chistyakova, T. V. Gubaidulina, V. S. Rusakov, *Czechoslov. J. Phys.* **2006**, *56*, E123–E131, DOI 10.1007/s10582-006-0478-7.
- [153] C. A. McCammon, A. Pring, H. Keppler, T. Sharp, *Phys. Chem. Miner.* **1995**, *22*, DOI 10.1007/BF00202676.
- [154] M. Nößler, D. Hunger, F. Reichert, M. Winkler, M. Reimann, J. Klein, S. Suhr, L. Suntrup, J. Beerhues, M. Kaupp, J. van Slageren, B. Sarkar, *Dalton Trans.* **2021**, DOI 10.1039/D1DT03535E.
- [155] L. Cambi, L. Szegö, *Ber. Dtsch. Chem. Ges. A/B* **1931**, *64*, 2591–2598, DOI 10.1002/cber.19310641002.
- [156] R. C. Stoufer, D. H. Busch, W. B. Hadley, *J. Am. Chem. Soc.* **1961**, *83*, 3732–3734, DOI 10.1021/ja01478a051.
- [157] E. Koenig, K. Madeja, *Inorg. Chem.* **1967**, *6*, 48–55, DOI 10.1021/ic50047a011.
- [158] A. Hauser, *Angew. Chem. Int. Ed.* **2013**, *52*, 10419, DOI 10.1002/anie.201306160.
- [159] J.-F. Létard, P. Guionneau, L. Goux-Capes in *Spin Crossover in Transition Metal Compounds III*, Topics in Current Chemistry, Springer-Verlag, Berlin/Heidelberg, **2004**, pp. 221–249, DOI 10.1007/b95429.
- [160] A. Grohmann, M. Haryono, K. Student, P. Müller, M. Stocker, *Eur. J. Inorg. Chem.* **2013**, *2013*, 662–669, DOI 10.1002/ejic.201201156.
- [161] C. P. Slichter, H. G. Drickamer, *J. Chem. Phys.* **1972**, *56*, 2142–2160, DOI 10.1063/1.1677511.
- [162] W. Nicolazzi, A. Bousseksou, *C. R. Chim.* **2018**, *21*, 1060–1074, DOI 10.1016/j.crci.2018.10.003.
- [163] A. V. Sinitskiy, A. L. Tchougréeff, R. Dronskowski, *Phys. Chem. Chem. Phys.* **2011**, *13*, 13238–13246, DOI 10.1039/C1CP20440H.
- [164] R. Kulmaczewski, J. Olguín, J. A. Kitchen, H. L. C. Feltham, G. N. L. Jameson, J. L. Tallon, S. Brooker, *J. Am. Chem. Soc.* **2014**, *136*, 878–881, DOI 10.1021/ja411563x.
- [165] L. Kreutzburg, C. G. Hübner, H. Paulsen, *Materials* **2017**, *10*, DOI 10.3390/ma10020172.
- [166] M. Sorai, S. Seki, *J. Phys. Chem. Solids* **1974**, *35*, 555–570, DOI 10.1016/S0022-3697(74)80010-7.
- [167] A. Bousseksou, J. Nasser, J. Linares, K. Boukheddaden, F. Varret, *J. Phys. I France* **1992**, *2*, 1381–1403, DOI 10.1051/jp1:1992217.
- [168] J. A. Nasser, *Eur. Phys. J. B* **2001**, *21*, 3–10, DOI 10.1007/s100510170206.
- [169] J. A. Nasser, K. Boukheddaden, J. Linares, *Eur. Phys. J. B* **2004**, *39*, 219–227, DOI 10.1140/epjb/e2004-00184-y.

- [170] M. Dimian, A. Rotaru in *Magnetic Materials*, (Ed.: K. Maaz), InTech, **2016**, DOI 10.5772/64281.
- [171] P. Guionneau, J.-F. Létard, D. S. Yufit, D. Chasseau, G. Bravic, A. E. Goeta, J. A. K. Howard, O. Kahn, *J. Mater. Chem.* **1999**, *9*, 985–994, DOI 10.1039/A808075E.
- [172] H. Paulsen, H. Grünsteudel, W. Meyer-Klaucke, M. Gerdan, H. F. Grünsteudel, A. I. Chumakov, R. Ruffer, H. Winkler, H. Toftlund, A. X. Trautwein, *Eur. Phys. J. B* **2001**, *23*, 463–472, DOI 10.1007/s100510170038.
- [173] R. L. Collins, R. Pettit, W. A. Baker, *J. Inorg. Nucl.* **1966**, *28*, 1001–1010, DOI 10.1016/0022-1902(66)80196-3.
- [174] C. E. Johnson, W. Marshall, G. J. Perlow, *Phys. Rev.* **1962**, *126*, 1503–1506, DOI 10.1103/PhysRev.126.1503.
- [175] P. R. Brady, J. F. Duncan, K. F. Mok, *Proc. R. Soc. Lond. A* **1965**, *287*, 343–362, DOI 10.1098/rspa.1965.0184.
- [176] M. Winkler, M. Schnierle, F. Ehrlich, K.-I. Mehnert, D. Hunger, A. M. Sheveleva, L. Burkhardt, M. Bauer, F. Tuna, M. R. Ringenberg, J. van Slageren, *Inorg. Chem.* **2021**, *60*, 2856–2865, DOI 10.1021/acs.inorgchem.0c03259.
- [177] X. Liu, S. Ibrahim, C. Tard, C. Pickett, *Coord. Chem. Rev.* **2005**, *249*, 1641–1652, DOI 10.1016/j.ccr.2005.04.009.
- [178] J. Müller, M. Brring in *Iron Catalysis in Organic Chemistry*, (Ed.: B. Plietker), Wiley-VCH Verlag GmbH & Co. KGaA, Weinheim, Germany, **2008**, pp. 29–72, DOI 10.1002/9783527623273.ch2.
- [179] E. Camprubi, S. F. Jordan, R. Vasiliadou, N. Lane, *IUBMB life* **2017**, *69*, 373–381, DOI 10.1002/iub.1632.
- [180] M. Okamura, M. Kondo, R. Kuga, Y. Kurashige, T. Yanai, S. Hayami, V. K. K. Praneeth, M. Yoshida, K. Yoneda, S. Kawata, S. Masaoka, *Nature* **2016**, *530*, 465–468, DOI 10.1038/nature16529.
- [181] H. Rao, L. C. Schmidt, J. Bonin, M. Robert, *Nature* **2017**, *548*, 74–77, DOI 10.1038/nature23016.
- [182] M. Capdevila-Cortada, *Nat. Catal.* **2019**, *2*, 470, DOI 10.1038/s41929-019-0314-7.
- [183] A. Buchard, M. R. Kember, K. G. Sandeman, C. K. Williams, *ChemComm* **2011**, *47*, 212–214, DOI 10.1039/C0CC02205E.
- [184] S. De, J. Zhang, R. Luque, N. Yan, *Energy Environ. Sci.* **2016**, *9*, 3314–3347, DOI 10.1039/C6EE02002J.
- [185] M. J. Dorantes, J. T. Moore, E. Bill, B. Mienert, C. C. Lu, *ChemComm* **2020**, *56*, 11030–11033, DOI 10.1039/D0CC04563B.
- [186] D. H. Pool, D. L. DuBois, *J. Organomet. Chem.* **2009**, *694*, 2858–2865, DOI 10.1016/j.jorganchem.2009.04.010.

- [187] A. D. Wilson, R. H. Newell, M. J. McNevin, J. T. Muckerman, M. Rakowski DuBois, D. L. DuBois, *J. Am. Chem. Soc.* **2006**, *128*, 358–366, DOI 10.1021/ja056442y.
- [188] M. L. Helm, M. P. Stewart, R. M. Bullock, M. R. DuBois, D. L. DuBois, *Science* **2011**, *333*, 863–866, DOI 10.1126/science.1205864.
- [189] F. Neese, E. I. Solomon, *Inorg. Chem.* **1999**, *38*, 1847–1865, DOI 10.1021/ic981264d.
- [190] J. Fulara, K. Filipkowski, J. P. Maier, *J. Phys. Chem. C* **2017**, *121*, 10694–10697, DOI 10.1021/acs.jpcc.6b10391.
- [191] M. D. Rowe, A. J. McCaffery, *J. Am. Chem. Soc.* **1973**, *59*, 3786–3794, DOI 10.1063/1.1680551.
- [192] K. Ishimura, M. Hada, H. Nakatsuji, *J. Chem. Phys.* **2002**, *117*, 6533–6537, DOI 10.1063/1.1504709.
- [193] J. L. Kneebone, V. E. Fleischauer, S. L. Daifuku, A. A. Shaps, J. M. Bailey, T. E. Iannuzzi, M. L. Neidig, *Inorg. Chem.* **2016**, *55*, 272–282, DOI 10.1021/acs.inorgchem.5b02263.
- [194] N. Lee, T. Petrenko, U. Bergmann, F. Neese, S. DeBeer, *J. Am. Chem. Soc.* **2010**, *132*, 9715–9727, DOI 10.1021/ja101281e.
- [195] C. J. Pollock, S. DeBeer, *J. Am. Chem. Soc.* **2011**, *133*, 5594–5601, DOI 10.1021/ja200560z.
- [196] L. Burkhardt, Y. Vukadinovic, M. Nowakowski, A. Kalinko, J. Rudolph, P.-A. Carlsson, C. R. Jacob, M. Bauer, *Inorg. Chem.* **2020**, *59*, 3551–3561, DOI 10.1021/acs.inorgchem.9b02092.
- [197] K. M. Lancaster, K. D. Finkelstein, S. DeBeer, *Inorg. Chem.* **2011**, *50*, 6767–6774, DOI 10.1021/ic200822b.
- [198] A. J. Atkins, M. Bauer, C. R. Jacob, *Phys. Chem. Chem. Phys.* **2013**, *15*, 8095–8105, DOI 10.1039/C3CP50999K.
- [199] P. Eisenberger, P. M. Platzman, H. Winick, *Phys. Rev. Lett.* **1976**, *36*, 623–626, DOI 10.1103/PhysRevLett.36.623.
- [200] O. V. Safonova, M. Tromp, J. A. van Bokhoven, F. M. F. de Groot, J. Evans, P. Glatzel, *J. Phys. Chem. B* **2006**, *110*, 16162–16164, DOI 10.1021/jp063416t.
- [201] P. Glatzel, M. Sikora, G. Smolentsev, M. Fernández-García, *Catal. Today* **2009**, *145*, 294–299, DOI 10.1016/j.cattod.2008.10.049.
- [202] A. J. Atkins, M. Bauer, C. R. Jacob, *Phys. Chem. Chem. Phys.* **2015**, *17*, 13937–13948, DOI 10.1039/C5CP01045D.
- [203] A. M. Messinis, S. L. J. Luckham, P. P. Wells, D. Gianolio, E. K. Gibson, H. M. O’Brien, H. A. Sparkes, S. A. Davis, J. Callison, D. Elorriaga, O. Hernandez-Fajardo, R. B. Bedford, *Nat. Catal.* **2019**, *2*, 123–133, DOI 10.1038/s41929-018-0197-z.

- [204] M. Reiners, D. Baabe, P. Schweyen, M. Freytag, P. G. Jones, M. D. Walter, *Eur. J. Inorg. Chem.* **2017**, 2017, 388–400, DOI 10.1002/ejic.201600873.
- [205] A. E. Gerbase, E. J. S. Vichi, L. Amaral, J. T. Moro, A. Vasquez, *Hyperfine Interact.* **1994**, 83, 169–174, DOI 10.1007/BF02074268.
- [206] K. C. MacLeod, D. J. Vinyard, P. L. Holland, *J. Am. Chem. Soc.* **2014**, 136, 10226–10229, DOI 10.1021/ja505193z.
- [207] U. Zahn, P. Kienle, H. Eicher, *Z. Phys.* **1962**, 166, 220–226, DOI 10.1007/BF01377953.
- [208] A. Houlton, R. A. Brown, J. R. Miller, R. Roberts, J. Silver, M. Thomas, *J. Organomet. Chem.* **1992**, 431, C17–C20, DOI 10.1016/0022-328X(92)83294-R.
- [209] C. Gouverd, F. Biaso, L. Cataldo, T. Berclaz, M. Geoffroy, E. Levillain, N. Avarvari, M. Fourmigué, F. X. Sauvage, C. Wartelle, *Phys. Chem. Chem. Phys.* **2005**, 7, 85–93, DOI 10.1039/B409958C.
- [210] D. Hollmann, F. Gärtner, R. Ludwig, E. Barsch, H. Junge, M. Blug, S. Hoch, M. Beller, A. Brückner, *Angew. Chem. Int. Ed. Engl.* **2011**, 50, 10246–10250, DOI 10.1002/anie.201103710.
- [211] Y. Alpert, Y. Couder, J. Tuchendler, H. Thomé, *Biochim. Biophys. Acta.* **1973**, 322, 34–37, DOI 10.1016/0005-2795(73)90171-2.
- [212] P. J. M. van Kan, E. van der Horst, E. J. Reijerse, P. van Jan M. Bentum, W. R. Hagen, *Faraday Trans.* **1998**, 94, 2975–2978, DOI 10.1039/a803058h.
- [213] A. Priem, P. J. M. van Bentum, W. R. Hagen, E. J. Reijerse, *Appl. Magn. Reson.* **2001**, 21, 535–548, DOI 10.1007/BF03162427.
- [214] H. Meštrić, R.-A. Eichel, K.-P. Dinse, A. Ozarowski, J. van Tol, L. C. Brunel, *J. Appl. Phys.* **2004**, 96, 7440–7444, DOI 10.1063/1.1808477.
- [215] F. Di Benedetto, G. Andreozzi, G. Baldi, A. Barzanti, G. P. Bernardini, V. Faso, L. A. Pardi, M. Romanelli, *J. Eur. Ceram. Soc.* **2006**, 26, 2301–2305, DOI 10.1016/j.jeurceramsoc.2005.04.007.
- [216] J. Krzystek, A. Ozarowski, J. Telsler, *Coord. Chem. Rev.* **2006**, 250, 2308–2324, DOI 10.1016/j.ccr.2006.03.016.
- [217] J. Telsler, J. van Slageren, S. Vongtragool, M. Dressel, W. M. Reiff, S. A. Zvyagin, A. Ozarowski, J. Krzystek, *Magn. Reson. Chem.* **2005**, 43 Spec no, S130–9, DOI 10.1002/mrc.1689.
- [218] J. Robert, N. Parizel, P. Turek, A. K. Boudalis, *Phys. Chem. Chem. Phys.* **2019**, 21, 19575–19584, DOI 10.1039/C9CP03422F.
- [219] M. H. Rakowsky, A. Zecevic, G. R. Eaton, S. S. Eaton, *J. Magn. Reson.* **1998**, 131, 97–110, DOI 10.1006/jmre.1997.1338.
- [220] L. Tesi, E. Lucaccini, I. Cimatti, M. Perfetti, M. Mannini, M. Atzori, E. Morra, M. Chiesa, A. Caneschi, L. Sorace, R. Sessoli, *Chem. Sci.* **2016**, 7, 2074–2083, DOI 10.1039/C5SC04295J.

- [221] M. Atzori, E. Morra, L. Tesi, A. Albino, M. Chiesa, L. Sorace, R. Sessoli, *J. Am. Chem. Soc.* **2016**, *138*, 11234–11244, DOI 10.1021/jacs.6b05574.
- [222] M. Atzori, S. Benci, E. Morra, L. Tesi, M. Chiesa, R. Torre, L. Sorace, R. Sessoli, *Inorg. Chem.* **2018**, *57*, 731–740, DOI 10.1021/acs.inorgchem.7b02616.
- [223] B. Epel, A. Pöpl, P. Manikandan, S. Vega, D. Goldfarb, *J. Magn. Reson.* **2001**, *148*, 388–397, DOI 10.1006/jmre.2000.2261.
- [224] G. Rao, A. B. Altman, A. C. Brown, L. Tao, T. A. Stich, J. Arnold, R. D. Britt, *Inorg. Chem.* **2019**, *58*, 7978–7988, DOI 10.1021/acs.inorgchem.9b00720.
- [225] Z. Li, C. Rieg, A.-K. Beurer, M. Benz, J. Bender, C. Schneck, Y. Traa, M. Dyballa, M. Hunger, *Adsorption* **2021**, *27*, 49–68, DOI 10.1007/s10450-020-00275-8.
- [226] J. Luo, C. Pardin, W. D. Lubell, X. X. Zhu, *ChemComm* **2007**, 2136–2138, DOI 10.1039/B700215G.
- [227] S. K. Goswami, L. R. Hanton, C. J. McAdam, S. C. Moratti, J. Simpson, *Acta Cryst.* **2014**, *70*, 130–133, DOI 10.1107/S1600536814017991.
- [228] N. B. Yapici, S. Jockusch, A. Moscatelli, S. R. Mandalapu, Y. Itagaki, D. K. Bates, S. Wiseman, K. M. Gibson, N. J. Turro, L. Bi, *Org. Lett.* **2012**, *14*, 50–53, DOI 10.1021/o1202816m.
- [229] J. Lee, S. Hong, Y. Heo, H. Kang, M. Kim, *Dalton Trans.* **2021**, *50*, 14081–14090, DOI 10.1039/d1dt03143k.
- [230] C. Altenbach, S. L. Flitsch, H. G. Khorana, W. L. Hubbell, *Biochemistry* **1989**, *28*, 7806–7812, DOI 10.1021/bi00445a042.
- [231] C. H. Wunderlich, R. G. Huber, R. Spitzer, K. R. Liedl, K. Kloiber, C. Kreutz, *ACS Chem. Biol.* **2013**, *8*, 2697–2706, DOI 10.1021/cb400589q.
- [232] M. A. Uddin, H. Yu, L. Wang, K.-u.-R. Naveed, F. Haq, B. U. Amin, S. Mehmood, A. Nazir, Y. Xing, Di Shen, *J. Polym. Sci.* **2020**, *58*, 1924–1948, DOI 10.1002/pol.20200039.
- [233] L. J. Berliner, *Spin Labeling: Theory and Applications*, Springer, New York, NY, **1989**.
- [234] H. Sato, V. Kathirvelu, G. Spagnol, S. Rajca, A. Rajca, S. S. Eaton, G. R. Eaton, *J. Phys. Chem. B* **2008**, *112*, 2818–2828, DOI 10.1021/jp073600u.
- [235] K. Furukawa, M. Shibuya, Y. Yamamoto, *Org. Lett.* **2015**, *17*, 2282–2285, DOI 10.1021/acs.orglett.5b01003.
- [236] M. M. Haugland, E. A. Anderson, J. E. Lovett in *Electron Paramagnetic Resonance*, (Eds.: V. Chechik, D. M. Murphy), Electron Paramagnetic Resonance, Royal Society of Chemistry, Cambridge, **2016**, pp. 1–34, DOI 10.1039/9781782629436-00001.
- [237] K. Halbmaier, J. Seikowski, I. Tkach, C. Höbartner, D. Sezer, M. Bennati, *Chem. Sci.* **2016**, *7*, 3172–3180, DOI 10.1039/C5SC04631A.
- [238] K. Halbmaier, J. Wegner, U. Diederichsen, M. Bennati, *Biophys. J.* **2016**, *111*, 2345–2348, DOI 10.1016/j.bpj.2016.10.022.

- [239] M. A. Slifkin, Y. M. Suleiman, *Radiat. Eff.* **1975**, *27*, 111–112, DOI 10.1080/00337577508233016.
- [240] A. Savitsky, M. Plato, K. Möbius, *Appl. Magn. Reson.* **2010**, *37*, 415–434, DOI 10.1007/s00723-009-0064-9.
- [241] V. Meyer, M. A. Swanson, L. J. Clouston, P. J. Boratyński, R. A. Stein, H. S. Mchaourab, A. Rajca, S. S. Eaton, G. R. Eaton, *Biophys. J.* **2015**, *108*, 1213–1219, DOI 10.1016/j.bpj.2015.01.015.
- [242] J. Nath, S. K. Mishra, *Fluid Phase Equilib.* **1998**, *145*, 89–97, DOI 10.1016/S0378-3812(97)00308-7.
- [243] A. Y. Zarubina, S. G. Kibets, A. A. Politiko, V. N. Semenenko, K. M. Baskov, V. A. Chistyayev, *IOP Conf. Ser.: Mater. Sci. Eng.* **2020**, *862*, 062085, DOI 10.1088/1757-899X/862/6/062085.
- [244] A. Anopchenko, T. Psurek, D. VanderHart, J. F. Douglas, J. Obrzut, *Phys. Rev. E* **2006**, *74*, 031501, DOI 10.1103/PhysRevE.74.031501.
- [245] B. R. Knauer, J. J. Napier, *J. Am. Chem. Soc.* **1976**, *98*, 4395–4400, DOI 10.1021/ja00431a010.
- [246] H. Steinhaus, *Mathematical snapshots*, 3. American ed., rev. and enl, Dover Publ, Mineola, NY, **1999**.
- [247] M. Davies, A. Edwards, *Trans. Faraday Soc.* **1967**, *63*, 2163, DOI 10.1039/TF9676302163.
- [248] Tseng, Turro, Durning, *Phys. Rev. E* **2000**, *61*, 1800–1811, DOI 10.1103/PhysRevE.61.1800.
- [249] K. Paeng, R. Richert, M. D. Ediger, *Soft Matter* **2012**, *8*, 819–826, DOI 10.1039/C1SM06501G.
- [250] P. A. Bobbert, *Nature materials* **2010**, *9*, 288–290, DOI 10.1038/nmat2718.
- [251] A. Lunghi, S. Sanvito, *Sci. Adv.* **2019**, *5*, eaax7163, DOI 10.1126/sciadv.aax7163.
- [252] J. L. Du, G. R. Eaton, S. S. Eaton, *J. Magn. Reson.* **1995**, *115*, 213–221, DOI 10.1006/jmra.1995.1169.
- [253] P. G. Klemens, *Phys. Rev.* **1962**, *125*, 1795–1798, DOI 10.1103/PhysRev.125.1795.
- [254] J. Murphy, *Phys. Rev.* **1966**, *145*, 241–247, DOI 10.1103/PhysRev.145.241.
- [255] M. Kveder, D. Merunka, A. Ilakovac, J. Makarević, M. Jokić, B. Rakvin, *Chem. Phys. Lett.* **2006**, *419*, 91–95, DOI 10.1016/j.cplett.2005.11.055.
- [256] S. Lijewski, M. Wencka, S. K. Hoffmann, M. Kempinski, W. Kempinski, M. Sliwinska-Bartkowiak, *Chem. Phys. Lett.* **2008**, *77*, 1203, DOI 10.1103/PhysRevB.77.014304.
- [257] K. J. Standley, *Electron Spin Relaxation Phenomena in Solids*, Springer, New York, NY, **1969**.

- [258] K. Gottschling, G. Savasci, H. Vignolo-González, S. Schmidt, P. Mauker, T. Banerjee, P. Rovó, C. Ochsenfeld, B. V. Lotsch, *J. Am. Chem. Soc.* **2020**, *142*, 12146–12156, DOI 10.1021/jacs.0c02155.
- [259] L.-Y. Wu, Y.-X. Xie, Z.-S. Chen, Y.-N. Niu, Y.-M. Liang, *Synlett* **2009**, *2009*, 1453–1456, DOI 10.1055/s-0029-1216745.
- [260] P. Sarode, S. Bahekar, H. Chandak, *Synlett* **2016**, *27*, 2681–2684, DOI 10.1055/s-0036-1588590.
- [261] D. A. Powell, H. Fan, *J. Org. Chem.* **2010**, *75*, 2726–2729, DOI 10.1021/jo100197r.
- [262] S. Lal, S. Díez-González, *J. Org. Chem.* **2011**, *76*, 2367–2373, DOI 10.1021/jo200085j.
- [263] P. N. Liu, H. X. Siyang, L. Zhang, S. K. S. Tse, G. Jia, *J. Org. Chem.* **2012**, *77*, 5844–5849, DOI 10.1021/jo3008572.
- [264] W. Duffy, D. L. Strandburg, *J. Chem. Phys.* **1967**, *46*, 456–464, DOI 10.1063/1.1840688.
- [265] M. Wriedt, A. A. Yakovenko, G. J. Halder, A. V. Prosvirin, K. R. Dunbar, H.-C. Zhou, *J. Am. Chem. Soc.* **2013**, *135*, 4040–4050, DOI 10.1021/ja312347p.
- [266] B. K. Hughes, W. A. Braunecker, D. C. Bobela, S. U. Nanayakkara, O. G. Reid, J. C. Johnson, *J. Phys. Chem. Lett.* **2016**, *7*, 3660–3665, DOI 10.1021/acs.jpcllett.6b01711.
- [267] A. Pivtsov, M. Wessig, V. Klovak, S. Polarz, M. Drescher, *J. Phys. Chem. C* **2018**, *122*, 5376–5384, DOI 10.1021/acs.jpcc.7b10758.
- [268] K. Scheffler, *Elektronenspinresonanz: Grundlagen und Anwendung in der organischen Chemie*, Springer, Berlin and Heidelberg, **1970**, DOI 10.1007/978-3-642-95170-1.
- [269] D. C. Johnston, *Phys. Rev. B* **2006**, *74*, 529, DOI 10.1103/PhysRevB.74.184430.
- [270] N. Stein, L. Mainali, J. S. Hyde, W. K. Subczynski, *Appl. Magn. Reson.* **2019**, *50*, 903–918, DOI 10.1007/s00723-019-01119-7.
- [271] L. Stegbauer, K. Schwinghammer, B. V. Lotsch, *Chem. Sci.* **2014**, *5*, 2789–2793, DOI 10.1039/C4SC00016A.
- [272] X. Chen, M. Addicoat, E. Jin, H. Xu, T. Hayashi, F. Xu, N. Huang, S. Irle, D. Jiang, *Sci. Rep.* **2015**, *5*, 14650, DOI 10.1038/srep14650.
- [273] Z.-J. Li, S.-Y. Ding, H.-D. Xue, W. Cao, W. Wang, *ChemComm* **2016**, *52*, 7217–7220, DOI 10.1039/C6CC00947F.
- [274] D. Dhaneswara, F. Delayori, S. Utami, F. R. Kuskendrianto, M. H. Abdurrahman, J. F. Fatriansyah, *E3S Web Conf.* **2018**, *65*, 05007, DOI 10.1051/e3sconf/20186505007.
- [275] M. L. Tummino, M. L. Testa, M. Malandrino, R. Gamberini, A. Bianco Prevot, G. Magnacca, E. Laurenti, *Nanomaterials* **2019**, *9*, DOI 10.3390/nano9020162.

- [276] L.-L. Li, H. Sun, C.-J. Fang, J. Xu, J.-Y. Jin, C.-H. Yan, *J. Mater. Chem.* **2007**, *17*, 4492, DOI 10.1039/B708857D.
- [277] M. Karimi, A. Badiei, G. Mohammadi Ziarani, *RSC Adv.* **2015**, *5*, 36530–36539, DOI 10.1039/C5RA02692J.
- [278] A. Akopyan, P. Polikarpova, O. Gul, A. Anisimov, E. Karakhanov, *Energy Fuels* **2020**, *34*, 14611–14619, DOI 10.1021/acs.energyfuels.0c02008.
- [279] J. Poirson, F. Bretenaker, M. Vallet, A. Le Floch, *J. Opt. Soc. Am. B* **1997**, *14*, 2811, DOI 10.1364/JOSAB.14.002811.
- [280] B. Elschner, *Ber. Bunsenges. Phys. Chem.* **1983**, *87*, 1230, DOI 10.1002/bbpc.19830871245.
- [281] P. Neugebauer, D. Bloos, R. Marx, P. Lutz, M. Kern, D. Aguilà, J. Vaverka, O. Laguta, C. Dietrich, R. Clérac, J. van Slageren, *Phys. Chem. Chem. Phys.* **2018**, *20*, 15528–15534, DOI 10.1039/C7CP07443C.
- [282] S. Stoll, A. Schweiger, *J. Magn. Reson.* **2006**, *178*, 42–55, DOI 10.1016/j.jmr.2005.08.013.
- [283] I. Tkach, A. Baldansuren, E. Kalabukhova, S. Lukin, A. Sitnikov, A. Tsvir, M. Ischenko, Y. Rosentzweig, E. Roduner, *Appl. Magn. Reson.* **2008**, *35*, 95–112, DOI 10.1007/s00723-008-0141-5.
- [284] P. Virtanen, R. Gommers, T. E. Oliphant, M. Haberland, T. Reddy, D. Cournapeau, E. Burovski, P. Peterson, W. Weckesser, J. Bright, S. J. van der Walt, M. Brett, J. Wilson, K. J. Millman, N. Mayorov, A. R. J. Nelson, E. Jones, R. Kern, E. Larson, C. J. Carey, I. Polat, Y. Feng, E. W. Moore, J. VanderPlas, D. Laxalde, J. Perktold, R. Cimrman, I. Henriksen, E. A. Quintero, C. R. Harris, A. M. Archibald, A. H. Ribeiro, F. Pedregosa, P. van Mulbregt, *Nat. Methods* **2020**, *17*, 261–272, DOI 10.1038/s41592-019-0686-2.
- [285] Y. Rechkemmer, J. E. Fischer, R. Marx, M. Dörfel, P. Neugebauer, S. Horvath, M. Gysler, T. Brock-Nannestad, W. Frey, M. F. Reid, J. van Slageren, *J. Am. Chem. Soc.* **2015**, *137*, 13114–13120, DOI 10.1021/jacs.5b08344.
- [286] Y. Rechkemmer, Spectroscopic investigations of the magnetic anisotropy of lanthanide- and cobalt-based molecular nanomagnets, **2016**, DOI 10.18419/opus-8783.
- [287] G. A. Bain, J. F. Berry, *J. Chem. Educ.* **2008**, *85*, 532, DOI 10.1021/ed085p532.
- [288] H. E. Gottlieb, V. Kotlyar, A. Nudelman, *J. Org. Chem.* **1997**, *62*, 7512–7515, DOI 10.1021/jo971176v.
- [289] T. D. Lee, J. F. W. Keana, *J. Org. Chem.* **1975**, *40*, 3145–3147, DOI 10.1021/jo00909a033.
- [290] J. D. Hunter, *Comput. Sci. Eng.* **2007**, *9*, 90–95, DOI 10.1109/MCSE.2007.55.
- [291] G. Ali, P. E. VanNatta, D. A. Ramirez, K. M. Light, M. T. Kieber-Emmons, *J. Am. Chem. Soc.* **2017**, *139*, 18448–18451, DOI 10.1021/jacs.7b10833.
- [292] B. J. Whitlock, H. W. Whitlock, *J. Am. Chem. Soc.* **1983**, *105*, 838–844, DOI 10.1021/ja00342a032.

Appendix

A.1 Set-up of a Mössbauer Spectrometer

A.1.1 Fit Parameters for the Different Aperture Settings

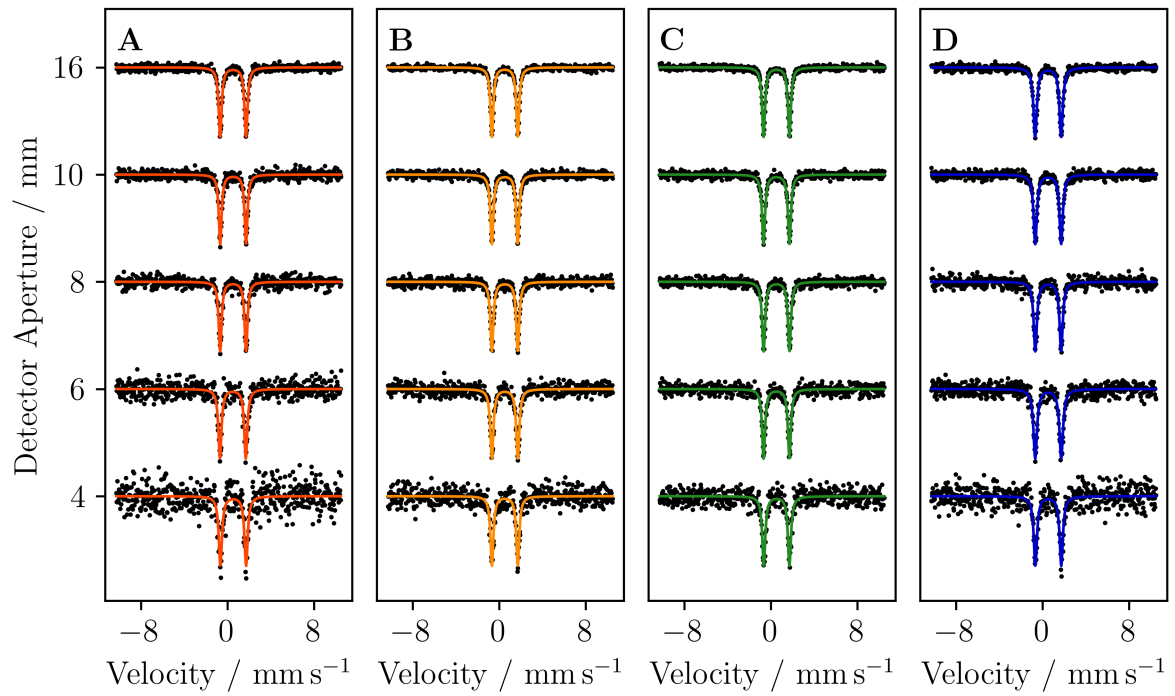


Figure A.1: Mössbauer measurements (black) with the same measurement time for the different aperture settings at the detector for source apertures of 4 (A), 6 (B), 8 (C) and 10 mm (D) with fits (coloured).

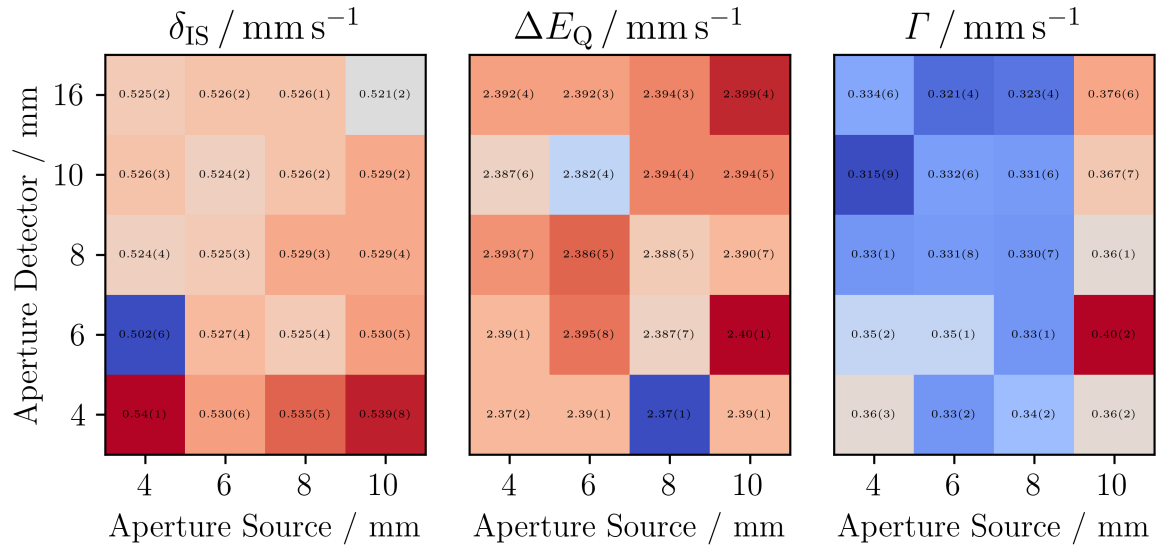


Figure A.2: Fit parameters and errors for the measurements depicted in Figure A.1.

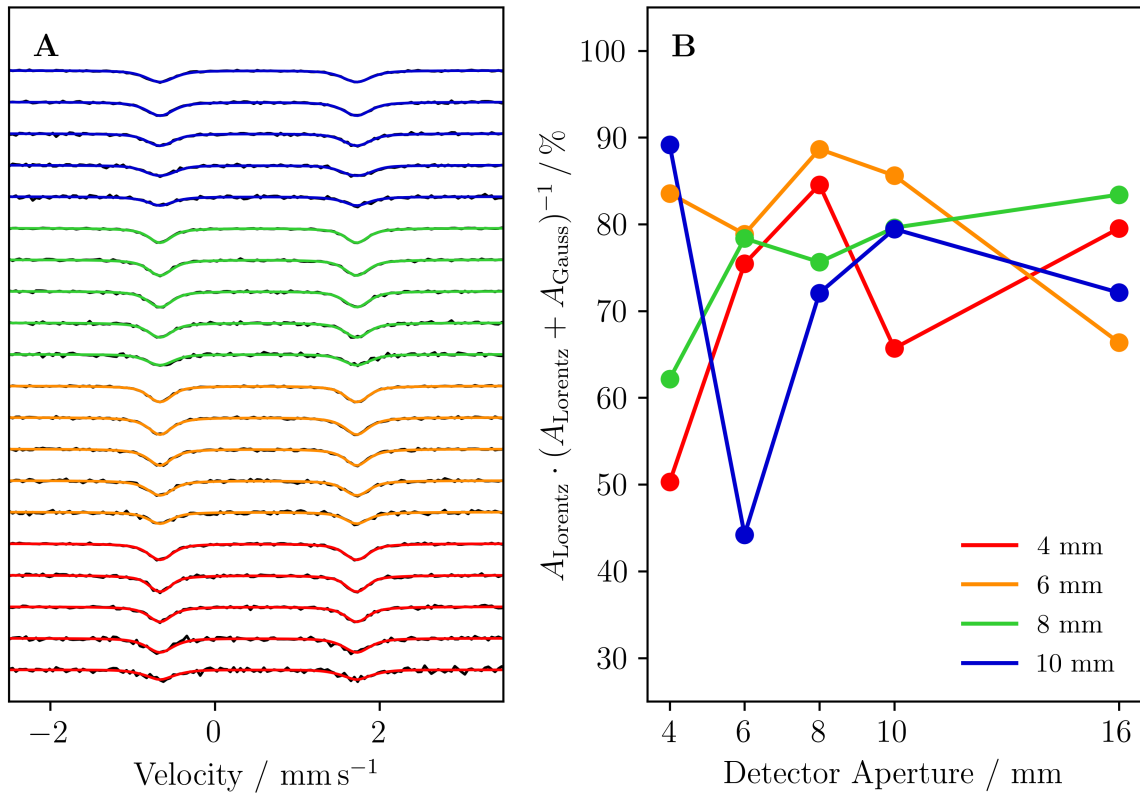


Figure A.3: A) Mössbauer measurements for all aperture settings with different colours for the source detector, see legend in (B). Higher aperture opening are at the top. B) Relative area of the Lorentzian line in the fit.

A.2 The Electronic and Geometric Structure of a Probe Molecule

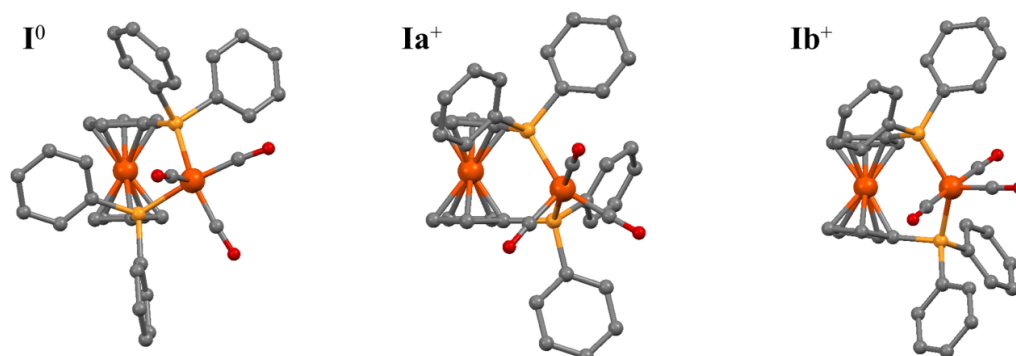


Figure A.4: Crystal structure of \mathbf{I}^0 and calculated structures of the two isomers of \mathbf{I}^+ . Data taken from [12]. Atoms are coloured as specified in the CPK colouring convention: iron (dark orange), phosphorus (orange), oxygen (red), carbon (grey). Hydrogen atoms are omitted for clarity.

A.2.1 Fit Parameters for the Mössbauer Spectra

Table A.1: Fit parameters of the Mössbauer spectra of \mathbf{Ia}^+ shown in Figure 4.9A.

T / K	$\delta_{\text{IS,Fe}^{\text{I}}} / \text{mm s}^{-1}$	$\delta_{\text{IS,Fe}^{\text{II}}} / \text{mm s}^{-1}$	$\Delta E_{\text{Q,Fe}^{\text{I}}} / \text{mm s}^{-1}$	$\Delta E_{\text{Q,Fe}^{\text{II}}} / \text{mm s}^{-1}$
298	0.33(3)	0.42(3)	0.80(3)	2.29(3)
235	0.35(3)	0.45(3)	0.80(3)	2.29(3)
90	0.35(4)	0.50(4)	0.80(4)	2.29(4)
50	0.35(5)	0.50(5)	0.80(5)	2.29(5)

Table A.2: Fit parameters of the Mössbauer spectra of \mathbf{Ib}^+ shown in Figure 4.9A.

T / K	$\delta_{\text{IS,FeI}} / \text{mm s}^{-1}$	$\delta_{\text{IS,FeII}} / \text{mm s}^{-1}$	$\Delta E_{\text{Q,FeI}} / \text{mm s}^{-1}$	$\Delta E_{\text{Q,FeII}} / \text{mm s}^{-1}$
298	-0.04(3)	0.50(3)	0.50(3)	2.33(3)
235	-0.02(3)	0.53(3)	0.52(3)	2.33(3)
90	0.01(2)	0.60(2)	0.50(2)	2.33(2)
50	0.11(1)	0.60(1)	0.50(1)	2.33(1)
10	0.15(1)	0.60(1)	0.50(1)	2.33(1)
7	0.06(1)	0.60(1)	0.50(1)	2.33(1)
3	0.03(1)	0.60(1)	0.50(1)	2.33(1)

Table A.3: Molar fraction of the isomer \mathbf{Ib}^+ for the fits shown in 4.9.

T / K	$x_{\mathbf{Ib}^+}$
298	55
235	66
90	71
50	93
< 10	100

A.2.2 EPR Spectra and Spin Relaxation Times

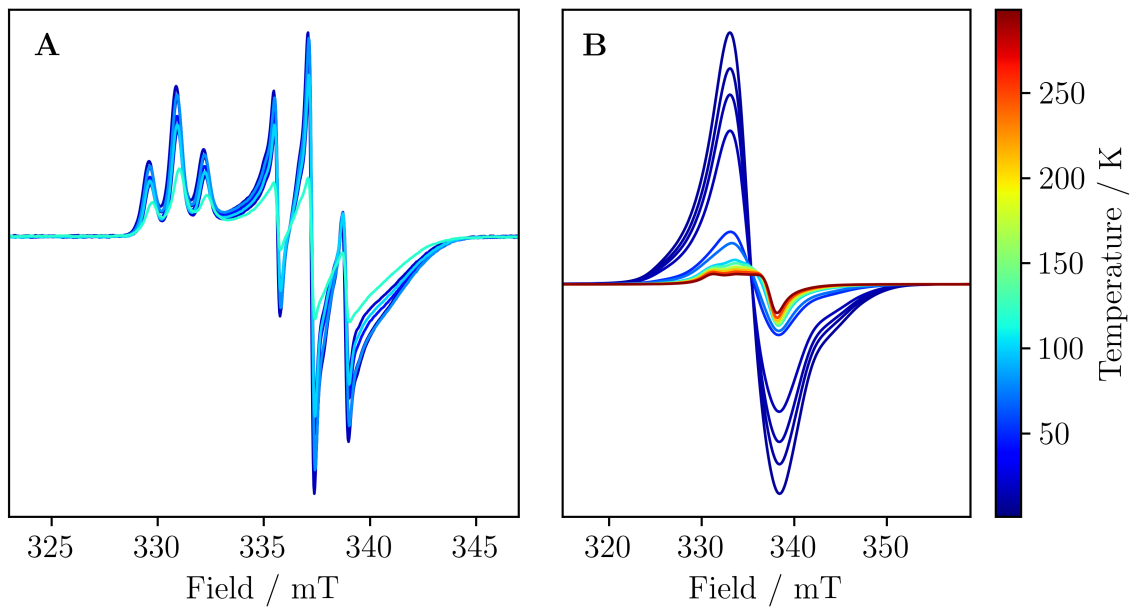


Figure A.5: X-Band EPR spectra of I^+ in 1 mmol l^{-1} DCM:toluene (1:1) (A) and as a powder (B).

Table A.4: Spin relaxation times of I^+ (1 mmol l^{-1} in DCM:toluene (1:1)) measured with EPR at Pos. 1, corresponding to g_{zz} and amount of the slow relaxation process x .

T / K	$T_{1,\text{slow}} / \text{ms}$	$T_{1,\text{fast}} / \text{ms}$	$x_{T_{1,\text{slow}}} / \%$	$T_M / \mu\text{s}$	k_{T_M}
10	19(2)	6.1(6)	35	5.61(3)	1.72
15	2.3(1)	1.09(6)	41	-	-
20	0.452(2)	-	100	4.74(4)	1.46
25	0.176(2)	-	100	-	-
30	0.086(1)	-	100	3.82(6)	1.28
40	0.030(1)	-	100	2.65(6)	1.10
50	0.005(1)	-	100	1.91	0.90

Table A.5: Spin relaxation times of \mathbf{I}^+ (1 mmol l^{-1} in DCM:toluene (1:1)) measured with EPR at Pos. 2, corresponding to g_{yy} and amount of the slow relaxation process x .

T / K	$T_{1,\text{slow}} / \text{ms}$	$T_{1,\text{fast}} / \text{ms}$	$x_{T_{1,\text{slow}}} / \%$	$T_M / \mu\text{s}$	k_{T_M}
10	13(1)	4.5(6)	44	-	-
15	2.26(5)	0.79(6)	70	5.54(2)	1.68
20	0.578(2)	-	100	5.08(2)	1.55
25	0.238(3)	-	100	-	-
30	0.115(1)	-	100	3.40(4)	1.16
40	0.039(1)	-	100	2.62(5)	1.00
50	0.007(1)	-	100	1.68(6)	0.83

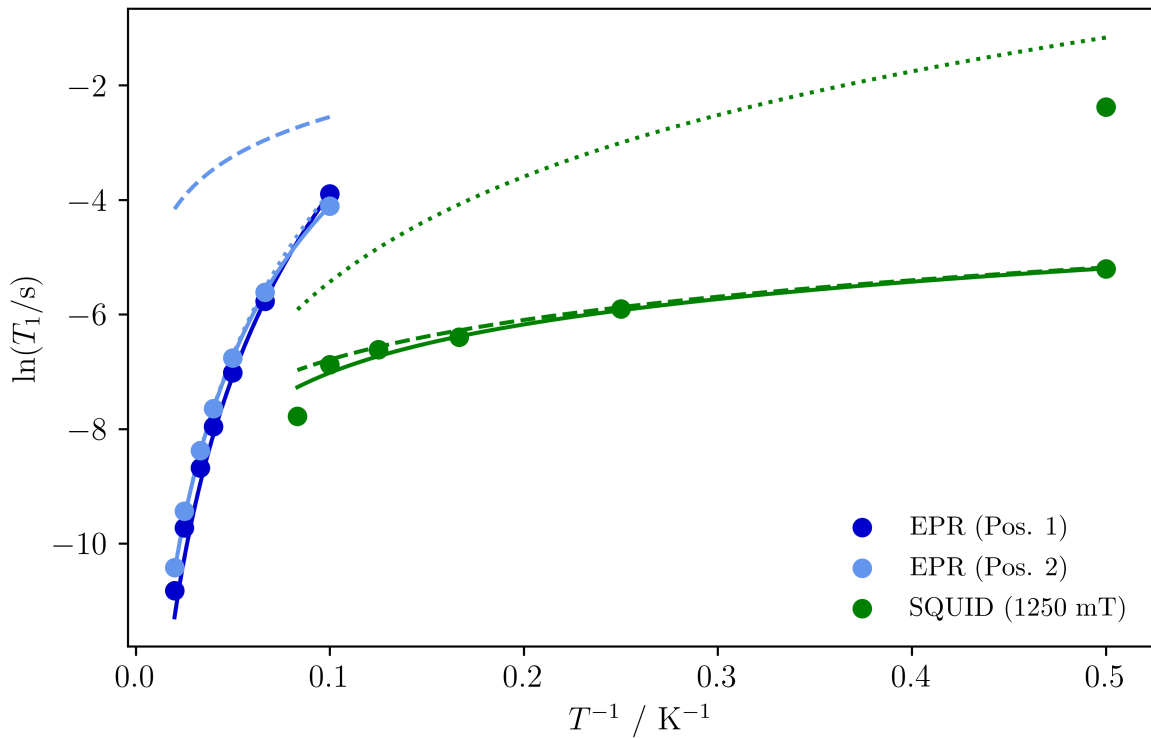


Figure A.6: Natural logarithm of the spin-lattice relaxation times versus inverse temperature determined in the inversion recovery experiments and from ac SQUID magnetometry. Fits show the contributions of direct (dashed) and Raman (dotted) processes as well as their sum (solid).

Table A.6: Spin relaxation times of a powder sample of \mathbf{I}^+ measured with ac SQUID magnetometry at 1250 mT.

T / K	$T_{1,\text{slow}} / \text{ms}$	$\alpha_{T_{1,\text{slow}}}$	$T_{1,\text{fast}} / \text{ms}$	$\alpha_{T_{1,\text{slow}}}$	$x_{T_{1,\text{fast}}} / \%$
2	92.67	0.07	5.49	0.15	61
4	2.73	0.16	-	-	100
6	1.67	0.09	-	-	100
8	1.34	0.01	-	-	100
10	1.03	0.05	-	-	100
12	0.42	0.001	-	-	100

Table A.7: Spin relaxation times of a powder sample of \mathbf{I}^+ measured with ac SQUID magnetometry at 1.8 K.

B / mT	$T_{1,\text{slow}} / \text{ms}$	$\alpha_{T_{1,\text{slow}}}$	$T_{1,\text{fast}} / \text{ms}$	$\alpha_{T_{1,\text{slow}}}$	$x_{T_{1,\text{slow}}} / \%$
0	< 1	-	< 1	-	-
100	4.15	0.25	1.26	0.001	41
200	10.62	0.21	2.41	0.02	44
300	20.00	0.14	3.36	0.34	30
400	45.00	0.16	5.53	0.19	38
500	61.90	0.001	7.28	0.21	62
600	62.03	0.001	6.72	0.17	52
700	76.04	0.001	7.00	0.18	47
800	66.66	0.22	4.80	0.001	72
900	92.97	0.04	8.34	0.37	55
1000	70.19	0.23	3.96	0.001	78
1100	122.98	0.001	9.02	0.36	58
1200	98.99	0.02	6.22	0.17	68
1300	112.44	0.17	5.12	0.001	75
1400	121.88	0.15	7.77	0.50	63
1500	147.45	0.002	9.47	0.41	62
1600	116.94	0.001	4.72	0.08	25
1700	130.35	0.22	3.00	0.22	81
1800	145.44	0.18	4.01	0.03	80
1900	110.42	0.13	4.33	0.001	20
2000	135.60	0.001	6.78	0.31	27

A.2.3 ESEEM, HYSCORE and ENDOR Measurements and Simulations

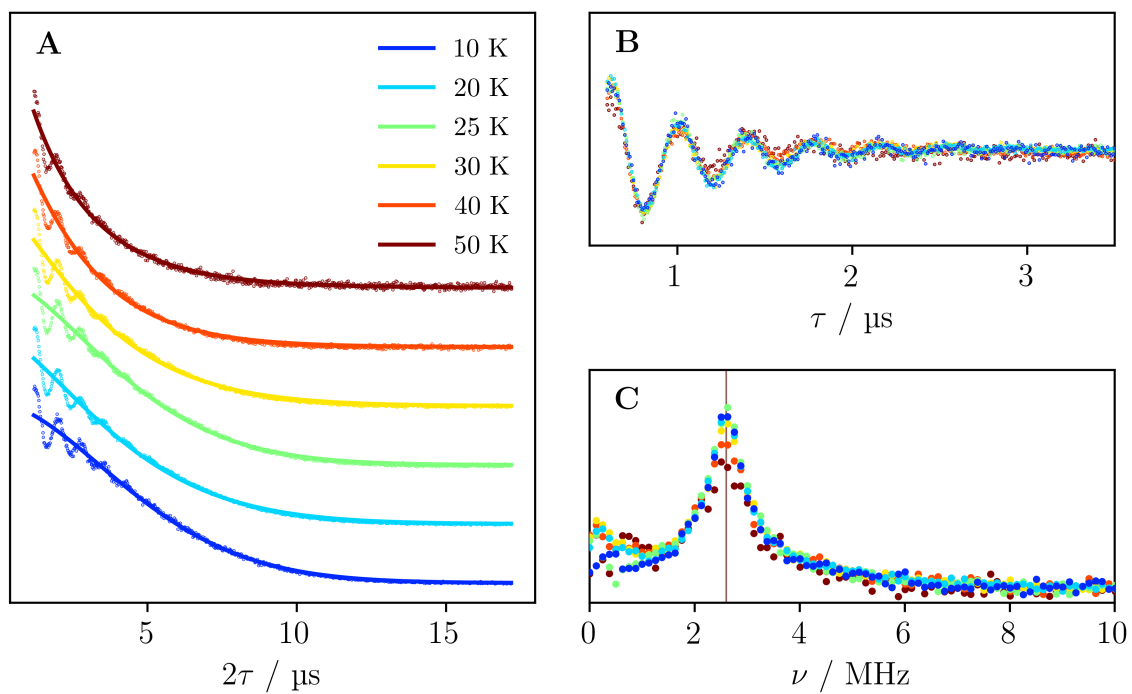


Figure A.7: A) Hahn echo decay curves of I^+ with a visible echo modulation measured at Pos. 1, corresponding to g_{zz} . The data after subtraction of the fit (B) and after Fourier transformation (C).

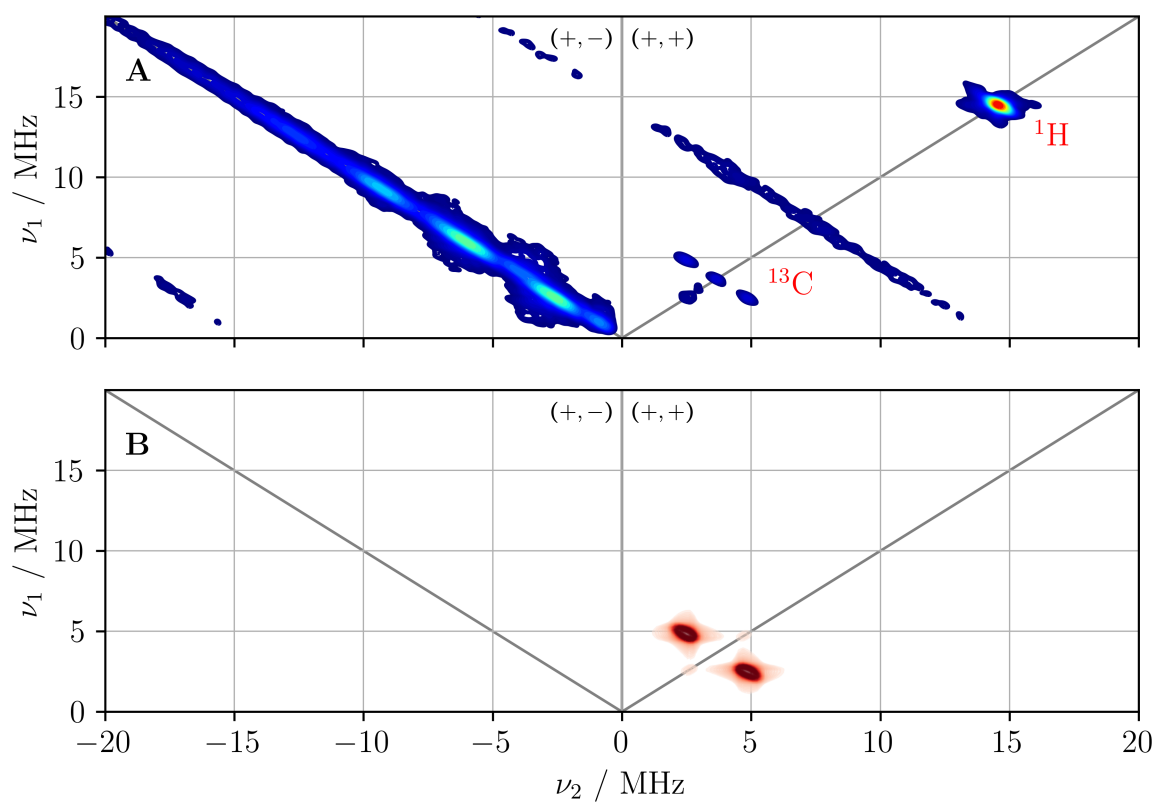


Figure A.8: X-Band HSCORE spectrum of I^+ (2 mmol l^{-1} in DCM:toluene (1:1)) measured at 15 K and a field position corresponding to g_{zz} with a delay of the first two pulses of 136 ns (A) and simulation of the coupling to ^{13}C (B).

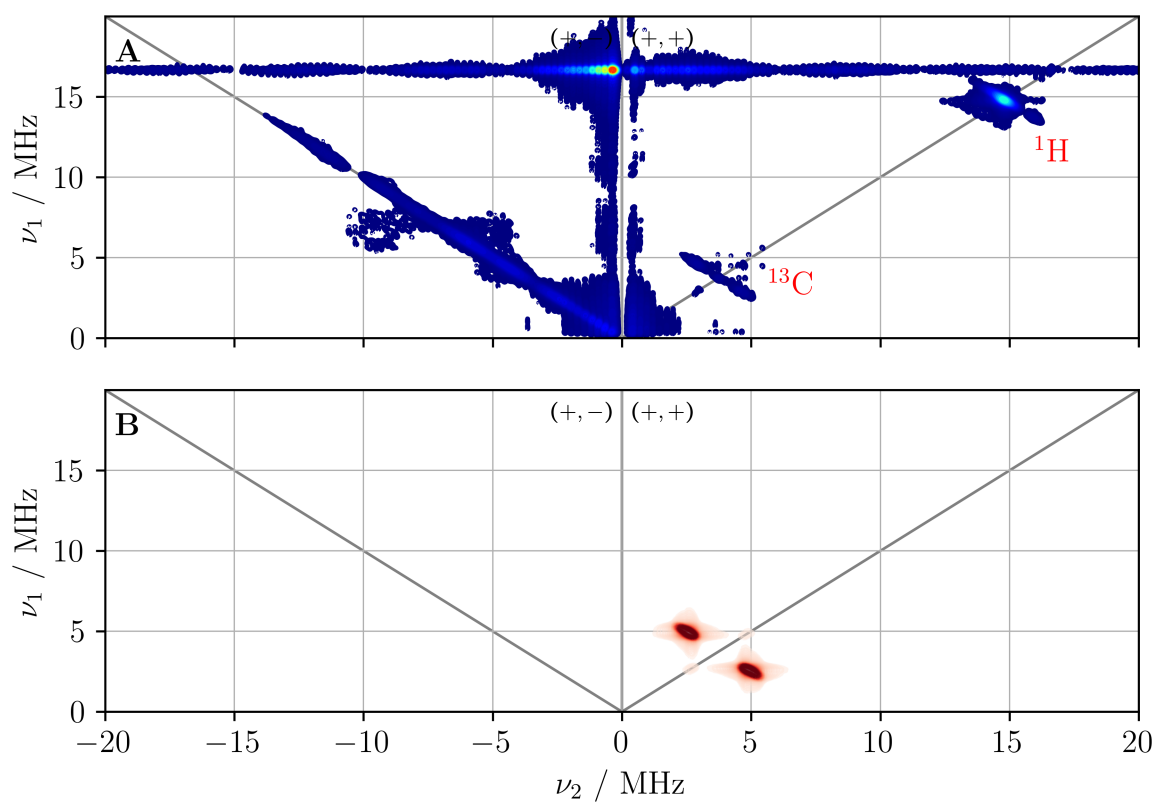


Figure A.9: X-Band HSCORE spectrum of I^+ (2 mmol l^{-1} in DCM:toluene (1:1)) measured at 15 K and a field position corresponding to g_{yy} with a delay of the first two pulses of 136 ns (A) and simulation of the coupling to ^{13}C (B).

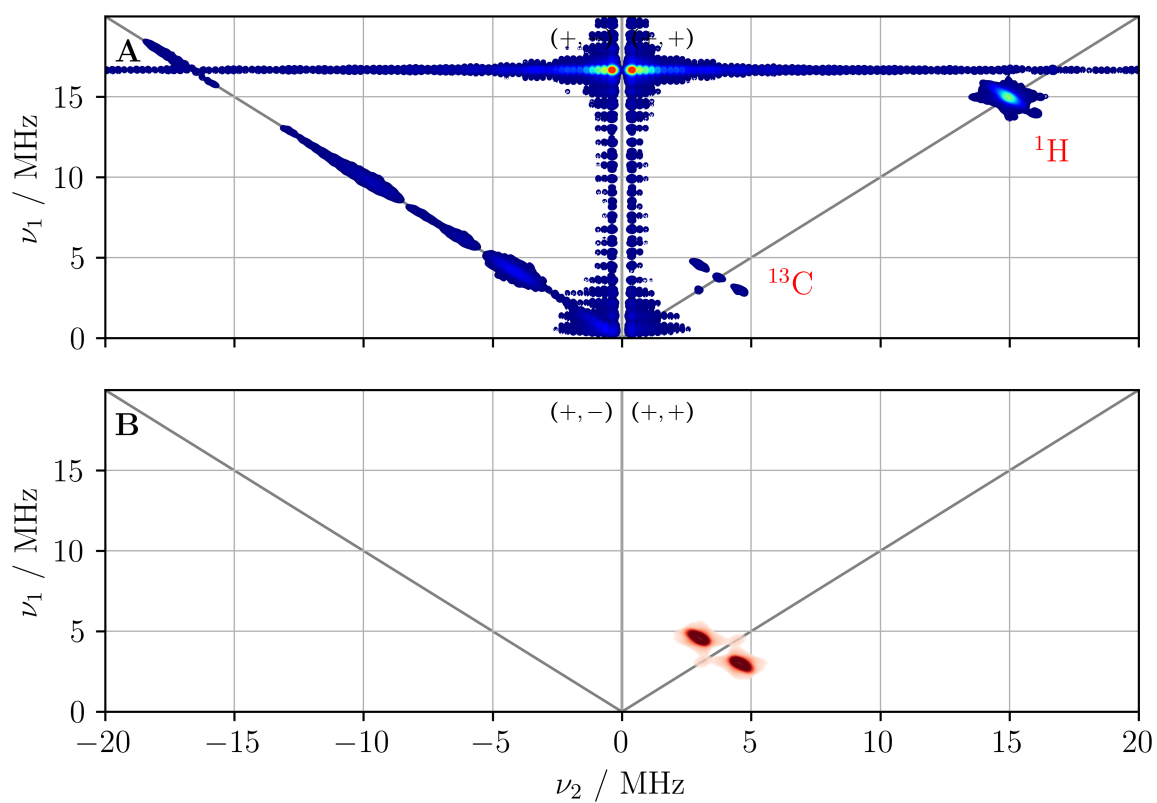


Figure A.10: X-Band HSCORE spectrum of I^+ (2 mmol l^{-1} in DCM:toluene (1:1)) measured at 15 K and a field position corresponding to g_{xx} with a delay of the first two pulses of 136 ns (A) and simulation of the coupling to ^{13}C (B).

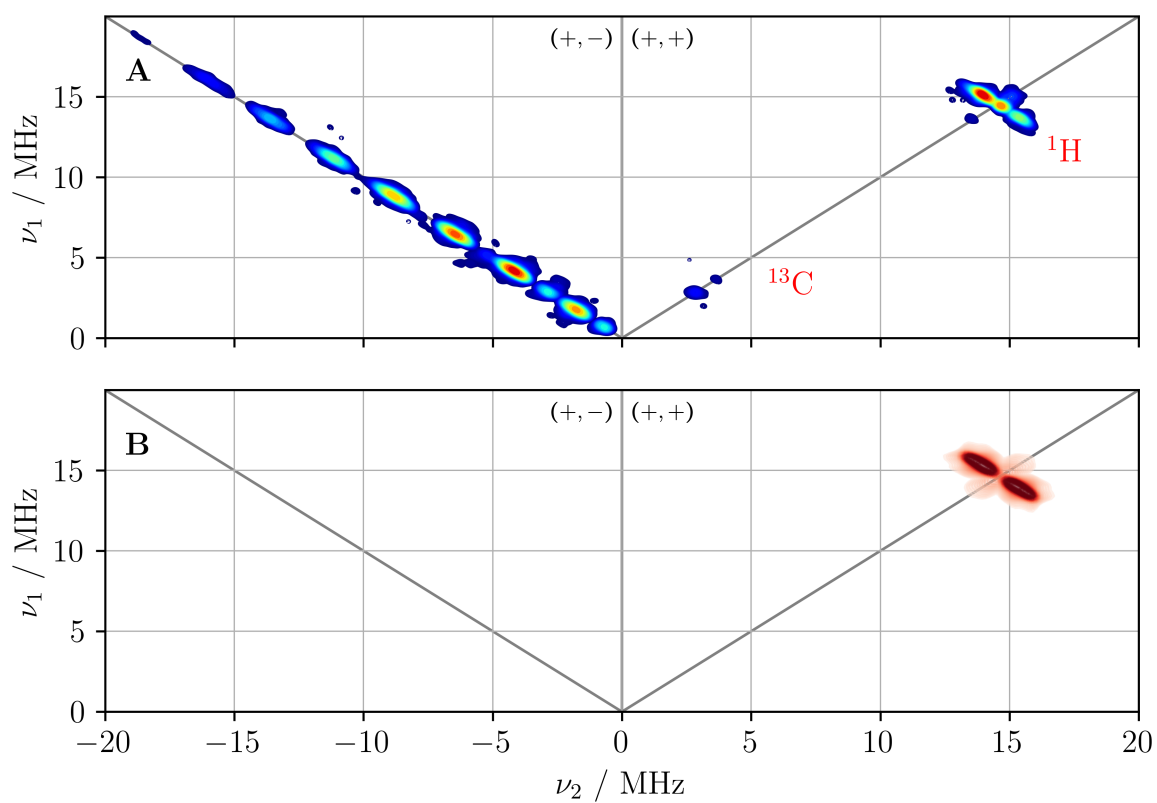


Figure A.11: X-Band HSCORE spectrum of I^+ (2 mmol l^{-1} in DCM:toluene (1:1)) measured at 15 K and a field position corresponding to g_{zz} with a delay of the first two pulses of 200 ns (A) and simulation of the coupling to ^1H (B).

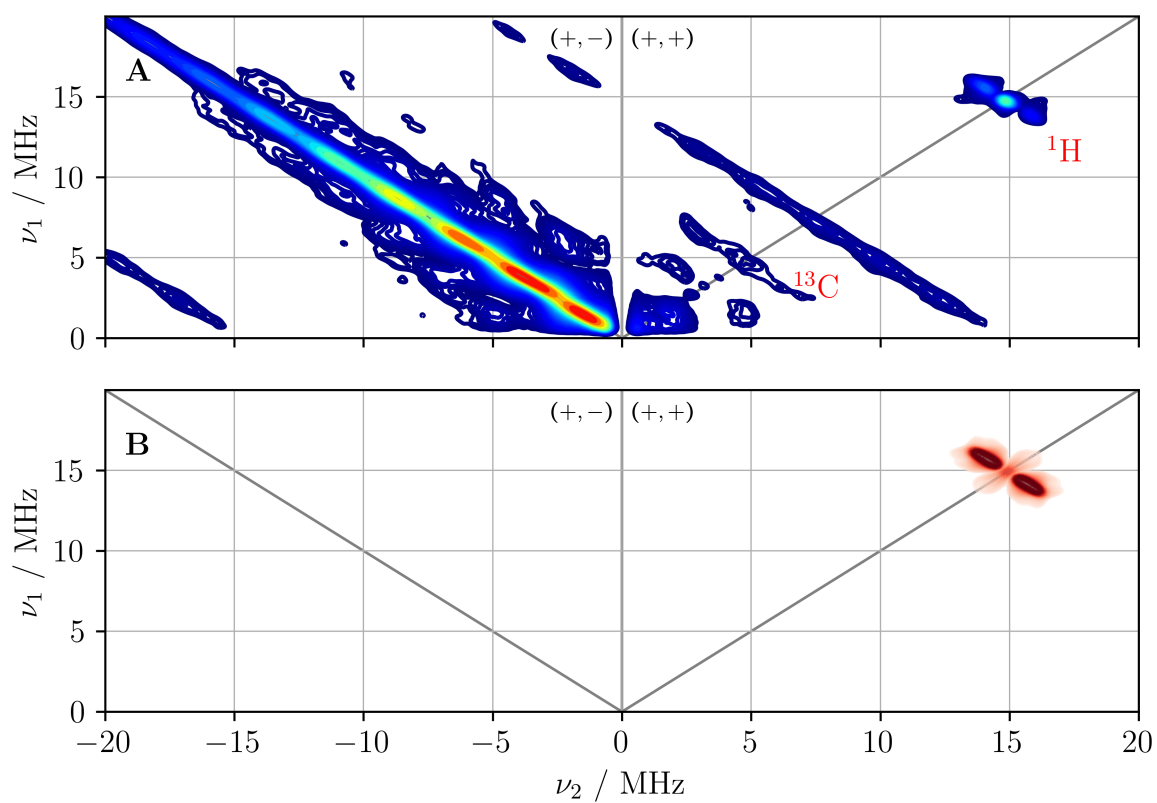


Figure A.12: X-Band HYSCORE spectrum of I^+ (2 mmol l^{-1} in DCM:toluene (1:1)) measured at 15 K and a field position corresponding to g_{yy} with a delay of the first two pulses of 200 ns (A) and simulation of the coupling to ^1H (B).

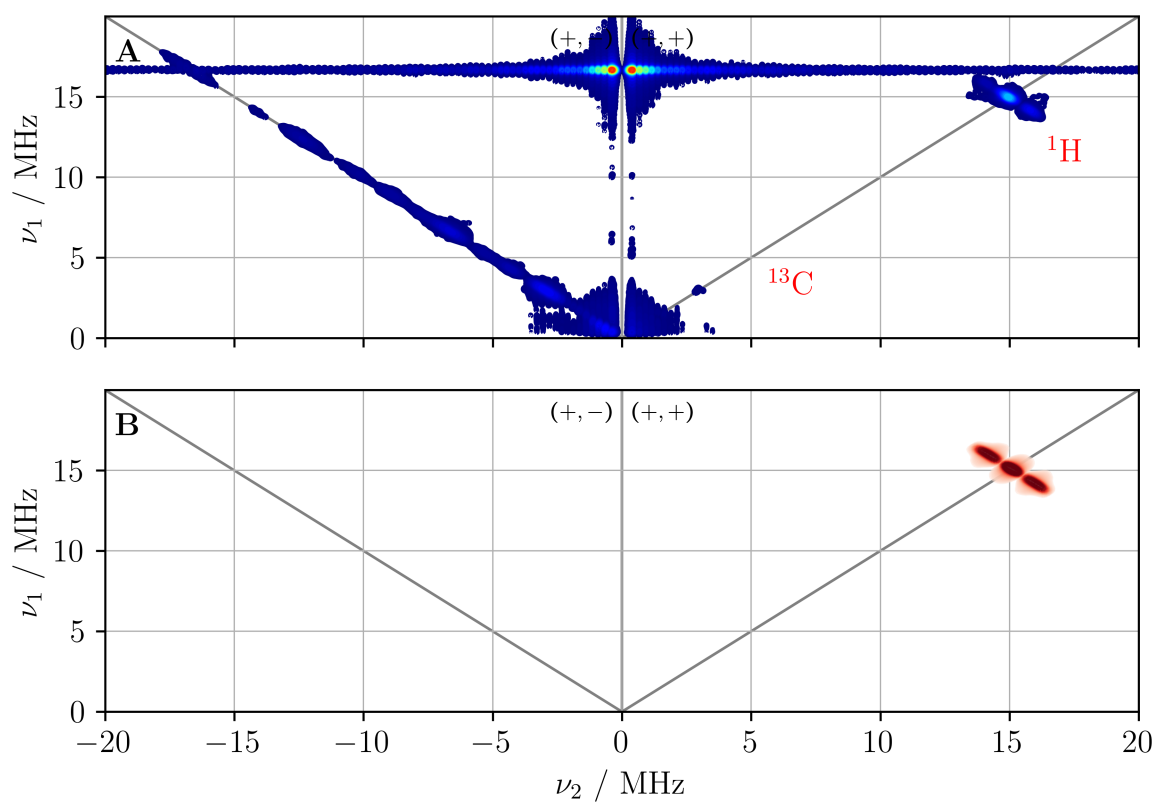


Figure A.13: X-Band HSCORE spectrum of I^+ (2 mmol l^{-1} in DCM:toluene (1:1)) measured at 15 K and a field position corresponding to g_{xx} with a delay of the first two pulses of 200 ns (A) and simulation of the coupling to ^1H (B).

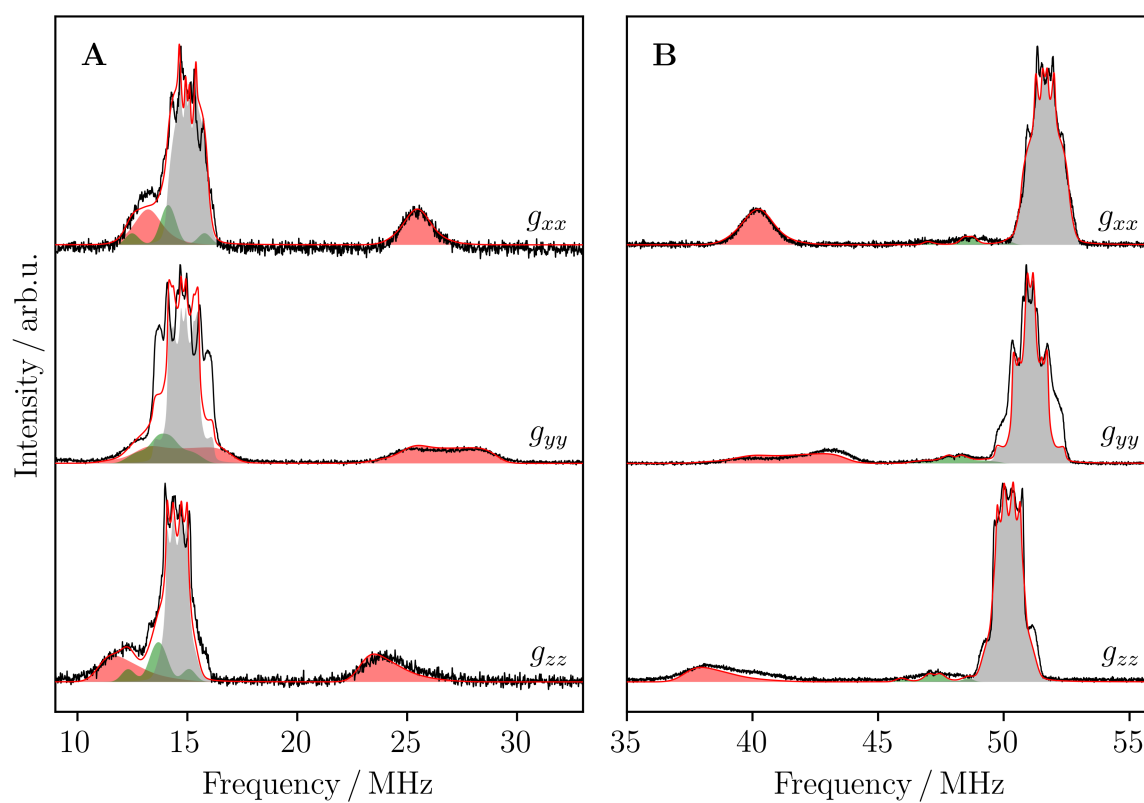


Figure A.14: X-Band (A) and Q-Band (B) ENDOR spectra of I^+ (4 mmol l^{-1} in DCM:toluene (1:1)) measured at 15K and different field positions with simulations for the coupling to ^1H (grey), ^{19}F (g_{zz}) and ^{31}P (red).

A.2.4 Immobilisation of the Probe Molecule

Table A.8: Fit parameters for the Mössbauer measurements shown in Figure 4.19.

	Ox. State	$\delta_{\text{IS}} / \text{mm s}^{-1}$	$\Delta E_{\text{Q}} / \text{mm s}^{-1}$	$x / \%$
I ⁰	0	-0.05(1)	2.15(1)	51
I ⁰	+2	0.51(1)	2.31(1)	49
II ⁰	0	-0.05(1)	2.32(1)	51
II ⁰	+2	0.51(1)	2.30(1)	49
II ⁺	0	-0.10(1)	2.65(1)	24
II ⁺	+2	0.53(1)	2.30(1)	76

A.3 Chemically Immobilised Radicals in Mesopores

A.3.1 Immobilisation with a Ruthenium catalyst

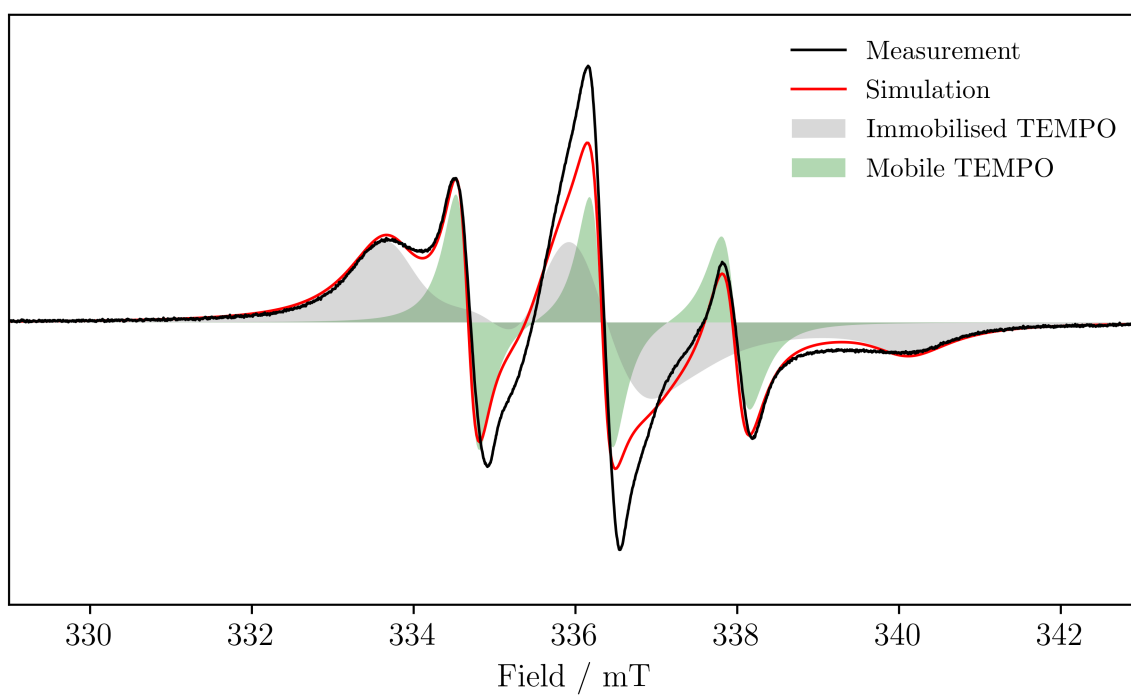


Figure A.15: Room temperature X-Band EPR spectrum of TEMPO-COF clicked with the ruthenium catalyst. The spectrum (black) is the sum of a mobile (green) and an immobile (gray) TEMPO species showing the incomplete reaction and impossibility to remove the mobile species. The simulations were performed with parameters typical for TEMPO.

A.3.2 EPR spectroscopy and SQUID magnetometry

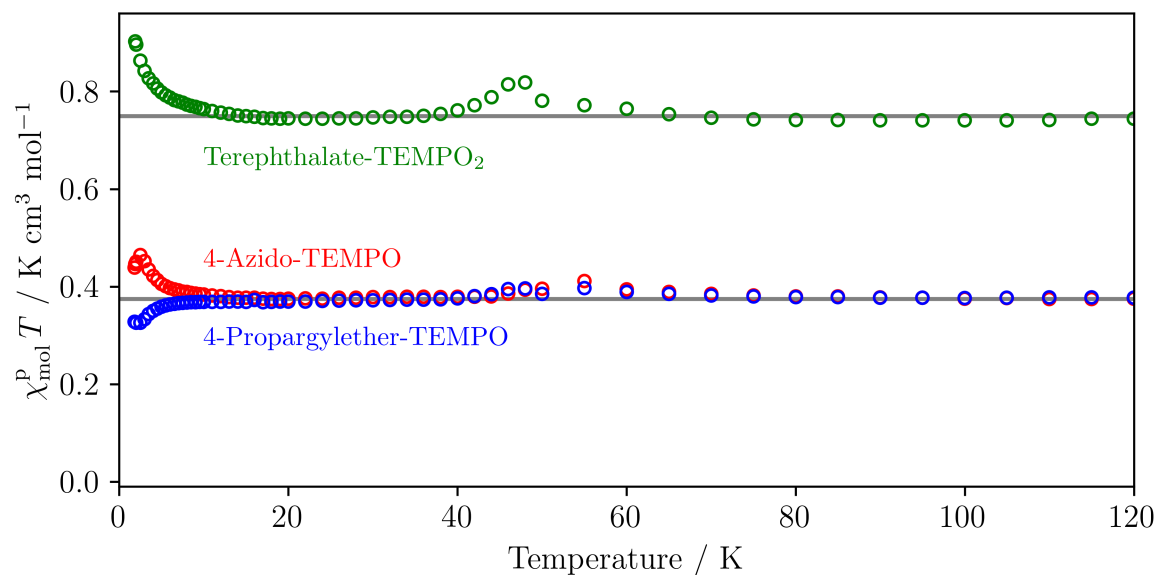


Figure A.16: Susceptibility-temperature product versus temperature for 4-propargylether, 4-azido-TEMPO and Terephthalate-TEMPO₂ for which the latter two show ferromagnetic interactions. All measurements were performed on samples in polystyrene (0.1 mmol g^{-1}).

Table A.9: Simulation parameters of the spectra of the TEMPO derivatives measured in frozen solution (1 mmol l⁻¹ in DCM:toluene (1:1)) at 7 K and 35 GHz.

	TEMPO	TEMPOL	4-Propargylether- TEMPO	4-Azido- TEMPO
g_{xx}	2.0098	2.0097	2.0097	2.0097
g_{yy}	2.0064	2.0064	2.0064	2.0064
g_{zz}	2.0022	2.0022	2.0022	2.0022
A_{xx} / MHz	20.0	20.0	19.1	20.0
A_{yy} / MHz	25.3	25.3	19.3	25.3
A_{zz} / MHz	98.0	99.0	98.5	99.0
$\Delta B_{pp,G}$ / mT	0.63	0.63	0.63	0.63
$\Delta B_{pp,L}$ / mT	0	0.07	0	0

A.3.3 Spin Dynamics of the Derivatives of TEMPO

Table A.10: Spin-lattice relaxation times T_1 and the contribution x of the slow process as well as phase-memory times T_M of TEMPO, see Figure A.17.

T / K	$T_{1,\text{slow}}$ / ms	$T_{1,\text{fast}}$ / ms	$x_{T_{1,\text{slow}}}$ / %	T_M / μs
7	190(6)	29(1)	46(1)	2.87(2)
10	55(2)	11(1)	55(3)	4.04(5)
15	22.9(6)	5.0(4)	66(2)	3.36(5)
20	11.4(7)	3.4(5)	60(6)	3.74(8)
30	3.4(3)	1.1(3)	62(11)	4.09(4)
40	1.6(2)	0.5(1)	61(12)	3.80(4)
50	0.62(1)	0.62(1)	100(0)	4.50(7)

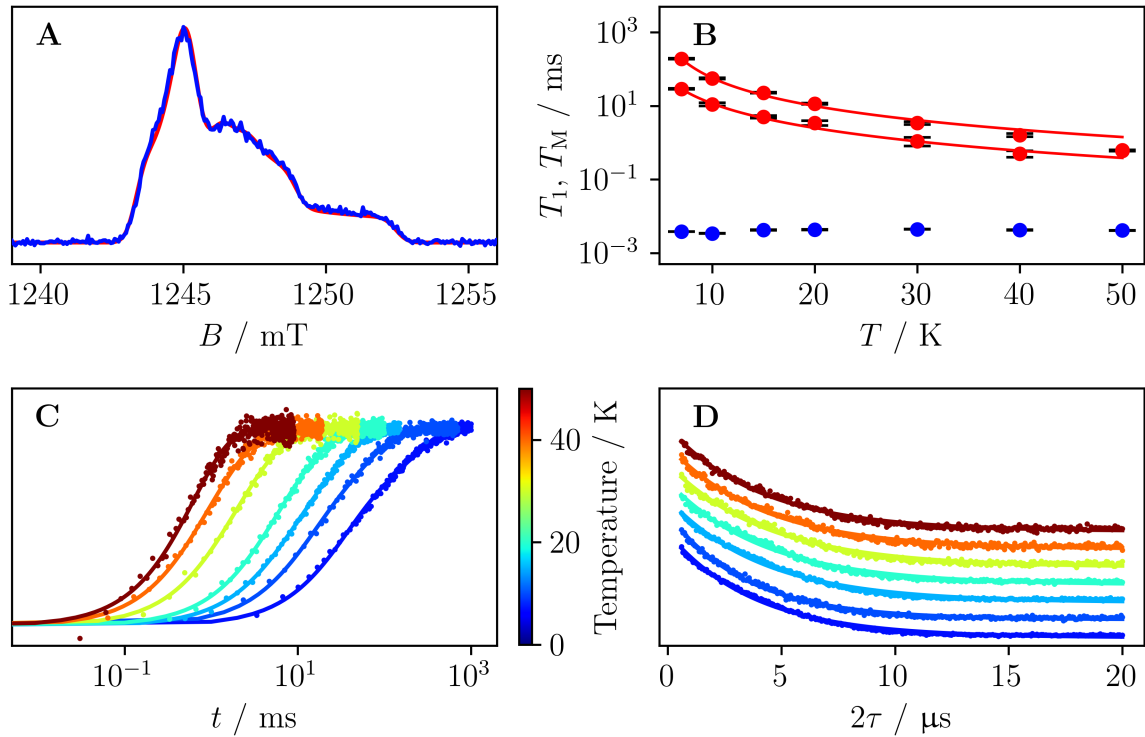


Figure A.17: A) EPR spectrum and simulation (red) of TEMPO (1 mmol l^{-1} in DCM:toluene (1:1)) measured at 7 K and 35 GHz. B) Spin-lattice relaxation times (red) with fits and phase-memory times (blue) extracted from the inversion recovery (C) and Hahn-echo decay curves (D).

Table A.11: Spin-lattice relaxation times T_1 and the contribution x of the slow process as well as phase-memory times T_M of TEMPOL, see Figure A.18.

T / K	$T_{1,\text{slow}} / \text{ms}$	$T_{1,\text{fast}} / \text{ms}$	$\chi_{T_{1,\text{slow}}} / \%$	$T_M / \mu\text{s}$
7	138(3)	26(1)	50(1)	2.87(2)
10	63(1)	10.9(5)	55(1)	4.04(5)
15	26.4(8)	5.4(4)	60(2)	3.63(5)
20	12.9(3)	2.9(2)	61(2)	3.73(8)
30	4.5(1)	1.18(6)	53(2)	4.09(5)
40	2.15(4)	0.64(2)	55(2)	3.80(4)
50	1.13(1)	0.26(1)	72(1)	4.51(7)

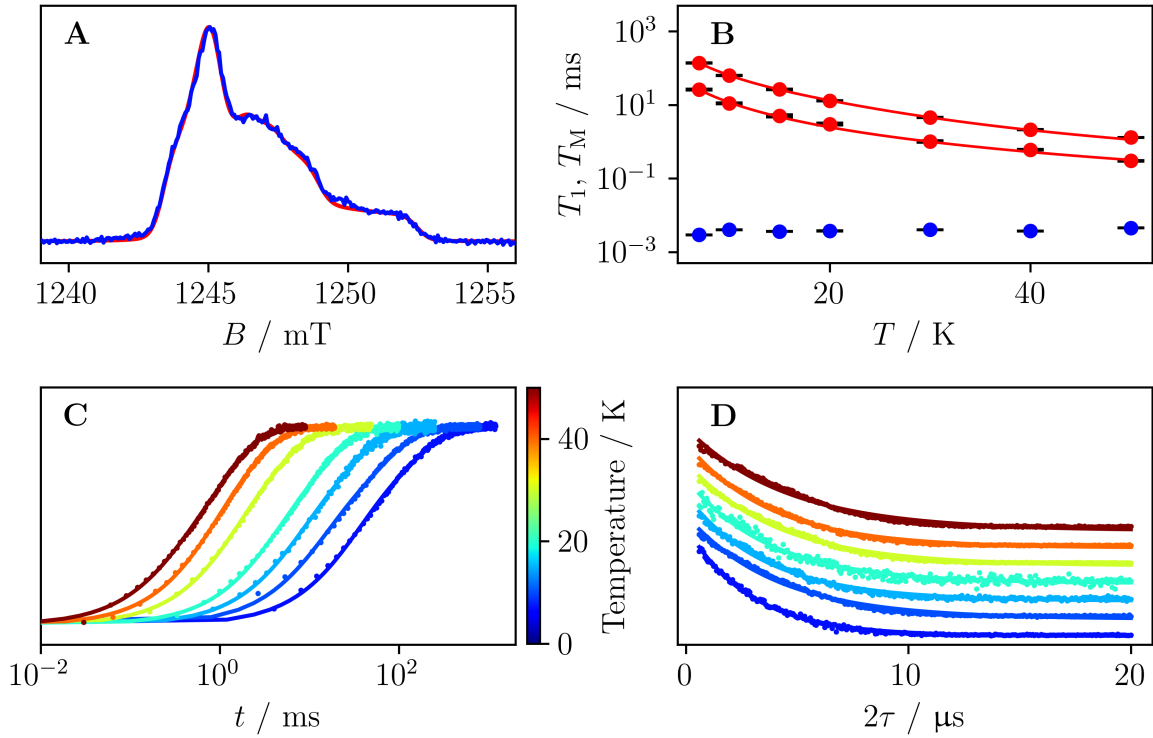


Figure A.18: A) EPR spectrum and simulation (red) of TEMPOL (0.2 mmol l^{-1} in DCM:toluene (1:1)) measured at 7 K and 35 GHz. B) Spin-lattice relaxation times (red) with fits and phase-memory times (blue) extracted from the inversion recovery (C) and Hahn-echo decay curves (D).

Table A.12: Spin-lattice relaxation times T_1 and the contribution x of the slow process as well as phase-memory times T_M of 4-azido-TEMPO, see Figure 5.10.

T / K	$T_{1,\text{slow}}$ / ms	$T_{1,\text{fast}}$ / ms	$\chi_{T_{1,\text{slow}}}$ / %	T_M / μ s
7	51(7)	13(7)	64(14)	2.45(3)
15	20(2)	4(2)	73(7)	2.30(4)
20	10.4(4)	2.5(4)	68(3)	2.02(7)
30	3.6(2)	0.7(1)	69(3)	4.40(4)
40	1.75(9)	0.6(1)	68(6)	4.33(7)
50	0.94(2)	0.21(4)	77(3)	3.76(6)

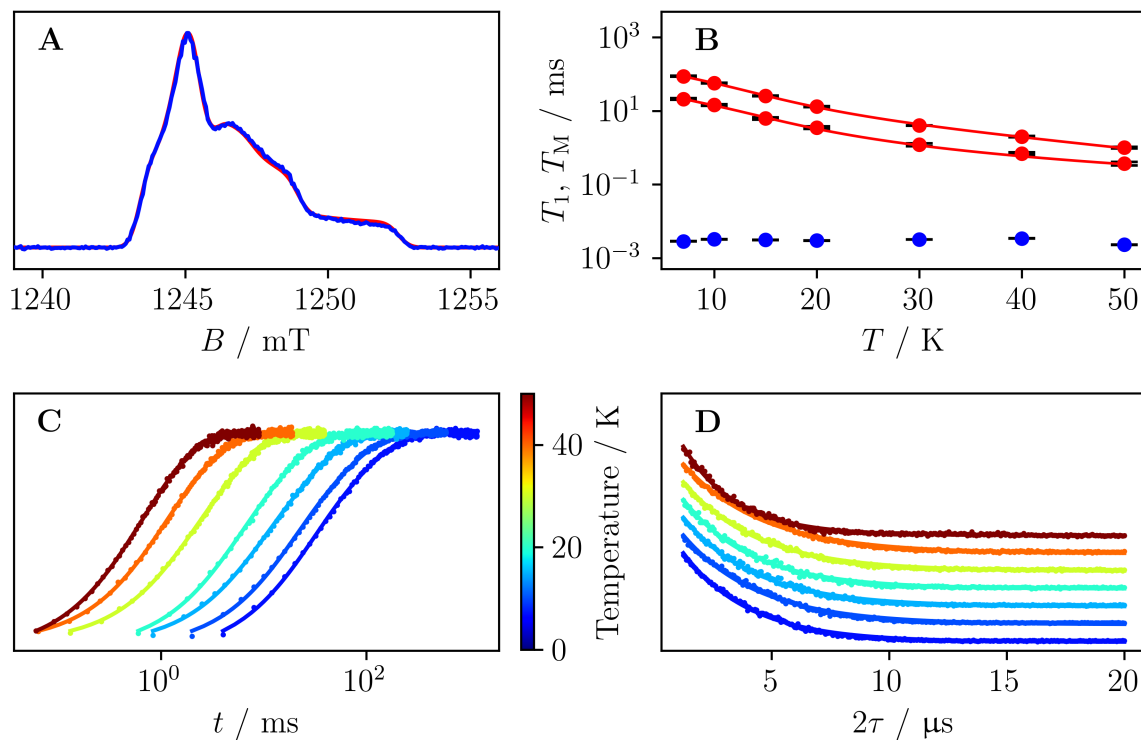


Figure A.19: A) EPR spectrum and simulation (red) of 4-propargylether-TEMPO (1 mmol l^{-1} in DCM:toluene (1:1)) measured at 7 K and 35 GHz. B) Spin-lattice relaxation times (red) with fits and phase-memory times (blue) extracted from the inversion recovery (C) and Hahn-echo decay curves (D).

Table A.13: Spin-lattice relaxation times T_1 and the contribution x of the slow process as well as phase-memory times T_M of 4-propargylether-TEMPO, see Figure A.19.

T / K	$T_{1,\text{slow}} / \text{ms}$	$T_{1,\text{fast}} / \text{ms}$	$\chi_{T_{1,\text{slow}}} / \%$	$T_M / \mu\text{s}$
7	87(2)	21(1)	50(2)	2.84(2)
10	57(1)	14.4(6)	52(1)	3.23(3)
15	25.7(6)	6.2(4)	62(2)	3.10(3)
20	13.0(4)	3.5(3)	62(8)	2.97(3)
30	4.2(1)	1.2(1)	65(3)	3.19(3)
40	2.00(7)	0.69(6)	60(4)	3.40(3)
50	1.00(4)	0.37(4)	66(5)	2.29(2)

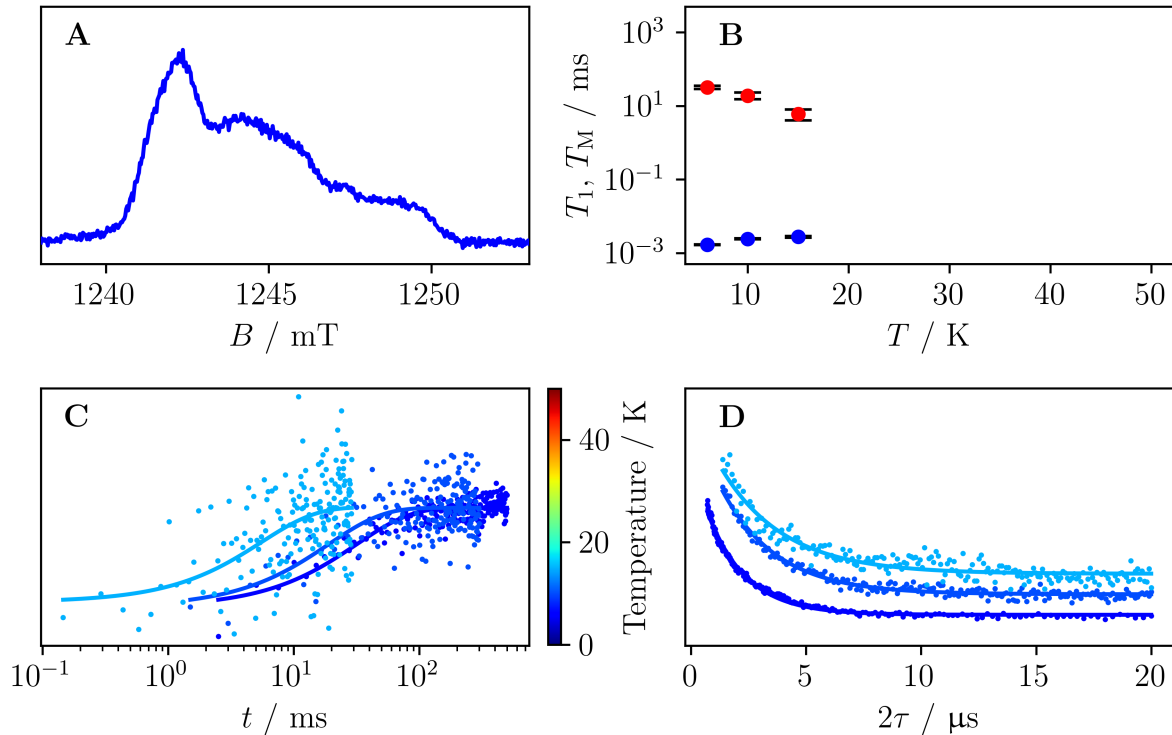


Figure A.20: A) EPR spectrum and simulation (red) of TEMPOL-Trehalose (300 ppb) measured at 6 K and 35 GHz. B) Spin-lattice relaxation times (red) with fits and phase-memory times (blue) extracted from the inversion recovery (C) and Hahn-echo decay curves (D).

Table A.14: Spin-lattice relaxation times T_1 and phase-memory times T_M of TEMPOL-Trehalose, see Figure A.20.

T / K	T_1 / ms	$T_M / \mu\text{s}$
6	32(3)	1.68(3)
10	19(4)	2.41(6)
15	6(2)	2.7(1)

A.3.4 Click Reaction

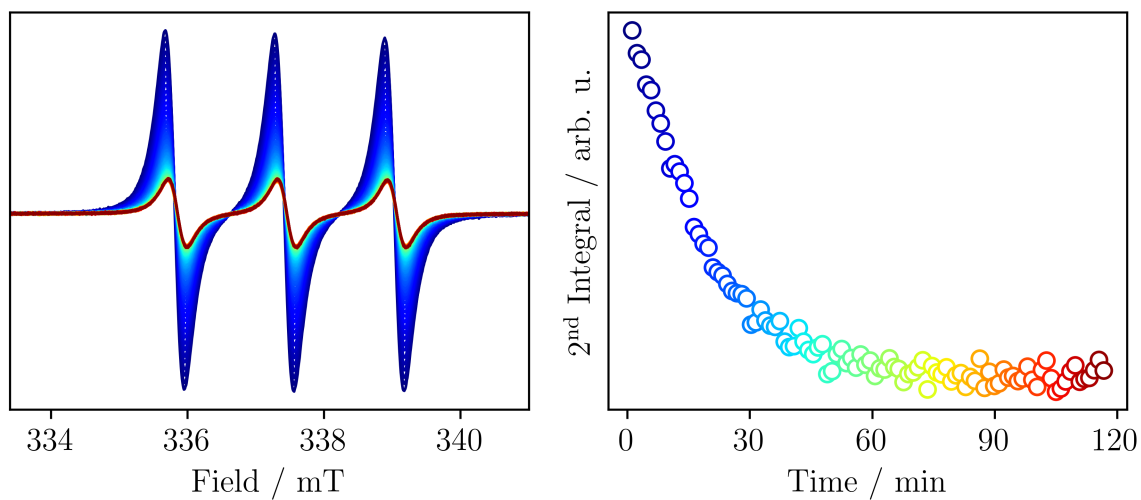


Figure A.21: EPR Measurement series of TEMPO in a mixture of toluene:DCM:EtOH (6:1:1) after the addition of ascorbic acid. The incomplete reaction can be explained by a limited solubility of the radical and ascorbic acid in the same phase and no stirring during the experiment.

A.3.5 EPR Measurements of TEMPO-Terephthalate

Table A.15: Simulation parameters of the X-Band EPR spectrum of Terephthalate-TEMPO₂ measured in solution (1 mmol l⁻¹ in DCM:toluene (1:1)) at room temperature (determination of g_{iso} , A_{iso} , ν_{Exchange} and t_{corr}) and 140 K, see Figure 5.12.

Terephthalate-TEMPO ₂	
g_{xx}	2.0097
g_{yy}	2.0064
g_{zz}	2.0023
g_{iso}	2.0061
A_{xx} / MHz	19.1
A_{xx} / MHz	19.3
A_{xx} / MHz	98.3
A_{iso} / MHz	44.2
$\Delta B_{\text{pp,G}}$ / mT	0.63
$\Delta B_{\text{pp,L}}$ / mT	0.16
ν_{Exchange} / MHz	8
t_{corr} / ps	79

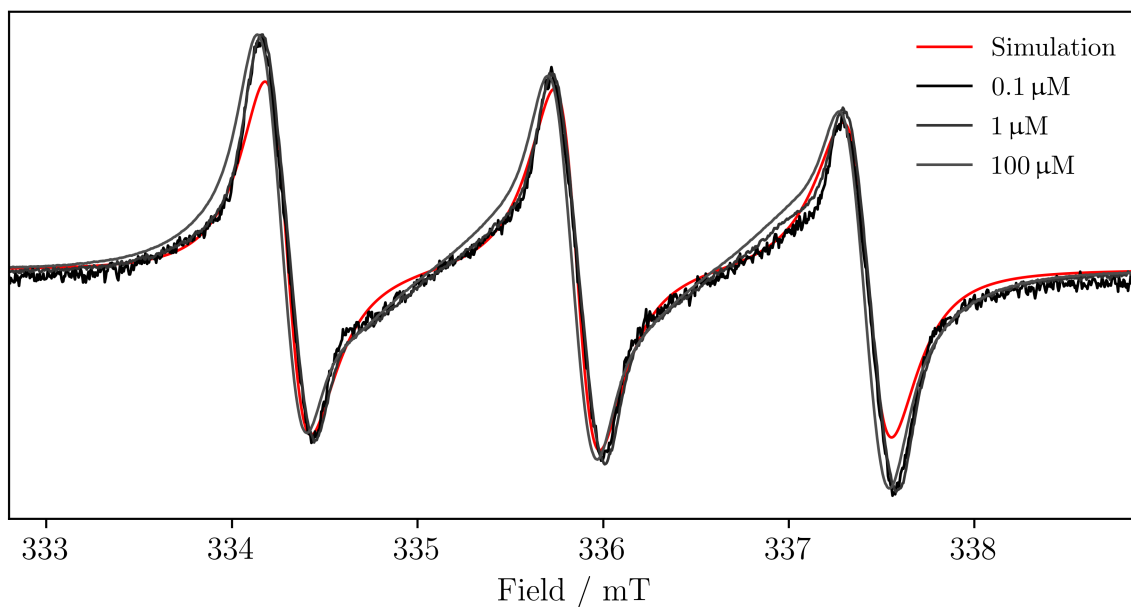


Figure A.22: X-Band EPR spectra of Terephthalate-TEMPO₂ measured at different concentrations in DCM:toluene (1:1) at room temperature.

Table A.16: Simulation parameters for the EPR spectrum of Terephthalate-TEMPO₂ shown in Figure A.22.

Terephthalate-TEMPO ₂	
g_{xx}	2.0085
g_{yy}	2.0060
g_{zz}	2.0031
A_{xx} / MHz	19.5
A_{xx} / MHz	14.6
A_{xx} / MHz	98.4
$\Delta B_{pp,G}$ / mT	0
$\Delta B_{pp,G}$ / mT	0.11
t_{corr} / ns	0.1
ν_{Exchange} / MHz	4.4

Table A.17: Spin-lattice relaxation times T_1 and phase-memory times T_M of Terephthalate-TEMPO₂ as well as the stretch factors for both decay processes, see Figure 5.17.

T / K	T_1 / ms	k_{T_1}	T_M / μs	k_{T_M}
7	3.8(1)	-0.68(2)	3.67(2)	1.23(1)
10	2.48(8)	-0.62(3)	6.23(3)	2.29(4)
15	1.28(3)	-0.83(2)	6.89(4)	2.74(6)
20	1.40(2)	-0.77(1)	5.43(2)	1.73(1)
30	0.66(1)	-0.64(1)	6.32(2)	2.04(2)
40	0.402(5)	-0.88(2)	5.62(2)	1.72(1)
50	0.293(4)	-0.82(2)	5.14(2)	1.56(1)

A.3.6 Spin Dynamics of TEMPO immobilised in the COF

Table A.18: Spin-lattice relaxation times T_1 and phase-memory times T_M of TEMPO-COF_{10%} as a powder as well as the stretch factors for both decay processes, see Figure 5.18.

T / K	T_1 / ms	k_{T_1}	$T_M / \mu\text{s}$
6	0.327(4)	0.419(4)	0.513(5)
10	0.19(1)	0.42(2)	0.61(2)
15	0.251(5)	0.462(6)	0.52(1)
30	0.162(6)	0.42(1)	0.47(2)
50	0.096(9)	0.41(3)	0.28(4)

Table A.19: Spin-lattice relaxation times T_1 and phase-memory times T_M of TEMPO-COF_{10%} submerged in toluene as well as the stretch factors for the T_1 decay process, see Figure A.23.

T / K	T_1 / ms	k_{T_1}	$T_M / \mu\text{s}$
6	0.093(3)	0.54(2)	0.390(6)
10	0.138(2)	0.515(5)	0.329(2)
15	0.120(3)	0.56(1)	0.345(4)
20	0.106(4)	0.61(2)	0.384(6)
30	0.079(7)	0.62(5)	0.44(1)

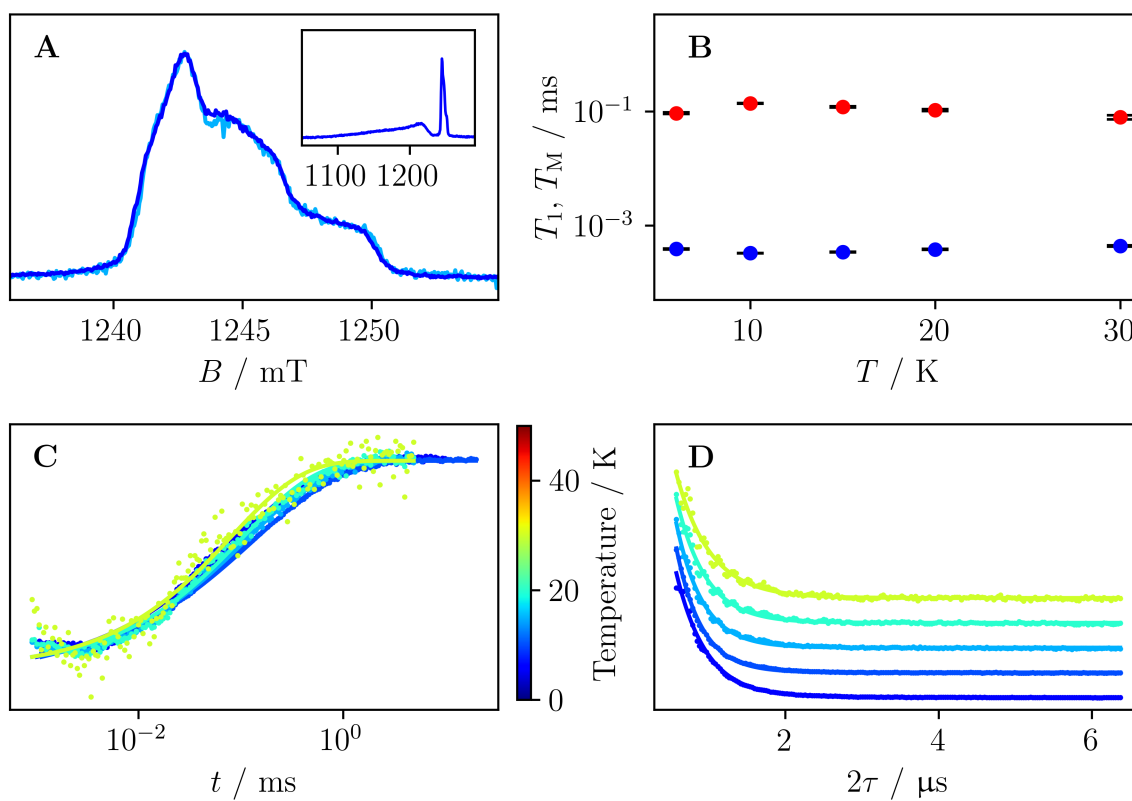


Figure A.23: A) EPR spectrum of TEMPO-COF_{10%} submerged in toluene measured at 6 K (dark blue) and 30 K (light blue) at 35 GHz. B) Spin-lattice relaxation times (red) and phase-memory times (blue) extracted from the inversion recovery (C) and Hahn-echo decay curves (D).

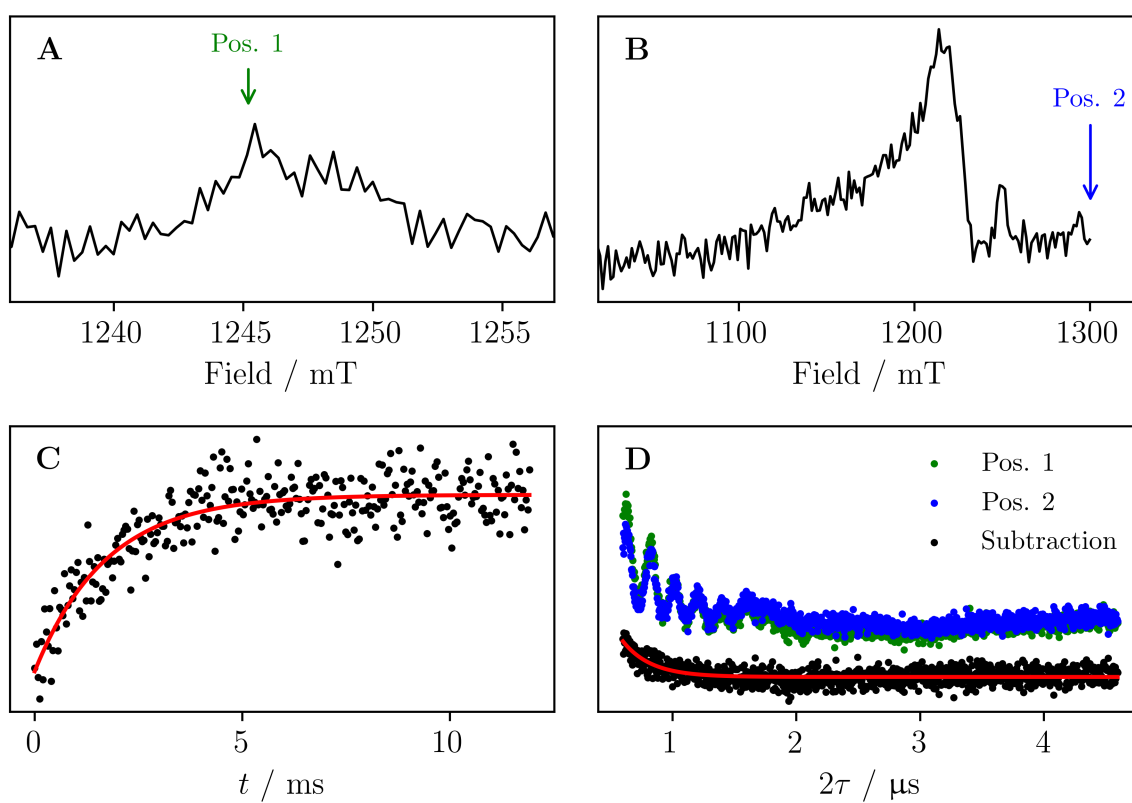


Figure A.24: EPR spectra of a powder sample of TEMPO-COF_{0.2%} measured at 6 K at 35 GHz (A, B), as well as the inversion recovery (C) and Hahn-echo decay curves (D).

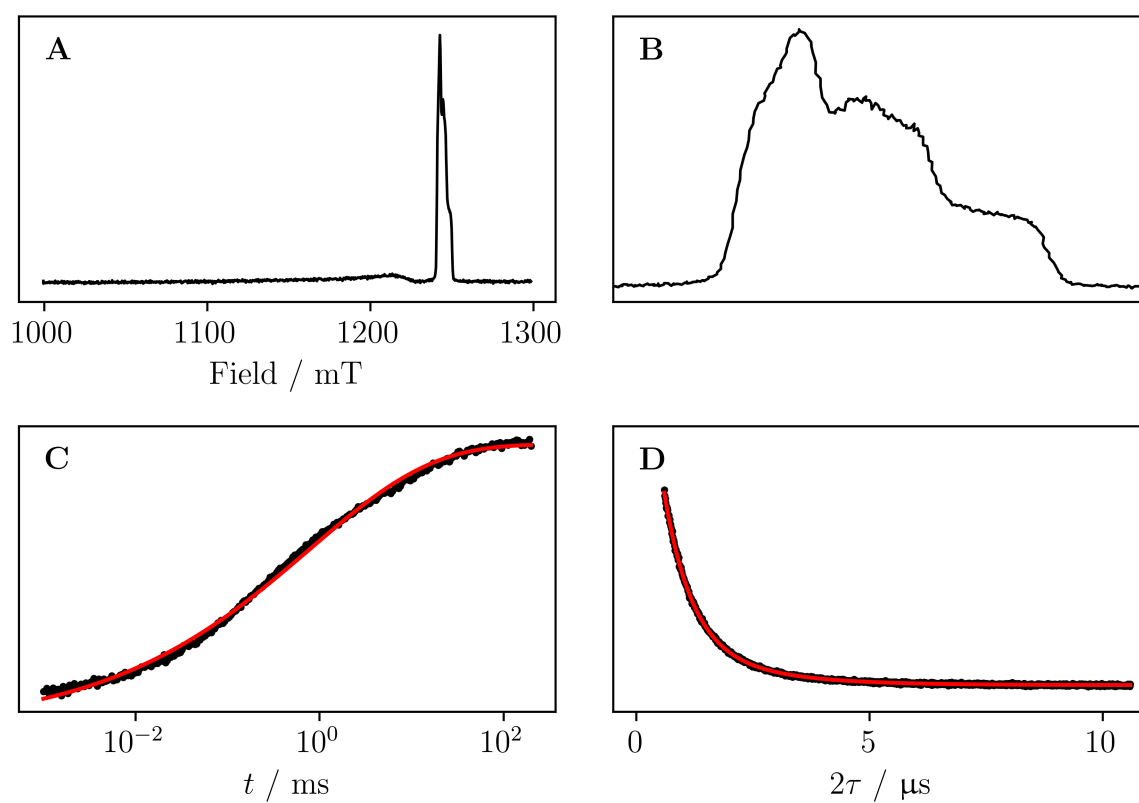


Figure A.25: EPR spectra of a powder sample of TEMPO-COF₂% measured at 6 K at 35 GHz (A, B), as well as the inversion recovery (C) and Hahn-echo decay curves (D).

A.4 Experimental Section

A.4.1 IR and Mass Spectra of the Synthesised Compounds

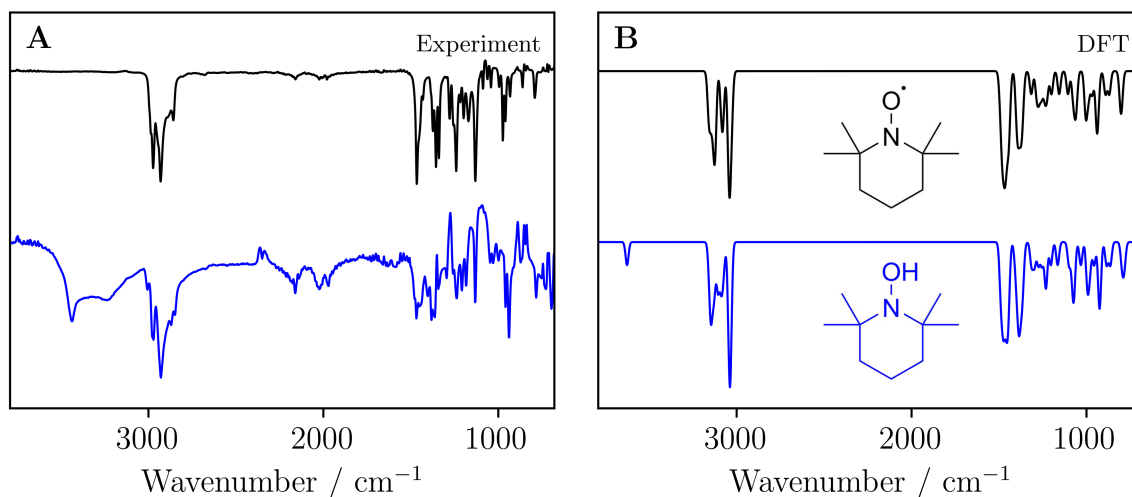


Figure A.26: (A) Experimental ATR-IR spectra of powders of TEMPO (black) and TEMPO-H (blue) immediately after the synthesis of the latter. The broad band at 3300 cm^{-1} is attributed to residual water. The sharp band at 3435 cm^{-1} results from the OH vibration of the reduced radical. (B) Calculated IR spectrum of the two compounds on DFT level of theory with the B3LYP functional and DEF2-SVP DEF2/J basis set to confirm the high energy vibration to be due to the OH vibration. The energy of the NO vibration changes from ca. 1440 cm^{-1} in the radical to ca. 1030 cm^{-1} in the reduced species.

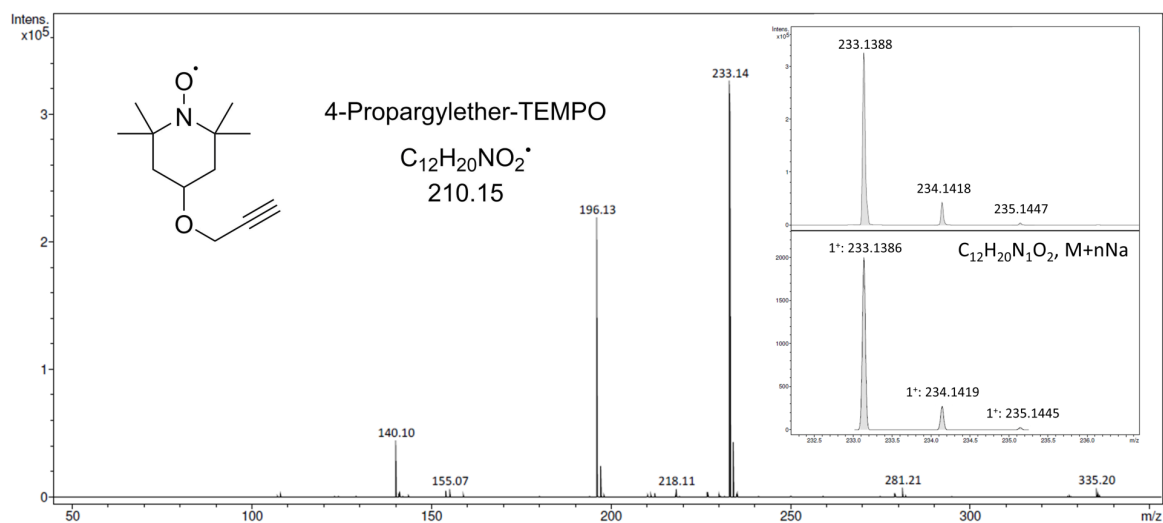


Figure A.27: Experimental and calculated (inset) mass spectrum of 4-propargylether-TEMPO.

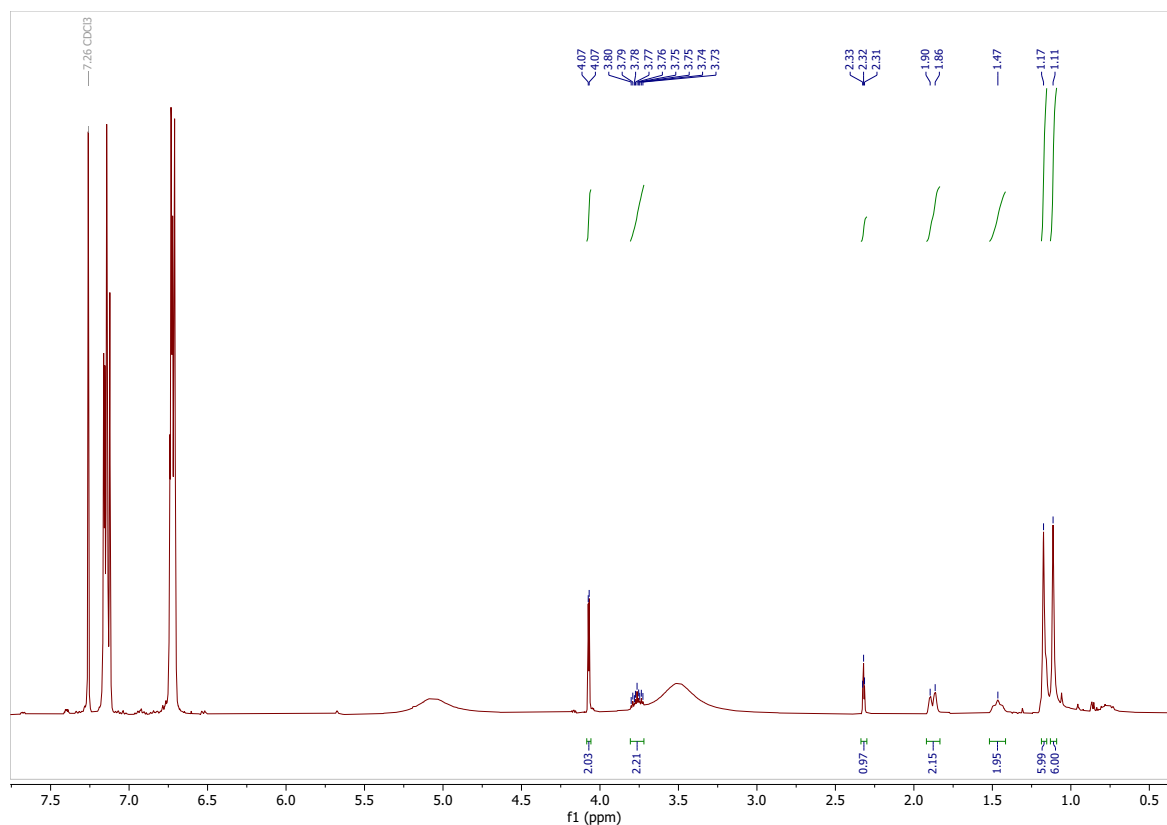


Figure A.28: 1H NMR spectrum of 4-propargylether-TEMPO reduced with phenyl hydrazine. The multiplets at 6.7-7.2 ppm are from the aromatic protons in phenyl hydrazine and the broad bands at 3.5 and 5.1 ppm are from the NH protons in phenyl hydrazine.

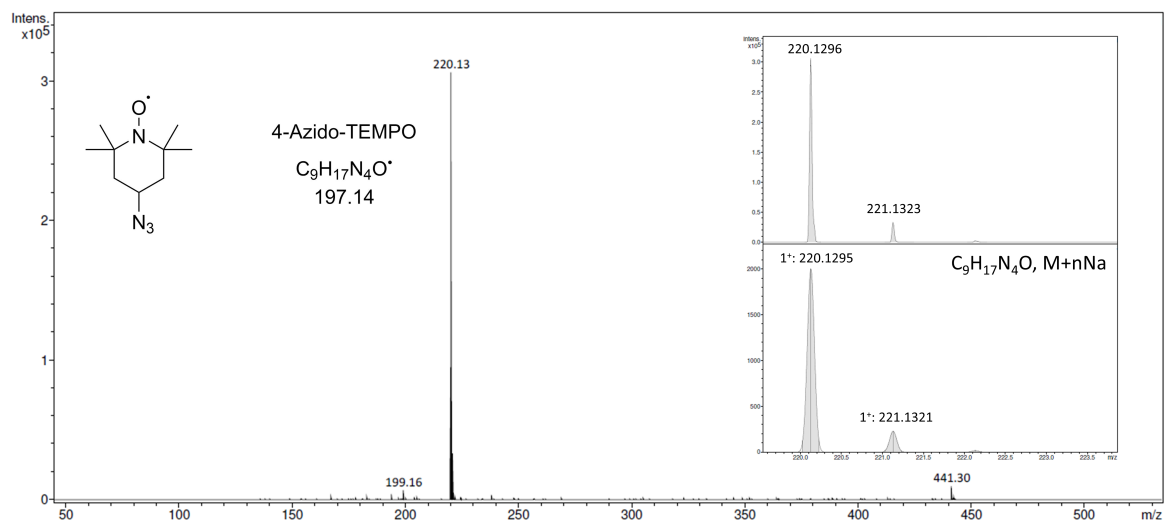


Figure A.29: Experimental and calculated (inset) mass spectrum of 4-azido-TEMPO.

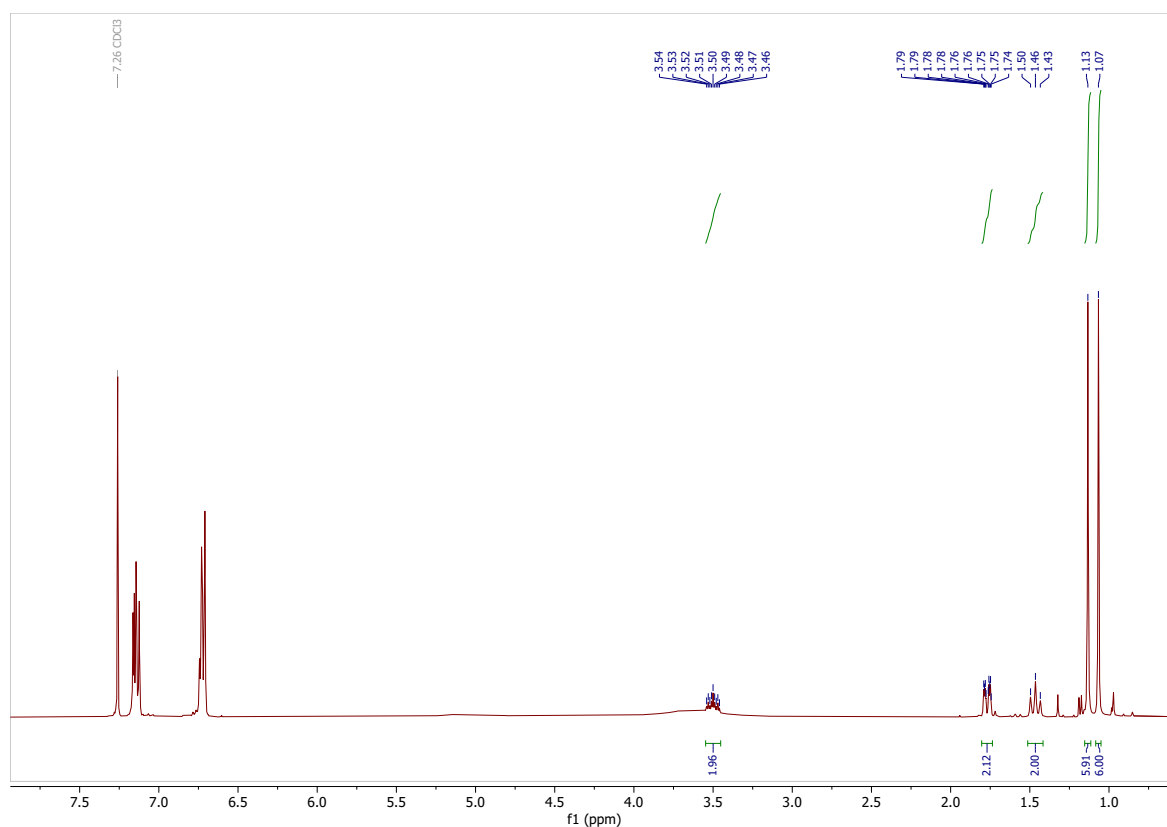


Figure A.30: ¹H NMR spectrum of 4-azido-TEMPO reduced with phenyl hydrazine. The multiplets at 6.7-7.2 ppm are from the aromatic protons in phenyl hydrazine and the broad bands at 3.5 and 5.1 ppm are from the NH protons in phenyl hydrazine.

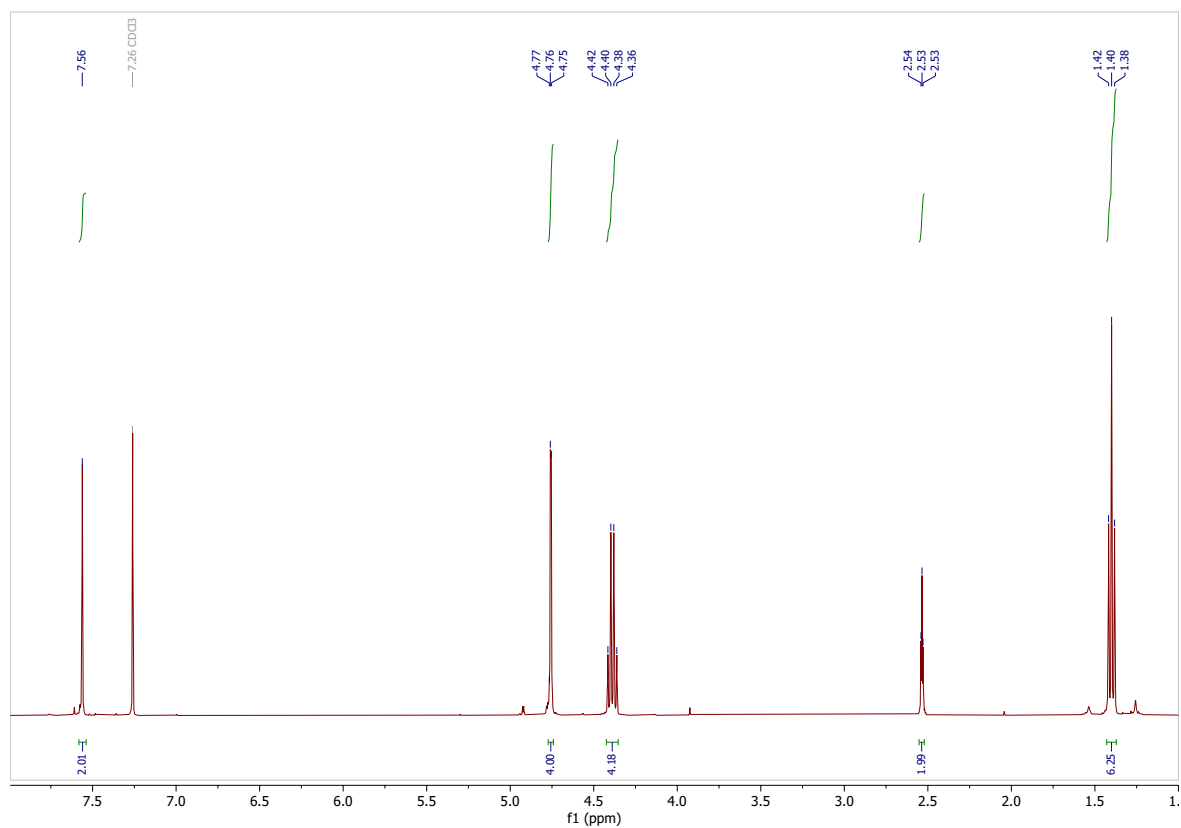


Figure A.31: ^1H NMR spectrum of the terephthalate-alkyne.

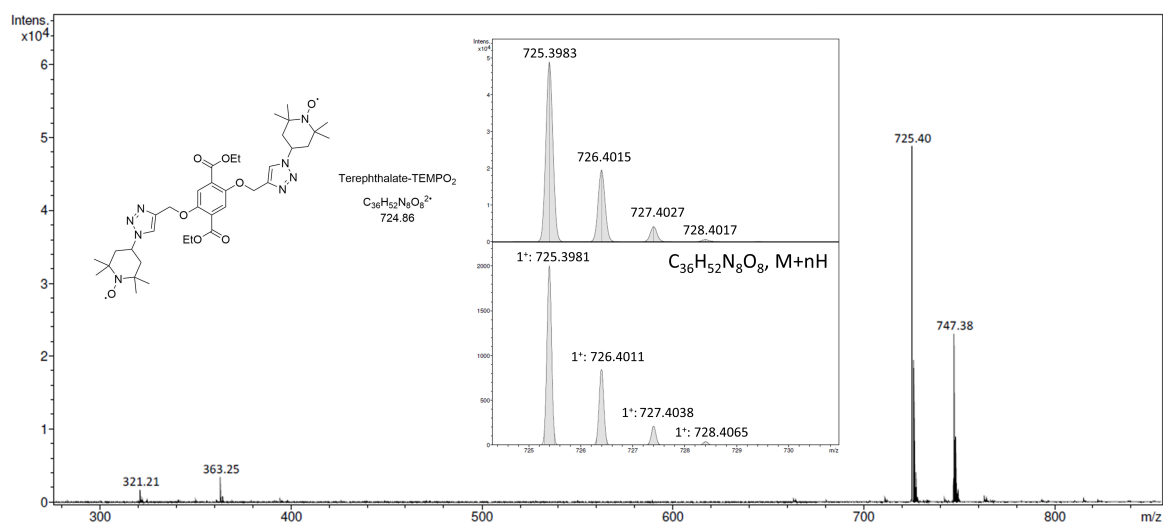


Figure A.32: Experimental and calculated (inset) mass spectrum of Terephthalate-TEMPO₂ clicked with the copper catalyst.

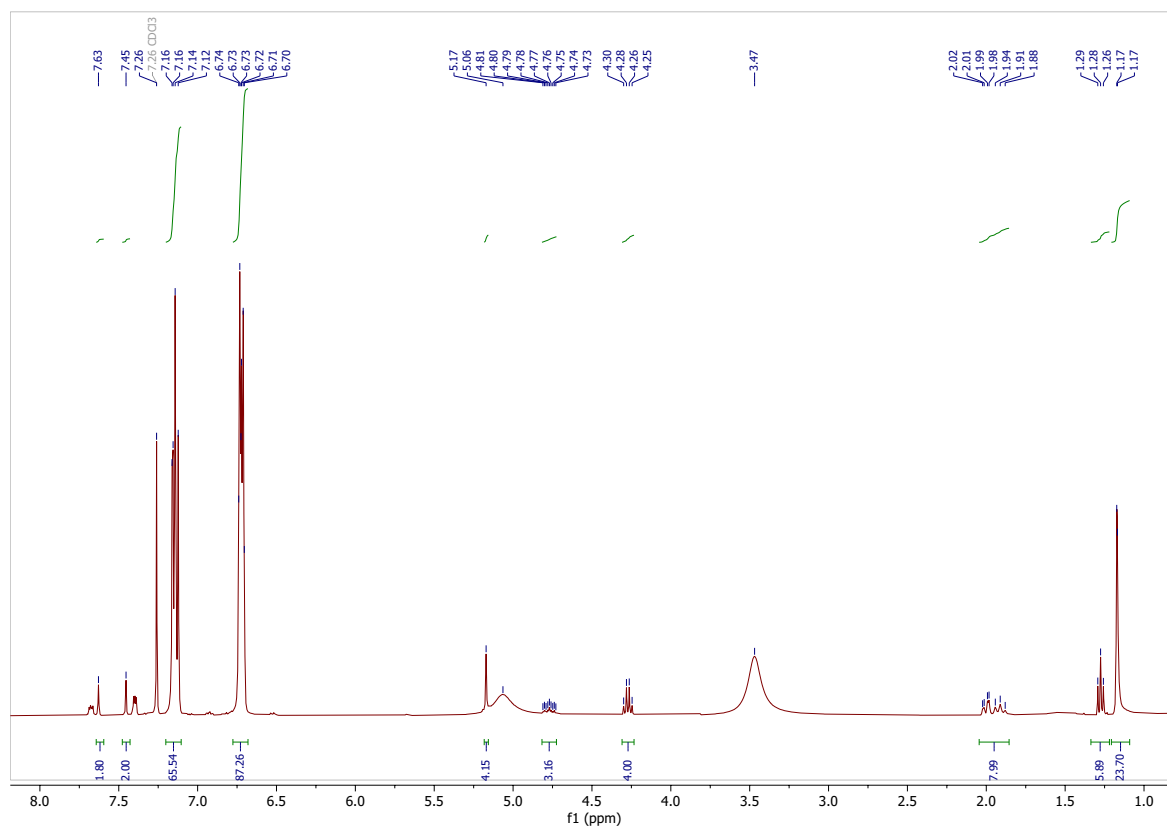


Figure A.33: ^1H NMR spectrum of Terephthalate-TEMPO₂ clicked with the copper catalyst and reduced with phenyl hydrazine. The multiplets at 6.7-7.2 ppm are from the aromatic protons in phenyl hydrazine and the broad bands at 3.5 and 5.1 ppm are from the NH protons in phenyl hydrazine.

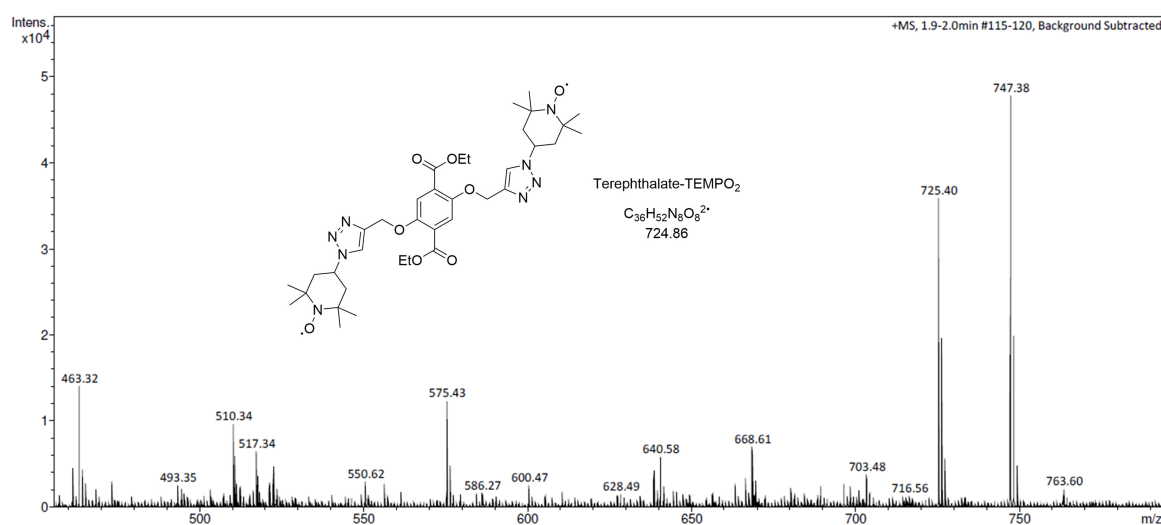


Figure A.34: Experimental mass spectrum of Terephthalate-TEMPO₂ clicked with the ruthenium catalyst.

Acknowledgements

First and foremost I would like to thank Prof. Dr. Joris van Slageren for the possibility to join his group for my Bachelor's thesis, giving me the opportunity to gain experience in modern spectroscopy, helping me to undertake a research stay abroad and then rejoining his group for my Master's thesis and the subsequent PhD thesis. I am very grateful for the experience in research, communication and management skills I gained because of his supervision.

I also want to thank the entire group for the great atmosphere during my time in the group. I would like to especially mention David Hunger and Lorenzo Tesi for the numerous fruitful scientific discussions; Dennis Schäfer and Jonathan Wischnat for the help during my time in the synthesis lab that would not have been as successful without them; Dominik Bloos, Heiko Bamberger, Samuel Lenz and Michal Kern for teaching me the basics of spectrometers and the theory behind the measurements; Martin Konečný for keeping the Mössbauer cryostat filled with liquid nitrogen; Felix Ehrlich, Kim-Isabelle Mehnert, Ralf Metzger, Florian Diehl and Lukas Bauder for their work in their respective Bachelor's theses.

Furtermore I would like to thank those in the institute who helped me during my thesis, namely Boris Tschertsche, Andreas Kübler and Thomas Weigend for repairing broken and improving unsatisfactory pieces of equipment as well as helping in designing and then manufacturing parts of the Mössbauer set-up and their involvement in the improvement of many other spectrometer set-ups; Herbert Dilger, Elisa Ilg, Diana Zauser and Gabriele Bräuning for helping with administrative issues.

I would like to thank also those in the low-temperature department of the physics institute, namely Bernd Schobel, Dario Profetto and Frank Wahl for providing liquid helium and nitrogen even on short notice to allow for our spectrometers to stay functional.

Many thanks also to cooperation partners without whom some of the measurements in this thesis would not have been possible, namely Marc Schnierle (Universität Stuttgart, group of Mark Ringenberg) for synthesising $(\text{dppf})\text{Fe}(\text{CO})_3$ and its derivatives; Edmund Little and Alena Sheveleva (University of Manchester, group of Floriana Tuna) for conducting the advanced pulsed EPR measurements; Lukas Burkhardt (Universität Paderborn, group of Matthias Bauer) for the X-ray emission measurements; Sebastian Emmerling (Max-Planck-Institut für Festkörperforschung Stuttgart, group of Bettina Lotsch) for providing the COF material; Ann-Katrin Beurer (Universität Stuttgart, group of Y. Traa) for providing the SBA-15 material.

Last but not least, I would like to thank my friends and family for their support.

Curriculum Vitae

Personal Data

NAME: Mario Winkler
DATE AND PLACE OF BIRTH: 10th June 1993 in Ostfildern, Germany

Education

- 2018 - 2023 PhD (Dr. rer. nat) in Physical Chemistry,
University of Stuttgart, Germany
Supervisor: Prof. Dr. Joris van Slageren
- 2015 - 2018 Master of Science in Chemistry
University of Stuttgart, Germany
Thesis: Investigations of Transition Metal β -Diketonate
Complexes in P3HT Matrices as Potential Qubit Systems
- 2012 - 2015 Bachelor of Science in Chemistry
University of Stuttgart, Germany
Thesis: Dekohärenz in Übergangsmetall-Phthalocyaninen

Publications

1. R. Bolney, M. Grosch, M. Winkler, J. van Slageren, W. Weigand, C. Robl, Facile synthesis and characterization of pure tochilinite-like materials from nanoparticulate FeS, *Z. Anorg. Allg. Chem.* **2022**, *648*, e202200219, DOI 10.1002/zaac.202200219.
2. M. Nöbler, D. Hunger, N.I. Neuman, M. Reimann, F. Reichert, M. Winkler, J. Klein, T. Bens, L. Suntrup, S. Demeshko, J. Stubbe, M. Kaupp, J. van Slageren, B. Sarkar, Fluorinated click-derived tripodal ligands drive spin crossover in both iron(II) and cobalt(II) complexes, *Dalton Trans.* **2022**, *51*, 10507-10517, DOI 10.1039/D2DT01005D.
3. M. Grosch, M.T. Stiebritz, R. Bolney, M. Winkler, E. Jückstock, H. Busch, S. Peters, A.F. Siegle, J. van Slageren, M. Ribbe, Y. Hu, O. Trapp, C. Robl, W. Weigand, Mackinawite supported reduction of C₁ substrates into prebiotically relevant precursors, *ChemSystemsChem* **2022**, *4*, e202200010, DOI 10.1002/syst.202200010.
4. M. Schnierle, M. Winkler, V. Filippou, J. van Slageren, M.R. Ringenberg, (Spectro)Electrochemistry of 3-(Pyrid-2-yl)-s-Tetrazine- or 1,2-(dihydro)pyridazine Tricarbonylrhenium(I)chloride, *Eur. J. Inorg. Chem.* **2022**, *10*, e202100998, DOI 10.1002/ejic.202100998.
5. M. Nöbler, D. Hunger, F. Reichert, M. Winkler, M. Reimann, J. Klein, S. Suhr, L. Suntrup, J. Beerhues, M. Kaupp, J. van Slageren, B. Sarkar, Spin-state control of

-
- cobalt(II) and iron(II) complexes with click-derived tripodal ligands through non-covalent and fluorine-specific interactions, *Dalton Trans.* **2021**, *50*, 18097-18106, DOI 10.1039/D1DT03535E.
6. A. Almidani, M. Benz, M. Winkler, Y. Ikeda, B. Grabowski, J. van Slageren, D. Estes, The Reaction of $\text{HV}(\text{CO})_4\text{dppe}$ with MoO_3 : a Well-Defined Model of Hydrogen Spillover, *Catal. Sci. Technol.* **2021**, *11*, 7540-7544, DOI 10.1039/D1CY01374B.
 7. R. Bolney, M. Grosch, M. Winkler, J. van Slageren, W. Weigand, C. Robl, Mackinawite formation from elemental iron and sulfur, *RSC Adv.* **2021**, *11*, 32464-32475, DOI 10.1039/D1RA03705F.
 8. M. Winkler, M. Schnierle, F. Ehrlich, K.-I. Mehnert, D. Hunger, A.M. Shevelova, L. Burkhardt, M. Bauer, F. Tuna, M.R. Ringenberg, J. van Slageren, Electronic Structure of a Diiron Complex: A Multitechnique Experimental Study of $[(\text{dppf})\text{Fe}(\text{CO})_3]^{+/0}$, *Inorg. Chem.* **2021**, *60*, 2856-2865, DOI 10.1021/acs.inorgchem.0c03259.
 9. M. Kern, L. Tesi, D. Neusser, N. Rußegger, M. Winkler, A. Allgaier, Y.M. Gross, S. Bechler, H.S. Funk, L.-T. Chang, J. Schulze, S. Ludwigs, J. van Slageren, Hybrid spintronic materials from conducting polymers with molecular quantum bits, *Adv. Funct. Mater.* **2021**, *31*, 2006882, DOI 10.1002/adfm.202006882.
 10. M. Benedikter, J. Musso, M.K. Kesharwani, K.L. Sterz, I. Elser, F. Ziegler, F. Fischer, B. Plietker, W. Frey, J. Kästner, M. Winkler, J. van Slageren, M. Nowakowski, M. Bauer, M.R. Buchmeiser, Charge Distribution in Cationic Molybdenum Imido Alkylidene N-Heterocyclic Carbene Complexes: A Combined X-Ray, XAS, XES, DFT, Mössbauer and Catalysis Approach, *ACS Catal.* **2020**, *10*, 14810-14823, DOI 10.1021/acscatal.0c03978.
 11. K. Bader, M. Winkler, J. van Slageren, Tuning of Molecular Qubits: Very Long Coherence and Spin-Lattice-Relaxation Times, *Chem. Commun.* **2016**, *52*, 3623-3626, DOI 10.1039/C6CC00300A.